Mechanistic Modeling Of Corrosion Fatigue Crack Growth Of Steels In Aqueous Solutions.

Order Number 9008094

Mechanistic modeling of corrosion fatigue crack growth of steels in aqueous solutions

Thomas, James Paul, Ph.D.

Lehigh University, 1989

U·M·I
300 N. Zeeb Rd.
Ann Arbor, MI 48106

MECHANISTIC MODELING OF CORROSION FATIGUE CRACK GROWTH OF STEELS IN AQUEOUS SOLUTIONS

BY

JAMES PAUL THOMAS

A DISSERTATION
PRESENTED TO THE GRADUATE COMMITTEE
OF LEHIGH UNIVERSITY
IN CANDIDACY FOR THE DEGREE OF
DOCTOR OF PHILOSOPHY
IN
APPLIED MECHANICS

LEHIGH UNIVERSITY
1989

Approved and recommended for acceptance as a dissertation in partial fulfillment of the requirements for the degree of Doctor of Philosophy.

September 25, 1989
(Date)

R. P. Wei
R. P. Wei, Professor in Charge

Accepted September 25, 1989
(Date)

Special Committee directing the doctoral work of Mr. James P. Thomas

D. G. Harlow
Professor D. G. Harlow, Chairman

F. Erdogan
Professor F. Erdogan

J. P. King
Professor J. King

G. W. Simmons
Professor G. W. Simmons

R. P. Wei
Professor R. P. Wei

ACKNOWLEDGEMENT

The author wishes to express his sincere appreciation to Professor Robert P. Wei, his dissertation advisor, for his support and guidance throughout the course of this dissertation research. Appreciation is also expressed to the members of the author's Special Committee: Professor Gary Harlow, Professor Jerry King, Professor Fazil Erdogan, and Professor Gary Simmons.

The helpful discussions and technical assistance of Mr. Metin Akbil, Dr. Donald Allison, Professor Dominic Edelen, Dr. Ming Gao, Dr. Paul Joseph, Mr. Carl Miller, Mrs. Shirley Simmons, Mr. Peiyan Xu, and Mrs. Hui Yin are greatly appreciated.

A special appreciation is expressed towards Professor Robert Little, for his advice during the author's undergraduate education, and for the introduction he gave to the interesting problems of fatigue and fracture.

The author gratefully acknowledges the generous financial support from the General Motors Foundation, in the form of the General Motors Teaching Fellowship, for four years of his doctoral program. Special thanks are given to Mr. Elmer Reese and Mr. Bill Collins of the General Motors Corporation, for their efforts, support, and encouragement of this Teaching Fellowship in the Mechanical Engineering and Mechanics Department at Lehigh University.

The author also acknowledges the financial support of this research program by the Office of Naval Research, under Contract N00014-83-K-0107, NR 4315 097, and Lehigh University in the form of a Teaching Assistantship.

And finally, the author would like to thank the members of his family; parents, Clifford and Margaret Thomas; and his sister and brothers, Nancy, John, and Allen Thomas, for their constant encouragement and support.

TABLE OF CONTENTS

LIST OF TABLES

LIST OF FIGURES

ABSTRACT

The primary objective was to develop a model for the effects of the range of stress intensity factor (ΔK), cyclic loading frequency (f), and temperature (T) on the enhancement of the crack growth rate (ECGR) for medium to high strength steels in aqueous environments. Also, an understanding was sought for the role played by ΔK, f, and T on the chemical and mechanical processes leading to an ECGR.

An experimental study was performed to determine the crack growth (CG) response of a HY-130 steel in de-aerated 3.5% NaCl solution, as a function of ΔK, f, and T. Tests were performed at three ΔK levels: 30, 21, and 14.5 MPa$\sqrt{m}$, with R=0.25; four temperatures, from 273 to 345 K; and eight frequencies, from 0.05 to 10 Hz; and polarization at −800mV (SCE). Reference rate tests were performed in dehumidified ultra high purity argon gas.

The crack growth rate (CGR) exhibited an exponential-like dependence on 1/f, with saturation occurring as the frequency decreased. Increases in ΔK increased the saturation CGR and shifted the data to lower frequencies. Increases in temperature shifted the CG response curve to higher frequencies, which corresponded to an apparent activation energy of 30 kJ/mol.

A modeling framework was developed to link the chemical and mechanical processes occurring at the crack-tip. ECGR was assumed to result from hydrogen embrittlement was controlled by the rate of the electrochemical surface reactions.

A model for the CG response, as a function of f and T, was developed based on the kinetic response of the transient surface reactions. The CG response is related to the charge transferred during the transient reactions, which explains the frequency and temperature dependence in terms of reaction kinetics and time.

A model for the CGR magnitude, as a function of K_{max} and the saturation charge transfer level, was developed based on the distribution of hydrogen at the crack-tip. The model accounts for the effect of K on the CGR in terms of its effect on the hydrogen distribution and the local crack-tip environment.

CHAPTER 1 - INTRODUCTION

SECTION 1.1 - BACKGROUND

The problem of corrosion fatigue is recognized as an important consideration in the design of engineering components and structures that are exposed to aqueous environments. The need for an accurate understanding of the problem is evident when considering the projected lifetimes of a number of engineering structures which can range from thirty years for offshore oil rigs and electric power plants to eighty years for bridges and even longer periods for high level nuclear waste storage. This has led to a considerable effort on the part of engineers and scientists to characterize and develop an understanding of the mechanisms for corrosion fatigue.

The problem of environmentally enhanced fatigue, or corrosion fatigue as it is known, seems to have first been noted in the early 1900's, by a publication of Haigh (1917), who showed that the presence of ammonia greatly decreased the fatigue life of some brasses. He also noted that a similar phenomenon had been observed in fatigue of mild steels and other metals when exposed to a number of corrosive environments. Since that time, research has shown Haigh's observations to be valid, and that both the initiation and the crack propagation phases of fatigue are accelerated by corrosive environments.

With the advent of linear elastic fracture mechanics in late the 1950's and early 1960's came a new approach for investigating the fatigue phenomenon. Environmentally assisted crack growth became an important area of research, with a focus on the complex interactions of the mechanical, environmental, and metallurgical variables. Work began by investigating the higher strength materials in simple gaseous environments, where an extensive data base was developed and used to obtain a mechanistic understanding of the influences of the key environmental, loading, and microstructural variables, and the effects of their interactions. It is only within the last decade that attention has been given to the more complicated problem of aqueous corrosion fatigue.

SECTION 1.2 - STATEMENT OF THE PROBLEM

At present, the understanding of the combined effects of the stress intensity factor range ΔK, the cyclic loading frequency f, and the temperature T, on the fatigue crack growth rate of medium to high strength steels in aqueous environments is

incomplete. This is especially true of the region of CG where ΔK is decreased towards the threshold level, ΔK_{th}, where the growth rate approaches zero.

An understanding of the effect of these variables on the crack growth rate is of considerable importance from the standpoint of elucidating the complex mechanical, environmental, and metallurgical interactions which occur during crack propagation. It is also important from the standpoint of estimating the reliability and durability of engineering components and structures with pre-existing cracks and flaws. Lifetime estimates must often be made using incomplete or limited laboratory data that have been obtained under test conditions more severe than those experienced in service. The required extrapolation to less severe operating conditions introduces unknown uncertainties into the estimate which have to be accounted for by large factors of safety. This underestimates the performance capability of the structure and adds to its cost. And so, in addition to the scientific interest in the problem, there is a genuine engineering need for a deeper understanding of corrosion fatigue and the variables which affect it.

SECTION 1.3 - THE RESEARCH OBJECTIVE

The main objective of this dissertation research is to contribute to the current understanding of the effects of the variables ΔK, f, and T, on the ECGR for medium and high strength steels in aqueous environments. The role and importance of these variables on the chemical and mechanical processes which govern the phenomenon will be examined by integrating mechanistic process models into a modeling framework for aqueous corrosion fatigue crack growth.

SECTION 1.4 - AN OUTLINE OF THE DISSERTATION RESEARCH

The approach taken in this dissertation is essentially an experimental one. Fatigue crack growth experiments are conducted on a single material & environmental system, under varying conditions of ΔK, f, and T. The results are used to provide a data base for the development and comparison of mechanistically based process models for the enhancement in the CGR.

A modeling framework for corrosion fatigue crack growth is developed and used to link the chemical and mechanical processes occurring in the crack. Mechanistic models for the surface reactions and the hydrogen diffusion process are examined and used to explain the effects of ΔK, f, and T on the enhancement of the CGR.

SECTION 1.5 - THE DISSERTATION STRUCTURE

Chapter 1 is an introduction to the dissertation research.

Chapter 2 is a technical review of the background material.

Chapter 3 is a description of the test objectives and experimental plan.

Chapter 4 is a description of the experimental techniques.

Chapter 5 is a description of the data analysis procedures.

Chapter 6 is a description of the experimental results with a discussion.

Chapter 7 is a description of the corrosion fatigue modeling.

Chapter 8 contains a comparison between the CF models and the FCG data.

Chapter 9 is a summary of the research and the conclusions.

CHAPTER 2 - TECHNICAL BACKGROUND

SECTION 2.1 - INTRODUCTION

This chapter serves as a review of the definitions, experiments, literature, and current level of understanding of the corrosion fatigue phenomena. The chapter is divided into four main sections. The first section deals with the definition of terms, the second with a review of the literature on experimental results, the third with a description of the chemical and mechanical processes which give rise to corrosion fatigue, and the fourth section contains a discussion based on the review which outlines the current research needs and the area investigated in this work.

SECTION 2.2 - DEFINITIONS

2.2.1 - The Definition of an Enhancement in the Crack Growth Rate

The enhancement in crack growth rate (ECGR) refers to the increase in CGR over some selected "reference" or "baseline" CGR and is expected to reflect the influence of an external environment on the cracking process. It is ***defined*** by:

$$\left(\frac{da}{dN}\right)_{cf} = \left(\frac{da}{dN}\right)_{e} - \left(\frac{da}{dN}\right)_{ref} \tag{2.1}$$

where the subscript "cf" refers to the ECGR, "e" refers to the physically observed or total CGR, and "ref" refers to a reference CGR.

Note that this definition does not imply the adoption of a "superposition" model (Wei & Landes, 1969; Wei & Gao, 1983) for crack growth. The identification of Equation 2.1 with a superposition model for CG requires an additional assumption that $(da/dN)_{cf}$ is independent of $(da/dN)_{ref}$. If for instance, $(da/dN)_{cf} = \alpha(da/dN)_{ref}$ where $\alpha=\alpha(f,T,etc.)$ is a multiplicative response function, then simple additivity no longer obtains and $(da/dN)_{tot} = (1+\alpha)\times(da/dN)_{ref}$.

On the other hand, if $(da/dN)_{cf}$ is taken to be independent of $(da/dN)_{ref}$, then the superposition model is applicable. In the most recent version of the model, Wei & Gao (1983) have parameterized the ECGR on the basis of experimental observation and a model for the weighted average of two parallel processes. The crack growth process is composed of two parallel CG processes, a "pure-mechanical" fatigue process with CGR, $(da/dN)_{ref}$, and a "pure-corrosion" fatigue process[1] with CGR, $(da/dN)_{max}$. The CGR

[1] The quantity $(da/dN)_{max}$ in this dissertation can be identified with the quantity $(da/dN)^{*}_{cf,s}$ in Wei & Gao (1983).

of each process is characteristic of the specific material/environment system under investigation. The overall growth rate is taken as a weighted average of the two processes which is equal to the sum of: (1) the fractional amount of the pure corrosion process times $(da/dN)_{max}$, and (2) the fractional amount of the pure mechanical process times $(da/dN)_{ref}$. Mathematically it is expressed as:

$$\left(\frac{da}{dN}\right)_e = \left(\frac{da}{dN}\right)_{max}\phi + \left(\frac{da}{dN}\right)_{ref}(1-\phi) = \left\{\left(\frac{da}{dN}\right)_{max} - \left(\frac{da}{dN}\right)_{ref}\right\}\phi + \left(\frac{da}{dN}\right)_{ref} \tag{2.2}$$

where

$$\left\{\left(\frac{da}{dN}\right)_{max} - \left(\frac{da}{dN}\right)_{ref}\right\}\phi = \left(\frac{da}{dN}\right)_{cf} \tag{2.3}$$

and

$$0 \leq \phi \leq 1 \tag{2.4}$$

and ϕ corresponds with the fractional amount of pure corrosion fatigue.

2.2.2 - The Driving Force for Crack Growth

Experimental evidence shows that the range of stress intensity factor ($\Delta K = K_{max} - K_{min}$) provides an excellent correlation[2] with the CGR for mode I loading conditions, when the assumptions of linear elastic fracture mechanics (LEFM) are satisfied (Paris & Erdogan, 1963; Johnson & Paris, 1968; and Erdogan, 1968; see also Section 2.3). This arises from the fact that K characterizes the stress and deformation fields at the tip of a crack (Rice, 1967; Erdogan, 1983), and led Paris et al. (1961) to suggest using ΔK as the "driving force" for crack growth.

For mixed-mode loading, Sih & Barthelemy (1980) and Badaliance (1980) have suggested using the range of the strain energy density factor, ΔS, as the driving force for crack growth. For mode I loading and satisfaction of the assumptions of LEFM, ΔS and ΔK are related (i.e. $\Delta S \propto \Delta K^2$), and either one can be used (see Chapter 4).

Having a measure of the driving force for crack growth has led to significant progress in understanding the mechanisms of fatigue, by uncoupling crack initiation and crack propagation (McEvily & Wei, 1972; and Wei, 1976). Interest in crack propagation phenomenon has resulted in a large number of proposed FCG "laws" (see for example: Paris & Erdogan, 1963; Erdogan, 1968; Hoeppner & Krupp, 1974) and led to advancement in the level of fatigue design (Paris, 1964; Hoeppner & Krupp, 1974; and Wei, 1978) by explicitly accounting for crack propagation in the design analysis.

---

[2] The correlation is valid only when the average stress intensity level ($\bar{K}$) is held constant. This condition is satisfied when the load or stress ratio (R) is held constant. See Section 2.3 for further details.

2.2.3 - Reference or Baseline CGR Characterization

The reference CGR refers to a CGR free of any environmental effects. It presumably can be determined by fatigue experiments in an "inert" environment (i.e., vacuum or inert gas) with the other controlling variables held constant (i.e., tests conducted with the same values of ΔK, T, etc.).

Unfortunately, problems can arise in that different, supposedly "inert" environments are known to give different CGR's (Liaw, et al., 1982; and Gao et al., 1988). This is probably due to causes such as the rewelding of the crack in a vacuum environment and inhibition of slip reversal by oxidation.

2.2.4 - Long and Short Corrosion Fatigue Crack Growth

Short crack growth phenomenon, or more precisely "chemically-short" CG phenomenon[3], refers to the observed behavior of small cracks in aqueous environments where the CGR is not a unique function of ΔK. Both ΔK and the chemical and mechanical enhancement processes depend on the crack length and this leads to a changing CGR with crack length under constant ΔK test conditions. The phenomenon has been observed for crack lengths shorter than 10 mm and generally leads to an increase in CGR over the long crack growth rate (see Table 2.2).

Long Crack Growth

Figure 2.1 is a schematic diagram representing the CG behavior of a number of different alloy-environment systems and is based on experimental observation (McEvily & Wei, 1972). Type A behavior is usually exhibited by aluminum-water systems, type B by steel-hydrogen systems, and type C behavior by most other alloy-environment systems, including the steels and environments considered in this dissertation. Note that the CG enhancement, $(da/dN)_{cf}$, is equal to the difference between the aggressive CGR and the inert CGR at a given value of K_{max}.

The diagram illustrates three important K values: the fracture toughness, K_{Ic} or K_c, the fatigue CGR threshold, K_{th}, and the stress-corrosion cracking threshold, K_{Iscc}. K_{Ic} or K_c are well known measures of the material's resistance to fracture, and K_{th} and K_{Iscc} are apparent threshold values for fatigue CG and stress-corrosion cracking (SCC) respectively and indicate K_{max} values at which the CGR approaches zero.

---

[3] There are also cracks that are referred to as "mechanically" short and "microstructurally" short. For general background on "small" crack phenomena, see Ritchie & Lankford (1986).

Short Crack Growth

Experimental observations have shown that the growth rate of short fatigue cracks (<10mm) in aqueous environments may be significantly different[4] than the expected behavior, based on longer crack data at a given ΔK level. A schematic diagram illustrating the effect is shown in Figure 2.2 (Nakai et al., 1986). The CGR is plotted versus crack length, for constant ΔK conditions showing several regimes of CG behavior and two characteristic crack lengths. This anomalous CG behavior was first reported by Gangloff (1981) who observed short CGR's an order of magnitude larger than the long CGR's, for an AISI 4340 steel in a NaCl solution at a given ΔK level.

The difference in CGR has been attributed to changes in the local crack-tip chemistry with crack length, via crack length effects on the electrochemical mass transport processes, and possibly to crack closure (Gangloff, 1981, 1985; Tanaka & Wei, 1985; Gangloff & Ritchie, 1985; Nakai et al., 1986; and Gangloff & Wei, 1986).

SECTION 2.3 - A REVIEW OF EXPERIMENTAL OBSERVATIONS

2.3.1 - Long Crack Growth Behavior

A large number of variables are known to have an effect on the CGR. They can be conveniently grouped into four categories of variables, namely: the mechanical, geometric, metallurgical, and environmental variables (Wei & Speidel, 1971, and Wei, 1979), as shown in Table 2.1. The primary variables, for a specific material/environment system, belong in either the mechanical or environmental categories. They include the variables ΔK, f, and T, specifically examined in this dissertation, as well as a number of others such as: R (load ratio), Φ_{ec} (applied electrochemical potential), pH, species concentration (c_i), etc. To provide some background on the effect of these variables and the evolution of aqueous corrosion fatigue modeling, a number of published results are summarized below.

Figure 2.3a shows the results of a study performed by Barsom (1971) on a 12Ni-5Cr-3Mo steel in aerated 3% NaCl solution at room temperature. The purpose of the investigation was to characterize the below K_{Iscc} fatigue CG behavior in terms of ΔK and f. He proposed an empirical model for the CGR:

$$\frac{da}{dN} = D_0 \Delta K^2. \qquad (2.5)$$

[4] The CGR is usually faster, but slower rates have also been observed (see Table 2.2 and Appendix A).

D_0 is taken as a function of cyclic loading frequency (i.e., $D_0=D_0(f)$) and reflects the frequency dependence of the CGR.

Figure 2.3b is a plot of $D_0(f)$ versus f showing the large increase in D_0 that occurs with decreasing f, and the asymptotic decrease towards the D_0 value obtained for tests in air, as f increases. He concludes, for this particular material/environmental system, that: (1) the primary factor affecting the CGR is the ΔK level, and (2) the $D_0(f)$ factor reaches a maximum value at small f, and a constant value, represented by the value in air, for increasing f.

Figure 2.4 shows results from Gallagher (1971) for a HY-80 steel in 3.5% NaCl solution and vacuum, under varying conditions of f and Φ_{ec}, at two ΔK levels[5]. The K_{max} for each case was below the K_{Iscc} value. The results show a number of important features: (1) vacuum data which is independent of f; (2) a saturating CG behavior at both the lower and upper values of f; (3) a CGR which approaches the vacuum CGR for higher f; (4) increasing CGR with increasing cathodic overpotentials; (5) relative values of enhancement (i.e., $(da/dN)_{cf}/(da/dN)_{ref}$) which are greater for the lower ΔK level; and (6) a possible shift in the CGR curves towards higher f values for the data at the lower ΔK level.

Using these results, and others not mentioned, Gallagher concluded that the below K_{Iscc} CG behavior depends strongly on the mechanical action of fatigue. It is taken to mean that the localized environmental attack will take place only when the crack is extended by the mechanical action of fatigue. He also concludes, on the basis of the cathodic polarization results, that hydrogen embrittlement is responsible for the ECGR.

Figures 2.5a and 2.5b show the results of Misawa et al. (1976) for a low alloy (0.5Cr-0.5Mo-0.25V) steel, in de-aerated, distilled water, at 20Hz, and different temperatures. The data in Figure 2.5a show a decrease in the number of cycles required for crack initiation and growth as the temperature is increased. Figure 2.5b shows the CGR behavior at several temperatures, over a range of ΔK levels.

Misawa et al. proposed an Arrhenius-type rate equation to describe the temperature dependence of the CGR:

$$\frac{da}{dN} = A \exp(-Q/RT). \tag{2.6}$$

[5] Note that the minimum load was held constant resulting in R values which varied during the test, and therefore, the results should be viewed with caution.

The coefficient A is a constant; R is the universal gas constant; T is absolute temperature; and Q is the apparent activation energy (see also Wei, 1968; and Telseren & Doruk, 1974, for similar models). Figure 2.5c is a plot of log(da/dN) versus 1/T which shows that the data exhibit a linear behavior. Figure 2.5d shows the calculated activation energies as a function of ΔK. They range from 4.2 to 21 kJ/mol and show some dependence on the ΔK level[6].

Unfortunately, they have neglected the possible influence of loading frequency which might account for the non-constant activation energy with ΔK level. This possibility is shown below in the discussion of Wei & Shim's results and also in Chapters 6 & 8.

Figures 2.6a through 2.6d are results taken from Vosikovsky (1978) showing the effects of ΔK, f, R, and Φ_{ec} on the CG behavior of a HY-130 steel in an aerated 3.5% NaCl solution. They show that the CGR increases with decreasing frequency, increasing R value, and increasing cathodic overpotential. They also show that an increase in R leads to a decrease in ΔK_{th}, and that the CGR curves for all the different frequencies converge to a single curve as ΔK approaches ΔK_{th}.

Figure 2.7a show the results of Wei & Shim (1984) for HY-130 steel in de-aerated, acetate buffer solution (pH = 4.2), for a single ΔK and R level and multiple f and T levels. The results show the effect of both frequency and temperature on the enhancement in CGR. A saturating, exponential-like CG behavior is observed with the saturation in CGR occurring as f decreases. The increasing temperatures are seen to produce a "shape-preserving", horizontal shift of the data towards higher f values.

As a first order approximation, Wei & Shim suggested the use of the simple, first order reaction kinetics model[7]:

$$\left(\frac{da}{dN}\right)_{cf} = \left(\frac{da}{dN}\right)_{sat} \left\{1 - \exp\left(-\frac{\nu}{f}\right)\right\} \tag{2.7}$$

where

$$\nu = \nu_0 \exp\left(-\frac{\Delta H}{RT}\right). \tag{2.8}$$

---

[6] Misawa et al. claim the activation energy is "sensibly" independent of ΔK level but that does not appear to be true on examining their data in Figures 2.5c & 2.5d.

[7] Note that the argument of the exponential function has been changed from $(\nu/2f)$ to (ν/f) to reflect the current understanding of the time available for the rate controlling reaction processes (Wei, 1985).

The factor $(da/dN)_{sat}$ is the saturation CGR, ν_0 is a constant, and ΔH is the apparent activation energy. The frequency and temperature dependence of the ECGR is expressed solely by the exponential term in Equation 2.7. Figure 2.7b shows a plot of ν versus 1/T, where an estimated activation energy of 39 kJ/mol is obtained.

The difference between Wei & Shim's interpretation of the temperature effect and that of Misawa et al. is by now obvious, and may be understood in terms of the CG response curve. The CG behavior exhibited in the $\log(da/dN)_{cf}$ versus $\log(1/f)$ plot is known as the CG response or CG response curve. The curve describes the characteristic functional behavior of the CGR on a loading cycle time base. The term or expression "characteristic functional behavior" refers to the fact that the rate controlling process (see Section 2.4) has a certain functional dependence on 1/f which is manifested by the CG response curve. The difference between CG response and CGR magnitude then, corresponds to the horizontal and vertical translations of the CG response curve. In other words, vertical shifts along the CGR axis correspond to changes in magnitude while horizontal shifts along the time or 1/f axis correspond to changes in response. Wei & Shim had looked at temperature as an effect on the CG response (horizontal behavior) whereas Misawa et al. looked at it as an effect on CGR magnitude (vertical behavior).

The model proposed by Wei & Shim is an extension of gaseous corrosion fatigue modeling to the aqueous corrosion fatigue problem. The model is based on the assumption that the ECGR results from embrittlement by hydrogen. $(da/dN)_{cf}$ is assumed to be proportional to the amount of hydrogen produced by the surface reactions each loading cycle, which is proportional in turn, to the "effective" crack area produced by fatigue during the prior loading cycles. They also assume that the electrochemical surface reaction processes are rate controlling with a time available for reaction directly proportional to 1/f.

Similarity between the activation energies for fatigue CG and the formation of an oxide layer on the bare surface of AISI 4340 steel via reaction with water vapor (i.e., 36 kJ/mol, Simmons et al. (1978)) tends to support the assumption of the surface reaction step as rate controlling. Further support is obtained from the experimental electrochemical results on bare surface reaction kinetics for steels in aqueous solutions (see Chapter 8, Section 2).

2.3.2 - Short Crack Growth Behavior

Table 2.2 lists a number of experimental results concerning the effect of crack size on the CGR of steels exposed to aqueous environments. The results show that both increases and decreases in the CGR have been observed, with the ratio $(da/dN)_{small}/(da/dN)_{long}$ ranging from 500 to 0.8.

Nakai et al. (1986) conducted a study of the short crack phenomenon on a HY-130 steel, in de-aerated, 3.5% NaCl solution, under constant ΔK test conditions, and two different Φ_{ec} levels. Their results are shown in Figures 2.8a and 2.8b, and 2.8c, where short crack effects were observed over crack lengths, extending sometimes to 12 mm. Figures 2.8a and 2.8b show the effect of ΔK on the short CGR for both the open circuit and zinc coupled conditions, and Figure 2.8c shows the effect of Φ_{ec}.

It can be seen that the short CG effect is not very pronounced at any of the given conditions. It appears that higher ΔK levels lead to a longer range of short crack effects (Figures 2.8a & 2.8b) as does higher cathodic overpotentials (Figure 2.8c). The effect of ΔK and Φ_{ec} on the ratio of the maximum short CGR to the long CGR show that the maximum ratio occurs at: (1) the lower ΔK level for the open circuit condition (Figure 2.8a), (2) the higher ΔK level for the zinc coupled test (Figure 2.8b), and (3) the open circuit condition for equal ΔK levels (Figure 2.8c). It is apparent that the zinc coupled specimens exhibit a higher overall crack growth rate for all ΔK conditions; this is consistent with the previously reviewed results.

SECTION 2.4 - THE CHEMICAL AND MECHANICAL PROCESSES OF CF

2.4.1 - The Concept of a Rate Controlling Process

In modeling the corrosion fatigue crack growth behavior, the concept of a rate controlling process becomes important. The enhancement in CGR occurs as a result of the interaction between a number of coupled, mechanical and chemical processes, which include: electrochemical (EC) mass transport, heterogeneous (and homogeneous) reaction chemistry, and some sort of enhancement mechanism, all acting in series (see Figure 2.9, and also Figure 7.1). It is clear that an analytical description of the enhancement process, if one is possible, will be difficult to formulate and difficult to solve.

In certain situations, the rate of a single process controls the overall rate. This occurs when the sequence of processes are all connected in series and the rate constant of one process is much smaller than all the others. The rate of the whole process is then

controlled by that single process and the other processes can be considered to proceed at their quasi-equilibrium rate or steady-state rate (Bockris & Reddy, 1977b; Conway, 1965). Note however that the rate constant of the controlling process often contains variables or quantities that can be affected by the preceding and/or subsequent processes (see Bockris & Reddy, 1977b). This provides the means for a non-rate controlling process to exert an influence on the kinetics of the process by effecting a change on the rate constant. The concept is very useful in modeling complex series processes in that only the dynamic response of "rate controlling" process need be considered. The concept arises traditionally in queuing theory whose concern is to relate the magnitude of the queue to the arrival and servicing rates (Van Kampen, 1984).

The rate controlling process in the corrosion fatigue problem will define the characteristic functional behavior of the CG response curve. For example, if the rate controlling process is described by an exponential function of time, then the fatigue crack growth response curve (i.e., $(da/dN)_{cf}$ versus $1/f$) will also be an exponential function of time ($1/f$). The other processes in the sequence occur at their steady-state or quasi-equilibrium rate and are only capable of producing a change in the vertical or horizontal location of the CG response curve in the $(da/dN)_{cf}$ versus $1/f$ plot.

Identification of the rate controlling process is made possible by comparing experimental CG response data with viable process models, developed from independent analysis and/or experiment. When the functional behaviors match, a candidate for the rate controlling process has been found. In the case where two or more processes have the same functional form which match with the CG response data, an examination of the effect of the other variables must be used. For instance, a number of processes are thermally activated in nature and the value of their activation energies provides a criterion for discriminating amongst competing models. Examples of this method applied to corrosion fatigue modeling can be found in Wei & Simmons, 1981; Wei & Shim, 1984; Shim & Wei, 1987; Wei, 1989.

2.4.2 - Electrochemical Mass Transport Processes

The theoretical description of the electrochemical mass transport processes is useful in determining the local crack-tip environment (i.e., the chemical species concentrations and electrochemical potential) which is known to influence the rates of electrochemical reactions in the crack-tip region. Analytical approaches have become necessary because of the small size of the crack-tip region where experimental probing

has not yet been accomplished in a totally satisfactory manner (see Turnbull, 1982). Unfortunately, obtaining solutions to the transport equations is difficult and must often be accomplished numerically, leading to a limited use of the results. Specification of the boundary conditions is also very difficult because of the lack of information concerning bare surface reaction kinetics. A review of the theoretical description of the electrochemical mass transport process is given below along with pertinent references to published results.

The spatial and temporal description of chemical species concentration and electrochemical potential, in and along an opening-and-closing, fluid filled crack, is an electrochemical mass transport problem. The theoretical formulation of the problem derives from the theory of mixtures within the field of non-equilibrium continuum thermodynamics (see Chapter 7, Section 7.3). The formulation consists of (1) the balance equations of mechanics: mass balance of the entire mixture, mass balance for each independent solute chemical species, and balance of linear and angular momentum; (2) the first and second laws of thermodynamics: balance of energy for the entire mixture, and non-negativity of entropy production; and (3) because the aqueous solution is ionic in nature, Maxwell's equations of electrodynamics.

The three steps listed above are capable of delivering the most general macroscopic description of an electrochemical mass transfer process. Completely general models have been formulated, but because of the resulting mathematical complexity, a number of assumptions must be made to simplify the problem and obtain a solution. The most important assumptions used are listed below and then a description of the EC mass transport process, for the localized crack geometry, is given with reference to the pertinent literature.

The assumption of an "infinitely dilute" solution, where the solute chemical species concentrations are vanishingly small, is usually applied, leading to the simplification of the chemical potential to the species concentration. The electrodynamics problem is simplified to one of electrostatics, and within this framework, further simplification comes from ignoring the charge distribution at the boundary, in the diffuse region of the electrode double layer, so that an assumption of electroneutrality may be imposed (see Newman, 1973). The water solvent is considered to be a simple Newtonian fluid with material properties that are uninfluenced by the presence of the chemical species. And thermal transport is neglected and a uniform temperature distribution is assumed.

Imposing these assumptions on the problem leads to a "relatively simple" set of governing equations, capable of describing the important details and serving as an useful approximation. They consist of a description of: (1) the movement of mobile solute chemical species, (2) material balances, (3) current flow, (4) electroneutrality, and (5) fluid flow, and are given below in their usual form (Newman, 1973).

(1) Species Flux

The following equation relates the molar flux of a minor component (i^{th} species) to the three driving forces for species movement namely, the electric field gradient (ionic migration), the concentration gradient (diffusion), and the bulk solution movement (advection).

$$\vec{J}_i = -z_i u_i F c_i \nabla\Phi - D_i \nabla c_i + c_i \vec{v} \tag{2.9}$$

where

$\vec{J}_i$ is the vector flux of the i^{th} species [mol/m^2·s],

z_i is the number of proton charges carried by the i^{th} species,

u_i is the mobility of the i^{th} species [m^2·mol/J·s],

F is Faraday's constant [coul/mol of electrons],

c_i is the molar concentration of the i^{th} species [mol/m^3],

Φ is the electrochemical potential [volts],

D_i is the diffusion coefficient of the i^{th} species [m^2/s],

$\vec{v}$ is the barycentric (mass center) velocity [m/s].

(2) Mass Balance for the Minor Species

$$\frac{\partial c_i}{\partial t} + \nabla \cdot \vec{J}_i = R_i \tag{2.10}$$

where

R_i is the rate of production of the i^{th} species [mol/m^3· s].

(3) Current Flow

$$\vec{i} = \sum_{i=1}^{n} F z_i \vec{J}_i \tag{2.11}$$

where

$\vec{i}$ is the current density vector [A/m^2]

n is the total number of minor species.

This equation expresses the current density in terms of the flux of the charged species.

(4) Charge Neutrality

$$\sum_{i=1}^{n} z_i c_i = 0 \tag{2.12}$$

This equation implies that in any region of space the total charge is equal to zero.

(5) Fluid Flow

The following well known equations for an incompressible, Newtonian fluid, are used to describe the bulk motion of the fluid. The first equation expresses the balance of mass for the entire mixture, and the second equation, the balance of linear and angular momentum.

Continuity Equation for an incompressible fluid

$$\nabla \cdot \vec{v} = 0 \tag{2.13}$$

Navier-Stokes Equation

$$\rho\left(\frac{\partial \vec{v}}{\partial t} + \vec{v} \cdot \nabla \vec{v}\right) = -\nabla p + \mu \nabla^2 \vec{v} + \rho \vec{g} \tag{2.14}$$

where

ρ is the fluid density [kg/m^2],

p is the thermodynamic pressure [N/m^2],

μ is the fluid viscosity [kg/m·s]

$\vec{g}$ is the vector acceleration of gravity [m/s^2].

In cracks and crack-like geometries, the problem is often further reduced to one spatial dimension by neglecting the variations of concentration, potential, and fluid flow, in the specimen thickness direction, and by assuming an average value for them in the crack opening direction.

The analysis of electrochemical systems by means of the above differential equations requires additional statements describing the geometry of the system, the conditions at the boundaries of the system, and the conditions throughout the system at time t=0. The boundary conditions must be obtained from equations describing the reactions at the surface (see below) and consist of the prescription of species concentrations or flux, c_i or $\vec{J}_i$, and electrochemical potential, Φ, at all points on the boundary, for all times. The initial conditions consist of the prescription of c_i and Φ, for all locations at time t=0.

Particular models and analyses of EC mass transport in a growing fatigue crack have been published. These will not be described here as there are a number of good reviews on the state of transport modeling and experimental measurement in the literature. These reviews include the papers by Turnbull (1982, 1983, and 1984a), Wei et al. (1984), and the books edited by Gangloff (1984), Staehle et al. (1974), and Turnbull (1984b).

In Chapter 8, some published results are examined with respect to the effect of ΔK on the CG response and magnitude via its effect on the local crack-tip chemistry.

2.4.3 - Heterogeneous Reactions in a Fatigue Crack

A number of factors complicate the description and understanding of reaction processes which occur at the interface between the aqueous environment and the metal surface. These include: the difficulty in specifying the local crack-tip chemistry (i.e., Φ, pH, c_i, etc.); the unknown electrode surface state (i.e., film characteristics, subsurface metal composition, surface area, etc.); lack of information on film-free surface reaction kinetics; and the small volume of the crack-tip region. An idealized outline of the reaction processes, as they occur in a growing fatigue crack, is given below. It is assumed, for simplicity, that there is no externally applied potential.

With each mechanical loading cycle, an increment of crack growth is produced exposing a small amount of bare (or film-free) surface to the surrounding environment. The bare surface is very unstable, with a potential that is negative with respect to its oxidized (filmed) state (see below), and it immediately reacts with surrounding environment to form a surface film and continues until a stable surface state is achieved.

Because the bare surface is in electrical contact with the adjacent oxidized (filmed) crack flanks, a current transient between the two surfaces results with anodic reactions taking place on the bare surface and cathodic reactions on the oxidized surfaces. Because the oxidized surfaces are much larger in area, the overpotential[8] at the oxidized surface is only slightly cathodic while the overpotential at the bare surface is highly anodic. It is like having the bare surface potentiostatically controlled at the oxidized surface potential, using the electrically connected oxidized surfaces as a potentiostat.

[8] The overpotential is a measure of the current producing potential on an electrode. It is equal to difference between the potential measured at the surface of the electrode and the free corrosion potential of the electrode for the given chemical environment (see Bockris & Reddy, 1977b; and Bockris, 1971). In the present case, the measured surface potential is taken to be equal to the mixed potential of the bare and oxidized surfaces.

The experiments on the nature of fresh metal surfaces in aqueous solutions, by Funk et al. (1957a, b, 1958), Giddings et al. (1959) and more recently, Anderson et al. (1969), showed that the sudden exposure of bare surface, via straining or scraping, led to a large shift in the measured potential. The bare surface potential was usually negative with respect to an oxidized surface and rose rapidly to the oxidized surface potential (see Figures 2.10a, 2.10b and 2.10c). The potential transients were described in terms of three parameters: the maximum potential, the potential rise time, and the potential decay time (Funk, et al., 1957a).

A number of environmental and experimental factors were found to effect the maximum potential difference between the bare and oxidized surfaces (this difference is denoted by ΔV or $(\Delta V)_m$ in Figures 2.10a and 2.10b). The most important factor in determining the magnitude of ΔV was the nature of the filmed surface (Giddings et al., 1959). Environmental conditions which led to little or no surface film, or materials that have a porous film (such as iron and zinc), were found to have much smaller potential differences. Other environmental factors such as: pH, species concentrations, and concentrations of dissolved gas were all found to affect the transient. The technique used for generating the bare surface, and the equipment's transient response capabilities also could have an effect.

Due to the restricted nature of these experiments, no information on the resulting current transients could be obtained. This information, however, is very important for modeling the enhancement of the crack growth rate in a growing fatigue crack. Knowing the current is equivalent to knowing the rate of the reactions on the bare and filmed surfaces. In the simplest reaction scheme (i.e., anodic dissolution of iron on the bare surface and hydrogen reduction on the oxidized surface) the rate of the reactions tells: (1) how fast the iron on the bare surface is being dissolved, and (2) how fast the hydrogen is being generated on the oxidized surface. This information is very important for both anodic dissolution and hydrogen embrittlement models for the enhancement of the CGR.

Quantitative information on both the potential and current densities, and their transients under dynamically changing conditions, is also important for mechanistic studies of the electrode reactions (Bockris & Reddy, 1977a, 1977b; Laidler, 1970; Vetter, 1967; Conway, 1965; and Petrocelli, 1951). These mechanistic studies attempt to mathematically model the electrode behavior in terms of the surface and environmental conditions existing at the electrodes. This type of information (either analytical or

empirical) is very important in connection with transport problem in corrosion fatigue, in that the problem specification is incomplete until the potential and species concentration or flux along the boundaries can be given.

An in-situ fracture technique has been recently developed to generate a bare surface to measure the resulting current and potential transients (Alavi et al., 1987; and Wei & Alavi, 1988; also see Newman, 1984a; and Wei et al., 1989). In this technique, a fresh or bare surface is generated by the fracture of a notched round tensile specimen. The specimen is contained within an electrochemical cell and is electrically connected to an "oxidized" electrode through a zero-resistance current measuring device. The notched specimen is loaded to fracture while the current and potential transients are recorded. The technique is being used to probe the effect of electrode composition, solution composition and concentration, pH, temperature, etc..

The experiments performed utilizing this technique have been oriented towards simulating the electrochemical processes which occur in a fatigue crack as opposed to the direct determination of electrochemical reaction mechanisms. From the measured current transients, the charge transfer between the bare and oxidized surfaces is calculated and is related to the CG response. A number of different environments, temperatures, and applied potentials have been used in the tests, and comparisons with the fatigue crack growth response have been made (Thomas et al., 1986; Wei & Alavi, 1988). The results are encouraging and have been applied in Chapter 8 to provide support for the hypothesis of surface reaction control and to demonstrate the effect of the local crack-tip environment on the CG response.

2.4.4 - The Cause of CG Enhancement

The precise manner in which the crack-tip reactions lead to an enhancement in the crack growth rate is still a debated issue but two particular mechanisms are favored for steels. The first is known as the "anodic-dissolution" mechanism; generally applied to the lower strength alloys, where film rupture and growth, and dissolution of the crack-tip material leads to the increased crack growth rate. The second mechanism is known as the "hydrogen embrittlement" model and is generally applied to the medium and higher strength alloys. This model assumes that atomic hydrogen, generated by a reduction reaction, "embrittles" or weakens the material at the crack-tip. The weakened material has less resistance to crack growth which combines with the ongoing mechanical fatigue process to increase the crack growth rate.

Both mechanisms are related by the electrical coupling of the conjugate oxidation and reduction electrochemical reactions (i.e., the electrons generated by the oxidation reaction are consumed by the reduction reaction). Both processes are examined below with respect to the current understanding and applicability to the modeling of corrosion fatigue.

2.4.5 - The Anodic Dissolution Mechanism for CG Enhancement

The anodic dissolution mechanism, incorporating the "slip-dissolution", "brittle-film", and "active-path-corrosion" models, is generally applied to ductile-alloy/aqueous-environment systems, including low-strength ferrous alloys. The mechanism has recently been applied to the problem of corrosion fatigue by Ford (1983, 1984), and Hudak (1988).

The ECGR is related to the oxidation reactions which occur at the crack-tip, when the filmed crack-tip surface is periodically ruptured by the straining of the metal substrate. Thus crack advance is related, via Faraday's Law, to the amount of charge transferred (via the oxidation reaction) over the time period of a film rupture event.

The two primary components are the oxidation and repassivation kinetics, and the rate of occurrence of the film rupture events at the crack-tip. The ECGR is related to the mechanism by the following model (Hudak, 1988):

$$\left(\frac{da}{dN}\right)_{cf} = \left(\frac{da}{dr}\right)\left(\frac{dr}{dN}\right) \tag{2.15}$$

where

$$\left(\frac{da}{dr}\right) = \frac{M}{\rho z F}\int_0^{t^*} i(t)dt \tag{2.16}$$

is the amount of crack growth per rupture event, and

$$\left(\frac{dr}{dN}\right) = \frac{\Delta\epsilon}{\epsilon_f} \tag{2.17}$$

is the number of rupture events (r) per loading cycle. In these equations, M denotes the molecular weight of the reacting crack-tip metal, ρ the density of the metal, z the average number of electrons transferred per metal atom, F is Faraday's constant, t^* is the amount of time between rupture events, i(t) is the functional representation of the current generated by the oxidation reaction, $\Delta\epsilon$ is the crack-tip strain range during a fatigue cycle, and ϵ_f is the failure strain of the oxide film.

Quantitative prediction requires estimates of the reaction kinetics (i(t)), the crack-tip strain, and the film rupture strain. Bare surface reaction kinetics experiments are used to determine the current generated during the repassivation of the bare surface after exposure by scraping or straining (Newman, 1984a, 1984b). The crack-tip strains are estimated using analytical solutions for the deformation fields at the crack-tip, and more recently by experimental measurement (Hudak, 1988). And the film rupture strain is determined by experiment.

A recent examination of the predictive capability of the model, applied to the corrosion fatigue problem, found evidence to suggest that the model does not account for the ECGR (as a function of loading frequency) for a 304 stainless steel in an aqueous environment (Hudak, 1988). Also, the results of Ford (1983, 1984) need to be reexamined in light of the incorrect interpretation given to the bare surface reaction kinetics data (Wei et al., 1989).

For the medium and higher strength steels, the hydrogen embrittlement mechanism is favored as the cause for the ECGR (Hirth, 1980; Oriani, 1978). For this reason, and the failure cited above, the anodic dissolution mechanism will not be considered any further in this work.

2.4.6 - Hydrogen Embrittlement Models for CG Enhancement

Hydrogen embrittlement models are generally applied to the medium and higher strength steels, in hydrogenous environments. A full understanding of the manner in which hydrogen leads to an enhancement in CGR has not yet been achieved, but a number of mechanisms have been proposed (see Bernstein & Thompson 1974, 1981; Hirth, 1980; Louthan & McNitt, 1976; Oriani et al. 1985; Oriani, 1972, 1978; and Staehle et al., 1977). These include: the pressure expansion theory (Tetelman, 1969); the slip softening model (Beachem, 1972); the adsorption models (Petch & Stables, 1952; and Petch, 1956); and the decohesion model (Oriani, 1972, 1974, and 1977).

A number of these have been criticized (Hirth, 1980; Louthan & McNitt, 1976; and Oriani, 1978) based on comparison with a number of experimental results, and the decohesion model seems to have withstood the criticism best, perhaps because of the difficulties in quantifying certain terms in the model. Most likely, a complex process composed of a number of coupled mechanisms is necessary to account for the observed phenomena. A qualitative model, similar in nature to the decohesion model, is used later in the dissertation and so a brief description of the decohesion model is included below.

The decohesion model (see Oriani, 1972, 1974, and 1977) supposes that hydrogen at high concentrations lowers the maximum cohesive force between the atoms of the iron-alloy lattice, at grain boundaries, and at interfaces. Bond breaking results when the local stress equals the hydrogen-lowered cohesive stress. The hydrostatic tensile stress at the crack-tip serves to concentrate the hydrogen by several orders of magnitude (see Chapter 7, Section 3), and to sever the atomic bonds weakened by the hydrogen. Unfortunately, an explicit formulation for the decohesion model is impossible at present because of the lack of knowledge of how the local stress behaves in terms of the macroscopic parameters, and by the lack of knowledge of the precise change in cohesive force for a given hydrogen concentration.

A conceptual model for hydrogen embrittlement, similar in nature to the decohesion model and applicable to the corrosion fatigue problem, has been proposed by Pao et al. (1977). The model supposes that a zone of "embrittled" material exists ahead of the crack-tip under steady-state conditions (i.e., prescribed ΔK, f, T, environment, etc.) and is related to the enhancement in CGR in a simple fashion. The model is shown schematically in Figure 2.11, where the damaged zone is depicted as circles, representing some appropriate hydrogen concentration contours ahead of the crack-tip. The elongated regions represent a changing hydrogen concentration, as the crack grows, that occurs after a change in the cyclic load frequency. Because more hydrogen is produced at the lower frequencies (longer reaction time), the size of the damaged zone or the amount of hydrogen within the zone is expected to be larger at these frequencies. On each cycle of loading, the crack extends, in one step, through a fraction of this zone. Following this increment of crack growth, a steady-state zone is reestablished ahead of the extended crack-tip through reactions of the environment with the freshly created crack surface, and hydrogen diffusion and redistribution. A criterion similar to this is adopted for the modeling performed in this dissertation and is explained further in Chapter 7.

2.4.7 - The Hydrogen Entry Process

The process of hydrogen entry into the metal matrix from its source along the filmed crack walls, or through the filming new surfaces at the crack-tip, is a complicated problem irrespective of the nature of the source. The rates of deposition of atomic hydrogen on the interface, combination of the adsorbed hydrogen to form hydrogen gas, and the transition from adsorbed to absorbed hydrogen are controlled by a number of factors. These include: (1) solution pH, (2) electrochemical potential, (3) chemical

composition of the aqueous environment local to the entry point, (4) composition of the metal, its inclusions, and the surface films, and (5) the mechanical and thermal state of the material and environment (Bockris et al., 1965; McBreen & Genshaw, 1969; Kim & Wilde, 1971; McCright, 1977; Wilde & Kim, 1981; and Scully & Moran, 1988a, 1988b). The rate of transition between the adsorbed and absorbed hydrogen determines the subsurface hydrogen activity, which sets the boundary conditions for the diffusion of hydrogen into the bulk of the metal. This is an important concern for modeling the diffusion of hydrogen in the crack-tip region, and it is considered further in Chapter 7.

Hydrogen permeation by cathodic charging has been used with some success in studying hydrogen absorption and hydrogen diffusion behavior under a number of different conditions (Beck et al., 1965; Bockris et al., 1965; McBreen, et al., 1966; Kim & Wilde, 1971; Bockris, 1977; Wilde & Kim, 1981; and Scully & Moran, 1988a, 1988b; see also Turnbull & Saenz de Santa Maria, 1989). The technique generates hydrogen on one side of a specimen and measures the flux of hydrogen on the other side. Depending on the specimen's thickness and other environmental conditions, either the surface reaction or the hydrogen diffusion is rate controlling.

2.4.8 - The Hydrogen Diffusion Process

The hydrogen diffusion process for a solid, with a crack, under stress is complicated by at least two factors. There is the effect of hydrogen trapping at the chemical and microstructural inhomogeneities, and the effect of mechanical stress on the diffusional driving force. The second effect is discussed in Chapter 7 where a stress-assisted diffusion model is used to connect the crack-tip stress field to the magnitude of the ECGR. A brief discussion of the hydrogen trapping effects is given below along with the phenomenology of hydrogen in steels.

Hydrogen dissolved in the lattice of iron exists predominantly in the dissociated atomic or protonic form and occupies interstitial positions. The solubility of hydrogen in α iron is very small, and therefore the major portion of the hydrogen in ferritic steels is the result of attractive interactions at the chemical and structural features in the metal (Oriani, 1969, 1978; Hirth, 1980; and Johnson, 1988). These attractive interactions are known to "trap" the hydrogen at grain boundaries, internal interfaces, dislocations, voids, microcracks, etc.. Such trapped hydrogen is not as mobile as when it is moving through the normal lattice positions. In transient diffusion problems, the trapping can lead to anomalous results because of the hydrogen stored in the traps.

The modeling of Chapter 7 is concerned with "steady-state" fatigue crack growth and this mitigates, to some extent, the necessity of considering the trapping effects in the diffusion problem. This is because a steady-state hydrogen atmosphere surrounds the crack-tip, filling the traps and eliminating the anomalous diffusion behavior.

SECTION 2.5 - DISCUSSION

The review has focused on two major aspects of the research efforts in the field of corrosion fatigue crack growth. The first aspect to be considered was the results of the previous experimental FCG investigations. Most of this work was geared towards assessing the effects of a number of important variables on the enhancement of the CGR. The second aspect to be considered was the chemical and mechanical processes which exist in the growing fatigue crack and give rise to the enhancement phenomenon. This type of research is interdisciplinary in nature, and has evolved over a long period of time.

The previous experimental results showed that ΔK, f, T, R, and Φ_{ec} all play an important role in the corrosion fatigue crack growth process. Most of the studies were exploratory in nature, and conducted by investigating only one, and sometimes two or three variables at a time. This was due to the level of understanding of corrosion fatigue phenomenon at that time, which precluded anything other than the simple experiments that were performed.

Research on the individual chemical and mechanical processes which contribute to the corrosion fatigue phenomenon is necessarily complicated and interdisciplinary in nature and is not strictly (directly) applicable to corrosion fatigue modeling. In addition, there is the added complexity of integrating the individual models into a framework for the entire corrosion fatigue process. There are ongoing investigations into many aspects of these individual chemical and mechanical processes, but applications to corrosion fatigue phenomenon go slowly because of the complicated nature of each process, and the lack of understanding of the actual conditions which exist in the fatigue crack.

A new level of experimentation began with the work of Wei & Shim (1984). FCG experiments were designed to probe the CG behavior in a mechanistically relevant manner. They began their research program with the hypothesis that the surface reaction processes were rate controlling. Experiments were run under varying conditions of loading frequency and temperature, in order to probe the CG response, and the results were used to develop a mechanistic model based on surface reaction processes.

There is a need for further studies of this type in order to assess the combined effects of the other variables on the corrosion fatigue cracking process. An experimental research plan is undertaken in this dissertation, to assess the combined effects of ΔK, f, and T on the enhancement of the CGR. The effects of f and T can be predicted based on the current level of understanding, but the combined effects of all three variables is at present unknown.

Because ΔK is known to affect both the electrochemical mass transport process and the hydrogen diffusion process, a modeling framework will have to be developed to integrate all of the chemical and mechanical processes which contribute to the enhancement of the crack growth rate. To limit the scope of the investigation, only the effect of ΔK on the hydrogen diffusion process will be considered in detail. In addition, further consideration will be given to the currently proposed models for the surface reaction processes.

CHAPTER 3 - EXPERIMENTAL STUDY

SECTION 3.1 - INTRODUCTION

There were two objectives for the experimental phase of the dissertation research. The first, and most important objective, was aimed at providing a data base for the effect of ΔK, f, and T on the enhancement in crack growth rate of a single material/environmental system. The second objective was to provide data on the effects of ΔK, f, and T on the short fatigue crack growth behavior.

SECTION 3.2 - THE LONG CRACK GROWTH TESTS

3.2.1 - Test Objective Number 1: Long Crack Growth Characterization

To characterize the fatigue crack growth rate, of a HY-130 steel in a de-aerated, 3.5% NaCl solution, as a function of ΔK, f, and T. The ΔK levels were selected to cover the lower range of ΔK values, as ΔK was decreased towards ΔK_{th}. The loading frequencies were selected to cover the range of maximum environmental effects, and the temperatures were selected to cover the range of applications for the solution and material.

Reference rate tests were also required. These were conducted in a dehumidified, ultra high purity (UHP) argon gas environment, with a 10 Hz loading frequency and the same ΔK and T values that were used in the saltwater tests.

3.2.2 - The Test Plan

The long crack growth tests are conducted over the range of crack lengths from 9 to 18 mm. The test variables ΔK and T, are held constant over this interval, while different f levels are used over small sub-intervals of crack growth. Figure 3.1 illustrates the manner in which the test variables were varied over the range long crack growth and Tables 3.1 and 3.2 list the test values used.

SECTION 3.3 - THE SHORT CRACK GROWTH TESTS

3.3.1 - Test Objective Number 2: Short Crack Growth Characterization

To determine the range of crack lengths over which the short crack effects were present, and to determine the effects of ΔK, f, and T on the short CGR.

3.3.2 - The Test Plan

The preliminary tests (13-20) were conducted at two different levels for each of test variables (i.e., ΔK, f, and T). The results of these tests established that the first 9 mm of crack growth was the range over which the short crack effects could be detected. For the subsequent tests, crack growth data obtained from the region starting from the notch to 9 mm in length was considered as belonging to the "short-crack" regime. Test conditions (i.e., ΔK, f, and T) were maintained constant in this region so that changes in the CGR could be detected and easily interpreted. Figures 3.1 & 3.2 illustrate the manner in which the test variables were varied over the range of crack growth and Tables 3.3 and 3.4 list the test values used.

CHAPTER 4 - EXPERIMENTAL TECHNIQUE

SECTION 4.1 : INTRODUCTION

This chapter describes the method, procedures, and equipment used to measure the fatigue crack growth behavior of HY-130 steel in a de-aerated, 3.5% sodium chloride solution, under varying conditions of crack driving force, loading frequency, and temperature.

SECTION 4.2 TEST MATERIAL AND SPECIMEN INFORMATION

4.2.1 - Introduction

The material used in this investigation is a quenched and tempered HY-130 steel, similar to a 5Ni-Cr-Mo-V steel. It has a high resistance to crack propagation, in heavy sections, for temperatures down to about −60C, but both conventional fatigue strength and fatigue crack growth behavior are deleteriously affected by sea water and salt solutions.

4.2.2 - Physical, Mechanical, and Chemical Properties

HY-130 is a medium strength steel with high toughness and good corrosion resistance. The available properties and composition of this steel are listed in Tables 4.1 and 4.2. Some of the values were estimated, and others obtained from the literature, and are so indicated along with their sources.

The expression for the mechanical driving force for crack growth (MDFCG), explained below, contains the elastic constants, G, the shearing modulus, and ν, the Poisson's ratio. Because the FCG tests are conducted over a range of temperatures, an expression for the elastic constants, as a function of temperature, is required.

Bell (1968, 1973) had experimented with a number of materials and found that ν did not change with temperature, and that, a simple empirical relation characterized the temperature dependence of G. The relationship he recommended for use is:

$$G(T) = \alpha \left(1 - \frac{T}{T_m}\right), \tag{4.1}$$

where

T = material's temperature (K),

T_m = material's melting temperature (K), and

α is a constant that can be determined using G(293) and T_m.

4.2.3 - Specimen Geometry and Analytical Expression for K

The specimen configuration used is a 25.4 mm wide by 7.62 mm thick, single-edge-notched (SEN) specimen, with a 0.25mm long crack starter notch[1] prepared by electrical discharge machining (see Figure 4.1). The specimens are machined in the LT orientation, from a 25.4mm thick plate. The final direction of grinding is perpendicular to the direction of crack growth.

An expression for the mode I stress intensity factor, K, for the case of pure bending, is obtained by least squares fitting a 6^{th} degree polynomial (BMDP Program 5PR; BMDP, 1985) to the data given by Kaya and Erdogan (1980), Joseph and Erdogan (1987), and Joseph (1986). The expression, so obtained, is given below:

$$K = \frac{3PL}{BW^{3/2}}\left(\frac{\pi(a/W)}{(1-a/W)^3}\right)^{1/2} F(a/W), \tag{4.2}$$

where the range of validity is $0 \leq a/W \leq 0.8$, and

P = applied load,

L = 25.19 mm (pin spacing of the four-point bend fixture),

B = specimen thickness,

W = specimen width,

a = crack length, and

$$F(a/W) = 1.122 - 2.987(a/W) + 8.920(a/W)^2 - 21.12(a/W)^3 + 31.79(a/W)^4 - 26.02(a/W)^5 + 8.755(a/W)^6.$$

4.2.4 - The Mechanical Driving Force for Crack Growth

The range of the strain energy density factor ($\Delta S = S_{max} - S_{min}$) is used as the mechanical driving force for crack growth (MDFCG). This was proposed by Badaliance (1978), and was examined by Sih and Barthelemy (1980), Badaliance (1980), Sih and Moyer (1983), and Moyer and Sih (1984).

The expression for ΔS, for plane strain conditions, is given below:

$$\Delta S = \frac{1-2\nu}{4\pi G(T)}\left(\frac{1+R}{1-R}\right)\Delta K^2, \tag{4.3}$$

where

ν is Poisson's ratio,

$G(T)$ is the shearing modulus as a function of the temperature (T),

[1] The specimen originally contained a 0.10 mm long notch, but due to initiation problems, it had to be increased to 0.25 mm (see Appendix A: Tests 3 and 4).

ΔK is the stress intensity factor range ($\Delta K = K_{max} - K_{min}$), and

R is the load ratio ($R = P_{min}/P_{max}$).

The advantages of using ΔS for the MDFCG include its greater generality and the explicit incorporation of the load ratio and the material's elastic properties.

4.2.5 - FCG Specimen Preparation

Each specimen requires preparation in the form of cleaning, dimensional measurements, scribing of location marks on the specimen, attachment of electrical leads via spot welding, attachment of a strain gage on the back face of the specimen, attachment of a temperature probe, and mounting of the specimen in an environmental containment chamber. These steps are described, in sequential order, in the paragraph below.

(1) The cleaning procedure for the specimens includes sanding the entire specimen with #240, 320, and 400 grit SiC sandpaper, and then ultrasonically cleaning the specimen in an acetone bath. (2) Each specimen's width, thickness, notch width, and notch depth are measured. (3) The attachment points for the current, potential, and potentiostat leads, and the back-face strain gage (BFSG) are scribed on the specimen. (4) The potential leads are spot welded and sealed with epoxy. (5) The BFSG is attached with an epoxy bonding agent and then cured for two hours at 80°C. (6) The BFSG leads are soldered and the gage coated with a flexible, polysulfide polymer protectant (Measurements Group, 1986). (7) The current supply and potentiostat leads are spot welded and epoxy sealed. (8) The temperature probe is attached to the specimen surface using an alcohol based silicon rubber sealant and an O-ring clamp. And (9) the specimen is secured in the environmental containment chamber, and sealed with an O-ring and silicon rubber sealant. A fully prepared specimen is shown in Figure 4.2.

At the end of a test, the specimen is immediately removed from the chamber, rinsed in distilled water, and then immersed in liquid nitrogen. When sufficiently cooled, it is placed in the load fixture and fractured, and then placed in a beaker of methyl alcohol until it reaches room temperature. The electrical leads and strain gage are removed, and the specimen ultrasonically cleaned in acetone. The fracture surface is then scribed to aid the final crack length measurement. Figure 4.3 shows the location of the scribe marks on the fracture surface.

SECTION 4.3 - THE TEST MACHINE, BEND FIXTURE, AND CHAMBER

4.3.1 - The Test Machine

The tests are conducted on a MTS Series 809 Axial/Torsional Materials Test System, which is a computer (automated) controlled servo-hydraulic system. The test control programs are user written, in MTS Basic, and run on a DEC PDP 11/23 Plus computer. The load frame uses a 90 kN load cell which is calibrated at least once a year.

The capabilities of the test system, for the given configuration (hardware and software), include: load control better than ±40 N, for all loading conditions, a frequency range of approximately 0.01 to 10 Hz, and the capability of acquiring data every 12.5 μm of crack growth, at all loading frequencies.

The data acquisition system consists of 16 multiplexed channels using 16 bit conversion. The full scale range of ±10 Volts measurement on each channel gives a conversion graduation of 3280 bits/volt or 300 μV/bit.

4.3.2 - The Four Point Bend Fixture

The load fixture is a four point load fixture which creates a constant bending moment in the test section of the specimen. An outer pin span of 117 mm and an inner pin span of 67 mm gives a 25 mm moment arm, and a minimum pin to crack separation distance of 34 mm. The pins are precision ground alumina rods (for electrical isolation) of diameter 15.88 mm, and are spring loaded to allow rotation under specimen flexure (Brown and Srawley, 1966).

A special alignment fixture is used to insure proper specimen to load fixture alignment. Two 0.25 mm thick brass shims, attached to the specimen under the inner load pins, helps to minimize any alignment or load distribution problems.

4.3.3 - The Environmental Chamber

An environmental chamber, shown in Figure 4.4, is used to contain the aqueous environment about the crack. It is constructed of a chlorinated polyvinyl-chloride (CPVC) material, having quartz glass windows on both sides of the chamber at crack level, and polyethylene plumbing fittings. The chamber is sealed to the specimen by clamping the chamber around the specimen; a Viton O-ring and alcohol based silicon rubber sealant are used to provide a water tight seal. The chamber has eight fluid or wire entrance ports; the ports containing wire leads are sealed by passing the wires through a rubber septum filled with silicon rubber sealant and then clamped shut. The

Luggin probe, for electrochemical potential measurements, is terminated about 1 mm from the specimen surface, close to the neutral axis of the specimen, and about 5 mm to the side of the crack path. The chamber fluid volume is 70ml with the specimen in place.

SECTION 4.4 - TEMPERATURE CONTROL AND MEASUREMENT

4.4.1 - Temperature Control of the Specimen and Solution

The temperature of the specimen is controlled by the attachment of two copper heat exchange blocks, clamped at both ends of the specimen. The solution entering the environmental chamber is also temperature controlled using a glass heat exchanger (a Graham condenser). The source of heating or cooling is a temperature controlled water bath with a remote circulation pump. The temperature of the bath is manually set and then maintained by a thermostatic controller. The specimen temperature is controlled to within $\pm 1^{\circ}C$, once the starting temperature is achieved. An improvement in temperature control could be achieved by incorporating an electronic feedback control system to directly control the bath temperature based on the specimen's temperature.

4.4.2 - Temperature Measurement

Temperature is measured on the surface of the specimen using a commercially available thermistor[2] probe. The probe is contained within a Teflon sheath and attached to the surface using silicon rubber sealant and an O-ring clamp (see Figure 4.2). The probe manufacturer's specified accuracy is $\pm 0.1^{\circ}C$, and the accuracy of the total temperature measurement system is estimated to be better than $\pm 0.5^{\circ}C$.

The temperature of the thermistor is determined by measuring its voltage drop for a constant 1.2 μA throughput current. The voltage is amplified and sent to the computer which converts it to a temperature using Ohm's Law and the Steinhart & Hart equation (Trietley, 1985a & 1985b; and Flora, 1985). Better accuracy could be obtained with a Wheatstone bridge arrangement for the resistance measurement.

SECTION 4.5 - THE SALTWATER AND ARGON GAS ENVIRONMENTS

4.5.1 - The NaCl Solution Preparation

The solution is 3.5% NaCl by weight, and is prepared in 50 l batches using reagent grade NaCl and distilled water. Class A precision glassware is used for the volumetric measurements. A standard reference state temperature of 20°C is used for

[2] A temperature sensitive resistor.

glass and fluid volumetric corrections due to temperature deviations during mixing (CRC Handbook, 1976).

The solution is de-aerated using high purity N_2 gas, passed through an Oxi-sorb cartridge and then bubbled into the stirred solution, in the reservoir, for at least 12 hours prior to the start of a test. The dissolved oxygen concentration, pH level, and specific gravity are measured 1 m downstream from the reservoir, in a sealed sampling chamber. The average measured value of these quantities is reported in Table 4.3.

4.5.2 - The Solution Supply System

The solution supply system, shown in Figure 4.5, consists of a 50 l supply reservoir, a peristaltic pump, a flowmeter, two glass heat exchangers, the environmental chamber, and the counter electrode chamber. Connections are made with Tygon tubing, and a 3.5 ml/min flowrate is maintained throughout the test. This results in a replenishment rate equal to 3 complete fluid replacements within the chamber per hour.

One of the glass heat exchangers is used only during the high temperature tests (T>320K) to remove excess dissolved N_2 from the solution; N_2 bubbles will form in the chamber otherwise.

4.5.3 - The Argon Gas System

The argon gas system is shown in Figure 4.6, and consists of the following components: the argon supply tank with pressure regulator, 3 liquid N_2 moisture traps, a (5×) zeolite molecular sieve[3], a 10 to 200 kPa pressure gage, an oil back diffusion trap, assorted fittings & valves, and polypropylene tubing. Commercially available, ultra high purity (UHP) argon gas (99.999%), in conjunction with purifying equipment is used to provide an atmosphere free from water vapor. During the test, a pressure of 27.6 kPa (gauge) is maintained on the system with a continuous flow of Argon.

SECTION 4.6 - THE CRACK LENGTH MEASUREMENT SYSTEM

4.6.1 - Introduction

In automated FCG testing, an indirect method for measuring the crack length is necessary. The AC and DC potential drop (PD) methods, the compliance method, and a number of other methods have been used for this purpose (Beevers, 1980, 1978; Hudak Jr. & Bucci, 1981; Birnbaum & Free, 1981).

[3]Purged and dried at 150°C for 24 hours before the start of the Argon tests.

The AC potential drop method is used in these experiments, and is capable of very precise crack length measurements. The method requires minimal computation to obtain a crack length from the measured voltage, is easy to use in hostile environments and small spaces, and has excellent noise filtering capabilities (Wei & Brazill, 1981; PAR TAN 115, 116, 127; Letzter & Webster, 1970; and PAR OSM 126).

A description of the AC potential drop method, the experimental equipment and setup, and the steps taken to generate the calibration data is given in the following subsections. A description of the relationship between the crack length and PD is given in the next chapter.

4.6.2 - The Theoretical Relationship Between Crack Length and PD

The electrical behavior of an metal, under the influence of a sinusoidal current, is described by the vector Helmholtz equation (Moon & Spencer; 1961, 1960, 1953). This equation follows from Maxwell's equations of electrodynamics, by introducing the simplifications which result from the fast relaxation time of a conductor and the sinusoidal nature of the applied current signal.

The presence of mechanical stresses in the conducting solid affects the electrical behavior of the system and accurate modeling requires the use of the equations of magneto-solid mechanics (Moon, 1984; Hutter and Ven, 1979; and Jordan & Eringen, 1964a, 1964b). A number of interesting interaction phenomena are known to occur in a solid under stress (see Williams (1931) for a particularly simple account) depending on the magnitude of the applied current and stress level, as well as the material's electro-mechanical properties. The presence of a crack, with possible crack face contact, further complicates the analysis (Gangloff, 1982). Fortunately, the electro-mechanical effects are second order (i.e., enter into the constitutive equations as squared terms) in the strain and current density magnitude which suggests that the electro-mechanical effects will be small for the present situation. The crack face contact effects may not be small, as shown by the results of tests 1 through 12 in Appendix A.

A theoretical description of the AC potential distribution for the SEN specimen was not attempted. Instead, an empirical approach was used, where a polynomial is fit by least squares to the crack length/potential drop data obtained by an experiment. Details of the method are presented below.

4.6.3 - The Test Equipment and Setup

A small alternating current of 950 mA (true RMS) is passed longitudinally through the SEN specimen via spot welded current supply leads attached at the sides of the specimen, as shown in Figure 4.2. Two small wires (0.25 mm diameter) spot welded across the notch (0.51 mm from the notch centerline) serve as voltage probes, measuring the differential voltage across the crack. Placement of the current supply leads away from the voltage probe leads and twisting of the voltage probe leads is done to minimize the induced voltages (Allison, 1988).

The electronic system consists of: (1) a lock-in amplifier (LIA), (2) a current amplifier, (3) an isolation transformer, and (4) an AC current ammeter (see Figure 4.7).

(1) The LIA is a specialized AC voltmeter which uses synchronous demodulation to measure signal strength and/or phase, even under severe noise conditions (PAR OSM 126, and PAR TAN's 115, 116, 127, and Letzter and Webster 1970). The output is a phase sensitive DC voltage which is proportional to the AC signal.

(2) The current amplifier takes a low level sinusoidal reference signal from the LIA and amplifies it to the desired level of 950 mA.

(3) The isolation transformer serves two purposes. It electrically isolates the specimen from LIA circuitry, and it increases the voltage and the apparent specimen impedance, resulting in better LIA preamplifier noise reduction (PAR TAN 226, and PAR OSM 1900/1/2).

(4) The current supplied to the specimen is monitored by an ammeter which produces a DC voltage proportional to its magnitude. This allows for a real time correction of the PD due to unavoidable current fluctuations.

4.6.4 - Experimental Determination of the Crack Length Versus PD Data

Calibration tests are run by growing a fatigue crack under constant ΔS conditions, and measuring the PD and changing the ΔS level at specified intervals. The change in ΔS produces a visible mark on the fracture surface, at the current crack front position so that a post-test determination of the crack length can be made.

The tests are conducted with alternating blocks of constant ΔS, with $R=0.25$, and $f=5$ Hz, in a de-aerated, 3.5% NaCl solution at room temperature. The crack is grown from the notch to a length of 18.0 mm, with changes in ΔS every 0.75 mm. This provides approximately 24 crack length versus PD data points per test.

Twelve "calibration" tests have been performed, but only the results from tests 11 and 12 are used in the calculation of the calibration relationship. This is due to large interaction effects, which required testing to quantify, and finally rectify. The effects are described below; a detailed description of the tests can be found in Appendix A.

4.6.5 - The Temperature and Current Fluctuation Effects

The measured PD was found to be affected by changes in the applied ΔS level, load ratio, loading frequency, specimen temperature, and supply current. All of these effects, except for the temperature and supply current fluctuations, were eliminated using the filtering capabilities of the LIA.

Two methods were tried for eliminating the effect of temperature and current. The first method used a normalized PD to eliminate the effects. It was defined by:

$$PD_{norm} = \frac{V - V_0}{V_0}, \tag{4.5}$$

where

V = the measured PD, and

V_0 = a reference PD.

An attempt was made to use this method using the PD measured before the start of cracking for V_0 (i.e., the notch PD), but large deviations in V_0 with notch geometry led to large errors in the normalized PD, and consequently, unacceptably large errors in the predicted crack length.

For the method to work properly, the reference PD should be measured on an uniform section of the specimen, and it should be measured each time V is measured. If the probe spacing for the reference PD measurement can be repeated in a precise fashion, then the normalized PD method for temperature and current corrections is best It is the simplest and most accurate possible method. Unfortunately, the method could not be used with the present electronic equipment.

The second method works by applying multiplicative correction factors to the measured PD. The corrected PD is defined as:

$$PD_{corrected} = V \times \frac{\rho_r(293.2K)}{\rho_r(T)} \times \frac{950mA}{I}, \tag{4.6}$$

where

V = the measured PD,

$\rho_r(293.2K)$ = the "reference resistivity" of the specimen,

$\rho_r(T)$ = the "resistivity" of the specimen at temperature T [K],

950mA = the "standard" supply current level, and

I = supply current level at the time of measurement.

An expression for $\rho_r(T)$ was obtained using final crack length (actual and calculated) and measured PD data from tests 13-20. The correction factors, calculated post-test, were used to obtain an empirical relation for $\rho_r(T)$ via a non-linear LS regression analysis (BMDP Program P3R, BMDP (1985)). The relation obtained was:

$$\rho_r(T) = -4.937 + 6.080\times10^{-2}\,T - 9.1\times10^{-5}\,T^2. \qquad (4.7)$$

This method of temperature compensation is adequate, but improvements are needed. The most important improvement could come from the method for generating the $\rho_r(T)$ relationship used in the data correction. More data, at different crack lengths, should be obtained.

The current correction factor is much simpler due to the fact that the effect of current on the PD is linear in nature. It could be eliminated altogether if a better current control system was implemented.

4.6.6 - The Crack Length and PD Measurements

Crack lengths are measured on the fractured calibration specimens using an optical microscope and a two stage micrometer table. The fracture surfaces of both halves of the specimen are scribed as shown in Figures 4.3a and 4.3b, and crack length measurements taken twice, for each half of the specimen, at five locations across the crack front (see Figure 4.3a). All four of the measurements, at each of the five positions across the crack front, is averaged, for a total of twenty measurements per crack length average. The standard deviation is determined by pooling the standard deviations determined for each of the five positions across the crack front (four measurements at each location).

The calculated standard deviation applies to the measured average crack length. It is used in the least squares analysis for the calibration relationship as a crack length weighting factor.

A value for the potential drop is obtained by averaging twenty consecutive PD measurements for each measured crack length. Estimates for the standard deviation of the PD measurement are also calculated and recorded.

In summary, the a-PD calibration data consist of the crack length and potential drop averages, $\bar{a}_i$ & $\overline{V}_i$, and standard deviations, $\hat{\sigma}_{a_i}$ & $\hat{\sigma}_{V_i}$, from tests 11 & 12.

4.6.7 - A Note on the Analysis of the Calibration Data

An important consideration for an indirect measurement technique is the accuracy of representation of the crack length/voltage calibration relationship, in that the uncertainty in the calculated FCG rate depends, in part, on the uncertainty in the calibration representation. Considerations of this nature fall under the heading of propagation of error and are properly considered within the framework of mathematical statistics. For that reason, a discussion of the analysis of the "calibration" data is deferred until the next chapter, where the appropriate statistical concepts and considerations are outlined in a comprehensive manner.

SECTION 4.7 : CRACK CLOSURE MEASUREMENT

4.7.1 - Introduction

Crack closure occurs when the faces of the crack make contact leading to contact forces. These contact forces, which are absent for the larger applied loads, gradually increase in strength as the applied load decreases, changing the apparent compliance of a specimen, as manifested by non-linear P-δ behavior. A technique known as the "Back-Face Strain Gage" (BFSG) or "Unloading Elastic Compliance" technique (Kikukawa et al., 1976) was developed to use the specimen compliance to indicate crack face loading.

4.7.2 - The BFSG Method of Crack Closure Detection

A strain gage on the back face of the SEN crack specimen[4] (see Figure 4.7) is used to measure the strain as a function of load. The gage is incorporated into an unbalanced Wheatstone bridge arrangement (quarter-bridge). The MTS DC signal conditioner serves as the voltage supply and signal amplifier for the bridge, giving a DC output signal proportional to the strain, with a full scale output of ±10 VDC. A computer algorithm corrects the strain data for temperature and nonlinearity effects (Measurements Group, 1986), and then performs an analysis to determine if crack closure loads are present while the test is in progress.

At preselected crack length intervals (0.75 mm) 25 pair of load-strain data (P_i-ϵ_i), evenly spaced with respect to load (i.e., 24 equal ΔP increments from P_{max} to

[4] Bonded opposite to the EDM notch and centered with respect to the notch.

P_{min}), are measured for 3 increasing and 3 decreasing load half cycles. Each of the six data sets is separately used to calculate a least squares straight line through the 14 P-ϵ points with P between ($0.85P_{max}+P_{min}$) and ($0.45P_{max}+P_{min}$). The slope of this line is the specimen stiffness (i.e., the reciprocal of compliance).

The least squares line is used to calculate strain values for given values of the load, as the load is decreased towards P_{min}. The calculated strain value can be compared with the actual measured strain value to detect deviations from ideal behavior. This is done for each of the 8 P-ϵ values, with $P \leq (0.45P_{max}+P_{min})$, and when the percent difference between the two is greater than 2%, crack face contact is assumed to have occurred. This criterion of crack closure is denoted as the strain difference criterion (SDC) (see Figure 4.8), and it can be shown that method is a more sensitive detection method than a similar criterion based on load deviations. A number of investigators (Newman & Elber, 1988; Donald, 1988; Gill et al., 1984; Macha et al., 1979; and Kikukawa et al., 1976) have used similar techniques.

The sensitivity of the SDC technique has not been established analytically. This would require an analytic expression for back-face strain as a function of the applied loads (both external and crack face contact), but it has been established experimentally.

Experimental evidence, from tests 9 and 13-24, indicates the method has sufficient sensitivity to detect closure loads. In test 9, with R=0.1, closure loads were detected (see Figure 4.9), while in test 13-24, with R=0.25, no closure was detected. The elimination of the closure loads with increasing R ratio is consistent with results presented in the literature (Unangst et al., 1977; and Shih & Wei, 1973).

The results indicate that the BFSG technique, when used with the SDC, is sensitive enough to detect crack closure, and that FCG tests with R=0.25 show no evidence of crack closure. The second result has been used in selecting the R value for the FCG tests, so that complications due to closure are eliminated.

SECTION 4.8 - THE FCG TESTS

4.8.1 - Introduction

This section describes the pretest preparations, the crack initiation procedures, the collected data and data intervals, the crack growth regimes, and the final crack length measurement.

4.8.2 - The Testing Procedures

At the start of a test, steps are taken to minimize the oxygen contamination and to stabilize the temperature and electrochemical potential. Before solution is allowed into the chamber, the plumbing network is flushed with N_2 gas for 10 minutes. Solution flow is started, the temperature and potentiostat controls properly set, and after reaching test temperature, the system is allowed to stabilize for at least one hour. After stabilization the test is started.

A precracking routine is used for all tests, with a standardized loading frequency and ΔS level. The frequency is 5 Hz, and the starting ΔS level is within the range $120 \leq \Delta S \leq 190$ (J/m^2), regardless of the level required for the test. If the test ΔS level is not within this range, ΔS is initially set to start at 150 (J/m^2) and then exponentially ramped to the test value, over 0.40 mm of crack growth, at which point the precracking routine ends. Tests with the ΔS level within this range are run with this value throughout the precracking routine. In this case, the precracking routine is used for the first 0.13 mm of crack growth.

The FCG rate testing begins after the precracking routine. The primary data collected or calculated are the: (1) observation number, (2) elapsed cycles, (3) maximum PD, (4) variance of the PD, (5) crack length, (6) ΔS, (7) R, (8) $(da/dN)_{sec}$, (9) T, (10) the electrochemical current, and (11) the electrochemical potential. Secondary data includes ΔS calculated using the measured closure load, and the ratio P_{op}/P_{max}.

The primary data is based on an average of ten consecutive measurements and is recorded every 12.7 μm of crack growth. The secondary (closure) data is based on the average of 6 consecutive measurements and is recorded every 0.75 mm of crack growth.

The crack grows from notch to 18 mm in length, and is divided into two crack length regimes. The first is the "short-crack regime" (SCR), extending from the notch to 9 mm, and the second is the "long-crack regime" (LCR), which extends from 9 to 18 mm. The SCR tests are conducted with constant ΔS, f, and T throughout the range of crack growth, while the LCR tests are constant ΔS and T, with different frequencies over small intervals of crack growth (1.0, 0.5, and 0.25 mm) (see Figures 3.1 and 3.2).

At the end of the test, the specimen is fractured and its final crack length measured in order to verify and correct the crack length data, when needed. This procedure is described in the next chapter.

CHAPTER 5 - ANALYSIS OF THE DATA

SECTION 5.1 - INTRODUCTION

This chapter contains a description of the statistical methods used to analyze the experimental data. Some basic statistical concepts are reviewed, and the nature of the FCG data is examined. A general look is taken at the methods of least squares and least squares splines and how they can be applied to the problem of determining the FCG rates and uncertainties. And finally, a description of the procedures used for analyzing the FCG data is given.

SECTION 5.2 - BACKGROUND ON THE METHODS OF STATISTICS

5.2.1 - Introduction

The concepts important to the statistical description of experimental data can be found in many different books; a more complete description of the topics to be discussed can be found in the books by: Mandel (1984), Gnedenko & Khinchin (1962), Natrella (1966), Box et al. (1978), Stuart & Ord (1987), and Ross (1984).

The statistical concepts of: (1) random variables (rv), (2) probability distribution or density functions (pdf), (3) cumulative pdf's, (4) parametric descriptions for a pdf, (5) populations and samples, (6) pdf parameter estimates from a sample, (7) the Central Limit Theorem, and (8) statistical independence and its quantification, are discussed below.

5.2.2 - The Statistical Concepts

A rv is a mathematical variable whose value is subject to chance fluctuations, and its value can be considered as the outcome of an experiment. The rv can either be discrete or continuous, but only continuous rv's are considered here.

For each rv there is an associated pdf, f(x), which associates with each value of the rv, say X, between the values of x and x+dx, a probability p. This is denoted by:

$$p = \text{Prob}\{ x \leq X \leq x + dx \} = f(x)\, dx, \qquad (5.1)$$

which reads "The probability that the outcome of the experiment, X, be contained in the small interval extending from x to x+dx, is equal to p." Note that a pdf has the property:

$$\int_{-\infty}^{\infty} f(x)\, dx = 1. \tag{5.2}$$

A cumulative pdf, F(x), associates with each rv, another probability, say P, defined as:

$$P = \text{Prob}\ \{ X \leq x \} = \int_{-\infty}^{x} f(\xi)\, d\xi = F(x), \tag{5.3}$$

which reads "The probability that the outcome of the experiment, X, be less than or equal to x, is equal to P." Note that F(x) is a monotonically increasing function with values that satisfy $0 \leq F(x) \leq 1$.

There are an infinite number of functions which could serve as pdf's. In statistics, a number of "standard" pdf's are recognized as being useful for the description of rv's including: the normal or Gaussian, log normal, extreme value (smallest and largest), Weibull, etc.

It is convenient to be able to describe a pdf using a small number of parameters. Two such quantities, the expected value and variance, are used for this purpose. The expected value of a rv is defined as:

$$E\,[x] = \int_{-\infty}^{\infty} x\, f(x)\, dx = \mu, \tag{5.4}$$

and is used as a measure of the "central" location of the pdf. It is commonly referred to as the "mean" or "average" value and is equal to the first moment of x about zero.

The variance of a pdf is a measure of the dispersion or spread of the distribution about the mean value and is described by:

$$VAR\,[x] = \int_{-\infty}^{\infty} (x - \mu)^2\, f(x)\, dx = \sigma^2 = E\,[(x - \mu)^2], \tag{5.5}$$

and it is equal to the second moment of x about the mean.

The sequence of quantities consisting of the mean, the variance, and all the successive moments about the mean, provides, in a mathematical sense, a complete characterization of the pdf from which they were derived.

The set of all hypothetically possible outcomes of an experiment, is called the population of a rv, and in many cases, is infinitely large. A finite subset of values from the population is called a sample.

To exclude the possibility of any form of bias in the measurement process, a method of sampling called random sampling is used. The method's function is to exclude biases of any form, such as a conscious, or even unconscious, process of discriminatory selection on the part of the experimenter, or the effects of a gradual shift in the measuring apparatus.

The importance of random sampling in statistical analyses should not be underestimated. From Mandel (1984):

> "The science of statistics establishes relationships between samples and populations. These relationships allow us to judge the reliability of the sample as a representation of the population. But in practically all cases, such relationships are based on the assumption of randomness in the selection of the sample. It follows that the drawing of inferences from sample to population by statistical means is unjustified and may in fact lead to serious errors if the conditions of randomness are grossly violated."

The expected value and variance of a pdf are population parameters, that is, they are calculated from the knowledge of the pdf, which characterizes the entire population. The term sample estimate refers to an estimate of a population parameter using a finite selection of items from the population. The two most common sample estimates for μ and σ^2 are the arithmetic mean:

$$\hat{\mu} = \frac{1}{n} \sum_{i=1}^{n} X_i, \tag{5.6}$$

and the estimated variance or standard deviation squared:

$$\hat{\sigma}^2 = \frac{1}{n-1} \sum_{i=1}^{n} (X_i - \hat{\mu})^2, \tag{5.7}$$

where

n = the number of items in the sample

X_i = the i^{th} outcome of an experiment, and

The overhead hat(ˆ) denotes an estimated quantity.

For the Gaussian pdf these estimates are the "best" in a statistical sense. They are the most efficient, non-biased, minimum variance estimates for the mean and variance (Stuart and Ord 1987). For distributions other than Gaussian, the arithmetic mean and standard deviation squared may not the best estimates for μ and σ^2.

A finite sample of experimental data cannot be used, all by itself, to prove that it comes from a specific pdf. It can only be used to test whether there is reason to doubt its identification with a certain pdf[1]. To positively identify the pdf for a rv, additional information concerning the nature of the chance fluctuations in the rv is required.

An important theorem in mathematical statistics is called the Central Limit Theorem. In words it states (Mandel 1984):

> "Given a population of values with a finite variance, if we take independent samples from this population, all of size N with values that are uniformly small with respect to the sum, then the population formed by the averages of these samples will tend to have a Gaussian pdf, regardless of the pdf of the original population; the larger the N, the greater the tendency towards 'normality'."

This theorem can be very useful in the analysis of experimental data. For instance, if: (1) the error or deviation of a rv from its expected value, $(X - \mu)$, is made up of many acting causes which are mutually independent, and (2) if the number of acting causes, N, is very large, and (3) if the action of each of these causes, in comparison with their total combined action, is small, then the pdf for the sum can differ only insignificantly from a normal distribution law. A large body of statistical tools exists for the analysis of rv's described by a normal distribution.

A number of situations arise in statistical analyses where a relationship between a multiple number of rv's exist. Consider two rv's, x and y, and their associated pdf's, $f_1(x)$ and $f_2(y)$. Let X and Y represent the outcome of an experiment in which both x and y are measured. Now consider the deviations $X - \mu_X$ and $Y - \mu_Y$. If the probability that the deviation $X - \mu_X$ assume a certain value is in no way affected by the value of $Y - \mu_Y$, and vice versa, the rv's x and y are said to be statistically independent. For independent rv's, the joint frequency distribution function, f(x,y), (i.e., the pdf for the joint occurrences of $x \leq X \leq x + dx$ and $y \leq Y \leq y + dy$) is equal to the product of the individual pdf's for x and y (i.e., $f_1(x) \cdot f_2(x)$). On the other hand, if they are not statistically independent, their joint pdf no longer equals $f_1(x) \cdot f_2(x)$.

An important distinction can be made between functional dependence and statistical dependence. Note that in the paragraph above, dependence between the variable deviations was described. This is done to eliminate any functional dependence, which would be contained in the relationship between the μ's. The statistical dependence of x and y does not, in general, depend upon any functional relationship between them.

A common measure of statistical association is the covariance of two rv's. It is denoted by COV [x,y] and is defined below.

---

[1] Note that statistical tests for the normality of a set of experimental data, which come from an infinite population of values, can only provide an answer to the following question; "Can we, with a given level of confidence, reject the following null hypothesis: 'the pdf of the data is no different from a Gaussian pdf'"?

$$\text{COV}[x,y] = \int_{-\infty}^{\infty}\int_{-\infty}^{\infty}(x-\mu_x)(y-\mu_y)\,f(x,y)\,dxdy = E[(x-\mu_x)(y-\mu_y)]. \quad (5.8)$$

Note that the covariance of two rv's is a population parameter and that COV [x,x] = VAR [x]. A sample estimate for the covariance is defined by:

$$\hat{\text{COV}}[x,y] = \frac{1}{n-1}\sum_{i=1}^{n}(X_i-\hat{\mu}_X)(Y_i-\hat{\mu}_Y). \quad (5.9)$$

In general, a normalized function of the covariance, called the correlation coefficient, is used to described the degree of association. It is defined by:

$$\rho_c(x,y) = \frac{\text{COV}[x,y]}{\sigma_x\sigma_y} \quad (5.10)$$

and it ranges from -1 to 1, inclusive. The sample estimate for the correlation coefficient is found by substituting the sample covariance and standard deviations into the above expression. For statistically independent quantities, x and y, the correlation coefficient equals zero, however the converse is not necessarily true.

SECTION 5.3 - THE GENERAL NATURE OF THE FCG DATA

5.3.1 - Introduction

It is the task of an experimenter to extract from the recorded FCG data, an estimate of the rate of change of crack length with respect to elapsed cycles, and some measure of uncertainty of the estimate. These estimates are used for: CG model development, discrimination amongst competing FCG models, design purposes, and even for test development procedures. The intended use of the data will dictate the nature of the CG experiment and the method of analysis. But regardless of the intended use, the task of obtaining the CGR and uncertainty estimates is quite difficult because of the inherent subjectivity in determining the rate from data that are subject to fluctuation.

The parameters used to model the FCG behavior (e.g., ΔK, f, and T) are macroscopic, continuous, and smooth in nature, while FCG phenomenon is inherently microscopic in nature (ASM, 1978; and Fong, 1979). A FCG model using these parameters is restricted to representing the macroscopic behavior. This means that the experimentally observed behavior, with fluctuations that arise from the material and the experimental technique, must be smoothed so as to obtain an averaged behavior. It is the averaged trend which is to be represented by the macroscopic continuum model.

The problem of quantitatively identifying the different sources of fluctuation requires special testing procedures and statistical analyses and is not considered in this work. If the various sources of fluctuation could be identified, more accurate FCG models could be developed. These would be continuum models which characterize the metallurgical (microscopic) state of the material using some sort of "internal variables", and would presumably account for some of the observed fluctuation.

5.3.2 - Definitions for da/dN and VAR(da/dN)

FCG data gathered from an experiment which uses an indirect method for crack length measurement, consists of the finite data set $\{V_i, \hat{\sigma}^2_{V_i}, N_i\}$. For generality, consider V_i as an arbitrary variable which is related to the crack length in a unique fashion (i.e., $a = f(V)$, where $f(V)$ is some function of the parameter V). The crack growth rate can then be related to the derivative of the calibration relationship and the recorded data by the following expression[2]:

$$\frac{da}{dN} = \frac{da}{dV} \cdot \frac{dV}{dN}, \tag{5.11}$$

where

da/dN = crack growth rate,

da/dV = slope of the calibration relationship,

dV/dN = slope of the V = V(N) relationship obtained from the FCG data.

An advantage of this procedure, as opposed to a direct conversion of V_i to crack length, and then differentiating, lies in the ability to express the uncertainty of da/dN as a function of both: (a) the uncertainty of the calibration relationship, and (b) the uncertainty of the FCG data. The uncertainty in the CGR which results from the uncertainty in the calibration relationship has not been considered before.

Assuming da/dV and dV/dN are statistically independent, an exact expression for the variance of da/dN can be derived:

$$\mathrm{VAR}\left(\frac{da}{dN}\right) = \left(\frac{dV}{dN}\right)^2 \mathrm{VAR}\left(\frac{da}{dV}\right) + \left(\frac{da}{dV}\right)^2 \mathrm{VAR}\left(\frac{dV}{dN}\right) + \mathrm{VAR}\left(\frac{dV}{dN}\right) \mathrm{VAR}\left(\frac{da}{dV}\right). \tag{5.12}$$

This equation relates the variance of da/dN to the uncertainties in the calibration relationship (i.e., $(dV/dN)^2 VAR(da/dV)$), uncertainties in the experimental $\{V_i, N_i\}$ data (i.e., $(da/dV)^2 VAR(dV/dN)$), and a cross product term involving both variances, which is a second order quantity and can be ignored for small component variances.

[2] Mathematical relationships defined in terms of experimentally measured quantities should be evaluated using averaged values for each of the variable arguments.

SECTION 5.4 - THE METHOD OF LEAST SQUARES

In order to determine the calibration and differential relationships required for estimating the FCG rate, differentiable functions must be fit to the experimental data in such a way that the average behavior of the data is represented. In addition to this, variance estimates for the fitted functions must be available. One simple method that is ideally suited to this task is the Method of Least Squares (MLS).

Consider the problem of determining a known functional relationship, from a finite sample of data $\{x_i,Y_i\}$ which is known to contain errors in the measured values. Let x_i be considered the independent variable, and Y_i the dependent variable[3]. If the value of the x_i is known exactly, or at least with much less error than Y_i, then the task of determining the relationship is simple. Each measured value of Y_i, for a given value of x_i, can be considered a sample from the hypothetically infinite population of possible outcomes. Therefore, each Y_i value should be considered a rv that is described by a conditional pdf[4]. The rv's form a conceptual series of vertically oriented pdf's, centered about the known functional relationship (see Figure 5.1).

When the random fluctuations (the "residuals") of the data satisfy a number of conditions (discussed below), the MLS supplies estimates for parameters such that the fitted curve passes through the estimated expected value of the rv at each x_i value (see Figure 5.1).

The MLS is used in this work to obtain an estimate for the parameters of a function that is linear in the parameters and can be expressed as:

$$y_i(\alpha_a,x) = \alpha_0 F_0(x) + \alpha_1 F_1(x) + \alpha_2 F_2(x) + \cdots + \alpha_a F_a(x), \qquad (5.13)$$

where

α_a are the parameters of the model,

x is the independent variable, and

$F_a(x)$ is a specified function of the independent variable.

---

[3] The upper and lower case notation for the independent and dependent variables arises from the expressions $Y=y+\epsilon_y$ and $X=x+\epsilon_x$, used in regression analysis. The lower case signifies the exact or true value, and the upper case signifies an experimentally measured value which equals the true value plus a random fluctuation, ϵ. This upper/lower case notation applies only in this subsection, on the discussion of general LS principles.

[4] A conditional pdf is a pdf which assigns a given probability to a rv, for a given value of another variable (Ross 1984). In this case, the conditional pdf assigns a probability to the random variable ϵ, or equivalently Y, for a given value of x.

The MLS applied to the curve fitting problem operates on the principal that the "best" parameter estimates are obtained when the sum of the squared deviations of the measured (Y) values from the predicted ($\hat{y}$) values[5] is minimized. To determine these values a statistical model for the data must be constructed. The model can be expressed as:

$$Y_i = \alpha_0 F_0(x_i) + \alpha_1 F_1(x_i) + \alpha_2 F_2(x_i) + \cdots + \alpha_a F_a(x_i) + \epsilon_i, \qquad (5.14)$$

where

Y_i is the experimentally measured value of the dependent variable at point x_i,

α_a are the parameters of the model,

x_i is the measured value of the independent variable,

$F_a(x_i)$ is a specified function of the independent variable, and

ϵ_i is the fluctuation or error in the measured value of Y_i (i.e., $\epsilon_i = Y_i - \hat{y}_i(\hat{\alpha}_a, x)$).

The quantity to be minimized (with respect to the α_a values) is:

$$\sum_{i=1}^{n} (\epsilon_i)^2 = \sum_{i=1}^{n} \{Y_i - \hat{y}(\hat{\alpha}_a, x_i)\}^2. \qquad (5.15)$$

To minimize this quantity, the expression is differentiated with respect to each α_a, and then set equal to zero. The result is a system of linear algebraic equations which can be solved to determine the estimated α_a values.

Once the "best" fitting curve is found, it can be differentiated to obtain an expression for the derivative. The method also provides estimates for the parameter standard errors and correlation coefficients, and these can be used to determine the variance of any linear combination of the parameters, including the expression for the derivative.

For the LS estimates to be valid, a number of assumptions are necessary. They are listed below and discussed with reference to the FCG data. The discussion also applies to the LS fitting of the calibration relationship. The Y_i correspond with the PD (V_i), and the x_i with the elapsed cycles (N_i). The assumptions are:

1. The $F_a(N_i)$ are known without error.
2. Each error term, ϵ_i, is normally distributed with constant variance.
3. The ϵ_i are statistically independent quantities (i.e., COV $[\epsilon_i, \epsilon_j] = 0$).

[5] Recall that the hat ($\hat{}$) over a variable denotes an estimated quantity so the quantity $\hat{y}(\hat{\alpha}_a, x_i)$ is taken to denote the fitted curve with its estimated parameters.

The first assumption is satisfied exactly because the functional form of $F_a(N_i)$ is specified, and the test equipment which measures N_i is not subject to errors. For the calibration data, the independent variable (PD) is not known exactly but its standard deviation is much less than that of the dependent variable (the crack length) (i.e., $\hat{\sigma}_{V_i} \ll \hat{\sigma}_{a_i}$) and so the first assumption is approximately satisfied.

The second assumption must be discussed with reference to the nature of the error terms. The ϵ_i terms are the error in measurement of the PD; each ϵ_i can be considered the sum of a large number of fluctuations from: the experimental apparatus, small changes in the specimen's wiring configuration, the electrical and FCG material properties, and other sources. If each of the fluctuations, from all the individual sources, is assumed to be small and approximately the same magnitude, then their sum should be normally distributed (by the Central Limit Theorem), thereby satisfying the first part of the second assumption.

The required constant variance of ϵ_i is assumed to be satisfied. Weights (i.e., $1/\hat{\sigma}^2_{V_i}$) are used in the LS analysis, and the residuals examined after the fitting to provide a check on this assumption. If the residuals show signs of abnormal behavior, a transformation of the data can be used (sometimes) to eliminate the problem (Draper and Smith 1985, and Cook 1982).

The third assumption is more troublesome. The fluctuations of the PD can vary depending on the crack length, the amount of crack surface contact, and the crack-tip deformation state, leading to the possibility of a crack length dependence of the error terms. The errors are "serially correlated", in this case, which means that the value of the current error depends wholly, or in part, on the magnitude of the previous error(s). The MLS is not valid in these cases.

If the errors are correlated, more advanced curve fitting techniques are required. Techniques are available for determining the extent of correlation, and accounting for it in the analysis (Beck, 1974; and Box & Jenkins; 1970), but the author's unfamiliarity with them precluded their use at this point.

The consequences of violating the third assumption has been investigated for the special case of a straight line fit with cumulative errors (Mandel 1958, 1964). He found that the application of the standard LS procedure, led to an unbiased, but inefficient estimate of the slope, and that the standard error of the slope was underestimated. This suggests that caution should be used in interpreting the FCG rate estimates, especially with the uncertainty estimates, which are likely to be underestimated.

The MLS cannot specify the functional form (FF), $F_a(N_i)$, that should be used in the analysis. This information must be supplied by the analyst. If a theory for the phenomenon is available, or known to be governed by a certain class of functions, then a FF can be specified, and if not, then any simple or convenient form can be chosen.

The most used FF, in the absence of auxiliary information, is the simple polynomial or powers of the x_i. For this choice, the F-test (Mandel 1984) is available to statistically test which polynomial best represents the data.

In this dissertation, simple polynomial functions have been chosen to represent the calibration relationship and the FCG data. The choice is one of simplicity due to the lack of auxiliary information.

SECTION 5.5 - THE ANALYSIS OF THE CALIBRATION RELATIONSHIP

The values of $\bar{a}_i$, $\hat{\sigma}_{a_i}$, and $\bar{V}_i$ are used to determine the polynomial relationship between crack length and potential drop, using software (BMDP Program 5PR; BMDP (1985)) on a mainframe Cyber computer. Relationships of the form:

$$a=\sum_{i=0}^{n} \alpha_i V^i \tag{5.16}$$

are determined, for n=1 to 5. The BMDP program supplies estimates for α_i, their standard errors, the parameter correlation matrix, and the analysis of variance (ANOVA) table for the residuals.

The value of da/dV is calculated by differentiation:

$$\frac{da}{dV} = \sum_{i=1}^{n} i\, \alpha_i\, V^{i-1}, \tag{5.17}$$

and the variance of this is given by:

$$VAR\left(\frac{da}{dV}\right) = \sum_{i=1}^{n} (iV^{i-1})^2 \times VAR\,[\alpha_i] + \sum_{i,j=1}^{n} (iV^{i-1} \times jV^{j-1}) \times COV\,[\alpha_i,\alpha_j], \tag{5.18}$$

where $i \neq j$, and VAR $[\alpha_i]$ and COV $[\alpha_i,\alpha_j]$ are determined using the standard errors and correlation matrix for the α_i.

The F-test, provided by the ANOVA table, and the magnitude of VAR(da/dV) were used to select the polynomial for the calibration representation. Figures 5.2 and 5.3 show scatter and residual plots for the third and fourth degree polynomials (best by F-

test). An examination of VAR(da/dV) shows that the third degree polynomial has the lowest variance values over the largest range of crack growth (see Figures 5.4 & 5.5). Based on this information, the third degree polynomial was selected for the calibration relationship. The results are summarized in Table 5.1.

SECTION 5.6 - THE ANALYSIS OF THE FCG DATA

5.6.1 - Introduction

The FCG data consists of data from the short crack regime (SCR) and the long crack regime (LCR). The analysis is different for each regime due to different method of testing in each regime. The SCR tests are conducted over the long intervals of crack growth, with constant ΔS, f, and T, while the LCR tests are conducted over small intervals of crack growth, with constant ΔS, f, and T (see Figure 3.1). Because of this, a different FF has been selected for use in each regime. A LS spline is used in the SCR data, and a LS straight lines are used in the LCR.

5.6.2 - LS Cubic Splines

A cubic spline is a set of third degree polynomials which are joined over the abscissa in a piece-wise fashion. In other words, the cubic spline is a curve which is represented by a number of different third degree polynomials, each representing a different section of the curve. Where one polynomial ends, another begins, and the point where they meet is called the knot. There are also continuity conditions which must be satisfied. The adjoining polynomials and their first and second derivatives, at each knot, must be continuous. This results in a continuous curve, with continuous first and second derivatives. The LS refers to the fact that the coefficients of the polynomials in the spline are determined using the methods of least squares.

Wold (1974, 1971) has described the representation of experimental data by spline functions in a very readable fashion. A number of mathematically oriented descriptions are also available (de Boor, 1987; Hayes, 1970; Greville, 1969; and Ahlberg et al., 1967), but are more difficult to follow for the non-specialist. The advantages of the LS splines are best explained by Wold (1974):

> "Spline functions have the property of being very flexible; they can approximate, infinitely well, any continuous variation of one variable, as a function of another variable. The behavior of a spline function fitted to a number of points, (V_i,N_i), is very stable with regard to the variation of position of an individual point, (V_k,N_k). Thus the form of the spline function in a small interval, Δ, is influence by all points in the total interval, T, where the influence decreases exponentially with the distance

between the point, (V_k, N_k) and the interval, Δ, (Powell 1969). The definition of spline functions, in terms of polynomials, has the statistically important consequence that a spline function, when fitted to the data by the method of LS, conserves the first two moments of the data (Schoenberg, 1964; and Whittaker, 1923) (i.e., the mean and variance of the data). These properties, which are unique to spline functions, are highly desirable for functions which are to be fitted to real data, which seldom conform to one single function over a large interval. They further make spline functions the ideal tool of analysis if one is interested in the *local* behavior of the data; it has been shown that spline functions are, by some criterion, optimal for the differentiation of data (Greville, 1969; and Ahlberg et al., 1967)."

In order to simplify the numerical calculations, use is made of the B-spline formulation for the numerical fit of the LS spline. Recall that the original problem is one of fitting piece-wise polynomials, with certain continuity requirements at the knots. This leads to a constrained LS minimization problem. Instead of solving this problem, a new set of functions are derived which have the advantage that the number of unknown parameters[6] is the same as the number of free parameters in the spline function. These functions are called B-splines or "Basis" splines (de Boor, 1987, and the references within). Once the position of the knots is specified, the problem of determining the value of the B-spline coefficients is linear. After computing the values of the B-spline coefficients, a transformation is affected to obtain the original cubic spline coefficients.

The IMSL Mathematical Software (The Variable Knot LS Cubic Spline Routine, IMSL 1987) is used to fit the splines. Unfortunately, the software does not supply the variance-covariance matrix for the fitted coefficients, and therefore, estimates for VAR(dV/dN) could not be obtained. A program capable of supplying this information could not, at present, be written.

5.6.3 - Preparation of the FCG Data for Analysis

The data collected during the FCG test is transferred from the test machine to a mainframe computer for analysis. Corrections must be made to the recorded PD to compensate for the errors in crack length measurement. These errors are due primarily to crack face contact, resulting in disagreement between the recorded and actual crack lengths. The magnitude of the error, at the final crack length, is defined by:

$$\frac{a_{rec} - a_{act}}{a_{act}} \times 100, \qquad (5.19)$$

[6] The number of unknown parameters equals the number of cubic polynomial pieces times four parameters per piece minus the number of knots times the three continuity conditions at each knot.

where

a_{rec} is the recorded final crack length, and

a_{act} is the actual final crack length.

The error was never greater than 4.5%, and was usually less than 0.5%.

A PD correction is made, at the end of each test, by linearly adjusting the PD value based on the true and recorded PD, at the initial and final crack lengths. The correction scheme is illustrated in Figure 5.6.

The final step, before the curve fitting, involves checking the PD data for outlying observations and transient effects (due to changes in the loading frequency) which would adversely affect the calculated CG rates. This is accomplished by LS fitting a 5^{th} degree polynomial to the $\{V_i,N_i\}$ data from the SCR, and a 2^{nd} degree polynomial to the $\{V_i,N_i\}$ data from the LCR[7], for each constant frequency interval. The residuals are visually examined to identify the transient and outlying data points, and then eliminated. A less subjective method (i.e., based on statistical principles) should be developed for eliminating the outliers (Draper & Smith, 1981; and Cook, 1982).

5.6.4 - Calculation of the CGR for the SCR Data

A LS fit cubic spline is fit to the SCR $\{V_i,N_i\}$ data using the reciprocal of the PD variance as a weighting factor (i.e., $W_i = 1/\hat{\sigma}^2_{V_i}$). The IMSL fitting routine requires specification of the number and initial position of the knots. It works by varying the knot positions until the residual squared error is a minimum (see IMSL, 1987; and de Boor, 1987 for further details). Once the best fit is determined, the B-spline coefficients are transformed back to the coefficients of the original spline. The resulting expression is differentiated and used to evaluate the CG rate at each recorded data point.

The selection of the number and initial location of the knots requires subjective judgment. The observed "smoothness" of the resulting CGR curve (as a function of crack length) has been used, in this case, as an indication of the proper selection. A better, and less subjective method, would be to use the second or third derivative of V(N) as a measure of smoothness.

The coefficients and knot locations of the cubic splines representing the SCR V=V(N) data of tests 21-32 is given in Appendix A.

---

[7] The 5^{th} and 2^{nd} degree polynomials were arbitrarily selected. This method for examining the residuals is documented in Hayes (1970).

5.6.5 - The Calculation of the CGR for the LCR Data

The BMDP Statistical Software (BMDP program P5R; BMDP, 1985) is used to perform the LS analysis of the LCR data. It is assumed that the CG rate is well defined (i.e., constant) when ΔS, f, and T, are held constant. This allows the analysis to be performed directly in terms of the crack length. Using the software, a LS straight line is fit to the $\{a_i,N_i\}$ data and used to calculated the CG rate (i.e., the slope of the fitted line is equal to the CGR). The software supplies estimates for the fitted coefficients, their standard errors, and a plot of the residuals.

The quantities, dV/dN and VAR(dV/dN) are required to determine the CG rate variance, as expressed by Equation 5.12. In that equation, the expression:

$$\left(\frac{da}{dV}\right)^2 VAR\left(\frac{dV}{dN}\right), \tag{5.20}$$

serves as a measure of the CG rate variance due to fluctuations in the FCG test. This is equal to the variance of (da/dN), which is determined from the LS analysis of the $\{a_i,N_i\}$ data, and therefore, VAR(dV/dN) is not required. The quantity dV/dN can be determined from Equation 5.11:

$$\frac{dV}{dN} = \frac{da/dN}{da/dV}, \tag{5.21}$$

where da/dN is known from the LS analysis and da/dV is known from the calibration relation.

Using these expressions, the CG rate and CG rate variance can be determined at each recorded data point. A single CG rate variance estimate is obtained for each constant frequency interval by averaging the variances at each recorded data point. A summary of the LCR results is contained in Appendix A.

SECTION 5.7 - ANALYSIS OF THE AUXILIARY DATA

The auxiliary data: ΔS, R, ΔK, T, Φ_{ec}, and electrochemical current are all based on the average of ten consecutive measurements taken during the test. BMDP software (BMDP Program P2D; BMDP, 1985) is used to calculate the average and median values, estimates of the uncertainty, the maximum and minimum values, and other statistics, over intervals of constant ΔS, f, and T, for both the SCR and LCR data. The results of this analysis are listed in Appendix A for tests 21-32.

CHAPTER 6 - THE EXPERIMENTAL RESULTS

SECTION 6.1 - INTRODUCTION

This chapter summarizes the experimental results for the fatigue crack growth tests. This includes data from the long and short crack regime, and results from the reference rate tests. The results from the long crack/saltwater solution tests are presented first, along with a discussion. Next, the results from the reference rate tests are presented. And finally, the results of the short crack tests are presented and discussed. A detailed compilation of results, with plots and descriptions, can be found in Appendix A.

SECTION 6.2 - THE LONG CRACK SALTWATER TEST RESULTS

The saltwater test results are presented in the form of plots of the enhancement in CGR, $(da/dN)_{cf}$, versus reciprocal cyclic loading frequency, in log-log coordinates (i.e., CGR response curves). Figures 6.1 through 6.3 are plots of the CG response, over the range of temperatures used, for each of the three different ΔK levels. Figures 6.4 through 6.7 are plots of the CG response, over the range of ΔK levels, for each of the four different temperatures. Seven similar plots, with the total measured CGR, $(da/dN)_e$, plotted instead of the enhancement, $(da/dN)_{cf}$, are given in Appendix A.

SECTION 6.3 - DISCUSSION OF THE RESULTS

Figures 6.1 through 6.3 show the effect of temperature on the CG behavior. The ECGR exhibits a saturating, exponential-like dependence on $1/f$, with what appears to be a temperature independent saturation rate, as time increases. An increase in temperature leads to a horizontal shift in the CG response curve to shorter times (larger f). This is in accordance with a thermally activated rate controlling process. It is also in accordance with a rate controlling surface reaction process where the effect of increasing temperatures would be to decrease the amount of time required for the reaction to go to completion (i.e., the time required for the bare surface to equilibrate with the filmed surfaces).

Because electrochemical reactions are modeled as thermally activated processes, it is instructive to plot the magnitude of the horizontal shift versus $1/T$ (i.e., an Arrhenius plot) to see if the data fall on a straight line. A straight line would indicate that the CG response curve is thermally activated, and the slope of the line would

correspond with the apparent activation energy. This is done in Chapter 8 where a semi-empirical model, similar to the one proposed by Wei & Shim (1986) (see Chapter 2), is fit to the data to model the temperature shift. Without going into the calculation details, the horizontal shift with temperature does plot as a straight line in the Arrhenius plot, with an apparent activation energy of 27.8±4.4 kJ/mol (±2σ), averaged over the three ΔK levels.

Figures 6.4 through 6.7 show the effect of ΔK on the CG behavior. The change in CGR magnitude is both obvious and expected. The change in CG response is not so obvious. It appears as though the CG response data shift to the left (faster times) as the ΔK level is decreased. This is apparent at all temperatures, except perhaps the 345K data shown in Figure 6.4. It should be noted that a change in the CG response with ΔK level has not been previously reported.

If the CG response is controlled by the electrochemical reaction processes, and if the direct effect of ΔK on the rate of reactions is small, then the only way ΔK can affect the CG response is through its effect on the electrochemical mass transport processes. This possibility is examined in Chapter 8.

SECTION 6.4 - THE REFERENCE RATE TEST RESULTS

The results of the reference rate tests are shown in Figure 6.8 and Table 6.1. The CGR is plotted versus the ΔK, in log-log coordinates. A power-law expression is used to characterize the CGR as a function of ΔK. The fitted parameter values are given in Table 6.1.

Figures 6.9 through 6.11 are plots of the measured CGR versus crack length. The data show that no crack length effects are present, except at very short crack lengths. This fact is important in interpreting the short crack effects in a deleterious environments. It shows that the crack length effects are related to the environment and not to some mechanical or microstructural factor.

SECTION 6.5 - SHORT CRACK TEST RESULTS AND DISCUSSION

The results of the short crack growth rate tests are given in Appendix A (Figures A.20 through A.39). Plots of the total CGR, $(da/dN)_e$, versus crack length are given for the preliminary short crack results (tests 13-20), and plots of the CG enhancement, $(da/dN)_{cf}$, versus crack length are given for tests 21-32. Tables A-1 through A-12 also contain short crack growth information, for tests 21-32, such as the

observed maximum CGR and corresponding crack length, the average test variable levels, and the spline coefficients and knot locations.

An examination of the results show that a increase in CGR is definitely present, but its magnitude is very small (i.e., less than 25% for the test conditions investigated). Because the crack-tip pH level is expected to be close to the bulk solution pH level, and because the applied electrochemical potential is very close to the material's free corrosion potential (i.e., $\Phi_{ec}=-800$ mV SCE versus $\Phi_{fc}=-760$ mV SCE), large short crack effects would not be expected. Because of this, no further consideration of these results will be given in this work.

CHAPTER 7 - MODEL DEVELOPMENT

SECTION 7.1 - INTRODUCTION

This chapter describes the modeling of corrosion fatigue crack growth under steady-state conditions (i.e., conditions where ΔK, f, T, R, Φ_{ec}, etc., are held constant). The first main section describes the development of a modeling framework to link the chemical and mechanical processes occurring in the crack. This is used in the next chapter to incorporate and interpret two different models for the surface reaction processes, and a model for the hydrogen diffusion process. The second section contains background information on diffusion modeling in a stressed solid and its connection with the corrosion fatigue phenomenon. A stress-assisted diffusion model is adopted from the literature and used to account for the K dependence of the CG enhancement. A comparison of the FCG results with the model predictions is given in Chapter 8.

SECTION 7.2 - A CONCEPTUAL MODEL FOR CORROSION FATIGUE

7.2.1 - A Description of the Chemical and Mechanical Processes in CF

It is assumed that the enhancement of the crack growth, for medium and high strength steels in aqueous environments, is due to hydrogen embrittlement. It is also assumed that the superposition model for CG, introduced in Chapter 2, correctly describes the total CGR in terms of: a "pure corrosion" fatigue CGR, a "pure mechanical" fatigue CGR, and the fractional amount of "pure corrosion" fatigue. The total CGR is the weighted average of the two CG process rates (from Chapter 2):

$$\left(\frac{da}{dN}\right)_e = \left(\frac{da}{dN}\right)_{max}\phi + \left(\frac{da}{dN}\right)_{ref}(1-\phi), \qquad (2.2)$$

where ϕ is the fractional amount of pure corrosion fatigue, and $0 \leq \phi \leq 1$.

The mechanical fatigue process is described empirically using the Paris-Erdogan law for crack growth (i.e., $(da/dN)_{ref} = C\Delta K^n$). The corrosion fatigue process, which controls the values of both $(da/dN)_{max}$ and ϕ, consists of a number of interacting chemical, mechanical, and metallurgical processes. These processes, and their interactions, are illustrated schematically in Figure 7.1.

The magnitude of $(da/dN)_{max}\phi$, denoted as "the environmental contribution to the CGR" (ECCGR), results from the conjoint action of mechanical fatigue and hydrogen embrittlement of the material in the crack-tip region. The hydrogen is

generated by the electrochemical reactions[1] occurring along the crack surfaces. The driving force for the reactions is the potential difference between the bare (and filming) surface, at the crack-tip, and the adjacent filmed surfaces along the crack flank.

The rate of the reaction, and hence the rate of hydrogen production, depends on the local "chemical environment" at the crack-tip region (i.e., Φ, pH, and c_i), and the nature of the reaction processes. The local environment is expected to be different from the bulk and is determined by the electrochemical mass transport processes and the reactions at the crack-tip and along the crack flank.

Adsorbed hydrogen, produced by cathodic reactions along the crack, undergoes a transition reaction to become absorbed hydrogen (i.e., $H_{ads} \rightleftarrows H_{abs}$ is the reaction and it is denoted as the "hydrogen absorption" process in Figure 7.1). This process, in conjunction with the $H_{ads} \rightleftarrows H_2$(gas) reaction, sets up the boundary conditions for the subsequent hydrogen diffusion process.

The absorbed hydrogen resides in the subsurface layer of metal and is available for transport to the crack-tip region. There are two driving forces for the hydrogen diffusion process. The first is the gradient of the hydrogen concentration, and the second is the gradient of the hydrostatic stress[2]. The net result is a large accumulation of hydrogen in the crack-tip region.

Once the hydrogen reaches this region, it is partitioned among the various microstructural elements (i.e., grain boundaries, internal interfaces, voids and microcracks, etc.), where a large percentage of it will be trapped (see Chapter 2, Section 4). The trapping results in the continuous need for additional hydrogen as the crack grows. Once the hydrogen is partitioned and trapped, the embrittlement occurs, and this lowers the material's resistance to crack growth. When combined with the ongoing mechanical fatigue CG process, an enhancement in the CGR results.

7.2.2 - The Kinetics of the ECCGR

The kinetics of the ECCGR are described in this section, following the statement of a working hypothesis. The hypothesis identifies a rate controlling process, its principal elements, and then describes the nature of the kinetic CG enhancement control.

---

[1] Only the hydrogen produced by electrochemical reaction is considered, and the possibility of hydrogen production by a purely chemical reaction is ignored.

[2] These two driving forces are obtained in the next section on hydrogen diffusion modeling. Their use entails a number of simplifying assumptions which are discussed in the next section.

A Working Hypothesis for the Rate Controlling Process

It is assumed that the surface reactions which give rise to the production of atomic hydrogen along the crack, are the rate controlling step in the corrosion fatigue crack growth process. The quantity $(da/dN)_{max}\phi$ is assumed to be proportional to the amount of hydrogen produced during a single loading cycle, which is proportional, in turn, to the amount of electrons that are made available through the anodic reactions.

Based on this hypothesis, the CG response curve (i.e., $(da/dN)_{cf}$ versus 1/f) will have the same functional form as the charge transfer curve, when both are expressed as a function of time. The logical starting point for kinetic modeling is the development of a model for the hydrogen production process. But before that is done, a number of points need to be considered so that the non-rate controlling chemical and mechanical processes can be properly incorporated into the model.

The fatigue process is assumed to generate an increment of new crack growth, each loading cycle, at the point of maximum load. The magnitude of the increment, per loading cycle, is equal to $(da/dN)_e$, so the amount of bare surface created each loading cycle, denoted by A_{bs}, can be expressed as:

$$A_{bs} = \{2\times B\times\left(\frac{da}{dN}\right)_e \times 1\text{cycle}\}\times SRF, \qquad (7.1)$$

where

B is the specimen thickness, and

SRF is a surface roughness factor.

The bare surface is very unstable, with a potential that is negative with respect to its filmed state. It immediately reacts with the surrounding environment to begin the formation of a surface film and continues until a stable state is achieved. Because the surface is in electrical contact with the adjacent filmed surfaces of the crack flank, a current (transient) will be induced between the two, with electrons flowing from the bare surface to the filmed surface through the metallic specimen[3].

The current transient peaks (is a maximum) at the moment of exposure of the bare surface, and then decays to a steady state value or zero as the film on the bare surface grows. The rate of decay reflects the reaction kinetics, and can change depending

[3] The overpotential at the bare surface is large and positive (anodic) while the overpotential at the filmed surface is small and negative (cathodic). See Chapter 2, Section 2.4 for further details.

upon the nature of the rate controlling reaction. The initial stage of the transient correspond with the charging of the double-layer, and is expected to be complete within milliseconds. The rest of the transient corresponds with growth of the film and is governed by the rate controlling reaction. Because the filmed surface area is much larger than A_{bs}, the mixed potential will be very close to the potential of the filmed surface.

The local crack-tip environment (i.e., Φ, pH, and the c_i) has an influence on the driving force for the reaction and the reaction rate constant. The local environment is influenced, in turn, by the variables which affect the electrochemical mass transport process, such as: (1) the applied electrochemical potential (Φ_{ec}); (2) the variables ΔK, R, and f which control the magnitude and frequency of the crack wall displacements; (3) the bulk solution composition (i.e., pH and c_i); and (4) the fluid flow conditions outside of the crack or specimen. The influence of these variables on the driving force and the rate constant is discussed in the next chapter.

The amount of hydrogen produced by the electrochemical surface reactions can be determined from the current transient. Assuming that the concentration of adsorbed hydrogen[4] ($c_{H_{ads}}$) is proportional to the total amount of charge transferred, the following expression can be written:

$$c_{H_{ads}} = \frac{\gamma}{A_{cs}F} q(\kappa t), \tag{7.2}$$

where the charge transfer, $q(\kappa t)$, is given by:

$$q(\kappa t) = A_{bs} \int_0^t i(\kappa \tau) d\tau, \tag{7.3}$$

and where

γ is a constant which reflects the proportion of current used to create hydrogen,

A_{cs} is the total area of the crack surface (2aB×SRF),

F is Faraday's constant,

$q(\kappa t)$ is the amount of the charge transferred over a single loading cycle,

A_{bs} is the total area of the bare surface,

$i(\kappa t)$ is the anodic current density on the bare surfaces,

κ is the reaction rate constant for the rate controlling reaction, and

$t = 1/f$, the time available for reaction (i.e., one load cycle).

[4] The adsorbed hydrogen is expressed as a surface concentration (i.e., mol/m^2) and is assumed, in this work, to be uniformly distributed along the entire length of the crack. The actual distribution is expected to be non-uniform and dependent on the local environment, and can be determined, in principle, by a proper analysis of the electrochemical mass transport processes.

The functional form of $i(\kappa t)$ reflects the nature of the rate controlling reaction process, and is determined by the kinetics of the reaction. The reaction rate constant (κ) contains a thermal activation term (Bockris & Reddy, 1977b; Conway, 1965; Eyring et al., 1939) which characterizes its temperature dependence. It is also a function of the potential and specific chemical species concentrations, at the electrode surface. These are affected, in turn, by: ΔK, f, R, Φ_{app}, etc.. Therefore, κ, in its most general form, can be expressed as $\kappa(T,\Delta K,f,R,\Phi_{app},etc.)$.

In the experimental work, only the influence of T and ΔK, on κ have been considered. The effect of the other variables is briefly examined in Chapter 8 using the results of a published model for the electrochemical mass transport process.

The reaction rate constant can also be used to defined a characteristic time scale (i.e., the time constant of the rate controlling reaction, $1/\kappa$). For times much greater than $1/\kappa$, the reaction will have completed, and the initially bare surface will be completely filmed. This corresponds with the maximum amount of transferred charge, whose value is denoted as the "saturation" charge level (q_s).

The connection between the amount of adsorbed hydrogen, and the quantity ϕ from the superposition model, can be made in the following manner. First, the quantity ϕ, which characterizes the CG response as a function of time (1/f) and temperature (T), is identified with the quantity θ ($0 \leq \theta \leq 1$) which represents the percent completion of the surface filming process (Simmons et al., 1978). Because the film at the bare surface is a product formed by the surface reactions, the amount of film growth is directly related to the amount of charge transferred during the reaction. Since θ and $c_{H_{ads}}$ are both proportional to $q(\kappa t)$, they are also proportional to each other. And because θ is a normalized quantity (i.e., $0 \leq \theta \leq 1$), its final relationship to $c_{H_{ads}}$ must be determined by normalizing $c_{H_{ads}}$, with respect to its saturation value (i.e., the point at which the surface filming process has gone to 100% completion). The final result is that:

$$\phi(\kappa t) = \theta(\kappa t) = \frac{q(\kappa t)}{q_s} = \frac{c_{H_{ads}}}{(c_{H_{ads}})_{sat}} = \frac{\int_0^t i(\kappa\tau)d\tau}{\lim_{t\to\infty} \int_0^t i(\kappa\tau)d\tau}. \qquad (7.4)$$

The quantity $\phi(\kappa t)$ can be determined, in general, by substituting $i(\kappa t)$ into the above equation, and integrating. This requires that $i(\kappa t)$ be known, either analytically or experimentally.

In the next chapter, two different models for $i(\kappa t)$ are examined. The first is a very simple analytical model, which is fit to the FCG data to determine κ. The second consists of some experimental bare surface reaction kinetics data which is numerically integrated to obtain $\phi(\kappa t)$, independent from the FCG results. A comparison of the data with the value of ϕ determined from the two models is made and the results discussed.

A connection between $c_{H_{ads}}$ and the subsequent hydrogen absorption, diffusion, and embrittlement processes can also be made. Assuming the hydrogen transition reaction is in equilibrium, the following relationship between adsorbed and absorbed hydrogen can be written:

$$c_{H_{abs}} = K_H c_{H_{ads}}, \tag{7.5}$$

where

$c_{H_{abs}}$ is the concentration of the absorbed hydrogen,
K_H is the rate constant for the transition reaction, and
$c_{H_{ads}}$ is the concentration of adsorbed hydrogen.

The hydrogen diffusion problem is examined in detail in the next section, where an expression for hydrogen concentration inside of the body, $c_H(r,\theta)$, is obtained as a function of $c_{H_{abs}}$ and K_{max}. This is used with a simple hydrogen embrittlement model, described below, to model the explicit K_{max} dependence of $(da/dN)_{max}\phi$.

The hydrogen embrittlement model is similar to the model proposed by Pao et al. (1977) (see Chapter 2, Section 4), and is given in the form of a working hypothesis.

The Hydrogen Embrittlement Working Hypothesis

$(da/dN)_{max}\phi$ is assumed to be linearly proportional to the distance ahead of the crack-tip, for which the concentration of hydrogen is greater than some critical value. The "critical" distance is denoted by δ^*, and the "critical" hydrogen concentration is denoted by c_H^*.

The quantity $(da/dN)_{max}$ is assumed to be directly proportional to the quantity δ^* (for $\phi(\kappa t)=1$), and is expected to reflect the influence of any variable or process which affects: (1) the overall magnitude of the rate controlling process (i.e., the value of q_s), and (2) the distribution of hydrogen at the crack-tip region.

7.2.3 - The Timing and Chain of Events Over a Loading Cycle

The chain of events occurring over a single loading cycle, can be summarized in the following manner. Start by assuming the load has just reached its maximum value in the load cycle. The crack is incremented at this point, and the equilibration reactions begin. The reactions continue as the load is decreased, with absorbed hydrogen distributing itself along the crack boundaries. After reaching the minimum load, the load begins to increase, and while the reaction processes continue to generate hydrogen, the diffusion process begins transporting hydrogen from the boundaries to the region at the tip of the crack. Upon reaching the maximum load, the extent of the hydrogen is at a maximum, and an increment of growth that is proportional to the extent of the distribution occurs.

SECTION 7.3 - STRESS-ASSISTED DIFFUSION MODELING

7.3.1 - Introduction

In this section, a macroscopic model for the transport of atomic hydrogen in a stressed, linear-elastic solid is examined to determine the explicit K_{max} dependence of $(da/dN)_{max}$.

7.3.2 - Diffusion Modeling in a Solid With a Growing Fatigue Crack

It is assumed that hydrogen generated during the previous loading cycles[5] is used for embrittling the material during the current cycle, and that the increment of crack growth occurs instananeously at the maximum load in the load cycle. It is assumed, therefore, that the extent of the embrittlement, and hence $(da/dN)_{max}\phi$, is governed by the hydrogen distribution at the point of maximum load.

There are three different types of hydrogen distribution that can be considered in the model. They are the: equilibrium, quasi-equilibrium, and transient distributions.

The equilibrium distribution refers to a distribution for which: (1) the diffusional driving forces are held constant, and (2) sufficient time is allowed to pass such that no changes in distribution are detected (i.e., $t \gg$ the time constant for diffusion).

A quasi-equilibrium distribution refers to a diffusion process that occurs extremely fast with respect to the scale of time for the observation. The distribution, at any instant of time, is considered equivalent to the equilibrium distribution that would be obtained for the instantaneous value of the driving force. This occurs when the time

[5] The amount of hydrogen used per cycle is equal to the amount of hydrogen generated during the prior loading cycle.

constant for diffusion is very small, and can be determined by solving the "steady-state" diffusion problem (i.e., all time derivatives set to zero) .

The transient distribution refers to the inherent time varying behavior of the diffusion process and is sometimes referred to as the "non-steady-state" behavior. When the time constant is of the same order of magnitude, or larger, than the time scale of interest, then the transient behavior must be considered.

Because of the time-varying loads involved with fatigue crack growth process (and moving crack tips in stress corrosion cracking processes), only the quasi-equilibrium and transient distributions of hydrogen are of interest.

The question of whether the transient behavior can be ignored should be answered by comparing models for both the quasi-equilibrium and transient distributions with the CG response. If the hydrogen diffusion process is rate controlling, then the CG response and transient diffusion model functional forms will be the same. If they are not the same, then the hydrogen diffusion process is not rate controlling, and *it becomes possible to consider the diffusion process as a quasi-equilibrium process.* The rate controlling process, in this work, is assumed to be the surface reaction processes, and if this assumption is correct, the use of the quasi-equilibrium distribution is acceptable.

7.3.3 - Background on Stress-Assisted Diffusion Modeling

The theoretical work of Fick, in many cases, is regarded as the phenomenological basis for diffusion, and forms the starting point for many of the current developments in diffusion modeling in solids. Reviews on the subject, from this point of view, can be found in the books by Shewmon (1963) and Crank (1970).

The incorporation of stress effects on the diffusion process has been considered by a number authors using: microscopic modeling concepts, equilibrium thermostatics, and modifications to Fick's Laws, to model the relevant phenomena (see Li et al., 1966; Bockris et al., 1971a, 1971b, 1972; Oriani, 1969; and Girifalco & Welsh, 1967).

A better understanding of diffusion can be obtained by developing the model within the framework of non-equilibrium thermodynamics. The advantages include: (1) the level of generality obtainable; (2) an explicit detailing of the assumptions in the model; and (3) the ability to restrict the constitutive function(al) so that the Second Law of Thermodynamics is not violated.

The stress-assisted diffusion model adopted in this work is based on non-equilibrium thermodynamics, and so a short review of the subject is given below as an assist to the reader.

7.3.4 - Non-Equilibrium Thermodynamics

A number of references on the subject are available, listed under the heading of non-equilibrium thermodynamics, rational thermodynamics of a continuum, and heterogeneous mixture theory. See, for example, the books by: de Groot & Mazur, (1984); Gyarmati, (1970); Prigogine, (1967); and Truesdell, (1984); and papers by: Aifantis (1980); Bataille & Kestin (1977); Bowen (1976); Atkin & Craine (1976a, 1976b); and Edelen, (1975).

There exist a number of different schools, each approaching the discipline of "non-equilibrium thermodynamics" in a different manner. The two major schools are known as "Onsager thermodynamics" and "Rational Thermodynamics". An overview of the classical Onsager thermodynamics can be found in the book by de Groot & Mazur (1984) (also see Edelen (1975)). For an overview of Rational Thermodynamics, the book by Truesdell (1984) should be consulted.

The diffusion model adopted in this work has been derived within the framework of Rational Thermodynamics, and so a short description of this theory is given below. The description of heterogeneous mixtures, in Rational Thermodynamics, follows two principles (Truesdell, 1965):

(1) Every property of the mean motion is a mathematical consequence of the properties of the motion of the constituents.

(2) If all effects of diffusion are taken into account properly, the equations for the mean motion are the same as those governing the motion of a simple medium. That is, the total medium does not "know" whether it is heterogeneous or homogeneous.

Theories developed within this framework assume that each of $\xi \geq 2$ constituents can be regarded as a *separate* deformable continuum. It is suggested that the mixture be viewed as the superposition of ξ single continua, each following its own motion, and that at any time, t, each place $\vec{x}$ in the mixture is occupied simultaneously by several different particles, $\{ X^{(\alpha)} | \ \alpha=1,...,\xi\}$, one from each constituent. Thus the motion of the mixture is described by ξ mapping functions referred to ξ co-occupying reference frames. Associated with each constituent is a mass density, $\rho^{(\alpha)}$, which represents the average density of the constituent, $C^{(\alpha)}$, taken over a small volume of the mixture.

The laws of balance for mass, linear and angular momentum, and energy, are considered for each component. This requires the postulated existence of separate: velocities, accelerations, stresses, body forces, temperatures, heat fluxes, internal energies, etc.. In addition, an "internal" diffusion force is postulated to exist which reflects the force exerted on a constituent $C^{(\alpha)}$, at $\vec{x}$, by all other constituents. A constitutive equation for this force is introduced and used to "properly" account for the different effects of diffusion.

Regardless of the particles' distinguishability, the mixture as a whole must satisfy global (integral) laws of balance for the mass, linear and angular momentum, and energy. This leads to conditions on the partial quantities that must be satisfied.

The next step consists of using the Second Law of Thermodynamics to restrict each component's constitutive description. The Second Law, in conjunction with a number of other "principles", is used to further simplify (or complicate) the problem (e.g., the principle of frame indifference, and the principle of equipresence, etc.; see Truesdell, 1984 and Truesdell & Noll, 1965). Also, the theory of invariants is used to represent the constitutive function(al) arguments as invariants of the material's symmetry groups (Rivlin, 1970; Spencer, 1971; and Truesdell & Noll, 1965).

And finally, a model is born! The validity of this approach, as a general theory applicable to all classes of mixtures, can be questioned. A number of the issues raised by this concern has been examined in the paper by Kestin & Bataille (1977). Because of the simplicity of the model adopted here, questions of such a fundamental nature will not be considered in this work.

7.3.5 - A Stress-Assisted Diffusion Model

A generalized model for the interstitial diffusion of gas or liquid in a stressed solid has been developed by Aifantis and coworkers using modern thermodynamic methods (see Aifantis, 1976; Aifantis & Gerberich, 1977a, 1977b, 1978; Wilson & Aifantis, 1982; and Unger & Aifantis, 1983). Aifantis et al. chose a specific version of the model and then applied it to the problem of hydrogen diffusion in a cracked solid. The specifics of this model and the assumptions used in its derivation are reviewed below.

The description begins by expressing the flux of the hydrogen species as a function of the diffusional driving force. The driving force consists of two components. The first is due to a gradient in the hydrogen concentration, and the second is due to the gradient of hydrostatic stress in the solid. An "effective" diffusion coefficient, which

depends on the magnitude of the hydrostatic stress, is also included. The equations for the flux and diffusion are given below:

$$\vec{J} = -(D + N\sigma_0)\nabla c_H + Mc_H\nabla\sigma_0 \tag{7.6}$$

$$\frac{\partial c_H}{\partial t} = (D + N\sigma_0)\nabla^2 c_H - (M - N)\nabla\sigma_0 \cdot \nabla c_H \tag{7.7}$$

where

$\vec{J}$ is the vector flux of atomic hydrogen in the metal lattice,

D, N, and M are phenomenological coefficients,

σ_0 is the trace of the stress tensor (3×hydrostatic stress), and

c_H is the molar concentration of hydrogen in the metal matrix.

The first equation is equivalent to Fick's First Law, expressing the flux as a function of the diffusional driving forces, and the second equation is equivalent to Fick's Second Law, a expression for the balance of mass of hydrogen. The quantity $D + N\sigma_0$ can be thought of as an "effective" diffusion coefficient, reflecting the influence of the hydrostatic stress on the diffusional properties of the solid.

7.3.6 - The Assumptions Used in the Modeling Process

A number of assumptions, over and above those implied by the approach, have been invoked in the derivation of the above equations, and they are outlined and discussed below.

(1) The hydrogen within the solid is assumed to behave as an infinitely dilute gas which occupies the interstitial positions of a defect-free solid.

This assumption is important because a number of assumptions logically follow, but care must be exercised in actual applications (i.e., the magnitude of c_H can become quite large at the tip of the crack).

(2) The solid's thermal and mechanical response is considered to be independent of the presence of hydrogen, and the solid is considered to have an isotropic, linear elastic response to loading. Thus, the constitutive equations for the solid are independent of the thermodynamic state variables for the gas (i.e., concentration, pressure, etc.).

This important assumption is justified in light of assumption #1. It permits an uncoupled description of the stress and deformation states of the solid, allowing the stress and deformations to be determined as a problem in linear elasticity with a constant value for the modulus of elasticity and Poisson's ratio.

(3) The hydrogen's thermal and mechanical response is assumed to depend on the variables which describe the thermodynamic state of the solid, (i.e., in this case, only the hydrostatic stress gradient). It is also assumed to behave as a non-viscous, ideal gas.

(4) The temperature of the hydrogen and the solid are assumed to be identical, and there are no thermal gradients in the solid. This simplifies the model and eliminates thermal conduction from consideration.

(5) All inertial effects are considered to be negligible.

These assumptions lead to a considerable simplification of the problem. Several further assumptions are applied, in reference to a model for the hydrogen distribution in cracked solid, with mode I fatigue loading, and are explained below.

7.3.7 - The Application of the Model

The model represented by Equations 7.6 and 7.7 is simplified further by assuming the magnitude of N is negligible[6]. This assumption simplifies the problem and allows for a comparison with previous theories, but it is not necessary (see Unger & Aifantis, 1983). The resulting equations for the flux and diffusion are given below:

$$\vec{J} = -D\nabla c_H + Mc_H\nabla\sigma_0, \tag{7.8}$$

$$\frac{\partial c_H}{\partial t} = D\nabla^2 c_H - M\nabla\sigma_0\cdot\nabla c_H. \tag{7.9}$$

The resulting diffusion equation is identical to the one used by a number of workers previously (see, for example, Lui, 1970, and Van Leeuwen, 1974). These workers applied their results to the problems of hydrogen embrittlement, stress corrosion cracking, and solute diffusion in solids.

---

[6] In a number of hydrogen permeation experiments with iron alloys, Beck et al. (1965), and Bockris et al. (1971b), found that the diffusion coefficient was unaffected by the application of tensile and compressive stresses, while the hydrogen permeation rate was, leading them to conclude that the solubility of hydrogen in iron alloys can increase or decrease depending on whether there are tensile or compressive hydrostatic stresses present. On the other hand, McAffee (1958a, 1958b), in series of interesting diffusion experiments on glass, found that a stress effect on the diffusion constant did exist for stresses greater than one-half the fracture strength. Aifantis & Gerberich (1978) and Varotsos & Aifantis (1980) also found an effect (from data published in the literature), but it was small for room temperature results. Since the permeation experiments of Beck et al. and Bockris et al. were conducted at low stress and temperature levels, it is possible the effect was not noticeable.

Because diffusion is assumed to be rapid, the steady state distribution of hydrogen is desired. This is obtained by setting the time derivative of c_H, equal to zero, resulting in:

$$D\nabla^2 c_H - M\nabla\sigma_0 \cdot \nabla c_H = 0 \tag{7.10}$$

This partial differential equation is to be solved for a two-dimensional planar solid of infinite extent, with a semi-infinite crack under mode I loading conditions.

For a cracked body in mode I loading, the asymptotic hydrostatic stress (σ_0) is defined by (Rice, 1967):

$$\sigma_0 = \frac{2(1+\nu)}{\sqrt{2\pi}} \; K \; \frac{\cos(\theta/2)}{\sqrt{r}} = A \; K \; \frac{\cos(\theta/2)}{\sqrt{r}} \tag{7.11}$$

where

σ_0 is trace (σ_{ij}),

ν is Poisson's ratio,

K is the stress intensity factor (the K value for the specimen of interest is chosen),

θ and r are polar coordinates centered at the crack-tip, and

$A = \{2(1+\nu)/\sqrt{2\pi}\}$.

Inserting this into Equation 7.10 results in the following differential equation for the H distribution:

$$\frac{\partial^2 c_H}{\partial r^2} + \frac{1}{r}\frac{\partial c_H}{\partial r} + \frac{1}{r^2}\frac{\partial^2 c_H}{\partial \theta^2} - \frac{M}{D}\left\{ \frac{\partial \sigma_0}{\partial r}\frac{\partial c_H}{\partial r} + \frac{1}{r}\frac{\partial \sigma_0}{\partial \theta}\frac{\partial c_H}{\partial \theta} \right\} = 0. \tag{7.12}$$

This is to be solved for $c_H(r,\theta)$, subject to boundary conditions along the crack flank and the boundaries at infinity.

7.3.8 - A Mathematical Solution

The solution outlined below follows Liu (1970) and Unger & Aifantis (1983). An elementary solution to Equation 7.12 is given by:

$$c_H(r,\theta) = c_0 \exp\left(\frac{MAK}{2D}\frac{\cos(\theta/2)}{\sqrt{r}}\right), \tag{7.13}$$

where c_0 is a constant. This corresponds to the problem with an uniform concentration of hydrogen (c_0) along the crack flanks and boundaries at infinity (see Figure 7.2a).

A general solution can be obtained by including spatial variations in the constant c_0, resulting in the expression:

$$c_H(r,\theta) = F(r,\theta)\exp\left(\frac{MAK}{2D}\frac{\cos(\theta/2)}{\sqrt{r}}\right), \tag{7.14}$$

where $F(r,\theta)$ can be determined by substituting into Equation 7.12, and solving the resulting differential equation, which is shown below.

$$\nabla^2 F - \left(\frac{M}{2D}|\text{grad } \sigma_0|\right)^2 F = 0, \tag{7.15}$$

or in expanded form:

$$r^2\frac{\partial^2 F}{\partial r^2} + r\frac{\partial F}{\partial r} + \frac{\partial^2 F}{\partial \theta^2} - \frac{1}{F}\left(\frac{MAK}{4D}\right)^2 F = 0. \tag{7.16}$$

Using a separation of variables approach with $F(r,\theta) = R(r)\Theta(\theta)$, the following identity is obtained:

$$\frac{r^2}{R}\frac{\partial^2 R}{\partial r^2} + \frac{r}{R}\frac{\partial R}{\partial r} - \frac{B^2}{r} = \lambda^2 = -\frac{1}{\Theta}\frac{\partial^2 \Theta}{\partial \theta^2}, \tag{7.17}$$

where

$B = \left(\frac{MAK}{4D}\right)$, and

λ is a constant.

There are two solutions for the problem depending on whether $\lambda > 0$ or $\lambda = 0$. The solution for $\lambda < 0$ is unrealistic and will not be considered. For either choice of λ, the differential equation for $R(r)$ is the modified Bessel equation for functions of a purely imaginary argument (McLachlan, 1955), while the equation for $\Theta(\theta)$ is a simple linear constant coefficient differential equation. The general solutions are given below.

$\underline{\lambda = 0}$

$$\Theta(\theta) = C_1\theta + C_2, \tag{7.18}$$

$$R(r) = C_3 I_0\left(\frac{2B}{\sqrt{r}}\right) + C_4 K_0\left(\frac{2B}{\sqrt{r}}\right), \tag{7.19}$$

$\underline{\lambda^2 > 0}$

$$\Theta(\theta) = C_1\cos\lambda\theta + C_2\sin\lambda\theta, \tag{7.20}$$

$$R(r) = C_3 I_{2\lambda}\left(\frac{2B}{\sqrt{r}}\right) + C_4 K_{2\lambda}\left(\frac{2B}{\sqrt{r}}\right), \tag{7.21}$$

where

C_1, C_2, C_3, C_4 are constants,

$I_{2\lambda}$ is a modified Bessel function of the first kind, and

$K_{2\lambda}$ is a modified Bessel function of the second kind.

A number of properties of the actual hydrogen distribution can be used to restrict the solution. For example, the distribution should be symmetric with respect to the plane of the crack, so that $c_H(r,\theta)$ should be an even function of θ, and this restricts the coefficients of sin $\lambda\theta$ and θ to zero. Also, the concentration at infinity ($r\rightarrow\infty$) must be finite, implying that the coefficients of $K_{2\lambda}$, $\lambda \geq 0$, must be zero (note that $2B/\sqrt{r}\rightarrow 0$ as $r\rightarrow\infty$ and $K_{2\lambda}$ diverges as its argument approaches zero).

To determine the remaining constants (and the permissible values of λ) the boundary values of $c_H(r,\theta)$ must be specified. It is assumed, for simplicity, that the concentration at infinity is constant and equal to c_0. Therefore, only $\lambda=0$ is considered, resulting in the following expression for $c_H(r,\theta)$:

$$c_H(r,\theta) = \left\{c_0 + c_1 I_0\left(\frac{2B}{\sqrt{r}}\right)\right\}\exp\left(\frac{MAK}{2D}\,\frac{\cos(\theta/2)}{\sqrt{r}}\right). \qquad (7.22)$$

The crack flank boundary concentration of hydrogen is uniform (c_0) for $c_1=0$, and can be modified to reflect an increase or decrease in concentration, as the crack-tip is approached, by varying the value of c_1.

This solution is expected to be valid for a region of material surrounding the crack-tip. The infinite concentration at the crack-tip is clearly invalid and results from the infinite nature of the hydrostatic stress at the crack-tip.

7.3.9 - Applications to Corrosion Fatigue Modeling

Recall that $(da/dN)_{max}$ is assumed to be proportional to δ^*, the distance ahead of the crack-tip for which $c_H(r,\theta=0)$ is greater than the critical level, c_H^*. An expression for δ^*, in terms of K_{max}, must be obtained from the diffusion model. Also, in order to have compatibility between the two working hypotheses, it is necessary for δ^* to be linearly proportional to $c_{H_{abs}}$.

Two different crack flank boundary conditions are investigated. The first case, Case I, corresponds to a uniform distribution, of magnitude c_0, along all boundaries (see Figure 7.2a). The second case, Case II, corresponds to the superposition of a uniform distribution, with an increase or decrease in concentration as the crack-tip is approached (see Figure 7.2b).

For Case II, the function for I_0 is approximated by the expression given below, in Equation 7.22 (McLachlan, 1955):

$$I_0\left(\frac{2B}{\sqrt{r}}\right) \simeq \frac{\sqrt[4]{r}\exp(2B/\sqrt{r})}{\sqrt{4\pi B}}, \tag{7.22}$$

which is valid for $r \ll 1$.

For Case I: $c_1=0$, $r=\delta^*$, $K=K_{max}$, and $c_H(r,\theta=0)=c_H^*(\delta^*,\theta=0)=c_H^*$, and

$$\delta^* = \left(\frac{MA}{2D}\right)^2\left\{\ln^{-2}\left(\frac{c_H^*}{c_0}\right)\right\}K_{max}^2. \tag{7.23}$$

For Case II: $r=\delta^*$, $K=K_{max}$, and $c_H(r,\theta=0)=c_H^*(\delta^*,\theta=0)=c_H^*$, and

$$c_H^* = \left\{c_0 + c_1\left(\sqrt{\frac{D}{2\pi MA}}\right)\left(\sqrt{\frac{1}{C_2}}\right)\exp\left(\frac{MA}{2D}C_2\right)\right\}\exp\left(\frac{MA}{2D}C_2\right), \tag{7.24}$$

where

$$C_2 = \frac{K_{max}}{\sqrt{\delta^*}}.$$

An explicit solution for δ^* has not been determined for Case II, but note that δ^* always appears in terms of a single parameter, C_2, implying a K_{max}^2 dependence. It is clear from these equations that the hydrogen distribution is directly related to the nature of the elastic singularity at the tip of the crack.

To show that δ^* is proportional to $c_{H_{abs}}$, the expression for c_0 in Equation 7.23 can be expanded in a Taylor's series to give:

$$\ln^{-2}\left(\frac{c_H^*}{c_0}\right) = \text{Constant} + \left(\frac{2}{c_0'}\right)\left\{\ln^{-3}\left(\frac{c_H^*}{c_0'}\right)\right\}c_0 + \text{Higher order terms}, \tag{7.25}$$

where

c_0' is a nonzero constant, and

$c_0 = c_{H_{abs}}$.

For values of $c_H^* \gg c_0'$, the higher order terms are assumed to be negligible, and the following expression is obtained for δ^*:

$$\delta^* \simeq \left(\frac{MA}{2D}\right)^2\left\{\text{Constant} + \left(\frac{2}{c_0'}\right)\left\{\ln^{-3}\left(\frac{c_H^*}{c_0'}\right)\right\}c_{H_{abs}}\right\}K_{max}^2. \tag{7.26}$$

This is related to $(da/dN)_{max}\phi$ by the hydrogen embrittlement hypothesis. Ignoring the constant in the above equation and lumping the remaining constants into a single one results in the expression(s) given below:

$$(da/dN)_{max}\phi = \left\{C_3(c_{H_{abs}})_{sat}\right\}K_{max}^2\phi, \tag{7.27}$$

or

$$(da/dN)_{max} = \left\{C_3(c_{H_{abs}})_{sat}\right\}K^2_{max}, \tag{7.28}$$

where

$C_3 = \left(\frac{MA}{2D}\right)^2\left(\frac{2}{c_0}\right)\left\{\ln^{-3}\left(\frac{c^*_H}{c_0}\right)\right\}$, is a constant, and

$$(c_{H_{asb}})_{sat} = \lim_{t\to\infty}\left(\frac{\gamma K_H}{F}\right)\left(\frac{A_{bs}}{A_{cs}}\right)\int_0^t i(\kappa\tau)d\tau.$$

This expression predicts an explicit K^2_{max} for $(da/dN)_{max}$. The validity of this prediction is examined in the next chapter by comparison with the experimental FCG results. Note that the quantity $(c_{H_{asb}})_{sat}$ has an intrinsic K_{max} dependence that arises from the effect of K_{max} on the mass transport process, which affects the local crack-tip chemistry. This K_{max} dependence is also investigated in the next chapter.

CHAPTER 8 - MODEL COMPARISON AND DISCUSSION

SECTION 8.1 - INTRODUCTION

This chapter describes the comparison of models for $(da/dN)_{max}$ and $\phi(\kappa t)$ with the experimental FCG data. There are two major sections, each containing a description of the model(s), a comparison with the FCG data, and a discussion of the results.

The first section examines two different models for $\phi(\kappa t)$, and compares them with the CG response data. The first model is developed using a simple decaying exponential function for $i(\kappa t)$ and then determining the value of κ from the FCG data. The second model is based upon independent surface reaction kinetics data for $i(\kappa t)$.

The second section examines the K_{max} dependence of $(da/dN)_{max}$, and then compares it with the prediction by the stress-assisted diffusion model.

SECTION 8.2 - THE FCG DATA AND MODELS FOR ϕ

8.2.1 - Introduction

This section begins by examining a simple model for $i(\kappa t)$, where $\kappa=\kappa(T,\Delta K)$ is determined from the FCG data. The model serves as an approximation to the actual $i(\kappa t)$ so that the CG response may be quantitatively examined. Next, some experimental surface reaction (ESR) data is used in a direct comparison with the room temperature CG response data. An activation energy for the ESR data is used to provide a comparison with the value determined from the empirical model. Also, a brief examination is made of the effect of ΔK on the local crack-tip environment and used to explain the effect of ΔK on the reaction rate constant.

As a matter of convenience, the CG response curves (i.e., $(da/dN)_{cf}$ - 1/f), are used to exhibit the FCG time response (i.e., $\phi(\kappa t)$). A conversion from $(da/dN)_{cf}$ to the quantities $(da/dN)_{max}$ and ϕ is easily accomplished. Recall that $(da/dN)_{cf}$ is related to $(da/dN)_{max}$ and ϕ by the following expression (Equation 2.3):

$$\left(\frac{da}{dN}\right)_{cf} = \left\{\left(\frac{da}{dN}\right)_{max} - \left(\frac{da}{dN}\right)_{ref}\right\}\phi = \left\{\left(\frac{da}{dN}\right)_{sat}\right\}\phi, \tag{8.1}$$

or

$$\left(\frac{da}{dN}\right)_{sat} = \left(\frac{da}{dN}\right)_{max} - \left(\frac{da}{dN}\right)_{ref}. \tag{8.2}$$

Regardless of the manner chosen to represent the FCG data (either $(da/dN)_{cf}$ or $(da/dN)_{max}\phi$; see Equations 2.1 and 2.2 in Chapter 2), the quantity ϕ remains the same, and when any two of the quantities in Equation 8.2 is known, the other can easily be determined.

In both of the models considered below, an expression, or experimental data, for $i(\kappa t)$ exists, and an expression (or numerical values) for $\phi(\kappa t)$ is required. In each case, it is obtained using the expression below (Equation 7.5):

$$\phi(\kappa t) = \frac{q(\kappa t)}{q_s} = \frac{\int_0^t i(\kappa\tau)d\tau}{\lim_{t\to\infty}\int_0^t i(\kappa\tau)d\tau} \tag{7.5}$$

8.2.2 - An Empirical Model for $i(\kappa t)$

A decaying exponential function has been chosen as an approximation to $i(\kappa t)$. This function was used by Wei & Shim (1984), and is capable of providing a good fit to the FCG data and quantitatively characterizing the CG response data. The model is shown below:

$$i(\kappa t) = i_p \exp(-\kappa t), \tag{8.3}$$

where

$$\kappa = \kappa_0 \exp\left(-\frac{\Delta E_a}{RT}\right), \tag{8.4}$$

and where

i_p is a peak current density,

κ is a thermally activated reaction rate constant,

$t=1/f$,

κ_0 is a pre-exponential factor,

ΔE_a is an apparent activation energy,

R is the universal gas constant, and

T is absolute temperature.

Substituting this into Equation 7.5, and integrating, results in the following expression for $\phi(\kappa t)$:

$$\phi(\kappa t) = \left\{1 - \exp\left(-\frac{\kappa}{f}\right)\right\}, \tag{8.5}$$

which is used with Equation 8.1 to represent $(da/dN)_{cf}$:

$$\left(\frac{da}{dN}\right)_{cf} = \left(\frac{da}{dN}\right)_{sat}\left\{1 - \exp\left(-\frac{\kappa}{f}\right)\right\}. \tag{8.6}$$

8.2.3 - Determination of $(da/dN)_{sat}$ and κ

The values of $(da/dN)_{sat}$ and κ, as a function of ΔK and T, are determined from the CG response data by non-linear, least squares regression analysis. The BMDP software (BMDP3R; see BMDP, 1985) is used to perform the analysis, supplying estimates for the two parameters and their standard errors. The use of the regression analysis prevents the inherent subjectivity in directly determining $(da/dN)_{sat}$ and κ from the data, a problem mentioned by Wei & Shim (1984).

8.2.4 - The Results

The results are shown in Table 8.1, where $(da/dN)_{max}$, $(da/dN)_{sat}$, and κ are listed, for each value of ΔK and T. Figures 8.1 through 8.3 show scatter plots of the model, for given values of ΔK, and different T levels. Figures 8.4 through 8.7 show scatter plots of the model, for a given value of T, and different ΔK levels.

The simple model appears to represent the FCG data quite well. There are some deviations though, particularly at the high frequencies, for the low T and high ΔK levels. The magnitude of the deviation is somewhat magnified because the regression has been performed in non-logarithmic coordinates whereas the plots are composed in logarithmic coordinates[1]. But the fact that $(da/dN)_{cf}$ is consistently underestimated in this region indicates that a problem exists with either the model for $i(\kappa t)$ or the FCG data or both.

The data problem can arise at the higher frequencies because $(da/dN)_{cf}$ is calculated as the difference of two quantities which are very close in value (i.e., $(da/dN)_{cf} = (da/dN)_e - (da/dN)_{ref}$). If there is any bias in the value of $(da/dN)_e$ or $(da/dN)_{ref}$, it will be accentuated in $(da/dN)_{cf}$ in the high frequency region. Also, the variance of $(da/dN)_{cf}$ is equal to the sum of the variances for $(da/dN)_e$ and $(da/dN)_{ref}$, and this results in a standard deviation for $(da/dN)_{cf}$ that can be quite large in comparison to the actual value of $(da/dN)_{cf}$. This makes the $(da/dN)_{cf}$ data in this region a poor choice for model comparisons.

The reaction rate constant has also been examined as a function of both ΔK and T. Equation 8.4 demands a specific functional form for the T dependence of κ, and this is verified in Figure 8.8 by plotting the data in an Arrhenius plot ($\log(\kappa)$ versus 1000/T). The straight line slope exhibited by the data corresponds with the apparent activation energy, ΔE_a, which appears to be about 30 kJ/mol for all three ΔK levels.

[1] The logarithmic coordinates tend to magnify the apparent size of a residual at the higher frequencies and attenuate it at the lower frequencies.

This information is important and will be used in support of the working hypothesis for surface reaction control.

It was previously mentioned (in Chapter 6) that the "horizontal placement" of the CG response data appears to depend on the ΔK level. This is obvious in Figures 8.4 through 8.7, but it can also be observed in the Arrhenius plot (Figure 8.8) where the intercept of each line (i.e., $\log(\kappa_0)$) exhibits a ΔK dependence. After investigating the fit of a number of different empirical relations, it was determined that a power law relationship for κ_0 as a function of ΔK works best. The results are illustrated in Figure 8.9 where a plot of $\log(\kappa)$ versus $\log(\Delta K)$ is shown, for the different temperature levels. The apparent value of the slope is about -2.3, which is quite large, indicating the importance of its effect on the CG response. The ΔK dependence of the CG response has not been previously noted in the literature, and is likely due to an interaction with the mass transport process.

The actual values assigned to κ_0 and ΔE_a have been determined using all of the data by a multiple least squares linear regression (BMDP2R; BMDP, 1985) of $\log(\kappa)$. Assuming κ_0 has a power law dependence on ΔK, the following expression can be written for κ:

$$\kappa = C_\kappa \Delta K^{n_\kappa} \exp\left(-\frac{\Delta E_a}{RT}\right). \tag{8.7}$$

A single estimated value is obtained for each of the quantities, C_κ, n_κ, and ΔE_a, by the regression analysis using the entire set of data in Table 8.1. The results are reported in Table 8.2.

8.2.5 - Bare Surface Reaction Kinetics Data for i(κt)

In this subsection, some recent experimental results on the kinetics of bare surface reactions are used in a direct comparison with the CG response data. The data is also used to determine an activation energy for the reactions, which is compared with the value for the FCG data obtained by the empirical model.

The in-situ fracture technique, described in Chapter 2 - Section 4, has been used to generate current transient data for an AISI 4340 steel, in de-aerated 3.5% NaCl solution, for four different temperatures, and with the bare surface controlled at a potential of -700 mV (SCE) (Wei & Xu, 1989). Figure 8.10 and 8.11 show an example of a typical current transient (long and short times), recorded during the experiment.

Note the distinct linear regions in each plot. The first region occurs within the first 0.1 second (or less) and corresponds with double layer charging at the bare electrode surface. A second linear region is apparent in the 2 to 20 second range (approximately), and a third region, corresponding to a very slow decay to a constant baseline value, occurs for times greater than about 20 seconds. This is to be contrasted with the behavior of the simple exponential model which would plot as a single straight line in these coordinates.

The current transients, for the four different temperatures, are numerically integrated (without subtracting the baseline currents) to give the charge transfer as a function of time (Figure 8.12). The similarity between charge transfer and CG response data is evident, and is examined by direct comparison, below. An estimated activation energy of 35.1±6.5 kJ/mol has been obtained for the data, which is very close to the apparent value obtained for the FCG data (i.e., 27.8±4.5 kJ/mol) ($\pm 2\sigma$ in both cases).

A comparison between the charge transfer data (with the base current subtracted), at room temperature, and the CG response data, at room temperature, and three ΔK levels, is made in Figure 8.13. The comparison is made by matching $(da/dN)_{sat}$, for each ΔK level, with q_s. The results are quite interesting. For the high ΔK level, the results match very well, even at the higher frequencies. As the ΔK level decreases, the curves fail to match due to the shift of the CG response to faster times. This can be interpreted in terms of the change in the crack-tip environment with changes in the ΔK level, as shown below.

8.2.6 - Discussion

A number of important observations can be made concerning the comparison of the models for $i(\kappa t)$ with the CG response data. First of all, the results are consistent with the hypothesis of surface reaction rate control. The match between the experimental charge transfer data with the CG response data, plus the similar values for the two activation energies, tend to support this hypothesis.

Further support can be given after examining some other experimental results in electrochemistry and the results of a published model for the mass transport process in a fatigue crack. These results are used to rationalize the effect of ΔK on κ in terms of changes in the local crack-tip chemistry.

Some experimental results which illustrate the effect of applied potential on $q(\kappa t)$, for a NiCrMoV steel in de-aerated 0.15N Na_2SO_4 solution, are shown in Figure

8.14. The results show that cathodic polarization apparently increases κ (shifts the $q(\kappa t)$ curves to faster times) and decreases the magnitude of $q(\kappa t)$.

The results of an experiment to determine the effect of solution pH on the free corrosion potential (Φ_{FC}), for an AISI 4340 steel in a de-aerated 3.5% NaCl solution at room temperature, are shown in Figure 8.15. The results show that Φ_{FC} increases (is more anodic) for decreasing pH, and decreases (is more cathodic) for increasing pH.

And finally, a recent paper by Turnbull & Ferriss (1986), reported the results of a mathematical model for the electrochemical mass transport process for a BS 4360 50D steel, in a number of saltwater environments, including a de-aerated 3.5% NaCl solution. The model accounted for mass transport by ionic migration, diffusion, and convection, and the principal electrochemical reaction was taken to be reduction of water. The effects on the crack-tip pH, potential and molecular hydrogen concentration of: (1) the externally applied potential, Φ_{ec}; (2) ΔK; (3) R; (4) the crack length, a; and (5) the cyclic loading frequency at a temperature of 5°C were investigated. Their results are shown in Tables 8.3 through 8.7 and Figure 8.16. The results show that the local crack-tip environment is very alkaline (pH>10) for all of the conditions investigated.

The main point of these three results is that the crack-tip pH level, for the material & environment, and for the conditions used in the FCG tests, is probably quite high (pH>10), and this implies that a significant decrease in Φ_{FC} occurs near the crack-tip. Now recall that the applied potential during the FCG tests was $\Phi_{ec}=-800$mV (SCE). Therefore, the applied external potential is probably acting to anodically polarize the material near the crack-tip, and since the potential drop down the crack is diminished as ΔK increases, it follows that the magnitude of the "applied anodic potential" increases as ΔK is increased, and decreases as ΔK is decreased. Assuming the reaction kinetics behave as shown in Figure 8.14, it would be expected that as ΔK increases, κ would decrease, and as ΔK decreases, κ increases.

This rationalization is consistent with the facts, and it illustrates the importance of the electrochemical mass transport processes in modeling corrosion fatigue crack growth. This rationalization is also used in the next section, where the effect of ΔK on the magnitude of $q(\kappa t)$, via the mass transport process, is examined.

SECTION 8.3 - THE FCG DATA AND THE MODEL FOR $(da/dN)_{max}$

8.3.1 - Introduction

In this section, the K_{max} dependence of $(da/dN)_{max}$ is compared with the predicted K_{max} dependence by the stress-assisted diffusion model.

8.3.2 - An Empirical Model for $(da/dN)_{sat}$

The value of $(da/dN)_{sat}$ has been determined in the previous section by a non-linear regression analysis of the CG response data. The results of this analysis are given in Table 8.1. The $(da/dN)_{sat}$ values show only slight differences at the different temperature levels, and the differences are insignificant when compared to the magnitude of the standard errors (σ_{sat}).

The values of $(da/dN)_{max}$, also given in table 8.1, are calculated using the expression given below.

$$\left(\frac{da}{dN}\right)_{max} = \left(\frac{da}{dN}\right)_{sat} + \left(\frac{da}{dN}\right)_{ref} \tag{8.8}$$

where

$(da/dN)_{sat}$ is obtained from the data in Table 8.1, and

$(da/dN)_{ref} = 2.13\times10^{-6}\Delta K^{3.37}$, for ΔK selected from the values in Table 8.1.

8.3.3 - The Results

Plots of $\log(da/dN)_{max}$ and $\log(da/dN)_{sat}$ versus $\log(\Delta K)$ are shown in Figures 8.17 and 8.18. The data appears to be well represented by a straight line, for both of the crack growth rates. The results of a least squares straight line fit to the data is reported in the figures and in Table 8.2.

The ΔK dependence of $(da/dN)_{max}$ is converted to a K_{max} dependence using the expression:

$$K_{max} = \frac{\Delta K}{1-R} = \frac{4}{3}\Delta K, \tag{8.9}$$

where the second equality results from taking R=0.25. The conversion from ΔK to K_{max} in the power law representation does not change the value of the exponent, only the value of the constant (i.e., by $(4/3)^{n_m}$).

The final form of $(da/dN)_{max}$ is:

$$\left(\frac{da}{dN}\right)_{max} = C_m\,(K_{max})^{n_m}, \tag{8.10}$$

where

$C_m = 6.82\times10^{-5}$, and

$n_m = 3.00$.

The value of n_m (i.e., n_m=3.0), exhibited by the FCG data, is compared with the value predicted by the stress-assisted diffusion model, in the next subsection.

8.3.4 - The Stress-assisted Diffusion Model for $(da/dN)_{max}$

The model for $(da/dN)_{max}$, obtained in Chapter 7, is written below:

$$\left(\frac{da}{dN}\right)_{max} = \left\{C_3(c_{H_{abs}})_{sat}\right\}K^2_{max} \tag{7.30}$$

where

$C_3=\left(\frac{MA}{2D}\right)^2\left(\frac{2}{c_0}\right)\left\{\ln^{-3}\left(\frac{c^*_H}{c_0}\right)\right\}$, and is constant, and

$$(c_{H_{abs}})_{sat}=\lim_{t\to\infty}\left(\frac{\gamma K_H}{F}\right)\left(\frac{A_{bs}}{A_{cs}}\right)\int_0^t i(\kappa\tau)d\tau.$$

The model predicts an explicit K^2_{max} dependence for $(da/dN)_{max}$, (this is true for both of the boundary condition investigated), which is different from the K^3_{max} dependence of the experimental FCG results.

8.3.5 - Discussion

Three possible reasons for the discrepancy in the exponent for the K_{max} dependence are discussed below, in order of increasing importance.

The first possibility is concerned with the assumption of ideality for the hydrogen gas, which was used in the derivation of the model. Equation 7.30 predicts an infinite concentration of hydrogen at the crack-tip, which in itself is unrealistic, but points to the fact that extremely large concentrations could exist. The modifications required to incorporate non-ideality of the hydrogen gas are not trivial, and all the assumptions which logically followed (i.e., the uncoupling of the elasticity problem, etc.) would need to be reexamined. Therefore, this possibility should not be considered until alternative explanations have been explored.

Another possibility involves a modification of the stress solution to account for plasticity at the crack-tip. The square root singularity at the tip of the crack is characteristic of the crack problem in linear elasticity, and solutions capable of giving

different singularities might be considered (e.g., the HRR crack-tip solution[2]). Again, this could complicate the formulation of the stress-assisted diffusion problem in that it would have to be recast in terms of strain[3] instead of the stress. This modification might be simple, and should be explored, but only after closer examination of the next, more likely explanation.

The best explanation for the lack of fit is the implicit K_{max} dependence of the quantity $(c_{H_{abs}})_{sat}$. The most important term in the expression for $(c_{H_{abs}})_{sat}$, in terms of its K_{max} dependence, is probably $i(\kappa t)$, which is affected by K_{max} through its interaction with the mass transport process.

Recall from the discussion in last section that a plausible explanation for the ΔK dependence of κ was given. This same rationalization can also be applied to explain the K_{max} dependence of $(c_{H_{abs}})_{sat}$. As K increases (K_{max} or ΔK), the magnitude of the anodic polarization increases, which in turn increases the magnitude of the charge transferred (i.e., $i(\kappa t)$ increases leading to an increase in $q(\kappa t)$; see Figure 8.14). In order for there to be a match between the model and the data, $(c_{H_{asb}})_{sat}$ must have a linear dependence on K_{max}, which is a very reasonable requirement.

---

[2] The HRR (Hutchinson, Rice & Rosengren) crack-tip solutions refer to the case of a cracked solid which undergoes plastic strain hardening (Hutchinson, 1968; and Rice & Rosengren, 1968). The result is a stress which goes as $\sigma \sim r^{-1/(n+1)}$ and a strain which goes as $\epsilon \sim r^{-n/(n+1)}$, for a material with constitutive behavior that is described by $\epsilon = \sigma + \alpha\sigma^n$, where n is the reciprocal strain hardening coefficient.

[3] It is really the hydrostatic strain gradient which drives the diffusion, and not the hydrostatic stress gradient, but since stress and strain are directly proportional in linear elasticity, either of the two may be used in the formulation with equivalent results.

CHAPTER 9 - SUMMARY AND CONCLUSIONS

SECTION 9.1 - SUMMARY OF THE DISSERTATION RESEARCH

Experimental and analytical studies were undertaken to develop a model for the effect of ΔK, f, and T on the magnitude and time response of the enhancement of the crack growth rate (CGR) for medium to high strength steels in aqueous environments.

The work began with a review of current understanding of corrosion fatigue crack growth phenomenon and the chemical and mechanical processes which govern the phenomenon. This provided an outline of the current research needs and set the stage for the work in this dissertation.

The experimental work was described next. The goal was to develop a data base for the effects of ΔK, f, and T on the CG enhancement. The tests were conducted on a HY-130 steel in de-aerated, 3.5% NaCl solution, and were run under constant ΔK conditions, with a variety of ΔK, f, and T levels. Reference CGR tests were run in a dehumidified Argon gas environment under the same conditions as the saltwater tests.

The results showed the presence of a short crack effect for crack lengths up to 9 mm. The effect was very small though, with a maximum increase in CGR of about 25%. The long crack data exhibited a saturating, exponential-like dependence on time (i.e., 1/f), where the saturation as the frequency was decreased. Increasing temperatures did not affect the saturation level, but did produce a shift of the CG response curve to higher frequencies (smaller 1/f values). Both the CG magnitude and the CG response were affected by ΔK. A decrease in ΔK led to a decrease in CGR magnitude, and a shift of the CG response curve to higher frequencies (smaller 1/f values).

A modeling framework was developed next. Hydrogen embrittlement was assumed to be responsible for the enhancement of the CGR, and a superposition model was used to model the CGR in terms of a mechanical and corrosion fatigue process (i.e., $(da/dN)_e=(da/dN)_{max}\phi+(da/dN)_{ref}(1-\phi)$).

The electrochemical surface reactions were assumed to be rate controlling, and $(da/dN)_{max}\phi$ was related to the amount of hydrogen produced during a single loading cycle. A model for ϕ was developed by assuming it to be directly proportional to the amount of charge transferred during the reactions, which was calculated as the integral of the transient current $i(\kappa t)$ between the bare (and filming) surfaces (at the crack-tip) and the filmed crack flank surfaces. Two models for $i(\kappa t)$ were developed and used to obtain estimates for $\phi(\kappa t)$, which were then compared with the CG response data.

A model for $(da/dN)_{max}$ was also developed by relating the hydrogen distribution in the crack-tip region to K_{max} and the saturation level of charge transfer. This was accomplished using a stress-assisted diffusion model from the literature. The result was a model for $(da/dN)_{max}$ that was proportional to K^2_{max}, and the amount of hydrogen absorbed along the crack flank.

SECTION 9.2 - CONCLUSIONS

The results of the CG experiments showed that the CG response exhibited the previously observed frequency and temperature dependence, with an apparent activation energy of 27.8±4.4 kJ/mol (±2σ limits). The value of the apparent activation energy compared very well with the value determined from independent bare surface reaction kinetics measurements (i.e., 35.1±6.5 kJ/mol, again with the ±2σ limits) giving further support to the working hypothesis for surface reaction control.

The CG response data exhibited a shift in time with changes in ΔK. The data shifted to lower frequencies (larger 1/f values) for increasing ΔK levels, and was explained in terms of a change in crack-tip chemistry with ΔK level.

The saturation CG rate exhibited a K^3_{max} dependence, whereas a stress-assisted diffusion model provided an explicit K^2_{max} dependence which results from the crack-tip stress singularity from linear elastic fracture mechanics. The difference is considered in terms an implicit dependence via terms related to the surface reaction process. The K_{max} dependence of the surface reaction processes arise from the effect of K_{max} on the mass transport process, which affects, in turn, the local crack-tip chemistry.

This research has demonstrated that to model the effects of ΔK, f, and T on the CG enhancement, all of the interacting processes have to be considered. It will be impossible to account for the effects of ΔK, f, T, R, Φ_{ec}, pH, etc. on the CG response and CGR magnitude without considering the entire set of interacting processes and the interactions between them. The implication is that future aqueous corrosion fatigue crack growth modeling is going to depend on the researcher's ability to model within a framework which accounts for all the chemical and mechanical processes, and not just one or two of them.

SECTION 9.3 - RECOMMENDATIONS FOR FURTHER WORK

For the continuation of this study, an investigation should be conducted of the "explanation" given for the change in CG response with ΔK level. The questions that

need to be answered are given below.

Are the crack-tip pH levels for this material/environmental system really that high? And do the charge transfer curves for this material/system really respond to an anodic polarization by shifting to slower times, and is that true for tests run in an environment with a high pH level? And what is the relationship between the change in polarization and the change in the magnitude of saturation charge level? And can this be related to the K_{max} dependence of the potential drop along the crack, and be used to explain the required linear K_{max} dependence[1] of the saturation level of charge transfer?

To answer these questions, two recommendations for work in the immediate future can be given:

(1) Studies should be conducted to determine the effect of applied potential and bulk pH levels on the kinetics of the bare surface reactions, using the in-situ fracture technique, for this particular material/environmental system.

(2) A study should be undertaken of the electrochemical mass transport problem for this material/environmental system, for the conditions used during the test to better understand the chemistry at the crack-tip.

In the long term, additional recommendations are given.

(1) Studies should be done in order to determine the effects of Φ_{ec} and R, in conjunction with the effects of ΔK, f, and T, on the enhancement of the crack growth rate.

(2) The possible modifications of the stress-assisted diffusion model to account for different crack-tip singularities should be investigated.

(3) Experimental measurements and analytical modeling of the contributing chemical and mechanical processes must be undertaken to link the entire set of processes to the enhancement of the CGR.

[1] In order to get the K^3_{max} dependence for $(da/dN)_{max}$, while using the model proposed in this work, the quantity $(c_{H_{abs}})_{sat}$ must be linearly dependent on K_{max}.

TABLE 2.1 - Some Significant Variables Affecting Fatigue [1]

Mechanical Variables

Maximum stress or stress intensity factor, σ_{max}, or K_{max}[2],
Cyclic stress or stress intensity factor range, $\Delta\sigma$ or ΔK[2],
Stress ratio, or load ratio, R[7], that is, ratio of minimum to maximum stress (load) or stress intensity factor in one load cycle,
Cyclic load frequency, f,
Cyclic load waveform (for constant amplitude loading),
Load interactions in variable amplitude loading,
State of stress, and
Residual stress.

Geometrical Variables

Crack size and relation to component dimensions,
Crack geometry,
Component geometry adjoining crack, and
Stress concentrations associated with design.

Metallurgical Variables

Alloy composition,
Distribution of alloying elements and impurities,
Microstructure and crystal structure,
Heat-treatment,
Mechanical working,
Preferred orientation of grains and grain boundaries—(texture), and
Mechanical properties (strength, fracture toughness, etc.).

Environmental Variables

Temperature, T,
Pressure,
Types of environments—gaseous, liquid, liquid metal, etc.,
Partial pressure of damaging species in gaseous environments, P_i,
Concentration of damaging (or beneficial) species in aqueous or other liquid environments, c_i,
Electrochemical potential, Φ,
pH,
Viscosity of environment, η,
Velocity of environment, and
Coatings, inhibitors, etc.

[1] Wei & Spiedel, 1972.

[2] These three parameters are interrelated. Only two of the three need be specified. For loading into compression, stress intensity factor is not defined and the effective K_{min} is either zero or nearly zero. An operational definition of $\Delta K = K_{max}$, with R specified in terms of the applied stress or load, has been adopted for $R \leq 0$ (ASTM, 1989).

Material	σ_{YS} (MPa)	Environment	Crack Size Type (mm)	da/dN Defined by ΔK?	$\frac{da/dN_{SMALL}}{da/dN_{LONG}}$	Limiting Small Crack Size (mm)	Comments	Reference	
AISI 4130 (.3C-.9Cr-.2Ni)	1330	3% NaCl	.1-40 Long 1.9 Wide Edge, Elliptical	Yes - Air, Vacuum No - NaCl	1.2 to 500	>2.5	Growth Retarded by Increased K_{max}, R; $1/\sqrt{\rho_{max}}$ Describes da/dN. 15 μm Grain Size.	13, 21	High Strength
ASTM A289-B (18.2Mn-4.8Cr-.6C)	1120	655 kPa H_2 Sat. H_2O 80°C	.1-40 Long 25 Wide Edge @ Notch	Yes - Air 23°C Yes - 10 Hz H_2 No - .02 Hz H_2	1.0 to 100	.8	Small Crack Growth Enhanced by Increased Initial ΔK and Loading Time. 100 μm Grain Size.	26.	
HY130 (.1C-.5Cr-5Ni)	930	3% NaCl	.1-40 Long 1.9 Wide Edge	Yes - Air No - NaCl	4	>1.0	Initial ΔK Not Important.	22	Medium Strength
	972	3% NaCl	.4-40 Long 7.6 Wide Edge	Yes - Air No - NaCl	2	1.1	Limiting Crack Size Unaffected by Δσ, R.	18, 27	
	972	3% NaCl	.4-40 Long 7.6 Wide Edge	Yes - Air No - NaCl	1.0-1.8 Free Corrosion 0.8-1.3 Cathodic	0.9-1.4 5	Limiting Crack Sizes Up to 10 mm at Constant ΔK. No Significant Crack Closure Measured.	28	
	950	Seawater	>.5 Long 12.7 Wide Edge	Yes	1.0	<.5	Limited Data.	29	
13 Cr (.03C-12.8Cr-5Ni)	770	Water	?	No	4	?	High Frequency, Near Threshold Data. Magnitude of Small Crack Effect Enhanced at High R.	25	
Q1N (.17C-1.2Cr-2.4Ni)	625	Seawater	.5-6 Long 12.7 Wide Edge	Yes - Air No - NaCl	4	2.0	No Crack Size Effect at R=0.5 or ΔK > 30 MPa$\sqrt{m}$. Limited Data for Air.	29, 30	Low Strength
BS4360:50D (.16C-1.2Mn)	370	Seawater	1-7 Long 23.5 Wide Edge	Yes - Air No - NaCl	3	1.0-3.0	Crack Size Effect Eliminated by Cathodic Polarization; da/dN Small to Large < 1.0.	31	
EN5 (.3C-.7Mn)	300	Seawater	.5-6 Long 12.7 Wide Edge	? - Air No - NaCl	2	2.0	Limited Data.	29	

TABLE 2.2: Literature Results Demonstrating the Effect of Crack Size on the Corrosion Fatigue Crack Growth Rate of Steels Exposed to Aqueous Environments (Gangloff & Wei, 1986).

TABLE 3.1: The Longcrack Saltwater Tests	
Tests in De-aerated 3.5% NaCl Solution: Tests 21 - 32	
ΔK levels: 30.6, 20.9, and 14.0 MPa$\sqrt{m}$	} 12 specimens total
T levels: 277, 298, 320, 345 K	
f levels: 10, 5, 2.5, 1, 0.5, 0.25, 0.1, 0.05 Hz	
R=0.25 and Φ_{ec}=−800 mV (SCE)	
Each specimen is tested at a single ΔK and T level while the f levels are scanned.	

TABLE 3.2: The Argon Gas Tests	
Tests in Dehumidified UHP Argon Gas: Tests 33 - 35	
ΔK levels: 28.3, 19.3, 13.4 MPa$\sqrt{m}$	} 3 specimens total
T levels: 284, 298, 320, 345 K	
f level: 10 Hz	
R=0.25	
Each specimen is tested at a single ΔK and f level while the T levels are scanned.	

TABLE 3.3: The Preliminary Short Crack Tests			
ΔK (MPa$\sqrt{m}$)	T (K)	f (Hz)	# of Tests
30.5	278	10	2
30.4	278	1	2
30.4	325	10	1
30.5	326	1	1
14.5	326	1	1
14.4	325	10	1
R=0.25, Φ_{ec}=−800 mV (SCE), Tests 13-18.			

TABLE 3.4: The Short Crack Saltwater Tests			
ΔK (MPa$\sqrt{m}$)	T (K)	f (Hz)	# of Tests
30.3, 21.1, 14.3	278	1	3
30.4, 21.0, 14.4	298	10	3
30.2, 21.0, 14.4	320	1	3
28.3, 21.0, 14.1	345	10	3
R=0.25, Φ_{ec}=−800 mV (SCE), One ΔK level per specimen, Tests 21-32.			

TABLE 4.1 : Properties of HY-130 Steel

Mechanical Properties

Proportional Limit[1] : 730 MPa

Yield Strength (2% Offset) : 932 MPa

Tensile Strength : 974 MPa

Reduction in Area : 66%

Hardness : 34.6 R_C

Physical Properties

Melting Temperature : 1760 K (est.)

Density[7] : 7890 kg/m^3

Magnetic Permeability[5] : 630 (max)

Electrical Resistivity[5] (20°C) : 0.35 $\mu\Omega$-m

Specific Heat[5] (20°C) : 489 J/kg-°C

Thermal Expansion[5] : 13.1×10^{-6} m/m-°C

Thermal Conductivity[5] (20°C) : 27.7 W/m-°C

Elastic Properties

Modulus of Elasticity[1] (20°C) : 205 GPa

Shear Modulus (20°C) : 79 GPA (est.[2])

Poisson's Ratio : 0.294 (est.[2])

Fracture Properties

K_{Ic} : 275MPa$\sqrt{m}$ (est.[3])

K_{Iscc}[6] : 110 MPa$\sqrt{m}$

K_{th}: 4 to 6 MPa$\sqrt{m}$ (est.[4])

Electrochemical Properties

(De-aerated 3.5% NaCl Solution)

Free Corrosion Potential : -760 mV SCE (est.[8])

References

1. Boblenz et al., 1966; 2. Bell, 1968; 3. Ryder & Gallagher, 1974;

4. Vosikovsky,1978; 5. Hamburg, 1971;

6. Fujii, 1984; 7. US Steel, 1968; 8. Xu & Wei, 1988.

TABLE 4.2 : Chemical Composition of HY-130 Steel

Weight Percent											wppm		
C	Mn	P	S	Si	Ni	Cr	Mo	V	Al	Fe	N	O	H
.08	.70	.010	.004	.23	4.66	.40	.39	.03	.02	Baln.	72	16	1.5

TABLE 4.3 : Average Bulk Solution Properties

$[O_2]$ = 0.33 ppm pH = 6.2 Specific Gravity = 1.0235 (T=24.3°C)

TABLE 5.1 : Calibration Results

$$V = V_{measured} \times \frac{950}{I} \times \frac{5.0436}{\rho\,(T)}$$

$$\rho\,(T) = -4.937 + 6.080\times10^{-2}\,T - 9.1\times10^{-5}\,T^2$$

$$a = -1.603 + 2.342\times10^{-1}\,V - 8.774\times10^{-4}\,V^2 + 2.575\times10^{-6}\,V^3$$

$$\frac{da}{dV} = 2.342\times10^{-1} - 1.755\times10^{-3}\,V + 7.725\times10^{-6}\,V^2$$

$$VAR\left(\frac{da}{dV}\right) = 1.270\times10^{-5} - 1.033\times10^{-6}\,V + 3.086\times10^{-8}\,V^2 - 3.900\times10^{-10}\,V^3 + 1.771\times10^{-12}\,V^4$$

V : [μV] I : [mA] T : [K] a : [mm]

TABLE 6.1 : Argon Gas Fatigue CGR Test Results

Crack Growth Law : $\left(\frac{da}{dN}\right)_{ref} = C\Delta K^{\,n}$

Crack Growth Law Parameters		
T (K)	C	n
284	2.47×10^{-6}	3.33
298	2.39×10^{-6}	3.31
320	2.25×10^{-6}	3.36
345	1.37×10^{-6}	3.50
AVERAGES:	2.13×10^{-6}	3.37

TABLE 8.1: The Semi-Empirical Model Parameter Values

$$\left(\frac{da}{dN}\right)_{cf} = \left(\frac{da}{dN}\right)_{sat}\left\{1-\exp\left(\frac{-\kappa}{f}\right)\right\}$$

$$\kappa = \kappa_0 \exp\left(-\frac{\Delta E_a}{RT}\right)$$

$$\left(\frac{da}{dN}\right)_{max} = \left(\frac{da}{dN}\right)_{sat} + \left(\frac{da}{dN}\right)_{ref}$$

ΔK	T	$\left(\frac{da}{dN}\right)_{max}$	$\left(\frac{da}{dN}\right)_{sat}$	σ_{sat}	κ	σ_κ
14.20	277.4	0.0804	0.0641	0.0037	0.645	0.0797
14.13	297.9	0.0712	0.0552	0.0020	2.248	0.2679
14.20	320.0	0.0827	0.0664	0.0027	4.718	0.7978
13.54	345.8	0.0747	0.0608	0.0067	9.467	4.9994
21.24	277.4	0.2731	0.2099	0.0166	0.262	0.0550
20.87	297.7	0.2405	0.1809	0.0062	0.949	0.1067
20.81	319.8	0.3015	0.2425	0.0197	1.187	0.3302
20.56	344.3	0.3071	0.2505	0.0238	2.950	1.3317
30.72	277.4	0.7239	0.5047	0.0704	0.115	0.0339
30.85	297.9	0.7864	0.5640	0.0193	0.342	0.0342
30.20	320.7	0.7827	0.5757	0.0198	0.976	0.1061
27.10	344.9	0.7053	0.5616	0.0505	1.470	0.4936

ΔK: [MPa$\sqrt{m}$] T: [K]; $\left(\frac{da}{dN}\right)_{max}$: [$\mu$m/cyc] $\left(\frac{da}{dN}\right)_{sat}$: [$\mu$m/cyc] κ: [cyc/sec]

σ_{sat}(Standard Error): [μm/cyc] σ_κ(Standard Error): [cyc/sec]

TABLE 8.2 : The Results of the Fitted Empirical Model

$$\left(\frac{da}{dN}\right)_{max} = C_m \Delta K^{n_m}$$

$$C_m = 2.871\times10^{-5} \;\&\; \hat{\sigma}_{\ln(C_m)} = 0.359$$

$$n_m = 3.005 \;\&\; \hat{\sigma}_{n_m} = 0.118$$

$$\left(\frac{da}{dN}\right)_{sat} = C_s \Delta K^{n_s}$$

$$C_s = 3.142\times10^{-5} \;\&\; \hat{\sigma}_{\ln(C_s)} = 0.468$$

$$n_s = 2.889 \;\&\; \hat{\sigma}_{n_s} = 0.154$$

$$\kappa = \kappa_0 \exp\left(-\frac{\Delta E_a}{RT}\right) \;\&\; \kappa_0 = C_\kappa \Delta K^{n_\kappa}$$

$$\Delta E_a = 27.83 \frac{kJ}{mol} \;\&\; \hat{\sigma}_{\Delta E_a} = 2.23 \frac{kJ}{mol}$$

$$C_\kappa = 2.871\times10^{7}$$

$$n_\kappa = -2.328 \;\&\; \hat{\sigma}_{n_\kappa} = 0.268$$

$(da/dN)_{max}$ & $(da/dN)_{sat}$: [μm/cyc] and ΔK: [MPa$\sqrt{m}$]

C_m, C_s, & C_κ: [(μm/cyc)/(MPa$\sqrt{m}$)^{n_i}], i=m, s, or κ

T: [K]

	ΔK	pH_m	$-\phi_m$(mV)	$-\phi_{max}$(mV)	$\Delta\phi$(mV)	$i_a^{1/2}$($A^{1/2}$ cm^{-1})	$[H_2]$($mol\,l^{-1}$)
sea water	10	10.7	87.9	90.3	5.7	7.3×10^{-4}	4.7×10^{-3}
Mg-free sea water		11.9	69.5	69.5	7.8		—
3.5% NaCl		12.3	30.7	30.7	13.0		—
sea water	20	10.7	67.8	68.7	6.0	9.3×10^{-4}	2.9×10^{-3}
Mg-free sea water		11.7	54.1	54.1	2.4		—
3.5% NaCl		12.1	22.8	22.8	10.8		—
sea water	40	10.8	47.4	49.6	5.3	1.2×10^{-3}	1.8×10^{-3}
Mg-free sea water		11.5	48.4	49.3	4.8		—
3.5% NaCl		11.9	21.8	21.8	15.0		—

$E^{ext} = -1000$ mV; $R = 0.5$; $f = 0.1$ Hz; $l = 2.0$ cm; T = 5°C.

TABLE 8.3: The Effect of ΔK (MPa$\sqrt{m}$) on the Crack-Tip pH and Potential (mV) (Turnbull & Ferriss, 1986).

	f	pH_m	$-\phi_m$(mV)	$-\phi_{max}$(mV)	$\Delta\phi$(mV)	$i_a^{1/2}$($A^{1/2}$ cm^{-1})	$[H_2]$($mol\,l^{-1}$)
sea water	0.01	10.8	51.3	54.6	8.5	1.0×10^{-3}	1.9×10^{-2}
Mg-free sea water		12.5	14.3	14.3	3.6		—
3.5% NaCl		12.6	7.0	7.2	2.4		—
sea water	0.1	10.7	67.8	68.7	6.0	9.3×10^{-4}	2.9×10^{-3}
Mg-free sea water		11.7	54.1	54.1	2.4		—
3.5% NaCl		12.1	22.8	22.8	10.8		—
sea water	1	10.0	121.7	131.6	18.1	1.2×10^{-3}	6.4×10^{-4}
Mg-free sea water		10.0	130.0	140.3	19.1		—
3.5% NaCl		11.5	125.9	126.9	106.0		—

$E^{ext} = -1000$ mV; $R = 0.5$; $f = 0.1$ Hz; $l = 2.0$ cm; T = 5°C.

TABLE 8.4: The Effect of Cyclic Frequency, f (Hz), on the Crack-Tip pH and Potential (mV) (Turnbull & Ferriss, 1986).

	l(cm)	pH_m	$-\phi_m$(mV)	$-\phi_{max}$(mV)	$\Delta\phi$(mV)	$i_w^{1/2}$($A^{1/2}$ cm^{-1})	$[H_2]$($mol l^{-1}$)
sea water	2.5×10^{-2}	10.9	2.5	2.5	0.1	2.0×10^{-3}	8.3×10^{-4}
Mg-free sea water		11.3	0.0	0.0	0.0		—
3.5% NaCl		11.5	0.0	0.0	0.0		—
sea water	0.2	10.9	5.9	5.9	0.5	1.8×10^{-3}	8.6×10^{-3}
Mg-free sea water		12.2	1.0	1.0	0.4		—
3.5% NaCl		12.2	0.3	0.3	0.0		—
sea water	0.6	10.9	19.7	19.7	2.4	1.6×10^{-3}	7.6×10^{-3}
Mg-free sea water		12.1	8.2	8.3	2.9		—
3.5% NaCl		12.2	3.0	3.0	0.5		—
sea water	2.0	10.7	67.8	68.7	6.0	9.3×10^{-4}	2.9×10^{-3}
Mg-free sea water		11.7	54.1	54.1	2.4		—
3.5% NaCl		12.1	22.8	22.8	10.8		—

$E^{ext} = -1000$ mV; $R = 0.5$; $\Delta K = 20$ MPa $m^{1/2}$; $f = 0.1$ Hz; $T = 5$°C.

TABLE 8.5: The Effect of Crack Depth on the Crack-Tip pH and Potential (mV) (Turnbull & Ferriss, 1986).

	R	pH_m	$-\phi_m$(mV)	$-\phi_{max}$(mV)	$\Delta\phi$(mV)	$i_w^{1/2}$($A^{1/2}$ cm^{-1})	$[H_2]$($mol l^{-1}$)
sea water	0.1	10.6	138.0	166.0	45.3	3.9×10^{-4}	1.3×10^{-3}
Mg-free sea water		11.1	135.8	162.6	45.7		—
3.5% NaCl		12.3	102.0	119.0	35.0		—
sea water	0.5	10.7	67.8	68.7	6.0	9.3×10^{-4}	2.9×10^{-3}
Mg-free sea water		11.7	54.1	54.1	2.4		—
3.5% NaCl		12.1	22.8	22.8	10.8		—
sea water	0.8	10.8	25.5	25.8	0.3	1.5×10^{-3}	1.9×10^{-3}
Mg-free sea water		11.8	15.6	14.7	0.9		—
3.5% NaCl		11.8	6.3	6.6	0.5		—

$E^{ext} = -1000$ mV; $\Delta K = 20$ MPa $m^{1/2}$; $f = 0.1$ Hz; $l = 2.0$ cm; $T = 5$°C.

TABLE 8.6: The Effect of R Value on the Crack-Tip pH and Potential (mV) (Turnbull & Ferriss, 1986).

Bulk environment	E^{ext}	pH_m	$-\phi_m$(mV)	$-\phi_{max}$(mV)	$\Delta\phi$(mV)	$i_w^{1/2}$($A^{1/2}$ cm^{-1})	$i_{ext}^{1/2}$($A^{1/2}$ cm^{-1})	$[H_2]$(mol l^{-1})
3.5% NaCl	−800	11.4	17.7	17.7	17.5	4.9×10^{-5}		—
3.5% NaCl (O_2 free)		10.9	1.5	1.5	0.1	1.2×10^{-4}		—
sea water (Mg free)		10.2	18.1	21.4	6.1	3.2×10^{-4}		—
sea water (HCO_3^- free)		10.6	3.8	4.0	0.3	1.9×10^{-4}		1.0×10^{-4}
sea water		10.2	16.9	19.9	5.3	3.3×10^{-4}	8.3×10^{-4}	8.2×10^{-4}
3.5% NaCl	−900	11.6	14.8	14.8	13.8	1.7×10^{-4}		—
3.5% NaCl (O_2 free)		11.4	3.6	4.6	1.0	2.3×10^{-4}		—
sea water (Mg free)		11.0	39.3	43.1	7.9	2.2×10^{-4}		—
sea water (HCO_3^- free)		10.6	13.6	15.4	3.3	5.6×10^{-4}		7.9×10^{-4}
sea water		10.6	37.5	41.2	6.6	4.3×10^{-4}	2.1×10^{-3}	1.2×10^{-3}
3.5% NaCl	−1000	12.1	22.8	22.8	10.8	5.0×10^{-4}		—
3.5% NaCl (O_2 free)		12.1	16.3	17.7	5.1	5.0×10^{-4}		—
sea water (Mg free)		11.7	54.1	54.1	2.4	3.6×10^{-4}		—
sea water (HCO_3^- free)		10.8	50.5	55.8	9.9	1.1×10^{-3}		3.2×10^{-3}
sea water		10.7	67.8	68.7	6.0	9.3×10^{-4}	5.5×10^{-3}	2.9×10^{-3}
3.5% NaCl	−1100	12.5	64.0	66.0	9.6	8.3×10^{-4}		—
3.5% NaCl (O_2 free)		12.5	64.0	66.0	9.0	8.3×10^{-4}		—
sea water (Mg free)		12.3	91.3	91.3	6.3	6.9×10^{-4}		—
sea water (HCO_3^- free)		10.9	121.0	126.9	8.2	1.5×10^{-3}		6.7×10^{-3}
sea water		10.8	126.0	129.1	8.2	1.4×10^{-3}	1.4×10^{-2}	6.0×10^{-3}
sea water	−1200	10.9	208.0	215.9	14.9	1.7×10^{-3}	3.5×10^{-2}	9.0×10^{-3}

$R = 0.5$; $\Delta K = 20$ MPa $m^{1/2}$; $f = 0.1$ Hz; $l = 2.0$ cm and $T = 5$°C.

TABLE 8.7: The Effect of Applied Potential on the Crack-Tip pH and Potential (mV) for Sea-Water and 3.5% NaCl (pH=6.0) (Turnbull & Ferriss, 1986).

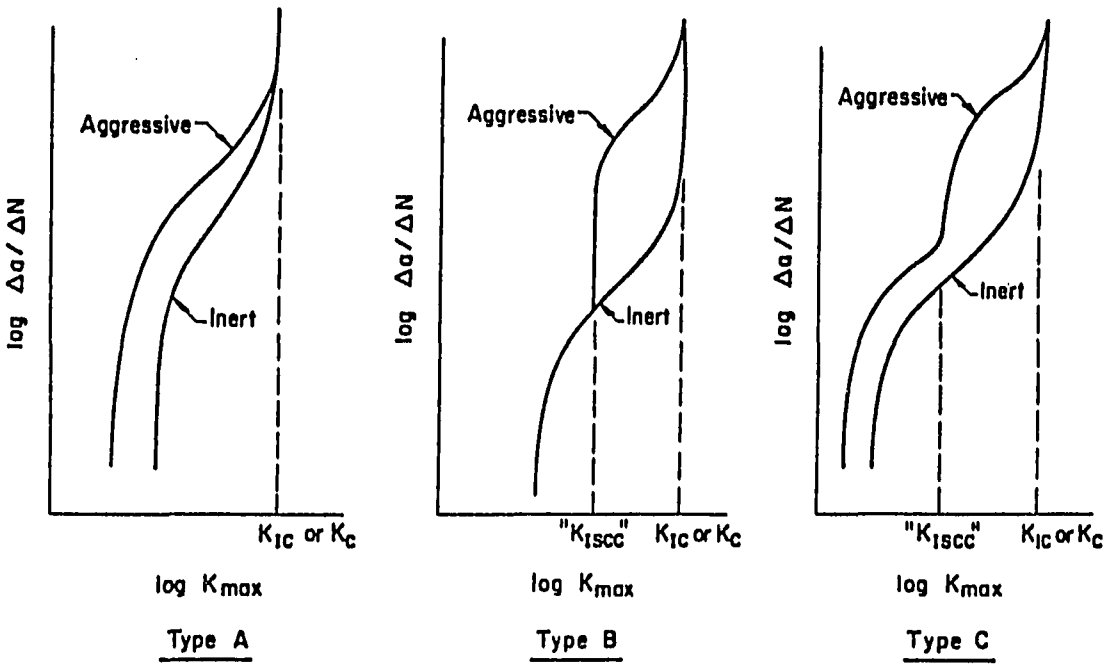

FIGURE 2.1: Types of fatigue crack growth behavior (McEvily & Wei, 1972).

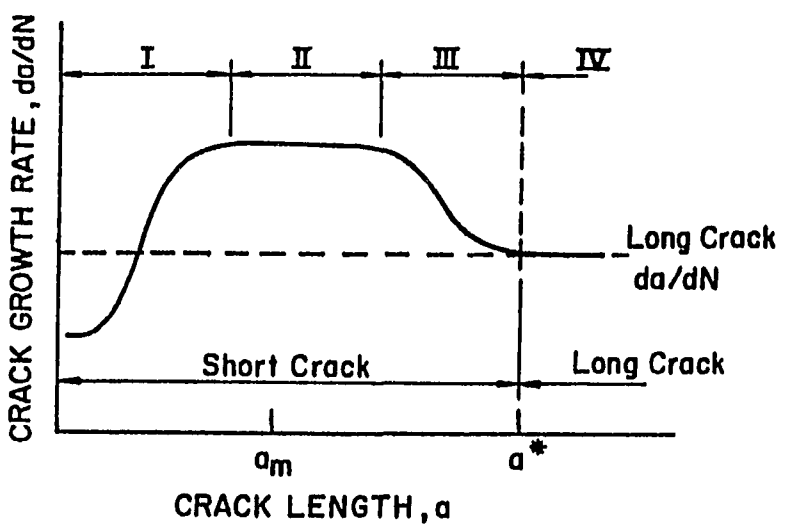

FIGURE 2.2: Schematic diagram for the change of the crack growth rate with crack length under constant stress intensity range loading (Nakai et al., 1986).

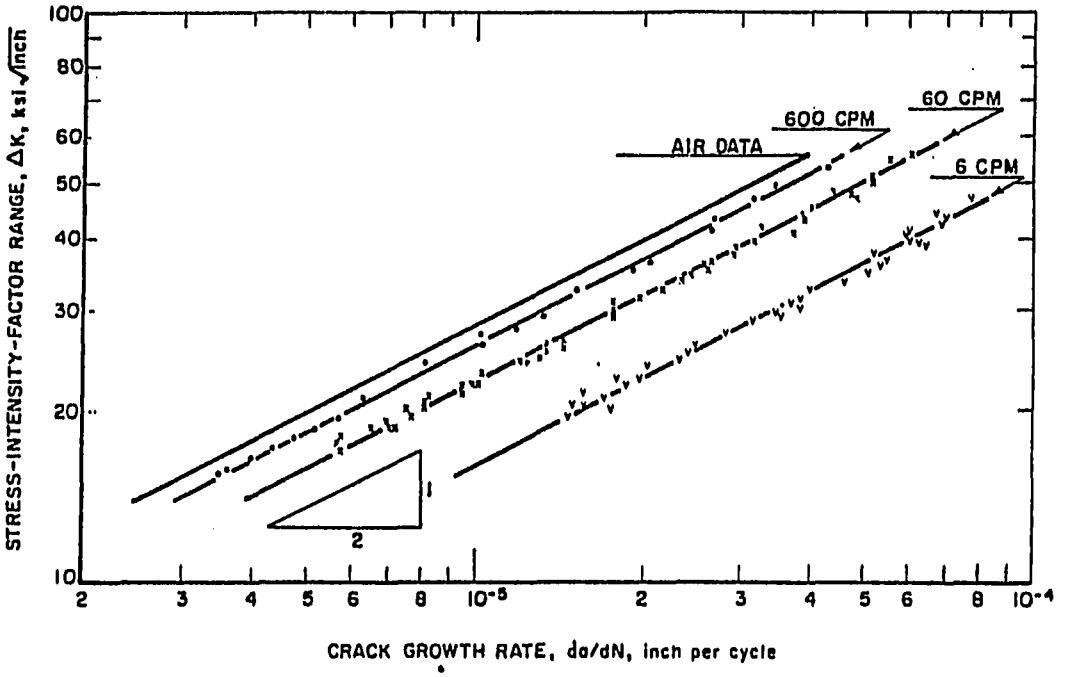

FIGURE 2.3a: Corrosion fatigue crack growth data as a function of test frequency for 12Ni-5Cr-3Mo steel tested in pH=7.0, 3% NaCl solution (Barsom, 1971).

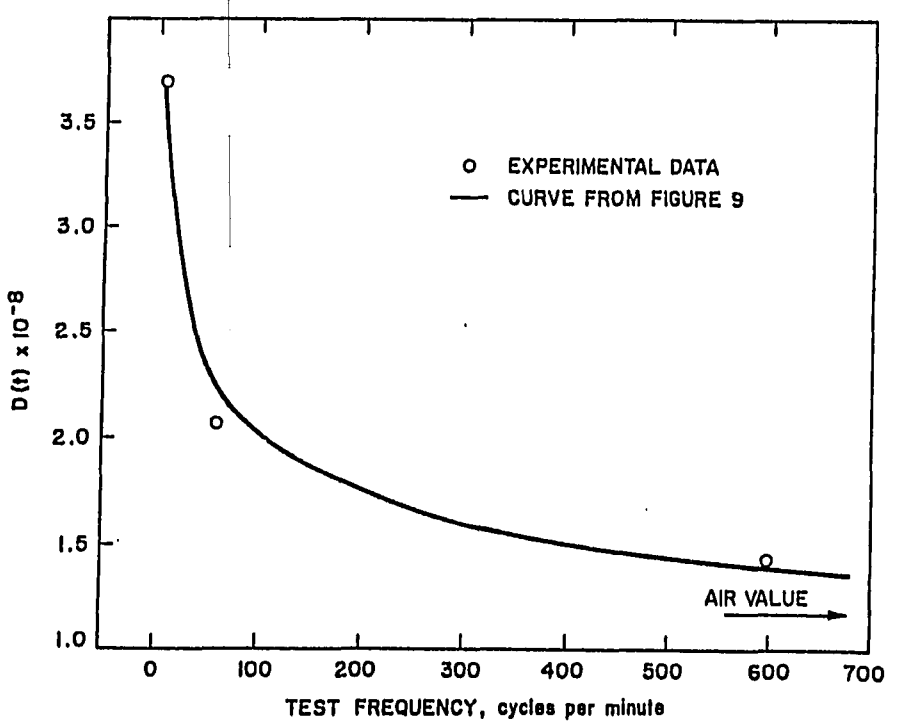

FIGURE 2.3b: Frequency dependent function D(t) versus the test frequency obtained from the data in Figure 2.3a (Barsom, 1971).

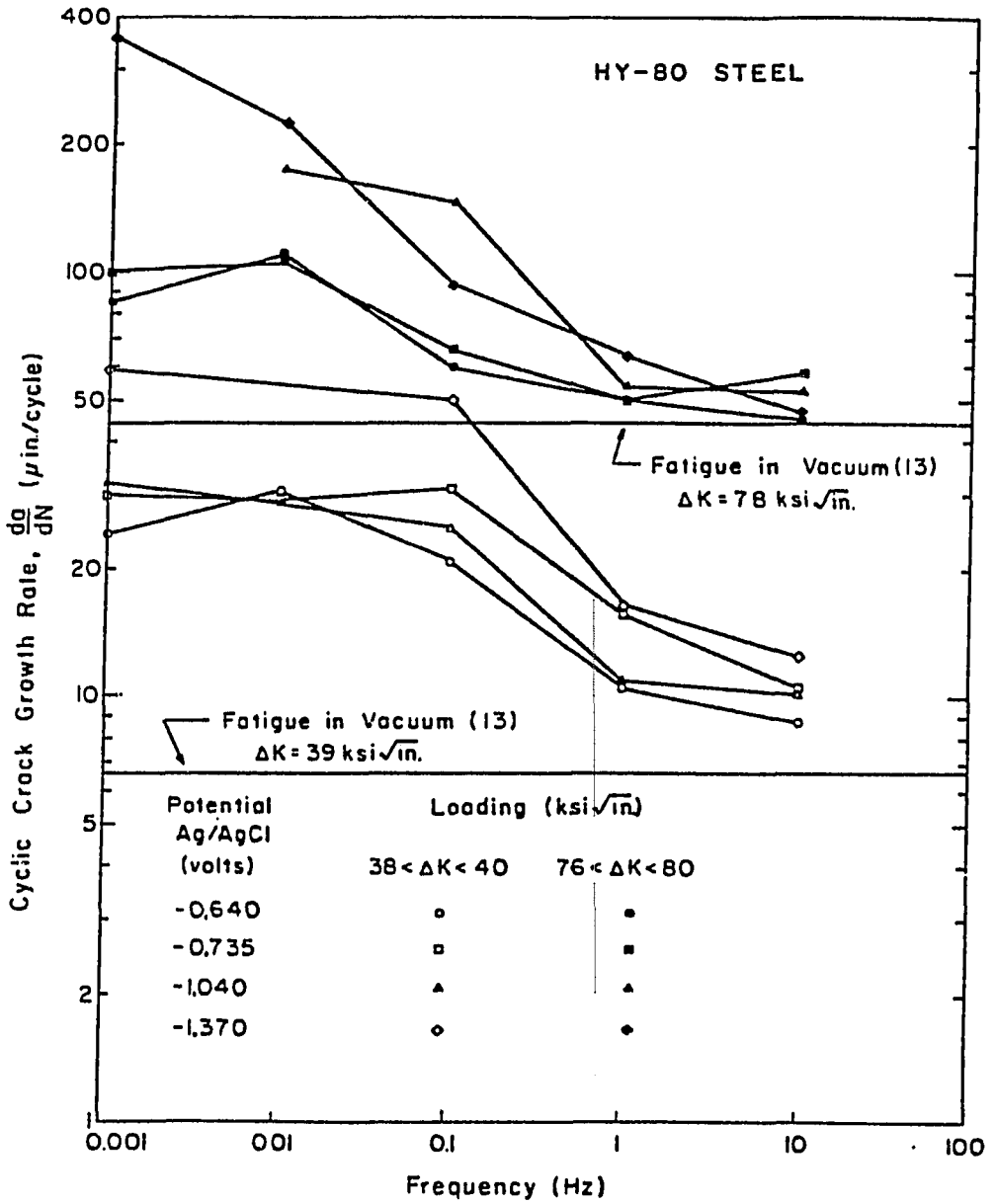

FIGURE 2.4: Corrosion fatigue cyclic crack growth rates in HY-80 steel as a function of frequency and electrochemical potential (Gallagher, 1971).

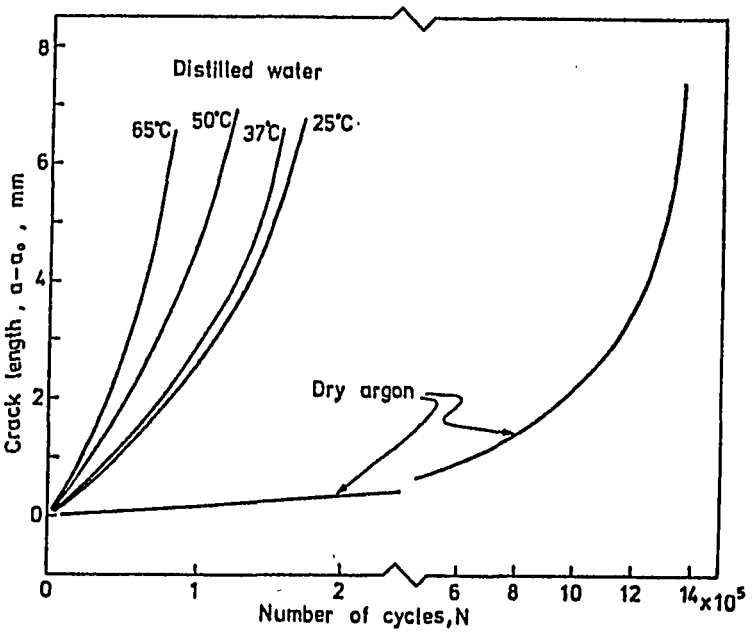

FIGURE 2.5a: Fatigue crack growth of a 0.5Cr-0.5Mo-0.25V steel at constant load range and frequency, versus elapsed cycles, for different temperatures and distilled water & dry Argon environments (Misawa et al., 1976).

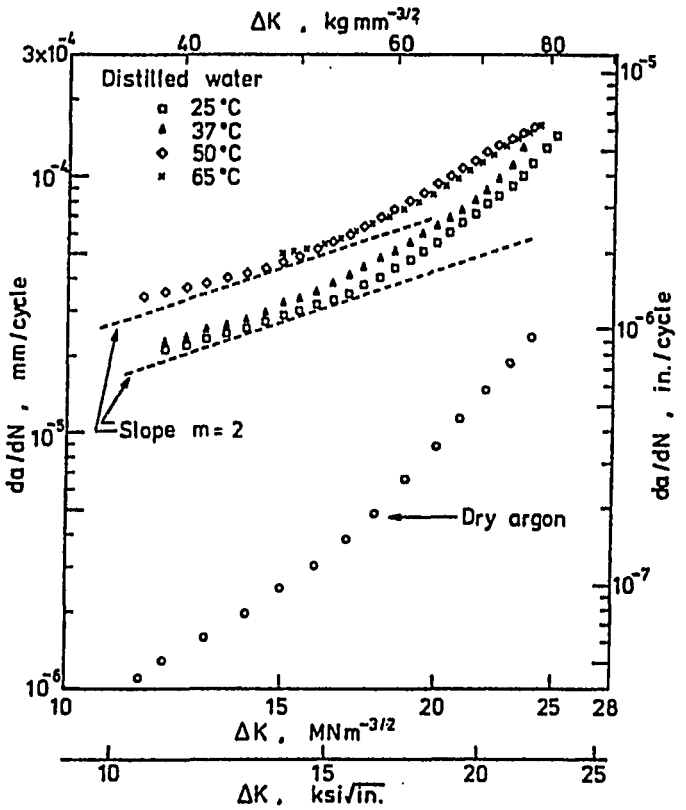

FIGURE 2.5b: Incremental fatigue crack growth versus ΔK for the different environments (Misawa et al., 1976).

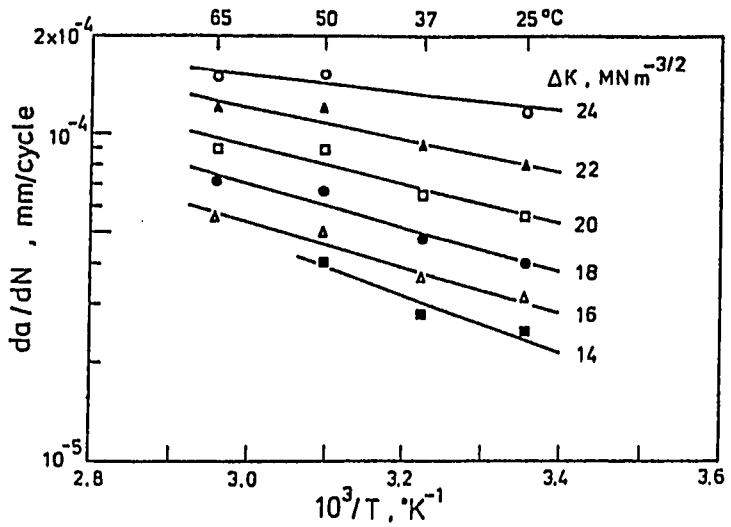

FIGURE 2.5c: Arrhenius plot of the incremental fatigue crack growth rate in the distilled water, for different values of ΔK (Misawa et al., 1976).

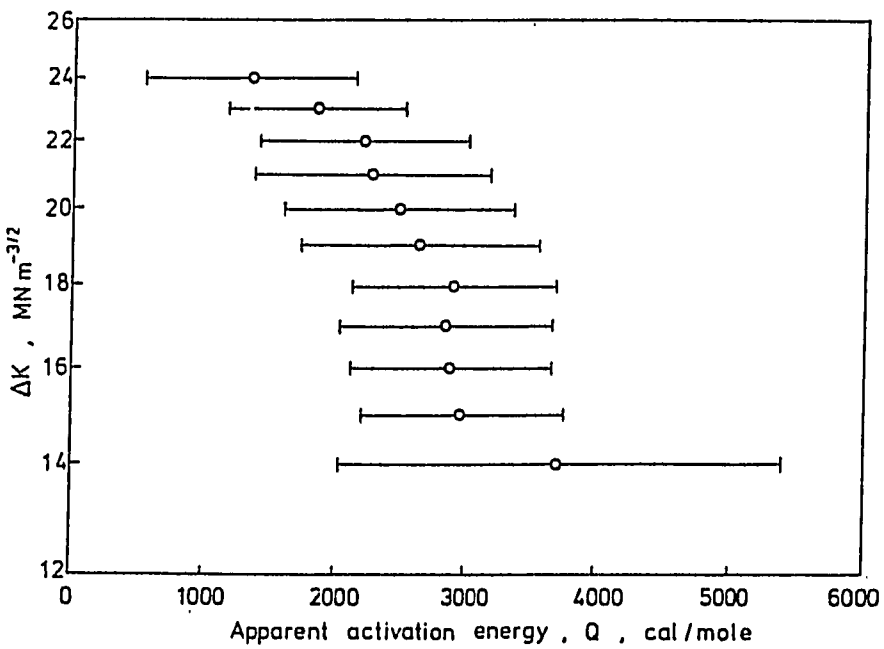

FIGURE 2.5d: The apparent activation energy for the rate controlling process in corrosion fatigue as a function of ΔK (Misawa et al., 1976).

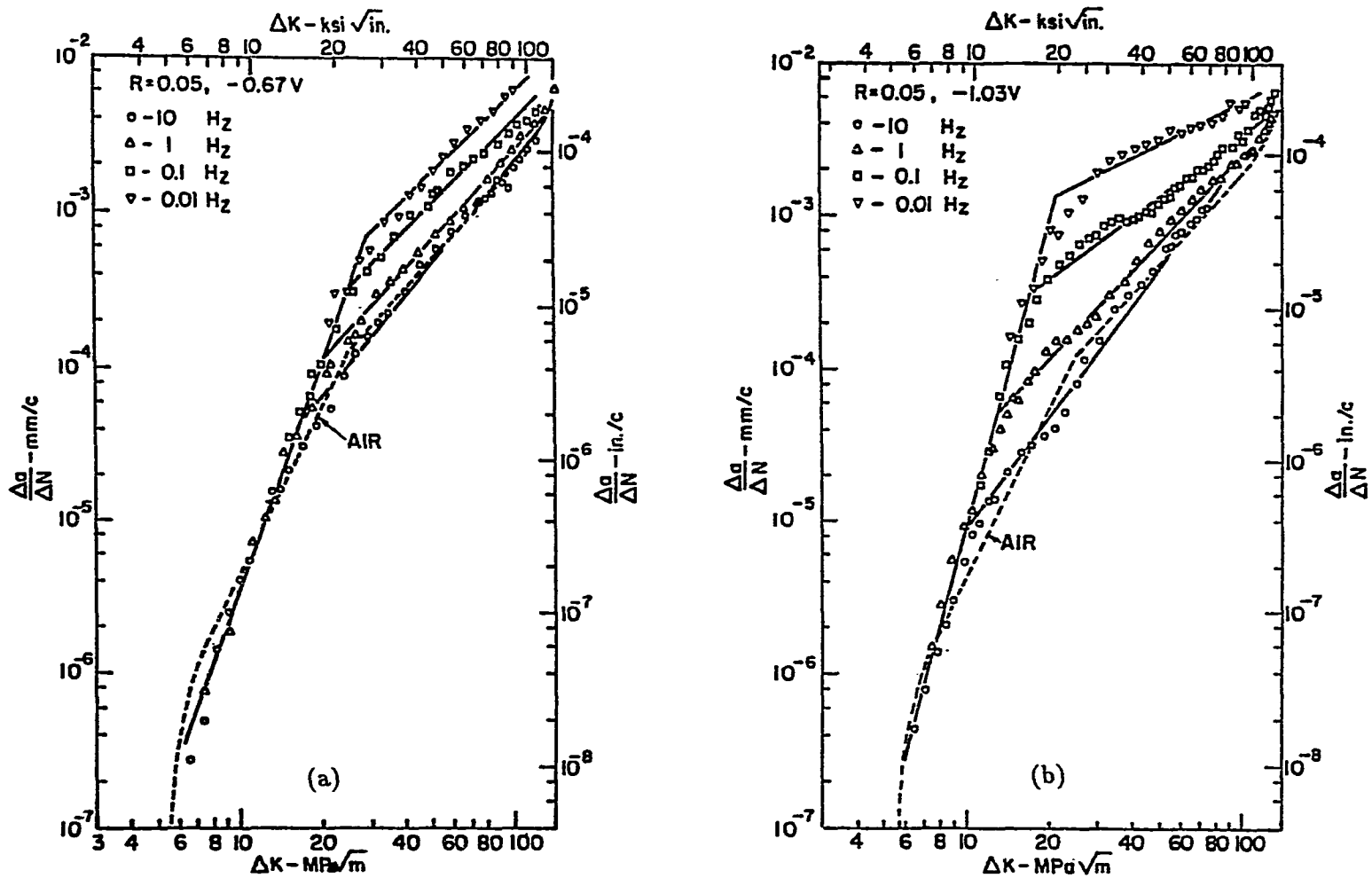

FIGURES 2.6a & 2.6b: The fatigue crack growth rate of HY-130 steel in 3.5% NaCl, and air, as a function of ΔK, for (a) the free corrosion potential, and (b) the Zinc corrosion potential, and four different loading frequencies (Vosikovsky, 1978).

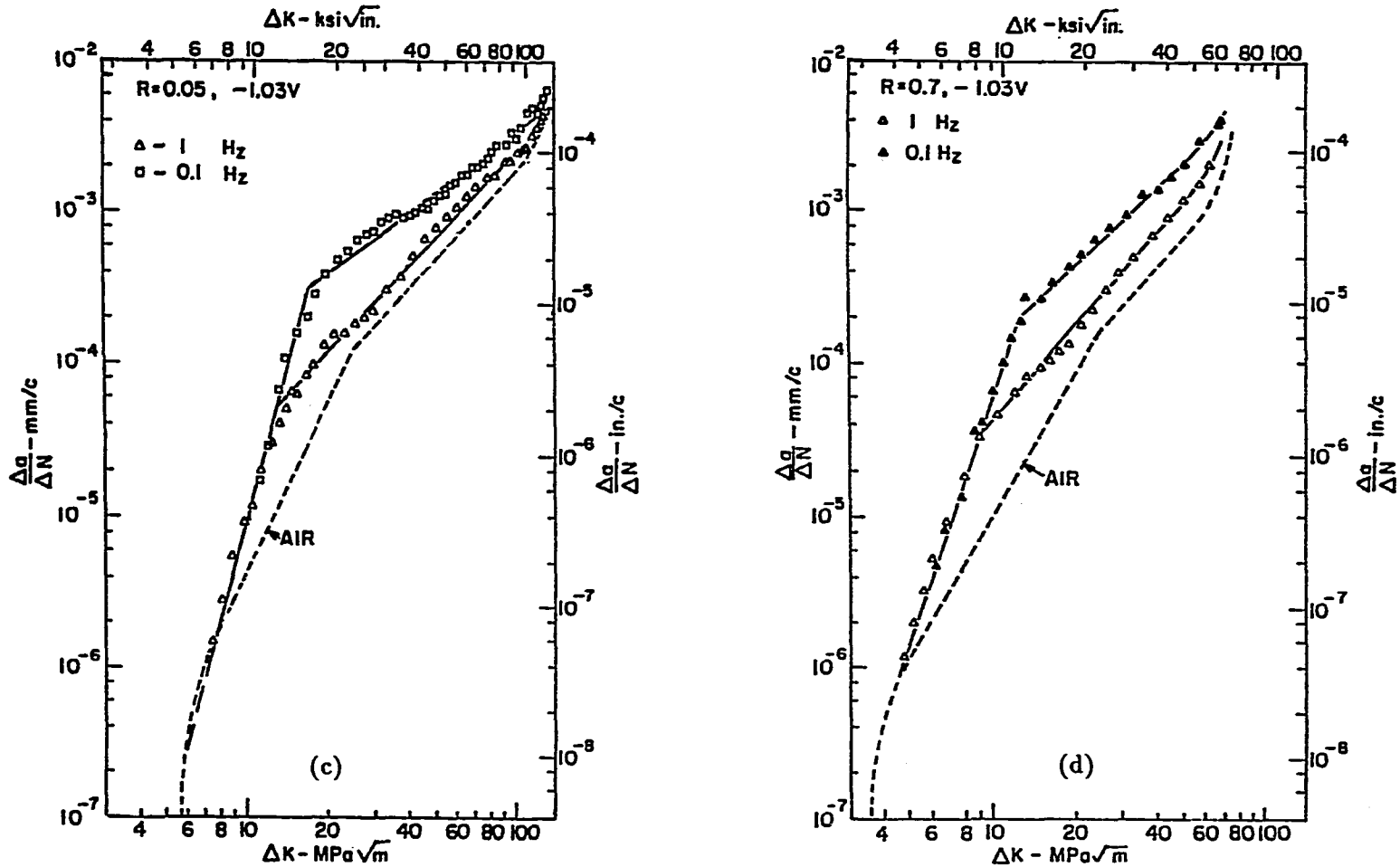

FIGURES 2.6c & 2.6d: The fatigue crack growth rate of HY-130 steel in 3.5% NaCl, and air, as a function of ΔK, for the Zinc potential, two loading frequencies, and (c) R=0.05, and (d) R=0.7 (Vosikovsky, 1978).

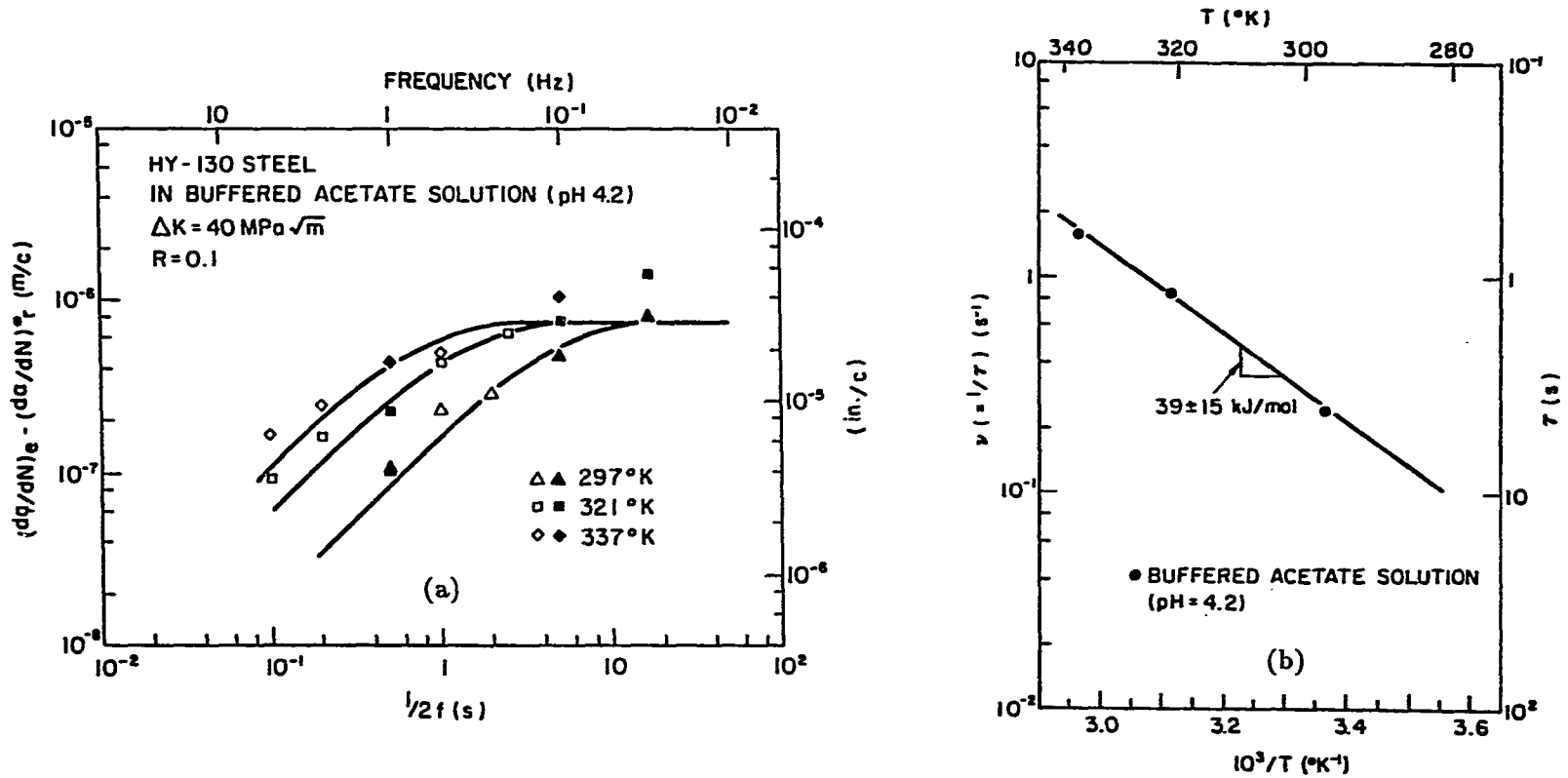

FIGURES 2.7a & 2.7b: (a) The influence of frequency and temperature on the fatigue crack growth rate for HY-130 (solid symbols) and modified HY-130 steel (open symbols) in buffered acetate solution (pH=4.2) (Wei & Shim, 1984).

(b) The effect of temperature on the characteristic frequency (ν) for fatigue crack growth in buffered acetate solution (pH=4.2) (Wei & Shim, 1984).

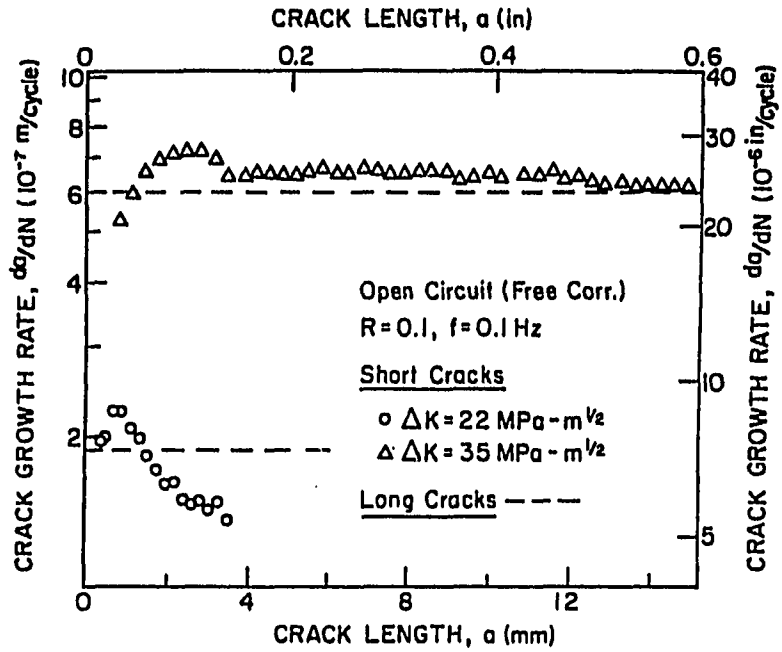

FIGURE 2.8a: Change of crack growth rate with crack length for the freely corroding condition under constant ΔK loading (Nakai et al., 1986).

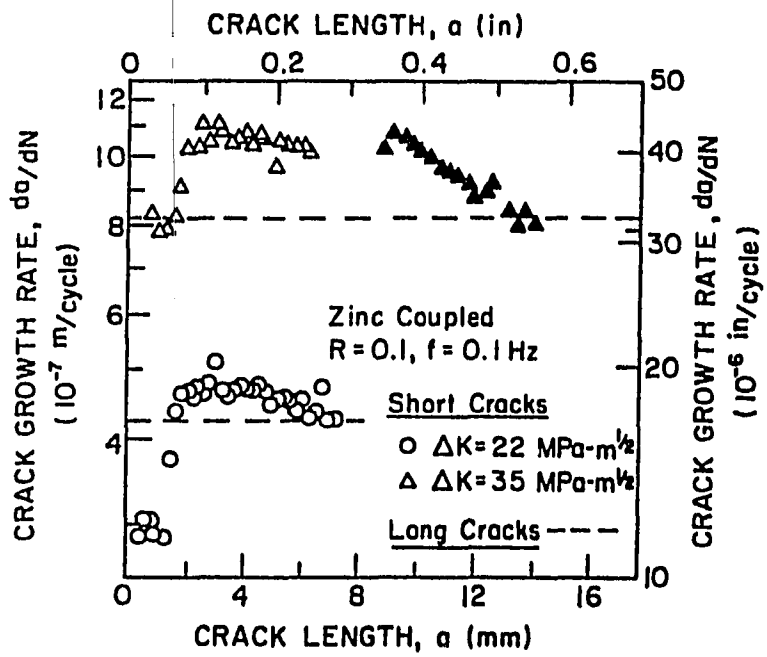

FIGURE 2.8b: Change of crack growth rate with crack length for the Zinc coupled condition under constant ΔK loading (Nakai et al., 1986).

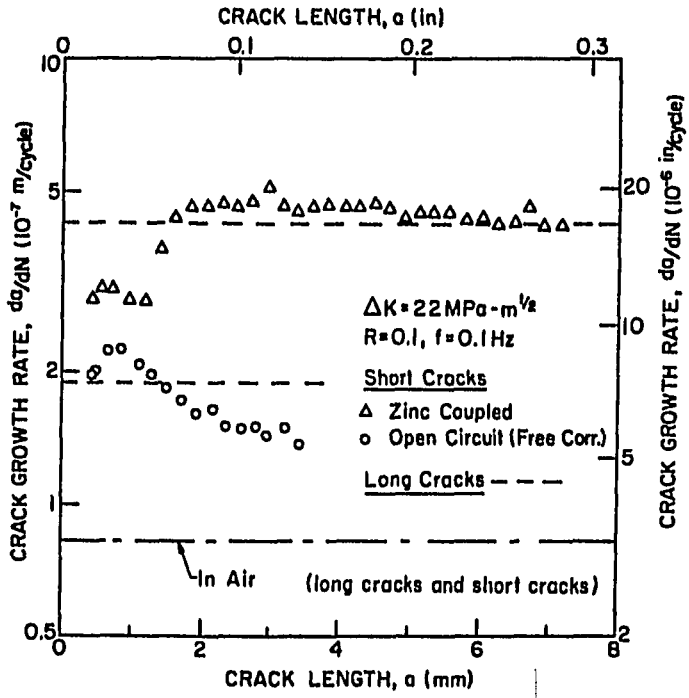

FIGURE 2.8c: Comparison of the crack growth rates in three environments at $\Delta K=22$ MPa$\sqrt{m}$ (Nakai et al., 1986).

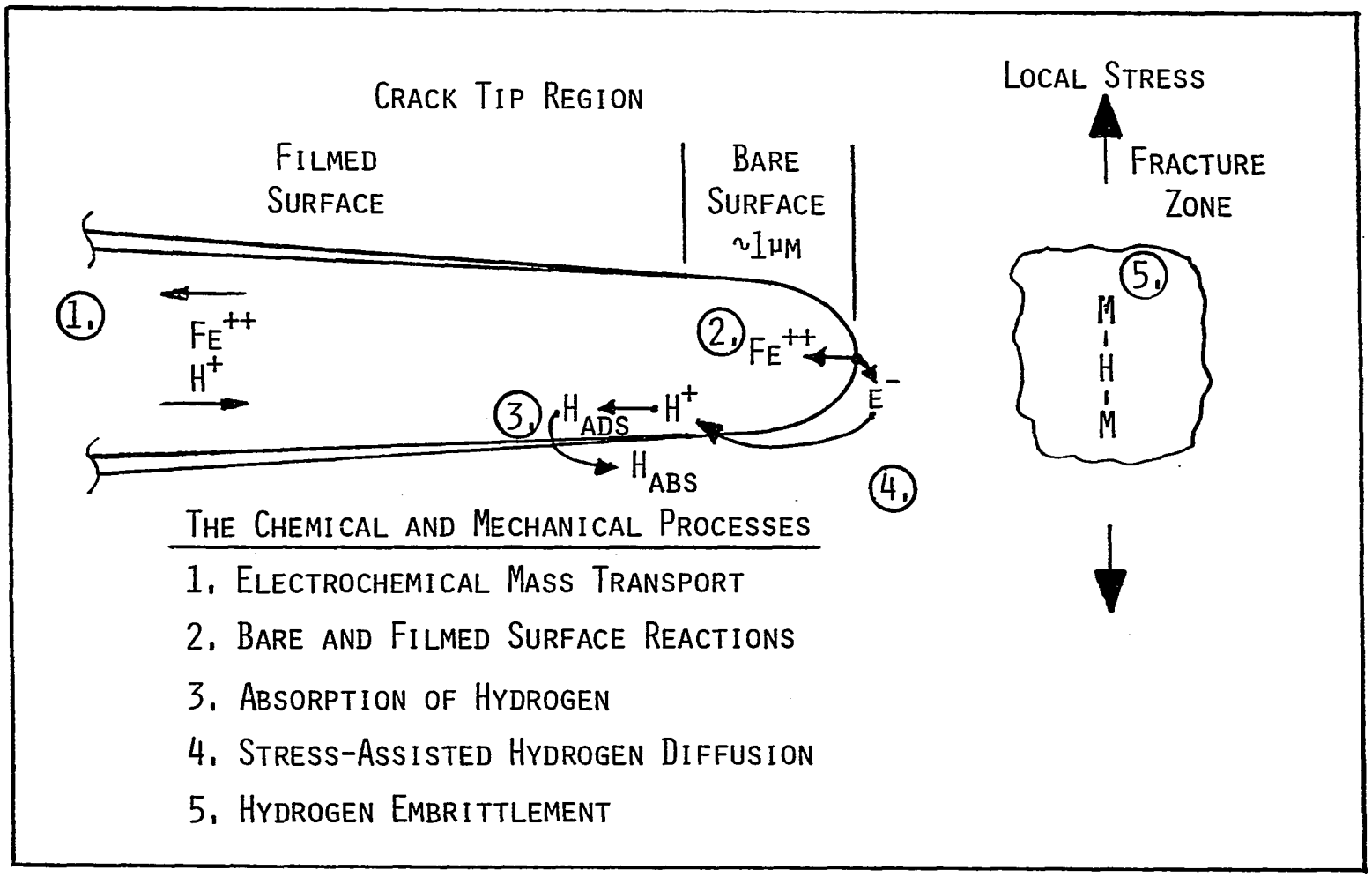

FIGURE 2.9: A schematic diagram illustrating the chemical and mechanical processes which occur in a growing fatigue crack in an aqueous environment.

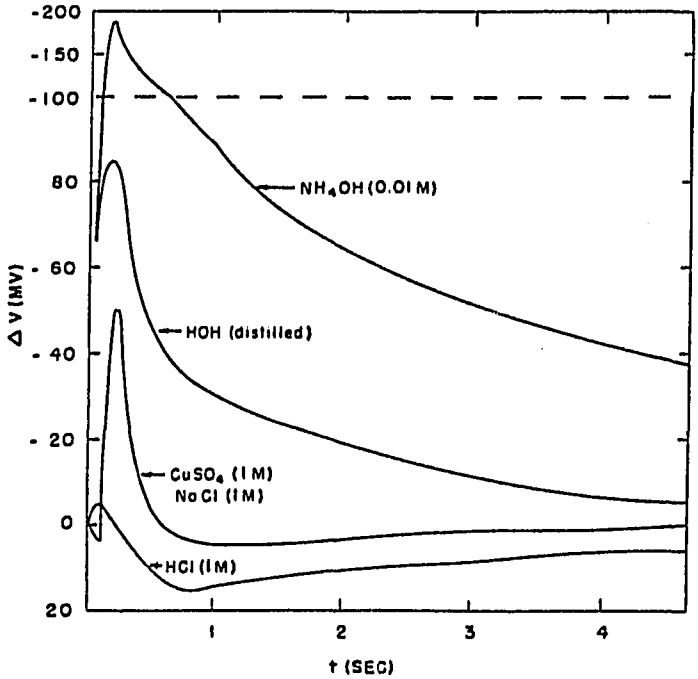

FIGURE 2.10a: Some example potential-time curves of strain electrometry for a copper material in a number of different environments (V measured with respect to a Cu electrode) (Funk et al., 1957a).

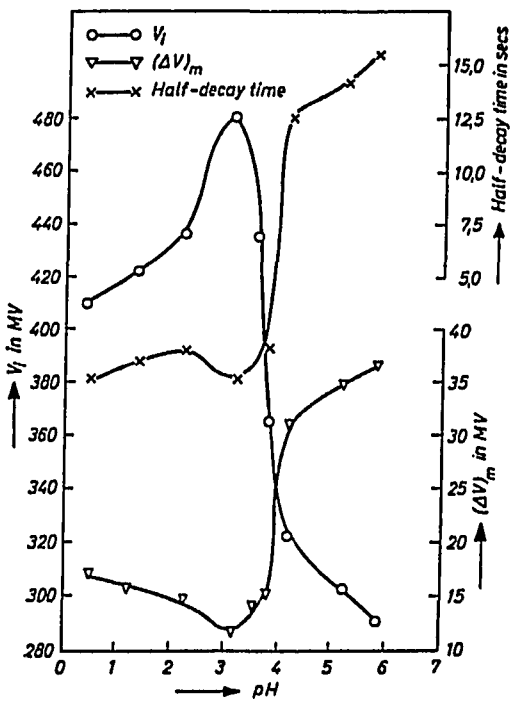

FIGURE 2.10b: The effect of pH on the free corrosion potential ($-V_i$), the maximum potential difference ($-\Delta V_i$), and the half-decay time, for iron in sulfuric acid, from the strain electrometry tests (V measured with respect to SCE) (Funk et al., 1958).

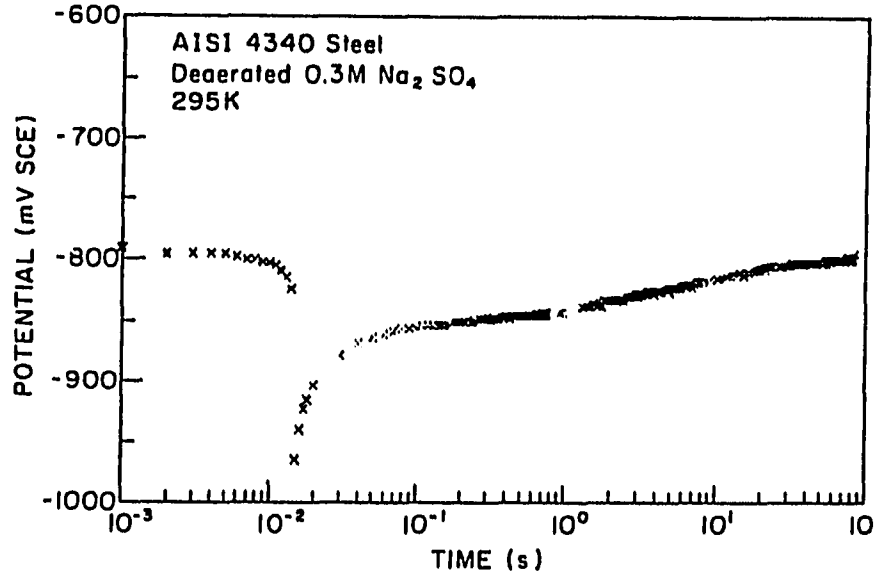

FIGURE 2.10c: A potential-time curve for an isolated bare surface of AISI 4340 steel in 0.3M Na_2SO_4 solution via the in-situ fracture technique (Wei & Alavi, 1988).

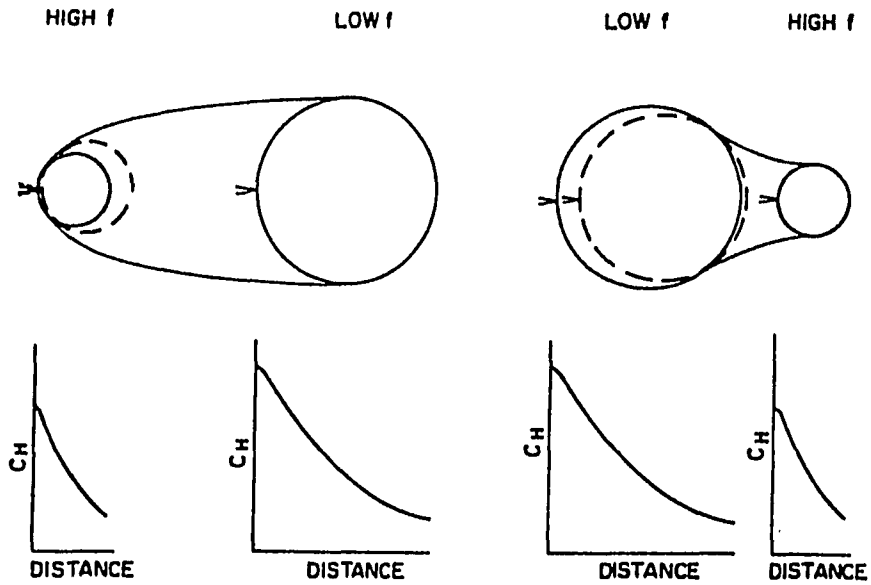

FIGURE 2.11: A conceptual model for the hydrogen distribution at the crack-tip for different frequencies. Note the change in size of the hydrogen distribution zone, with crack growth, after a change in the loading frequency (Pao et al., 1977).

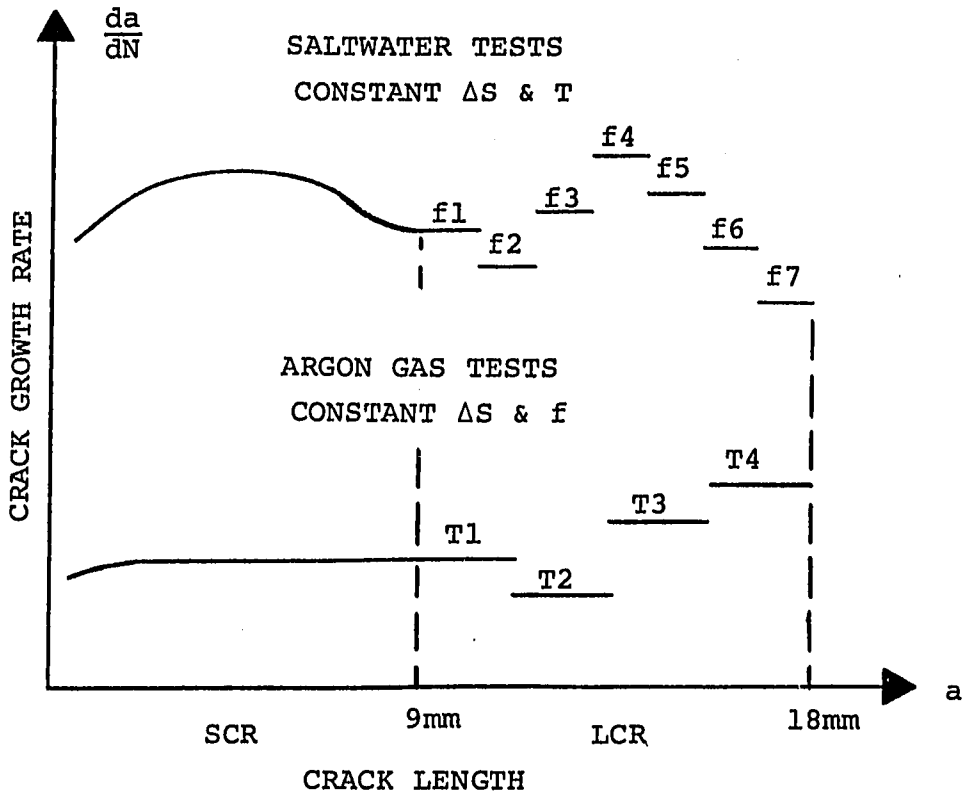

FIGURE 3.1: A schematic diagram for the test variable levels, as a function of crack length, for the long crack growth tests.

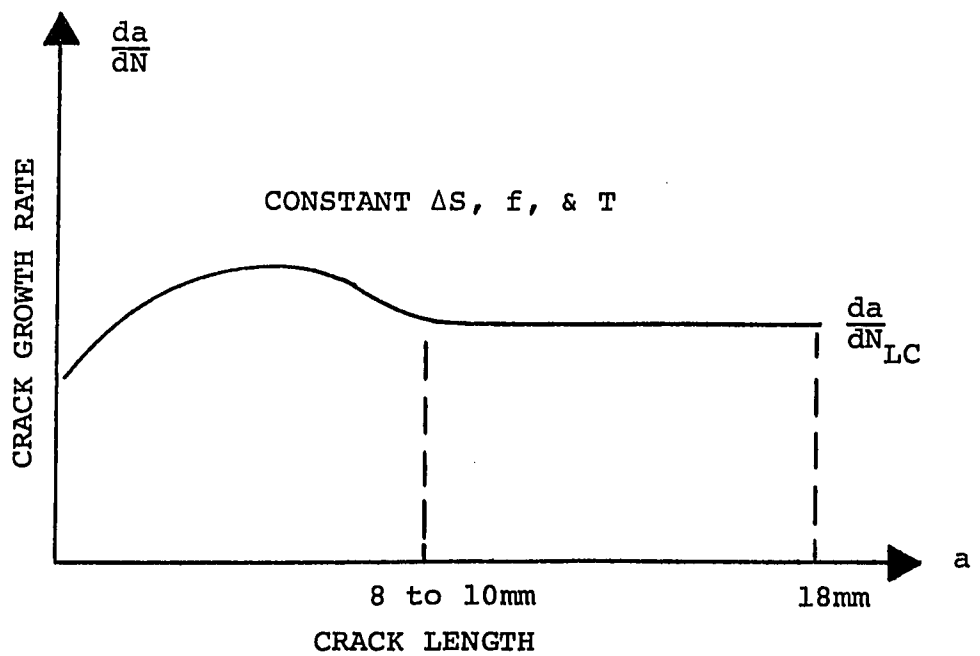

FIGURE 3.2: A schematic diagram for the test variable levels, as a function of crack length, for the preliminary short crack growth tests.

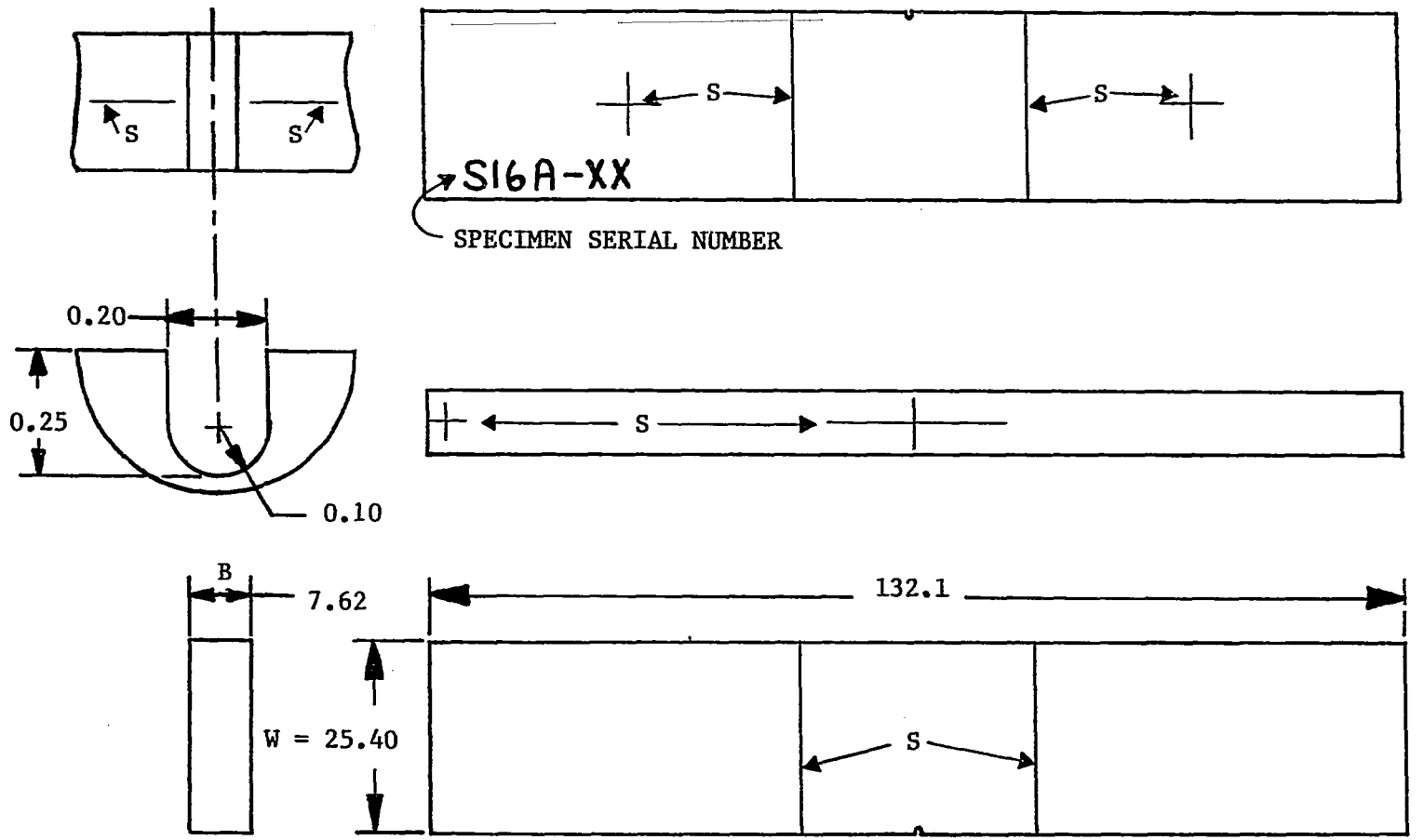

NOTES: "S" DENOTES SCRIBE MARKS; ALL DIMENSIONS IN MILLIMETERS

FIGURE 4.1: A diagram of the single-edge notch (SEN), four point bend specimen.

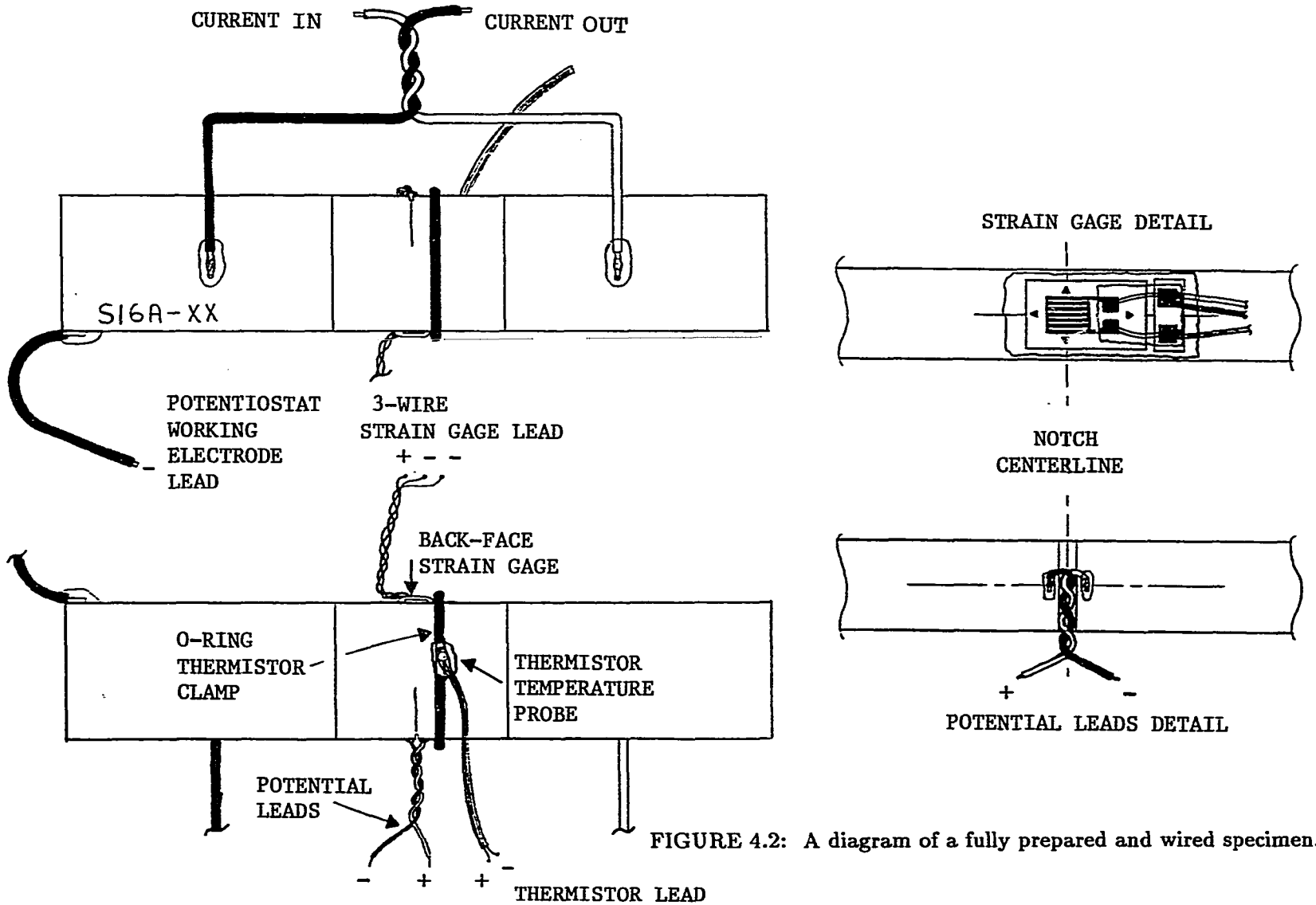

FIGURE 4.2: A diagram of a fully prepared and wired specimen.

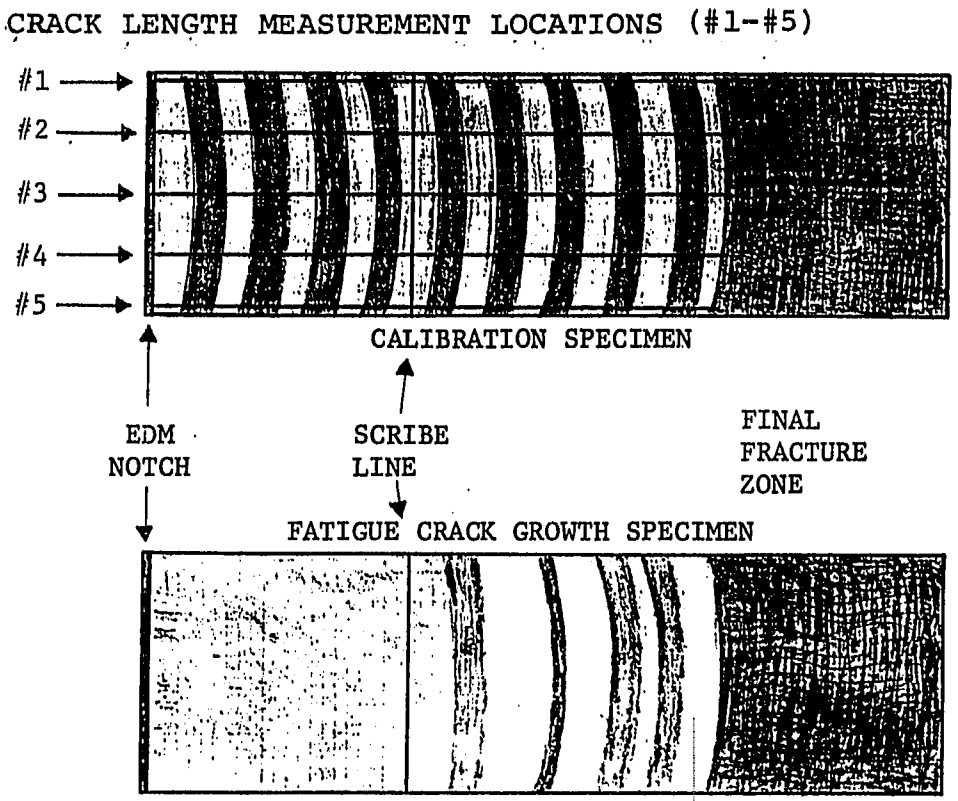

FIGURE 4.3a: A schematic diagram of the calibration and FCG test fracture surfaces showing the distinct surface zones and the crack length measurement scribe marks.

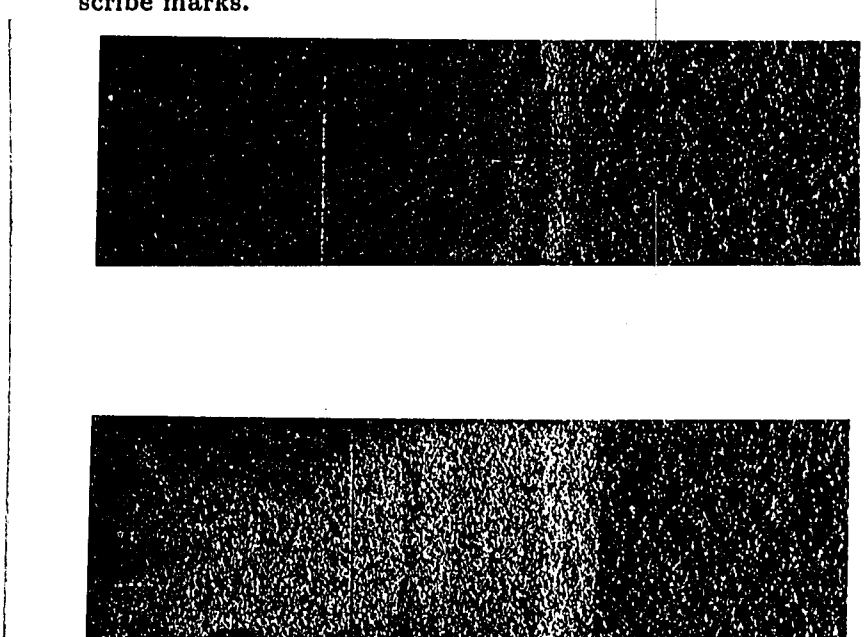

FIGURE 4.3b: A photograph of the calibration and FCG test fracture surfaces showing the distinct surface zones and the crack length measurement scribe marks.

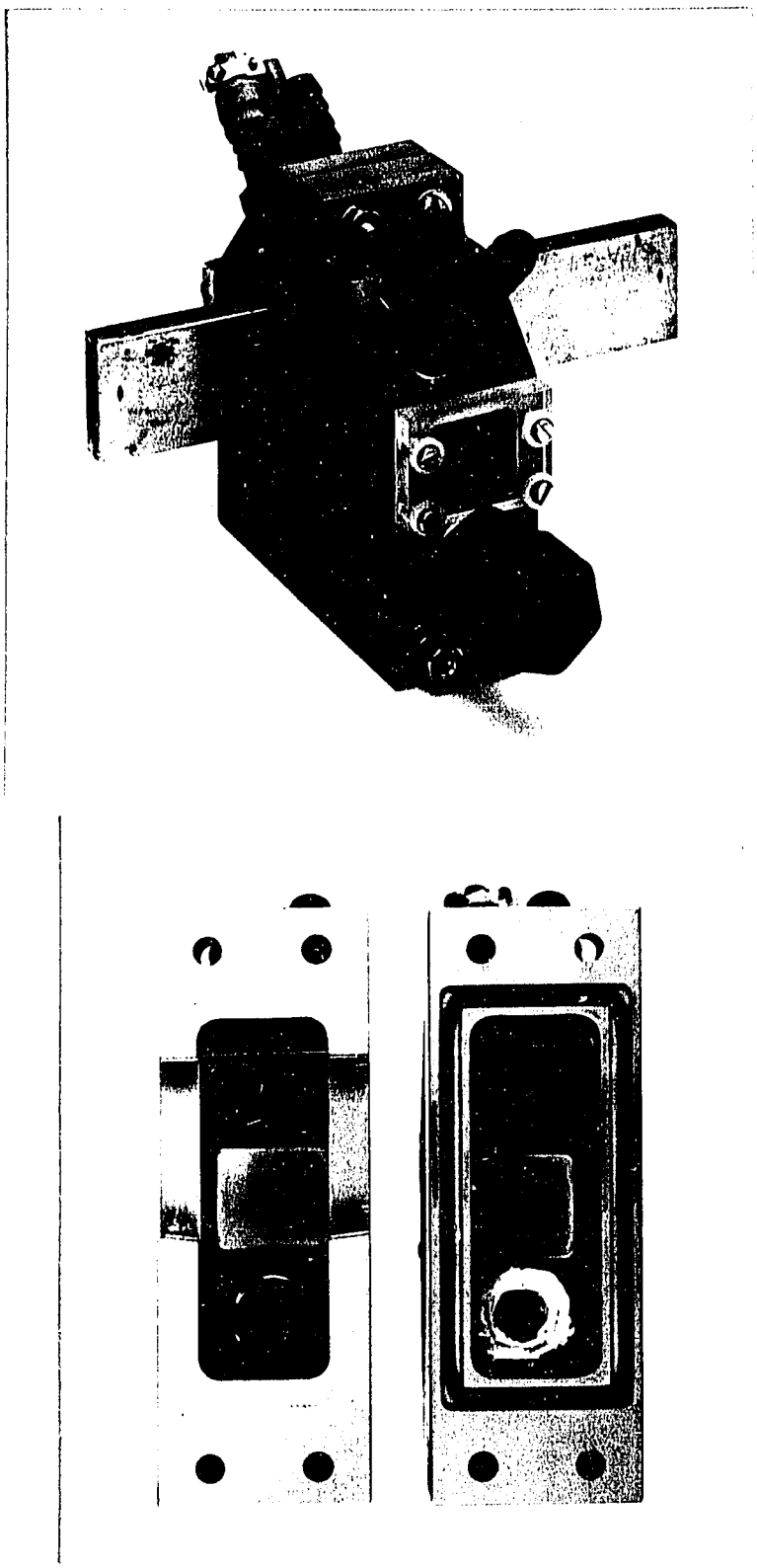

FIGURE 4.4: Photographs of the environmental chamber.

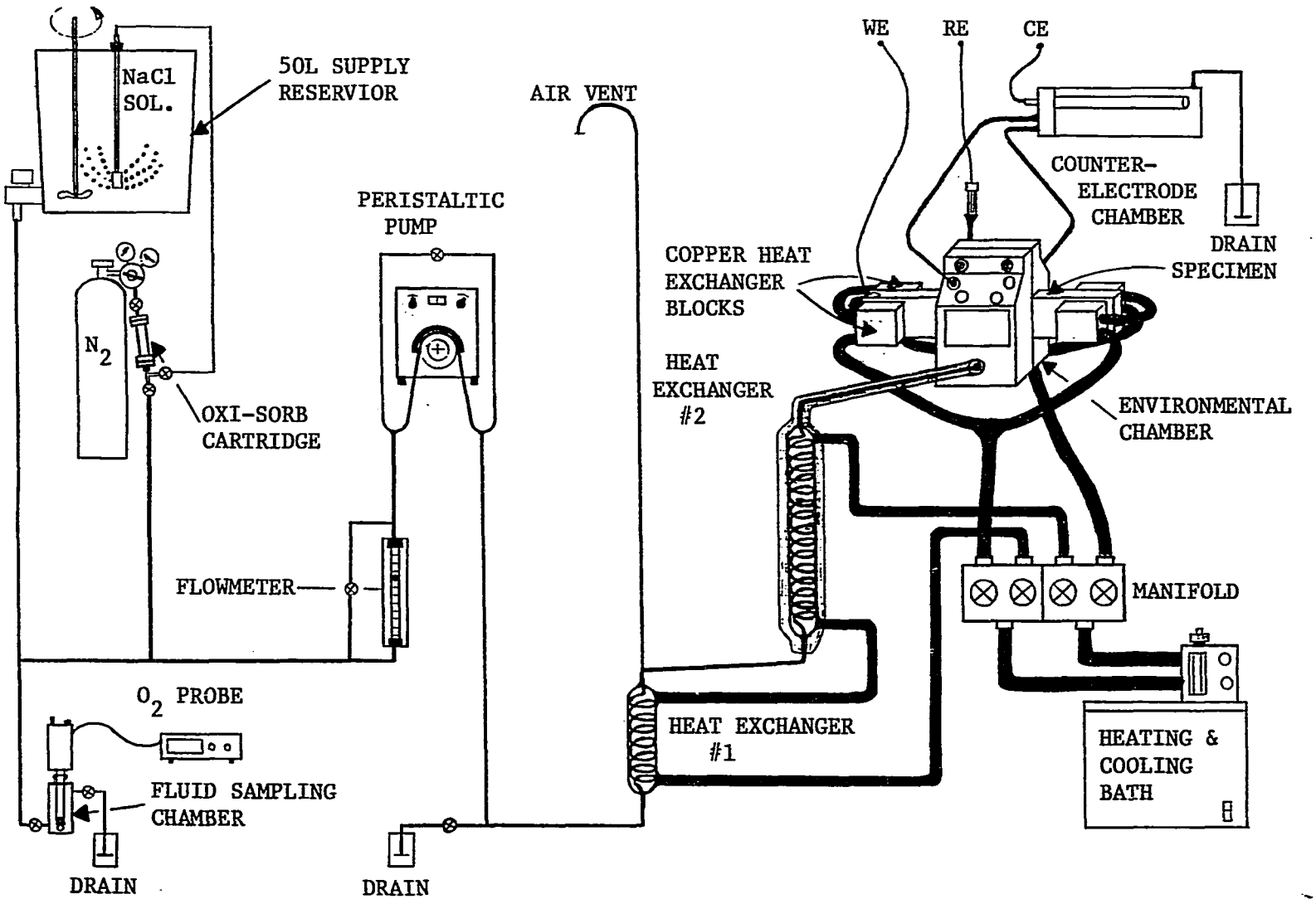

FIGURE 4.5: A diagram of the saltwater solution supply system and the temperature control system.

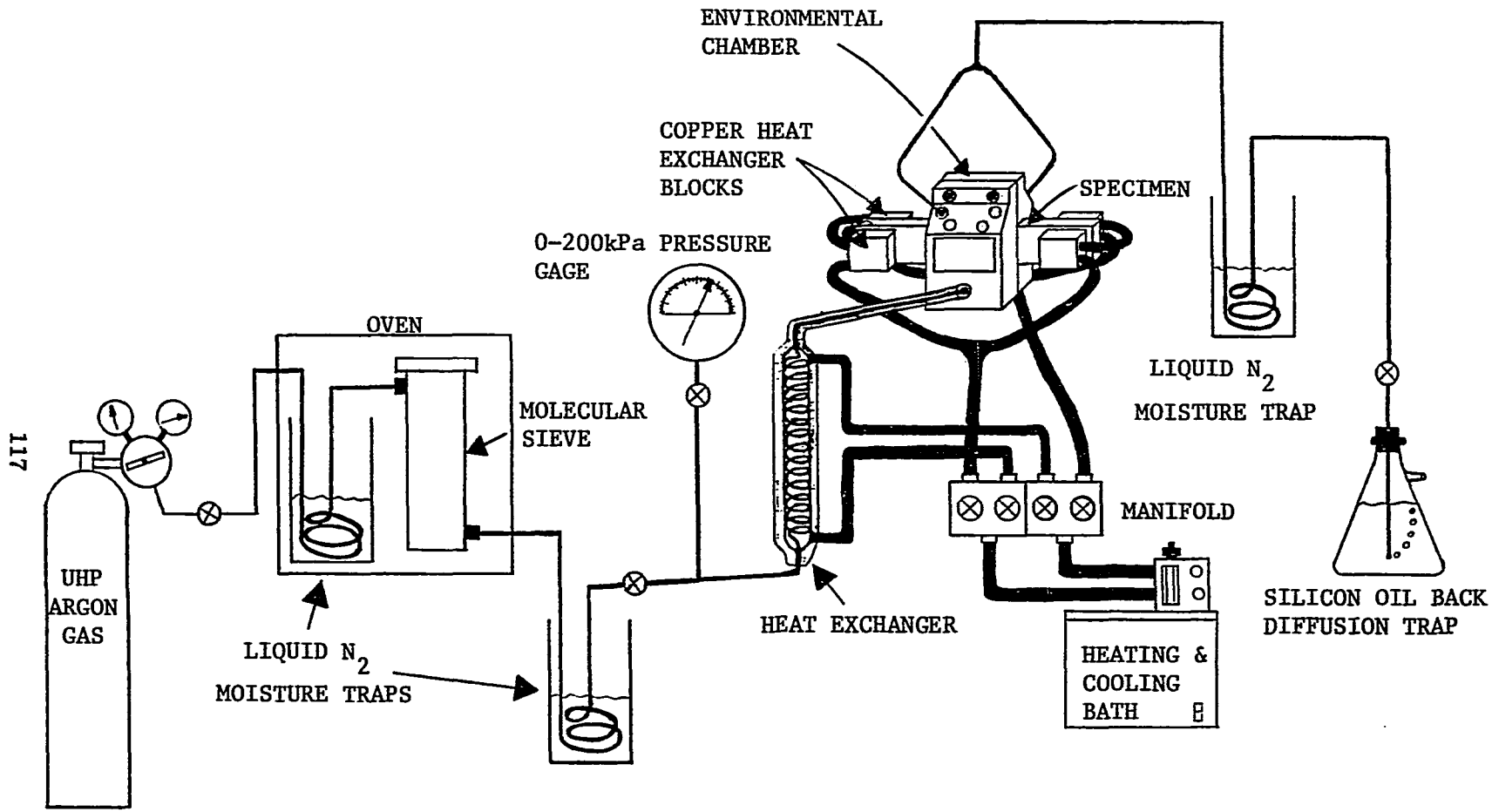

FIGURE 4.6: A diagram of the Argon gas supply system and the temperature control system.

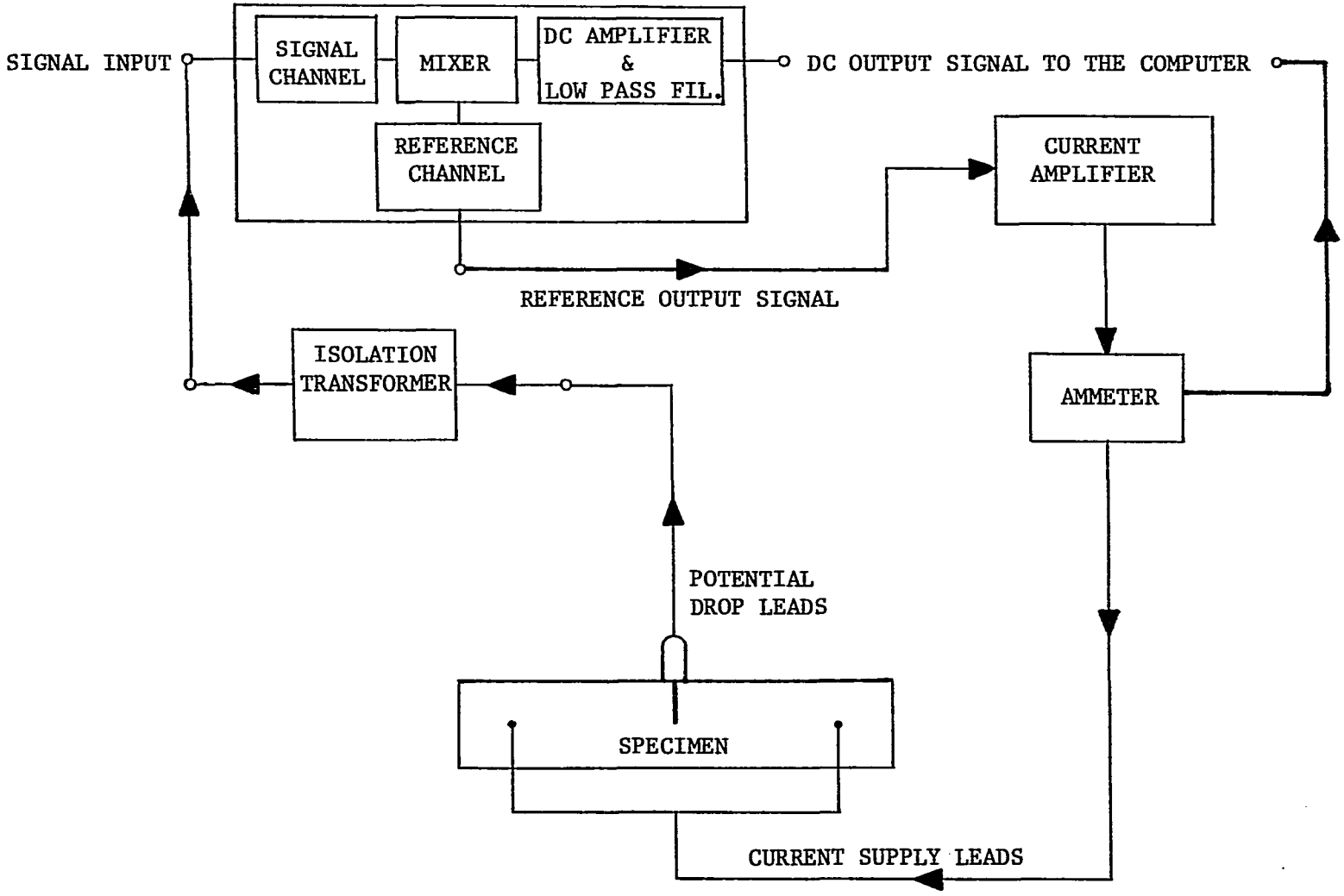

FIGURE 4.7: A schematic diagram of the ac potential crack length measurement system.

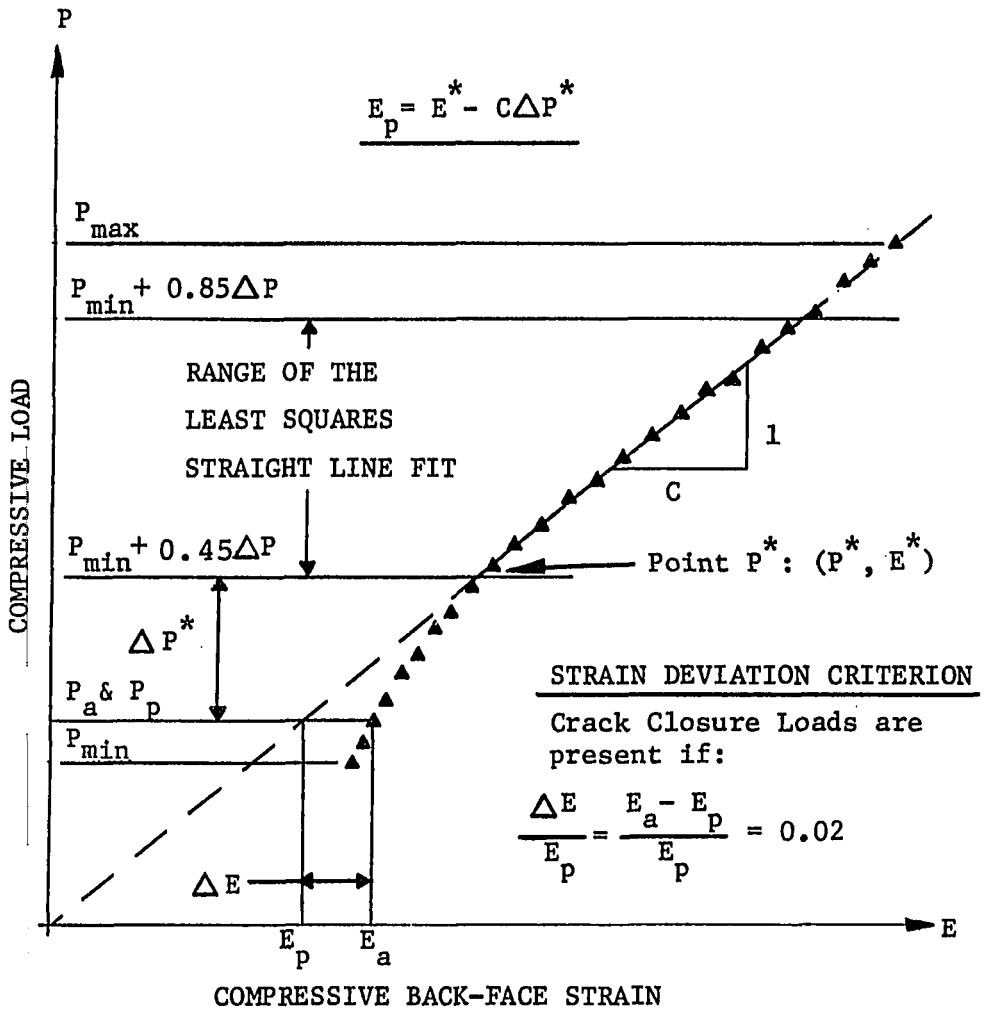

FIGURE 4.8: A schematic diagram of the procedure used for detecting the presence of crack closure.

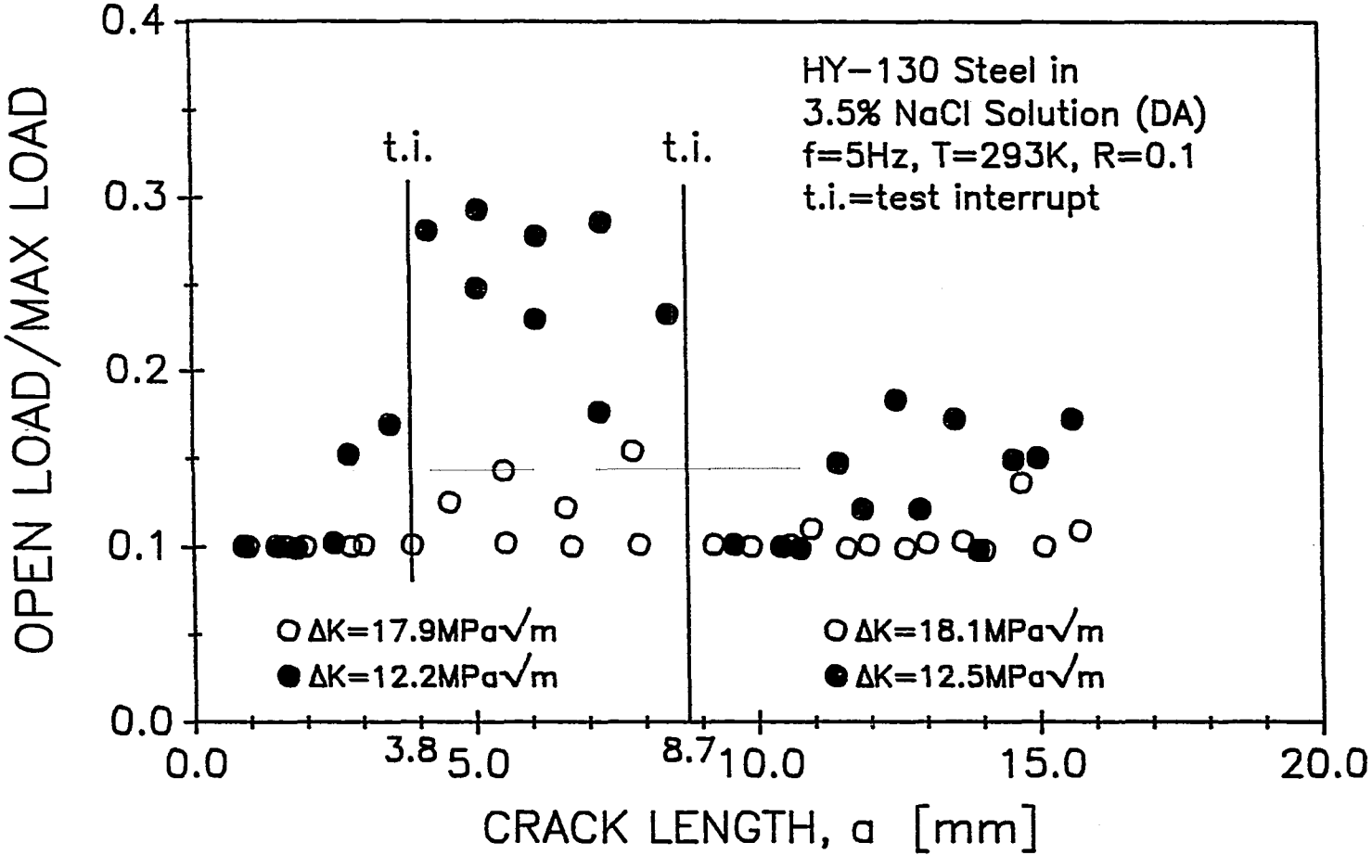

FIGURE 4.9: The results of test 9 showing the ratio of the crack closure load to the maximum load for an alternating ΔK calibration test. Note the presence of crack closure for the lower ΔK levels as indicated by the data points with ordinate values greater than 0.1.

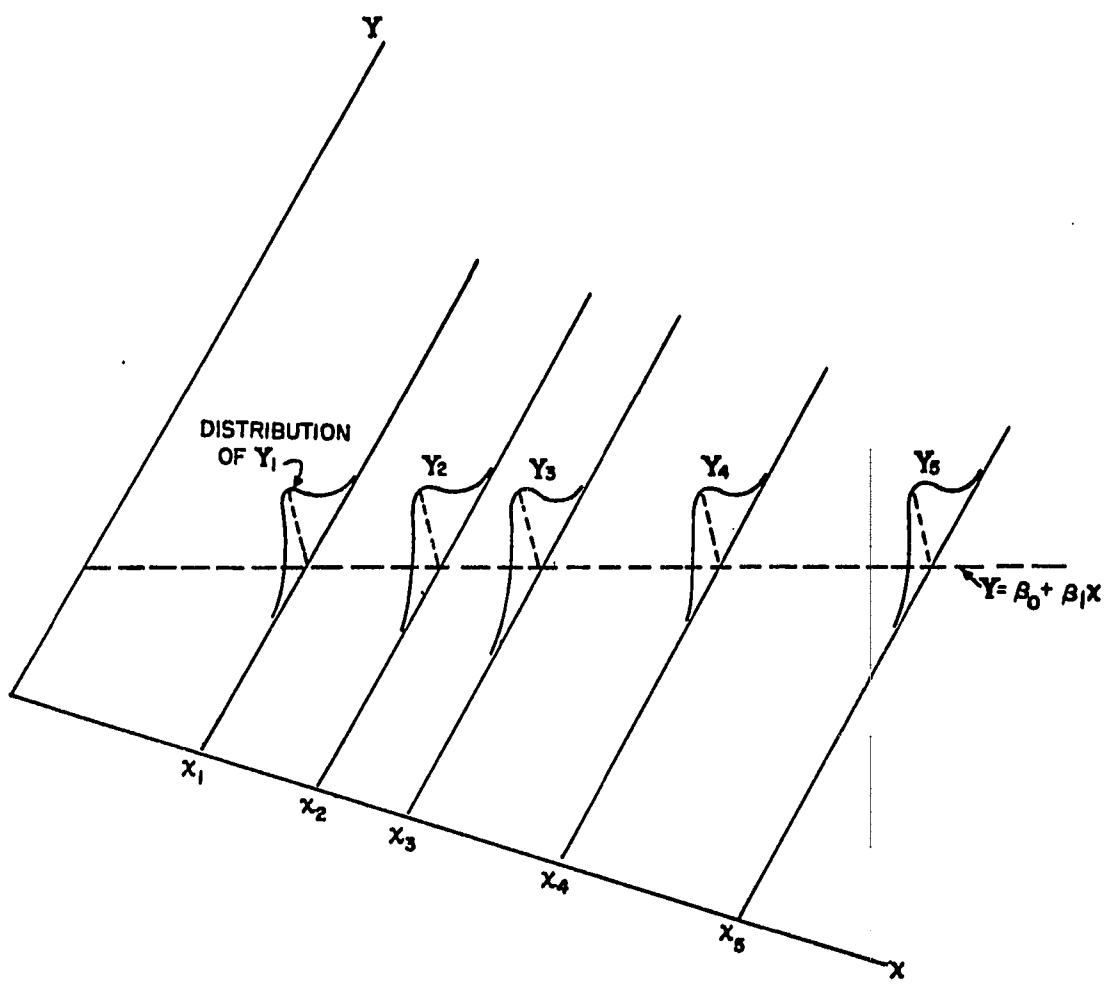

FIGURE 5.1: A schematic diagram of a linear functional relationship fit to some experimental data, with only the Y_i values affected by an error in measurement. Note that the least squares fit relationship passes through the estimated expected values of the Y_i. The method estimates the expected values and variance of Y_i (Natrella, 1966).

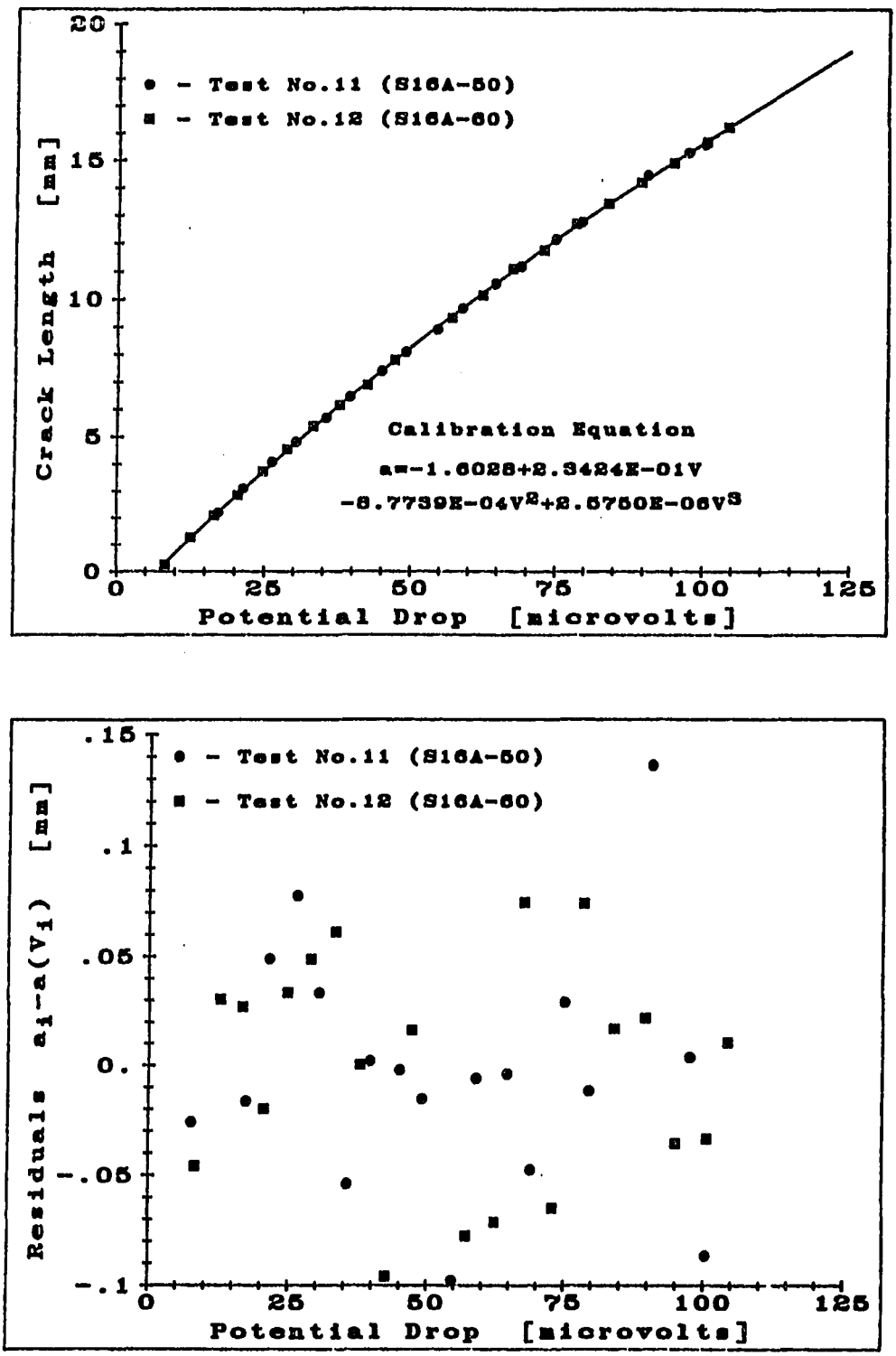

FIGURE 5.2: Plots of the scatter (top) and residuals (bottom) for a third degree, least squares fit polynomial for the calibration relationship.

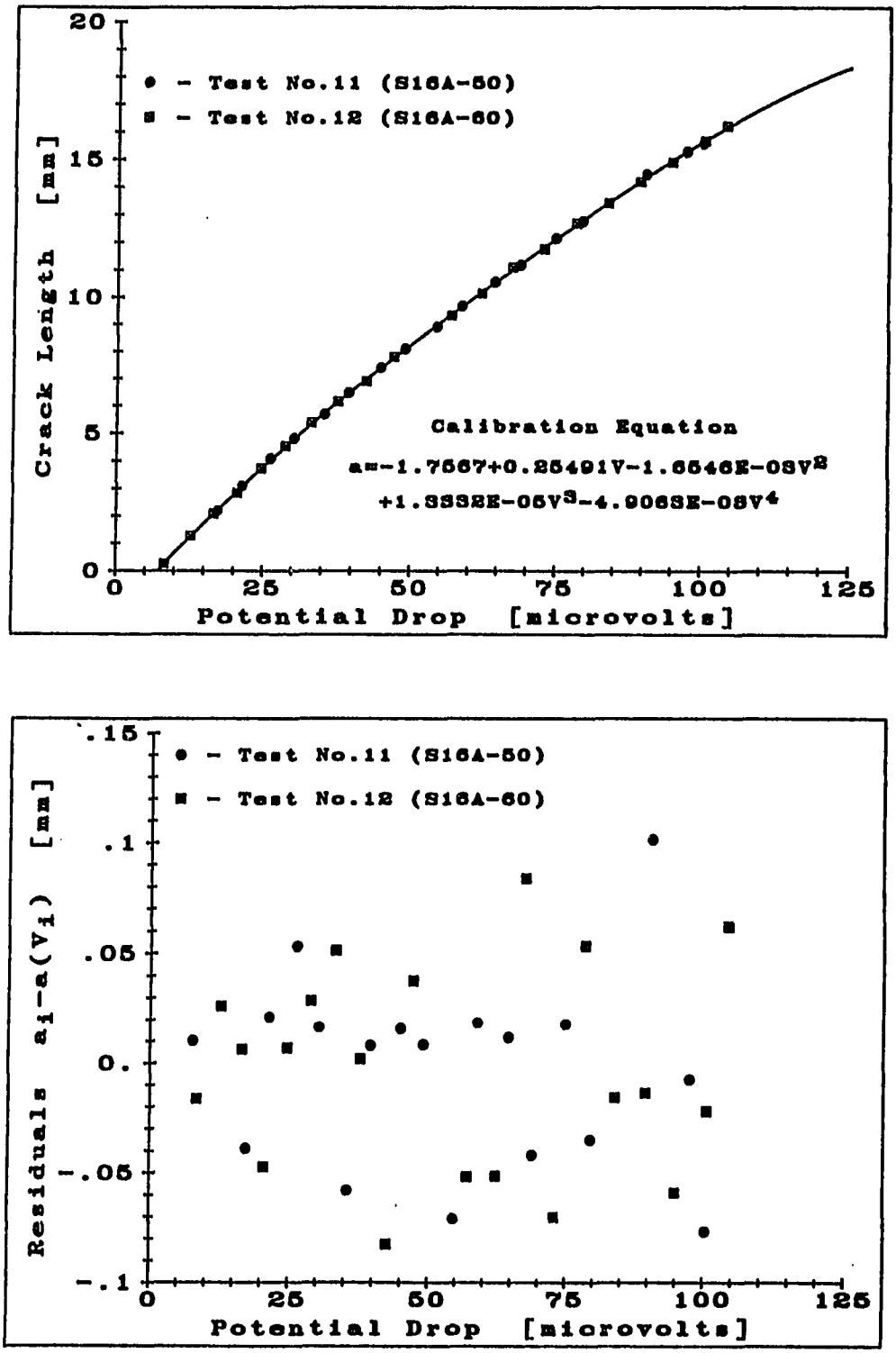

FIGURE 5.3: Plots of the scatter (top) and residuals (bottom) for a fourth degree, least squares fit polynomial for the calibration relationship.

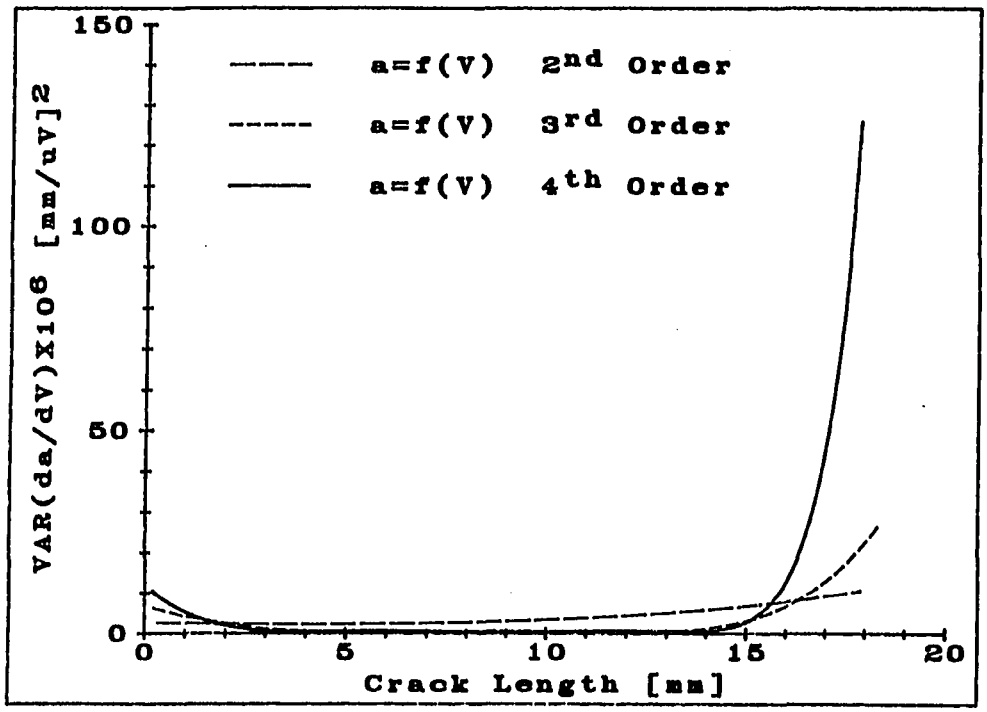

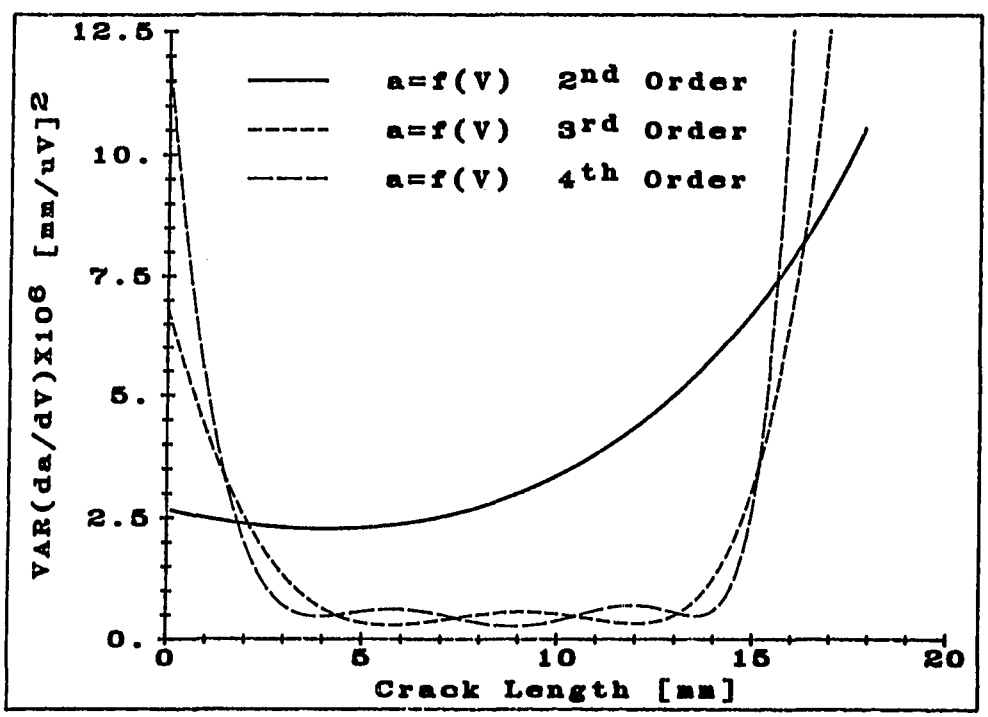

FIGURE 5.4: Plots of the variance of the slope of the a=f(V) calibration relationship versus crack length for second, third, and fourth degree polynomial calibration relationships.

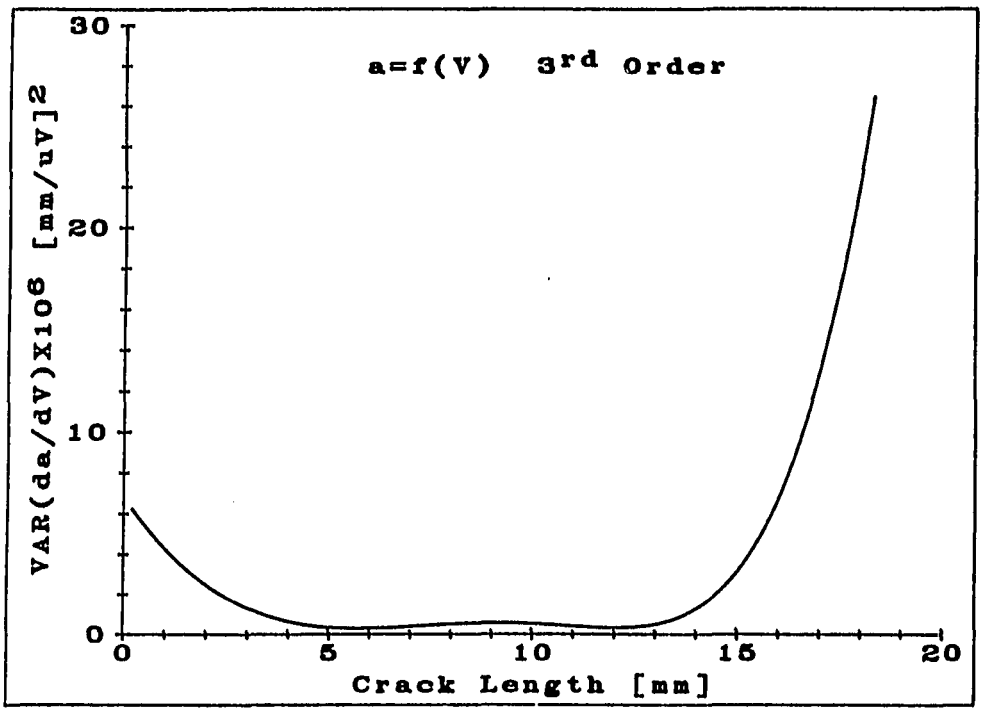

FIGURE 5.5: An expanded plot of VAR[da/dV] versus crack length for a third degree polynomial calibration relationship.

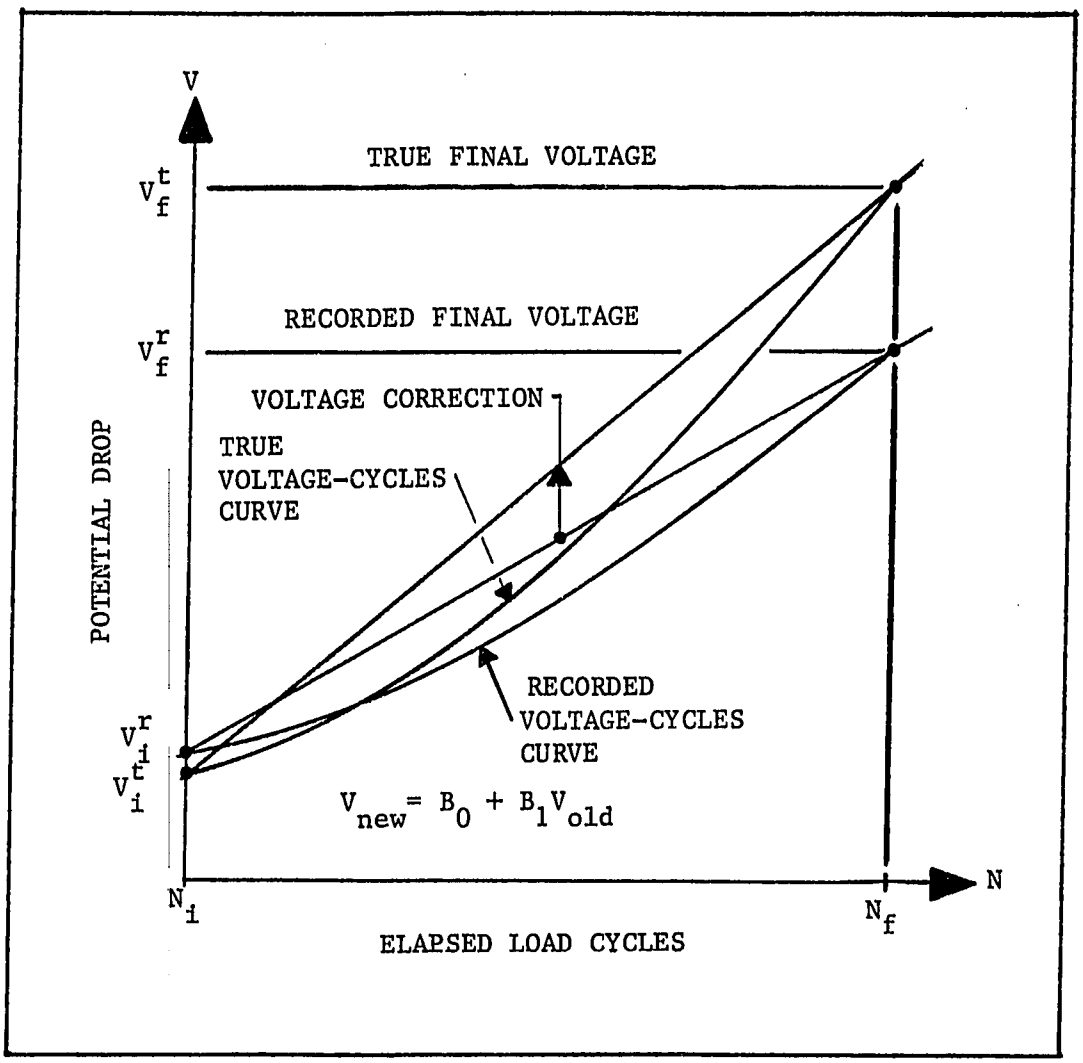

FIGURE 5.6: A schematic diagram of the potential drop correction scheme. The actual and recorded crack lengths (initial and final) did not always agree and so a correction was made at the end of each test. The correction made a linear change to the recorded voltage data where $V_{new}=\beta_0+\beta_1 V_{old}$, and $\beta_0=\{(V_i^t V_f^r - V_f^t V_i^r)/(V_f^r - V_i^r)\}$ and $\beta_1=\{(V_f^t - V_i^t)/(V_f^r - V_i^r)\}$.

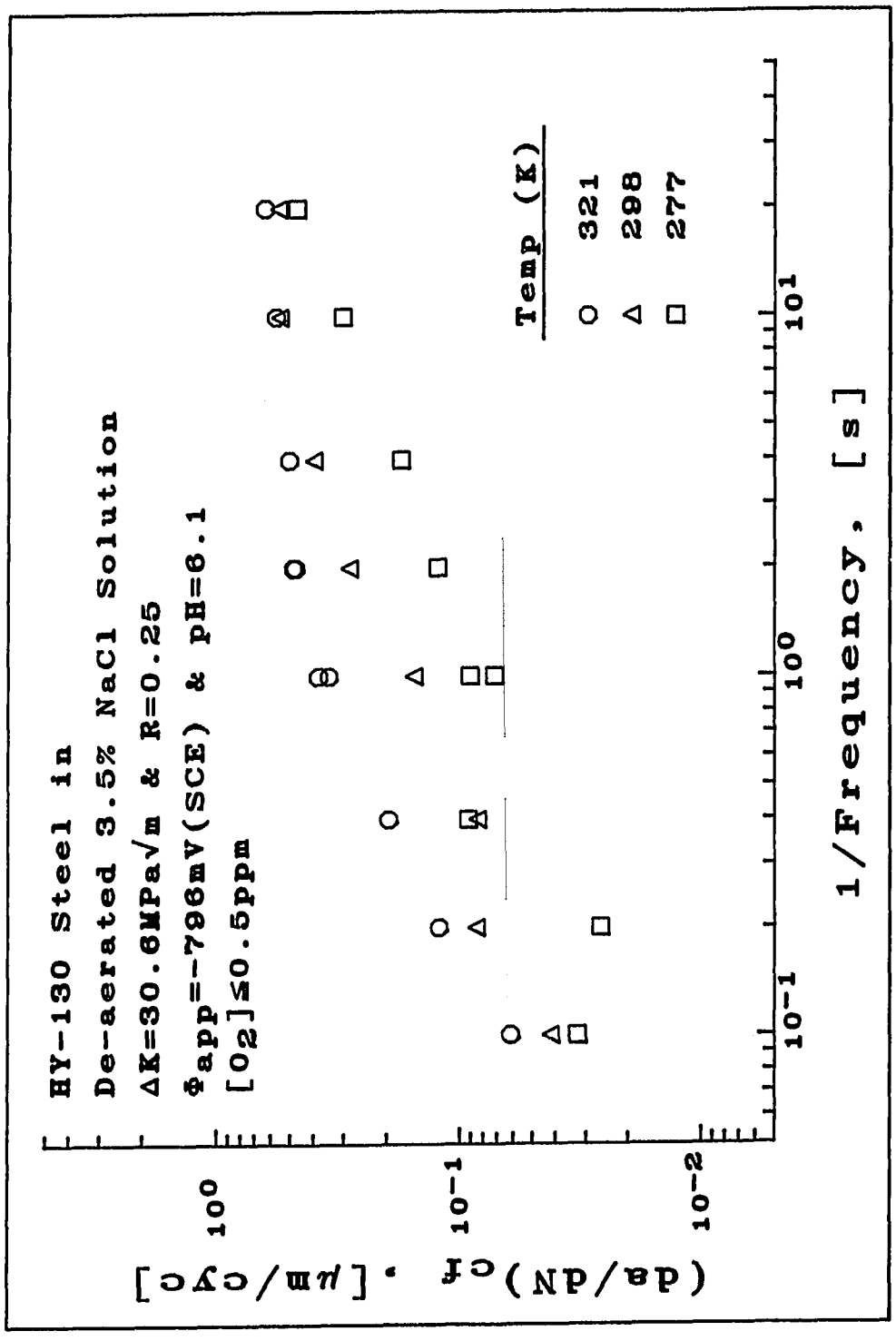

FIGURE 6.1: The influence of frequency and temperature on the enhancement of the crack growth rate at ΔK=30.6 MPa$\sqrt{m}$.

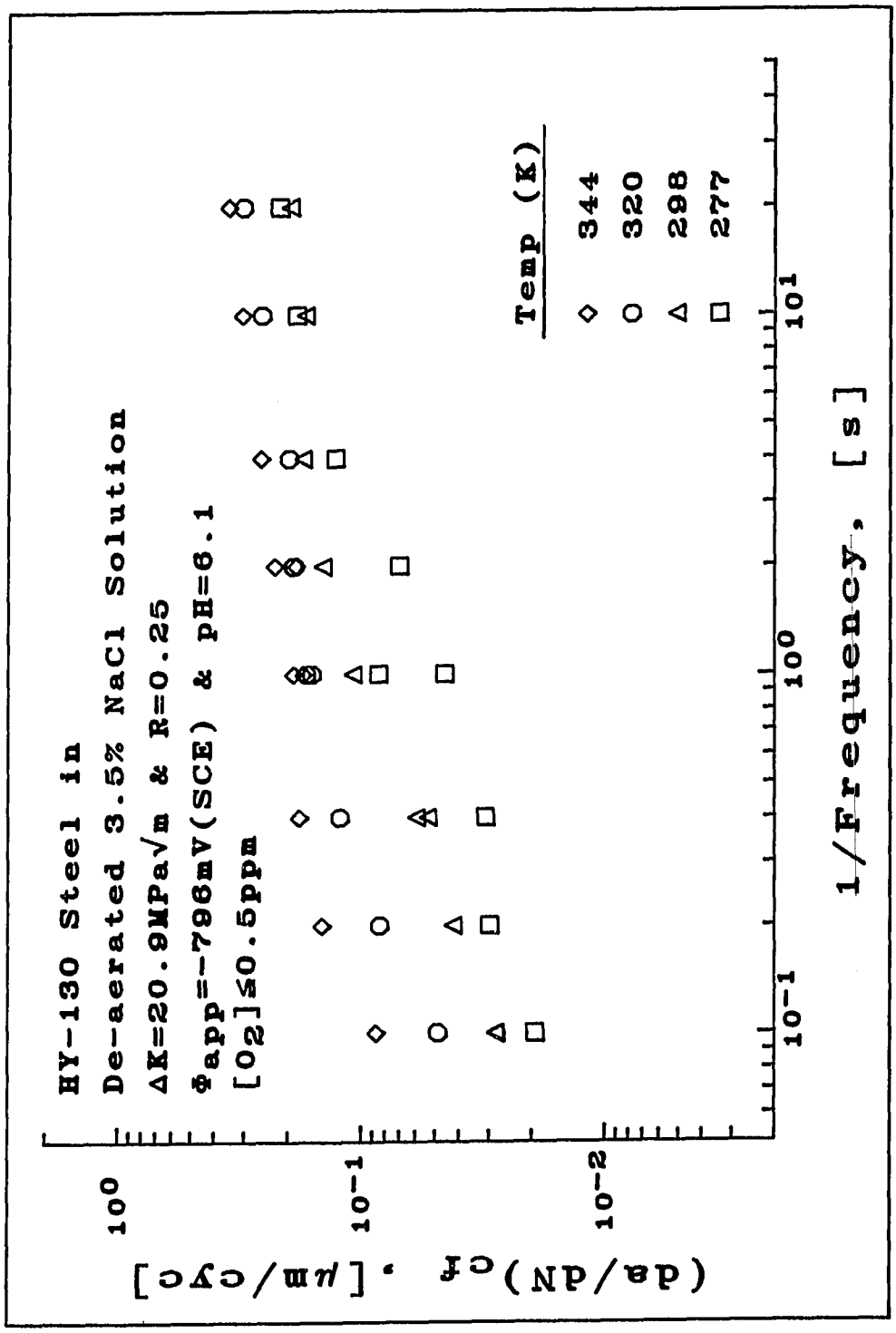

FIGURE 6.2: The influence of frequency and temperature on the enhancement of the crack growth rate at ΔK=20.9 MPa$\sqrt{m}$.

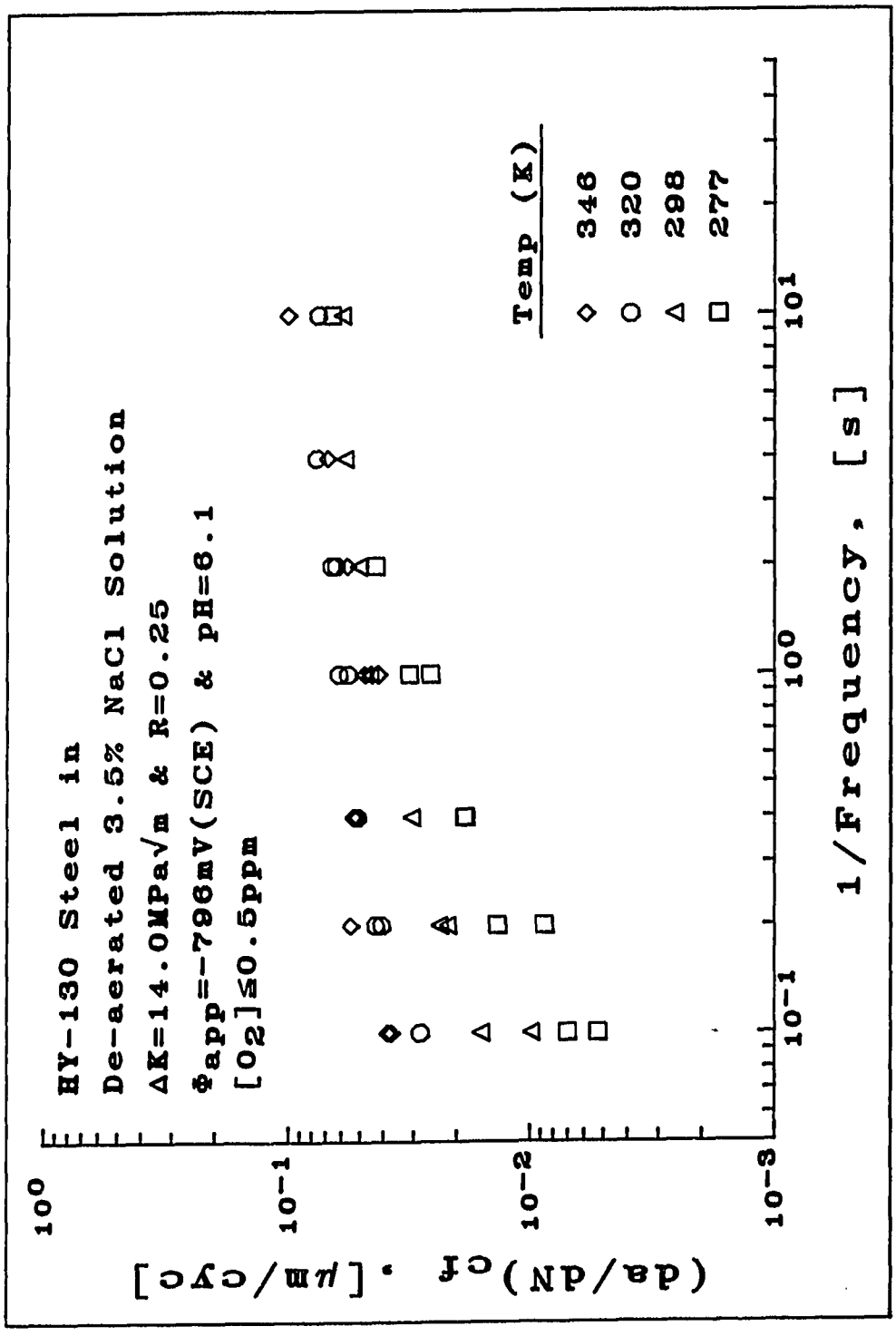

FIGURE 6.3: The influence of frequency and temperature on the enhancement of the crack growth rate at ΔK=14.0 MPa$\sqrt{m}$.

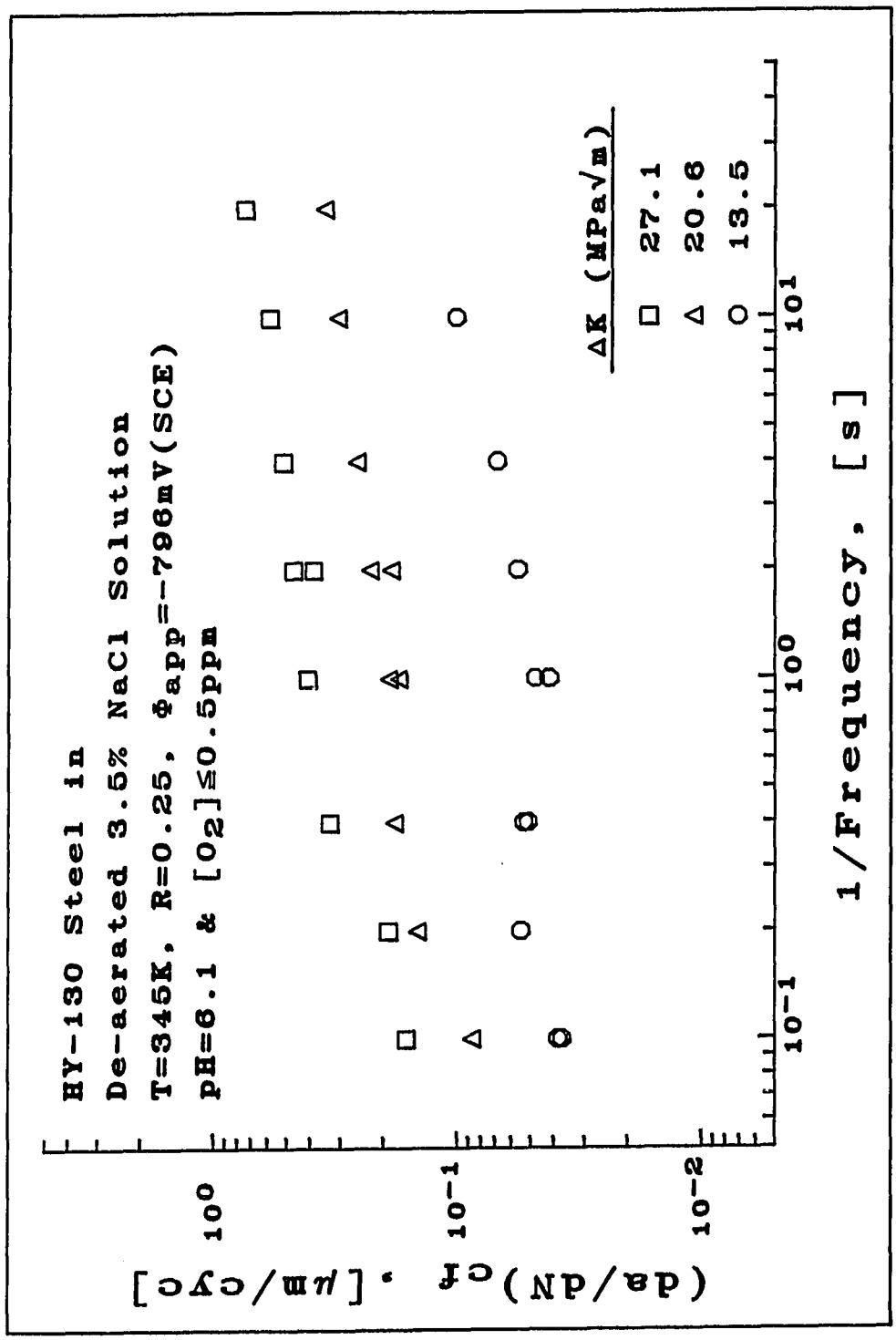

FIGURE 6.4: The influence of frequency and ΔK level on the enhancement of the crack growth rate at T=345K.

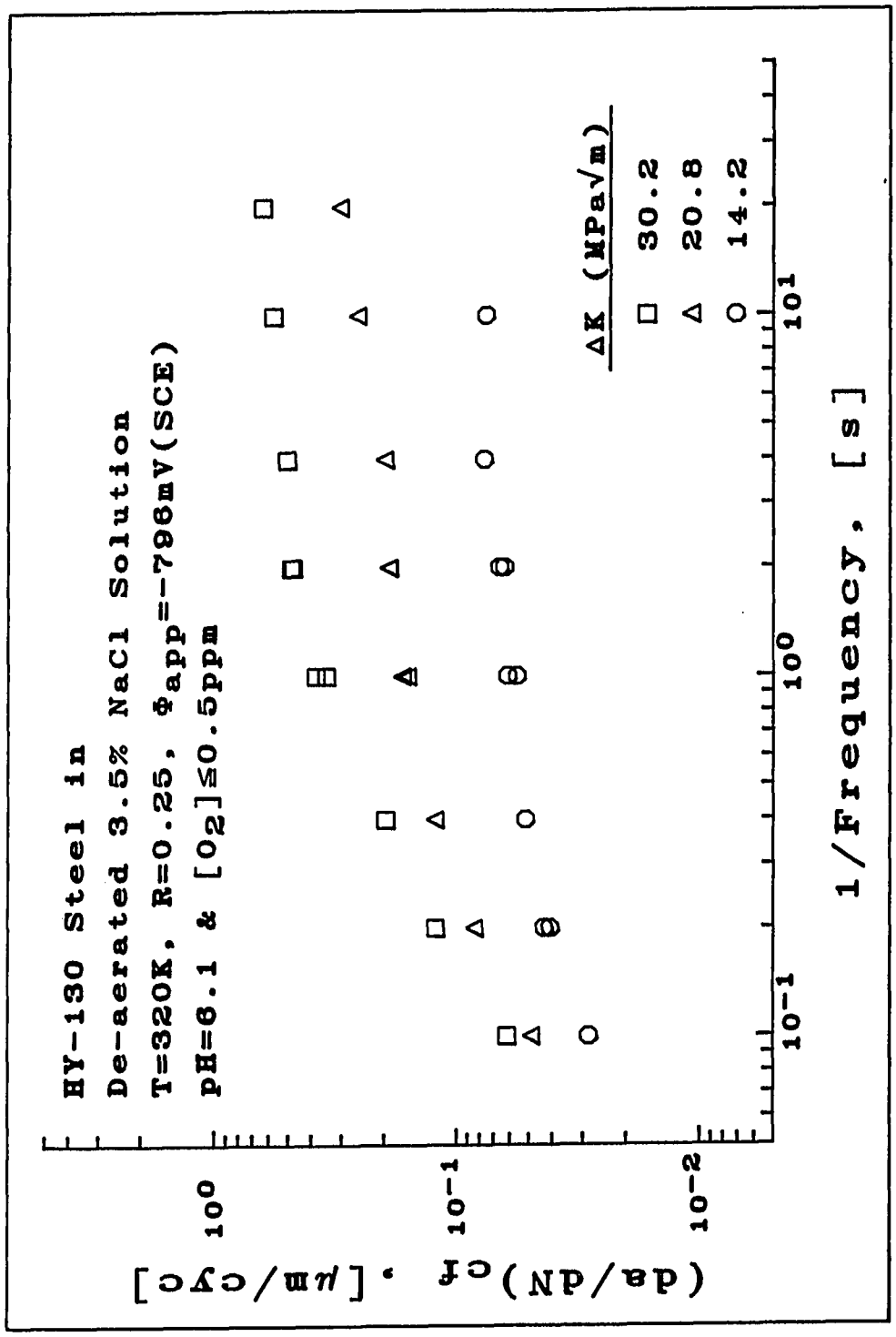

FIGURE 6.5: The influence of frequency and ΔK level on the enhancement of the crack growth rate at T=320K.

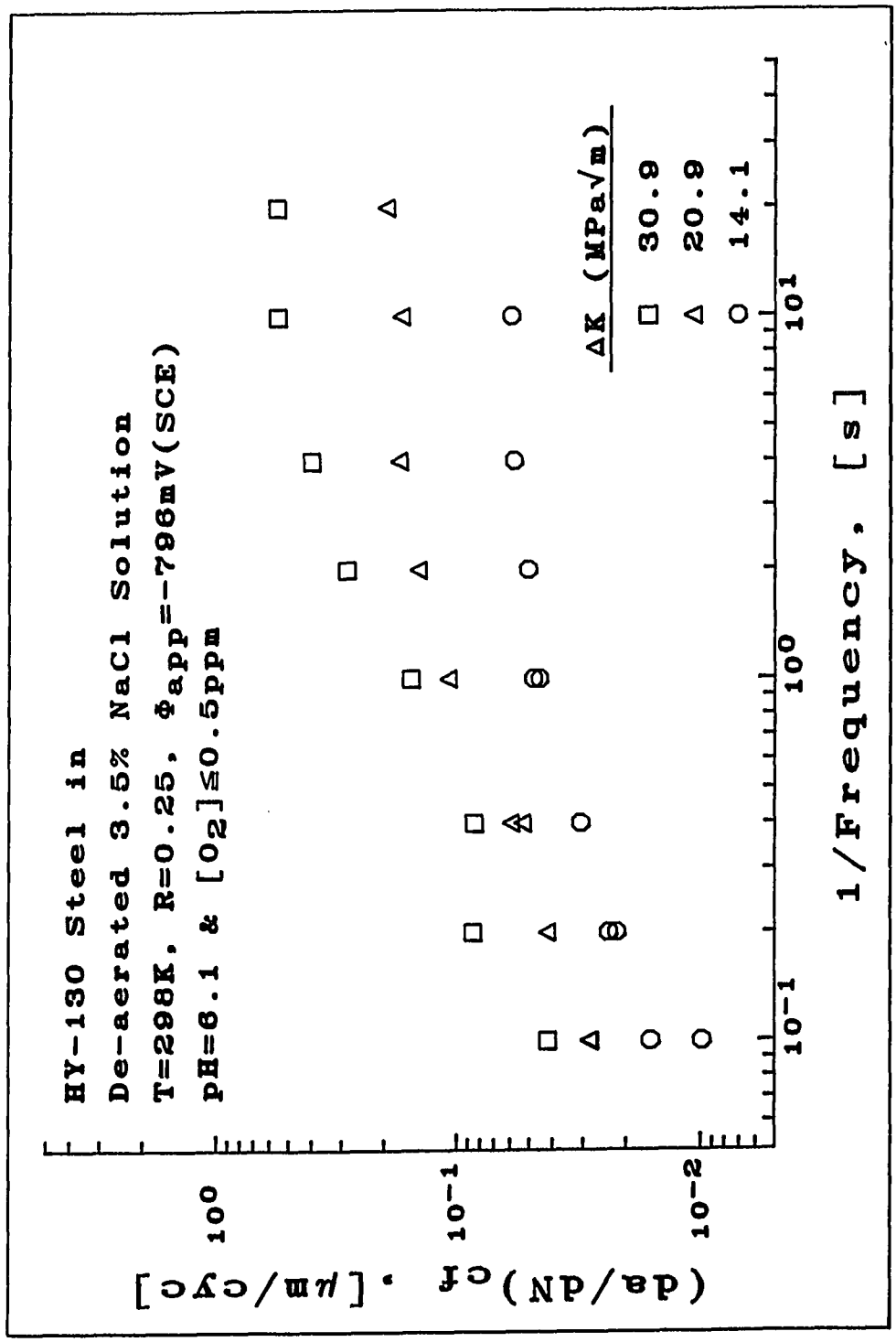

FIGURE 6.6: The influence of frequency and ΔK level on the enhancement of the crack growth rate at T=298K.

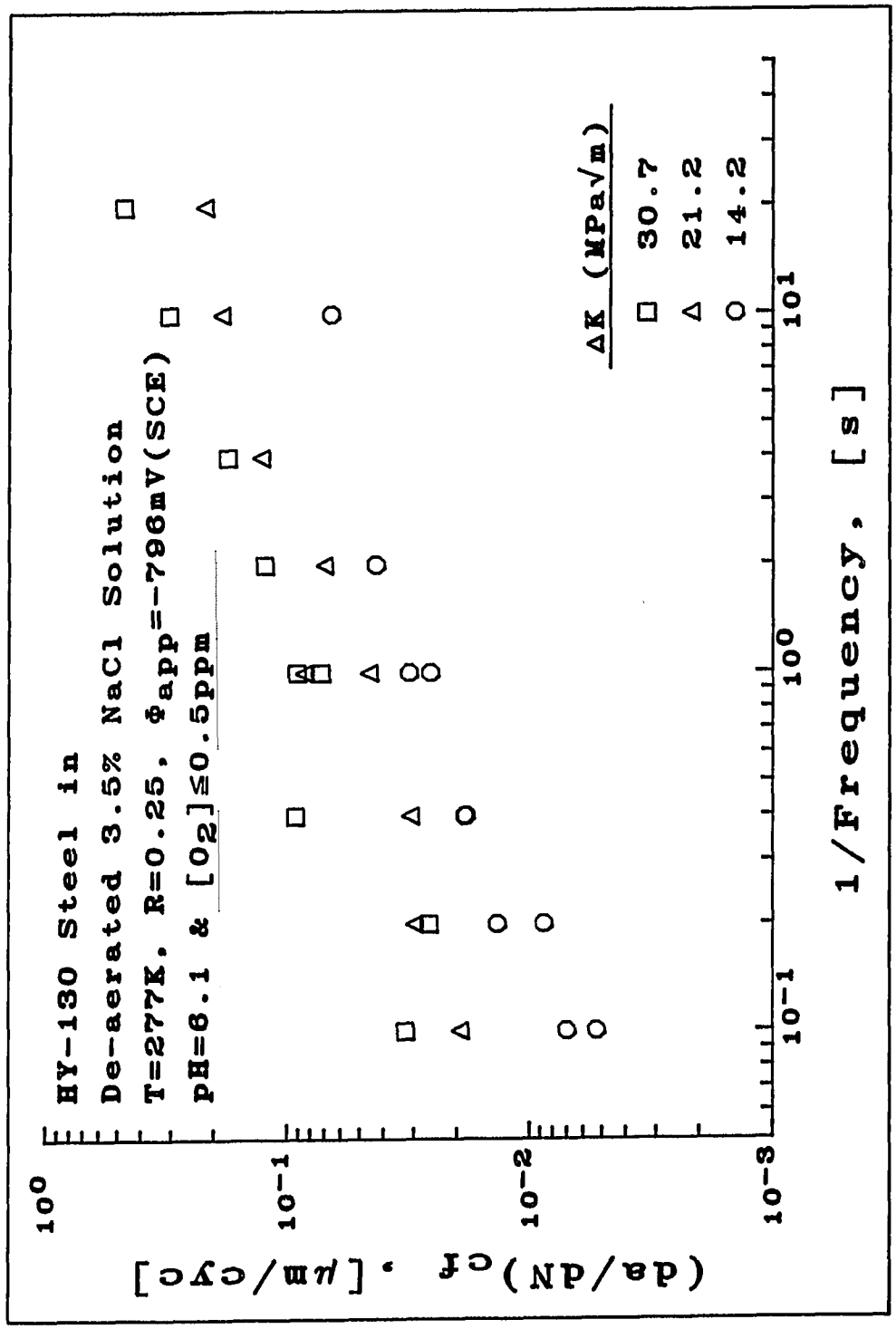

FIGURE 6.7: The influence of frequency and ΔK level on the enhancement of the crack growth rate at T=277K.

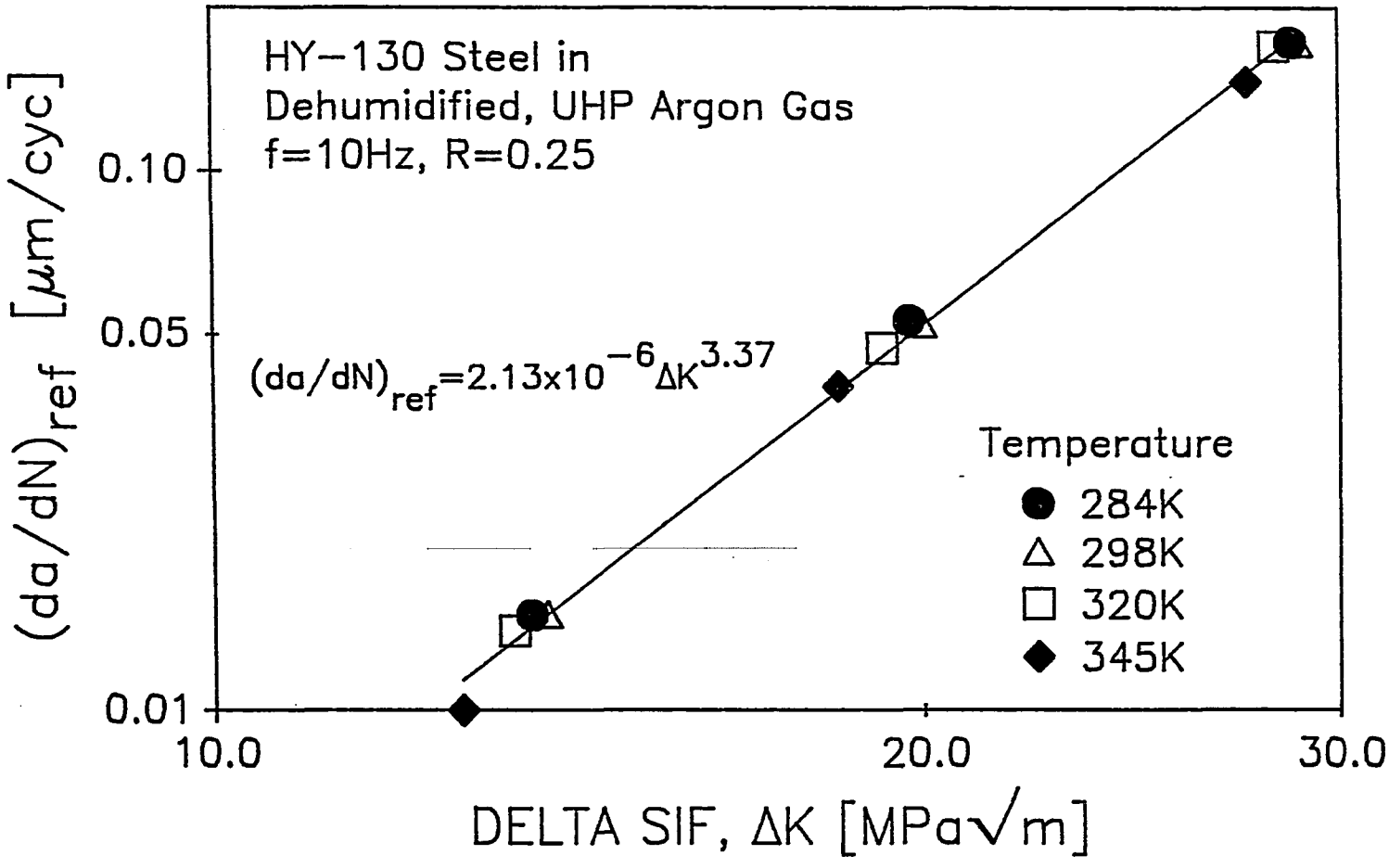

FIGURE 6.8: Crack growth rate versus ΔK level in a dehumidified UHP Argon gas environment at multiple temperature levels.

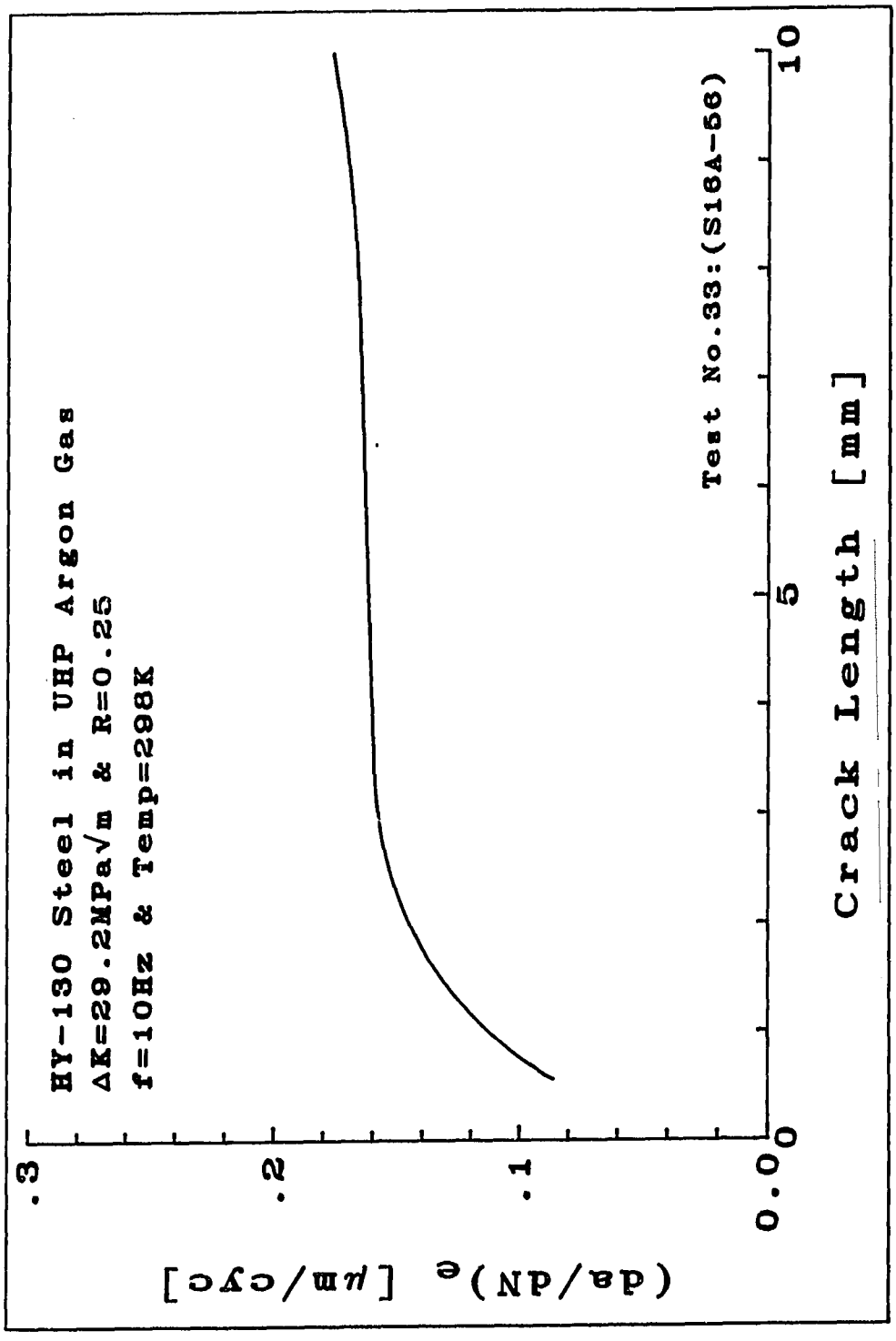

FIGURE 6.9: The influence of crack length on the rate of crack growth in a dehumidified UHP Argon gas environment for $\Delta K=29.2 MPa\sqrt{m}$.

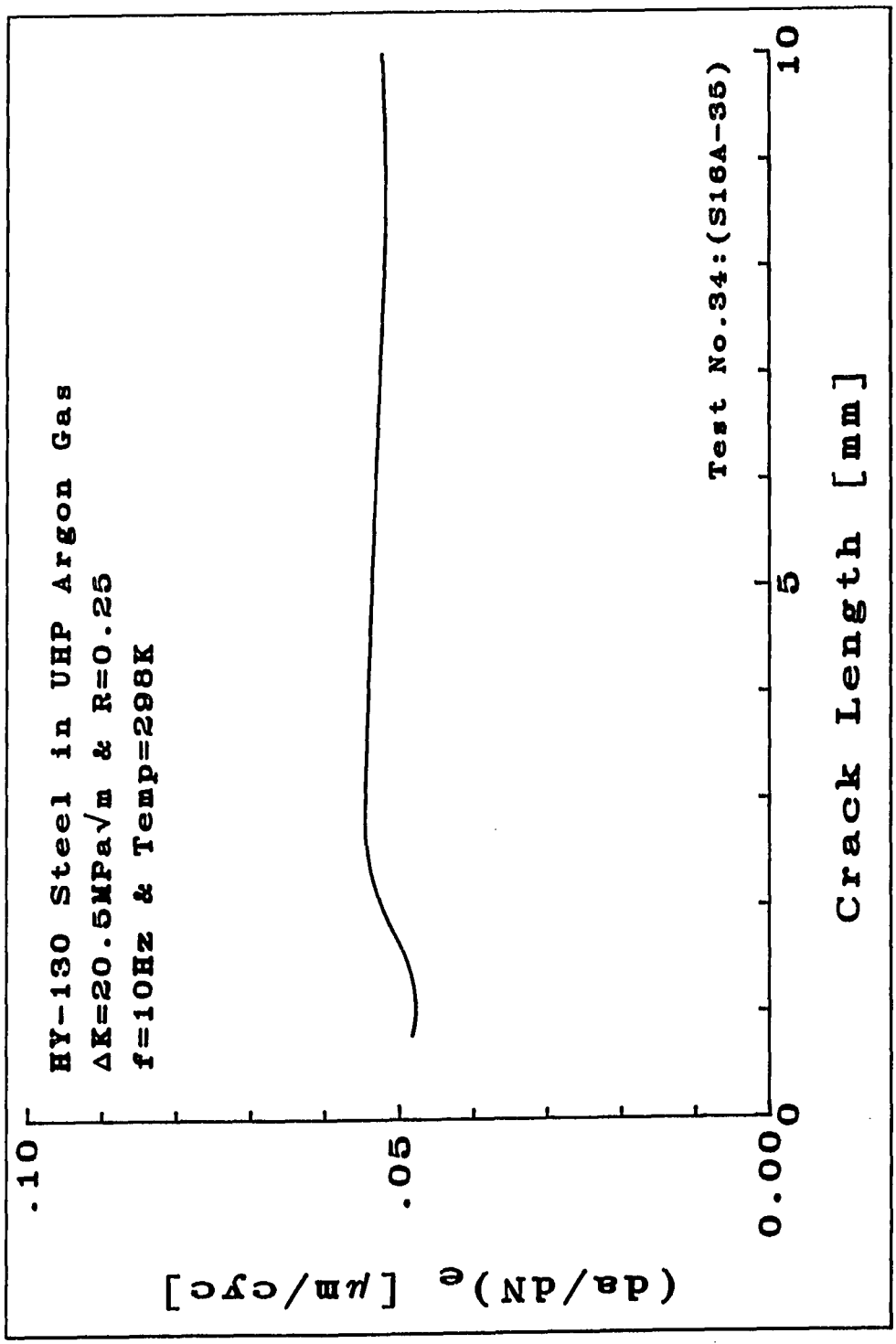

FIGURE 6.10: The influence of crack length on the rate of crack growth in a dehumidified UHP Argon gas environment $\Delta K=20.5MPa\sqrt{m}$.

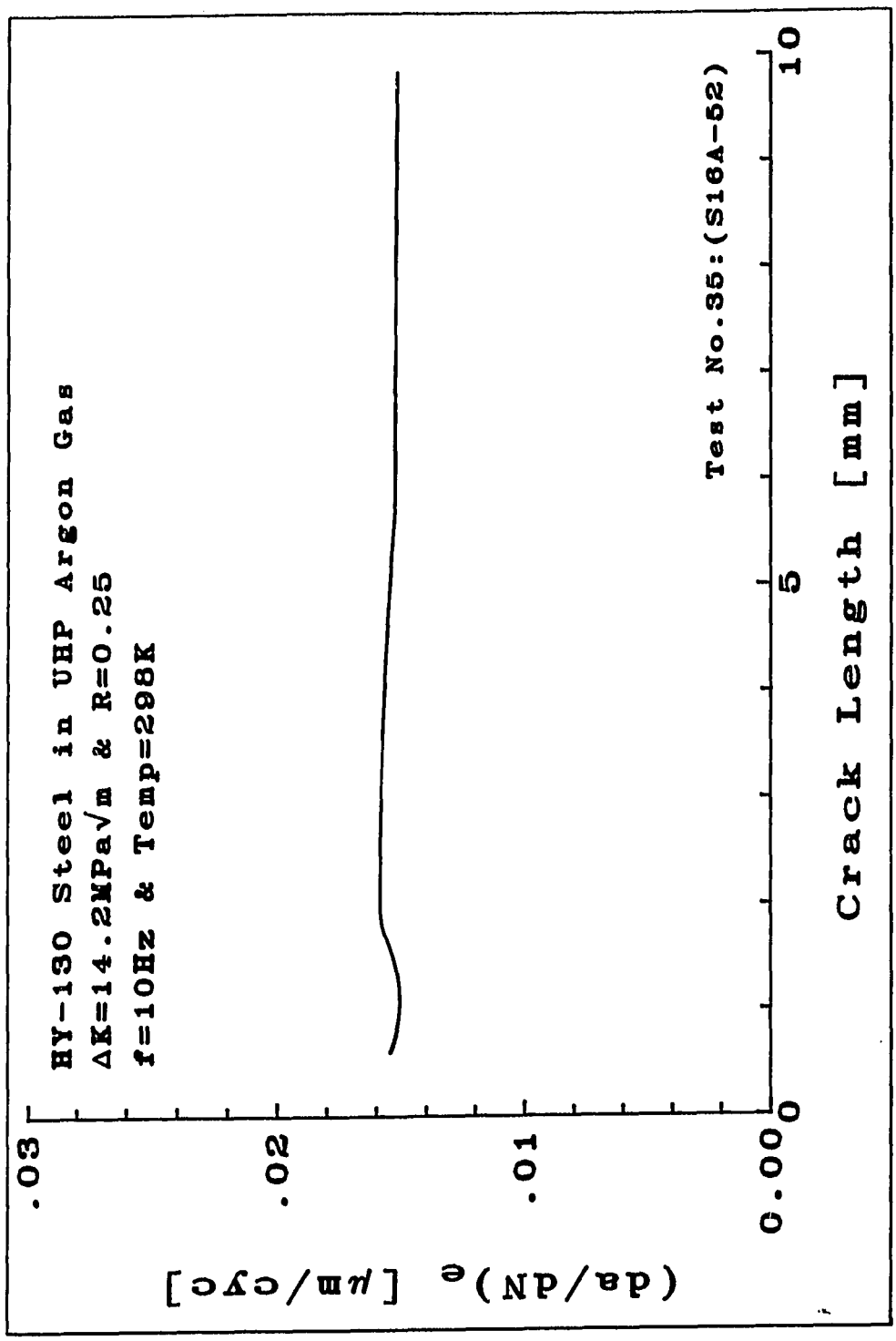

FIGURE 6.11: The influence of crack length on the rate of crack growth in a dehumidified UHP Argon gas environment $\Delta K=14.2MPa\sqrt{m}$.

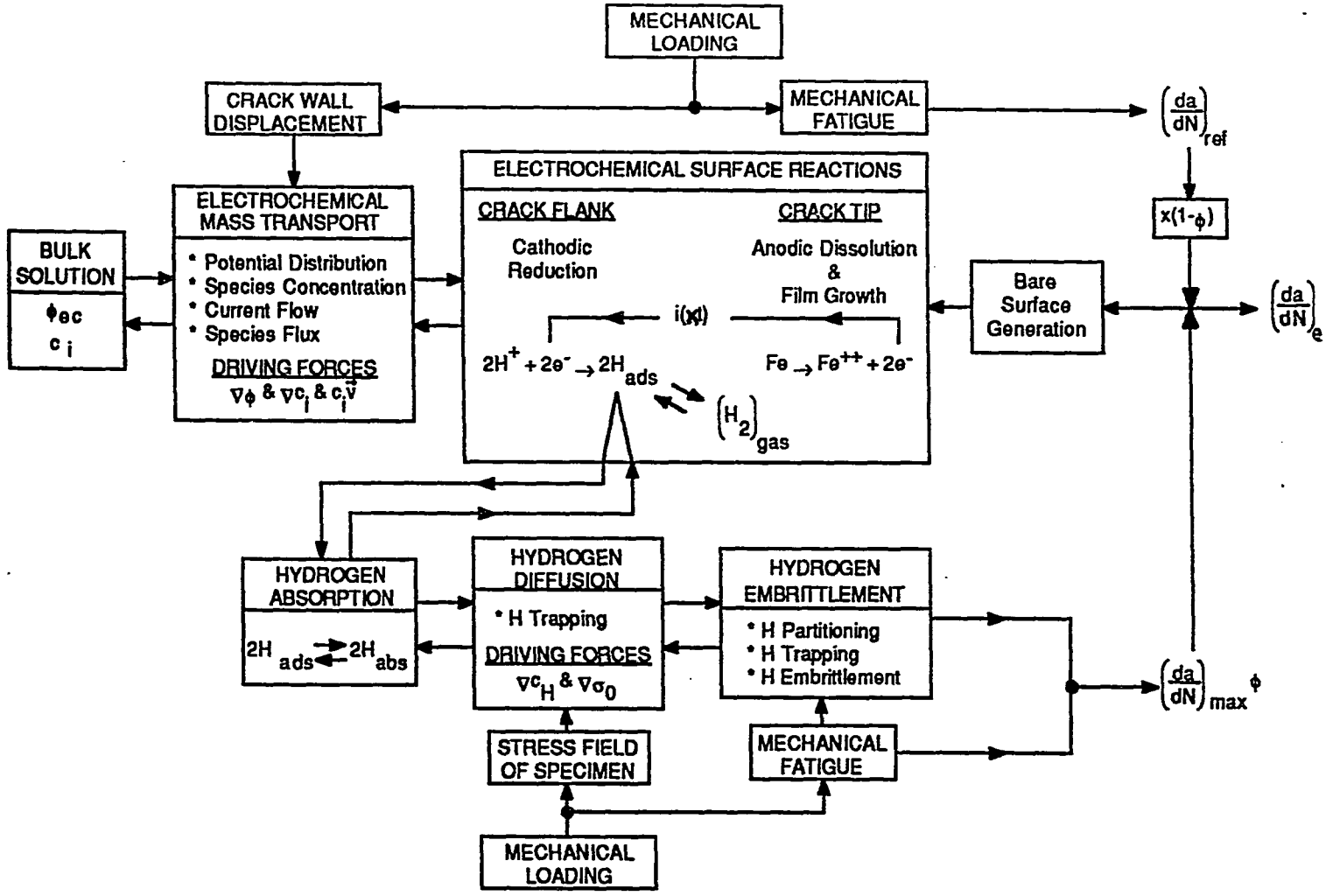

FIGURE 7.1: A schematic diagram of the conceptual model for the interacting chemical and mechanical processes which occur in a growing fatigue crack in an aqueous environment.

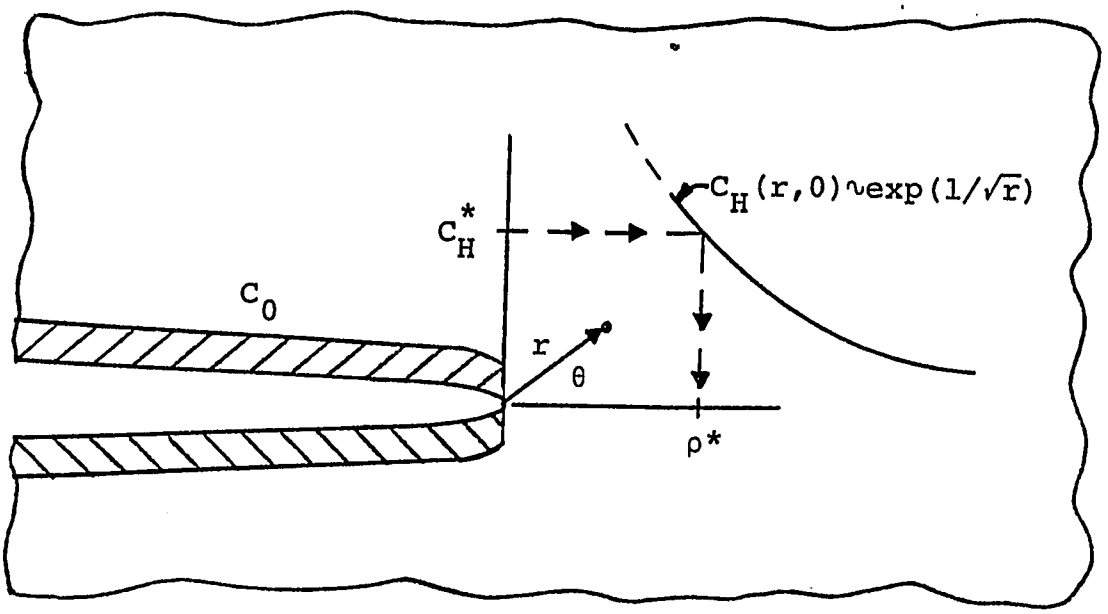

FIGURE 7.2a: The infinite planar geometry and boundary conditions for the stress-assisted diffusion problem - Case I: Uniform crack flank boundary conditions.

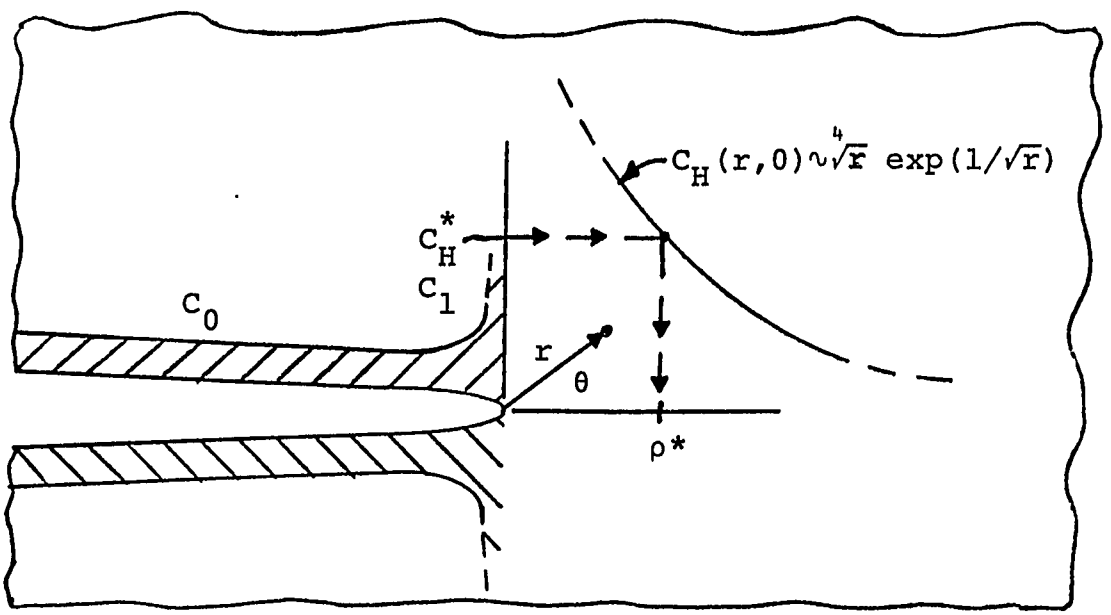

FIGURE 7.2b: The infinite planar geometry and boundary conditions for the stress-assisted diffusion problem - Case II: Modified crack flank boundary conditions to reflect an increase in the boundary concentration as the crack-tip is approached.

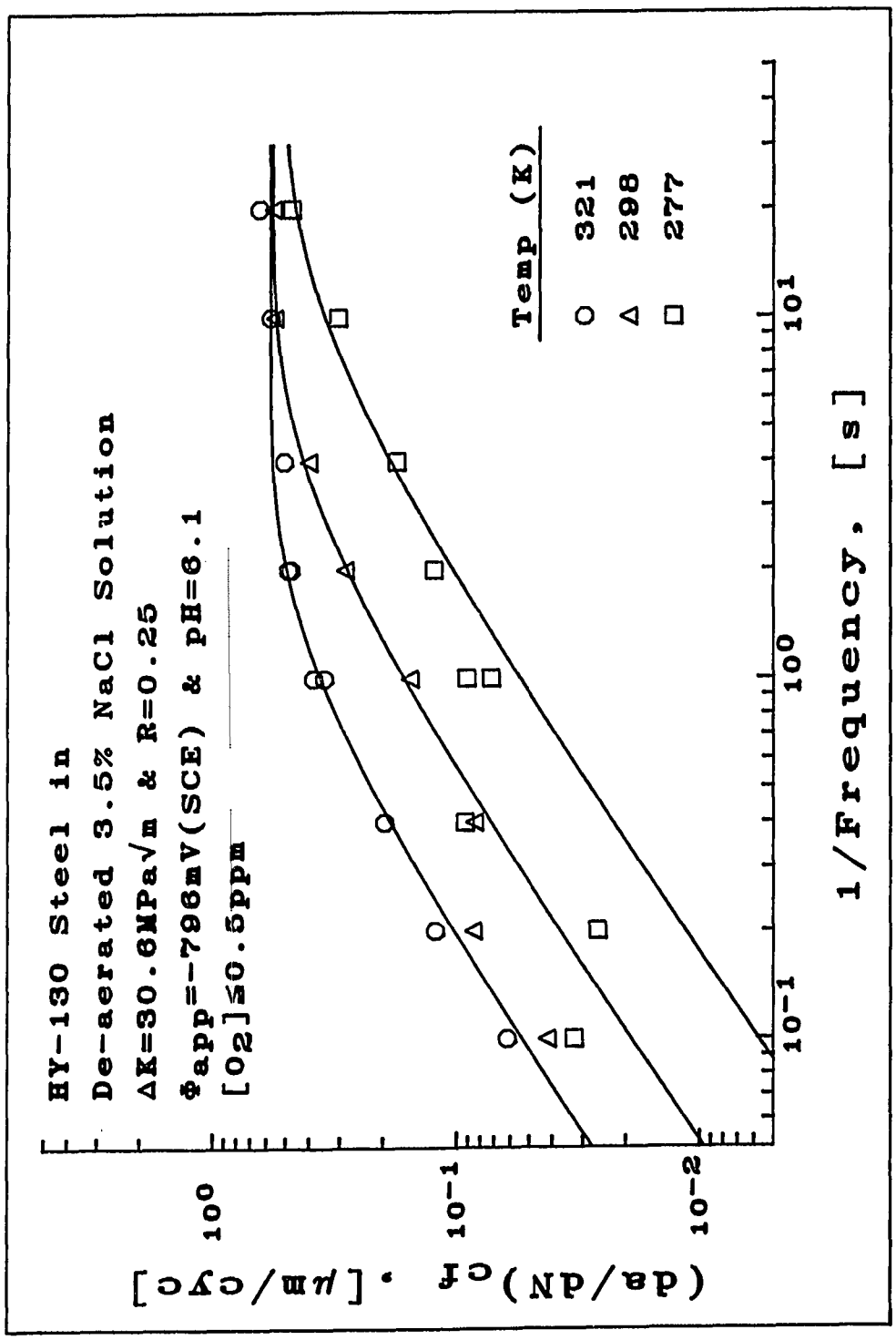

FIGURE 8.1: Comparison of the semi-empirical exponential model for $\phi(\kappa t)$ with the CG response data at ΔK=30.6 MPa$\sqrt{m}$.

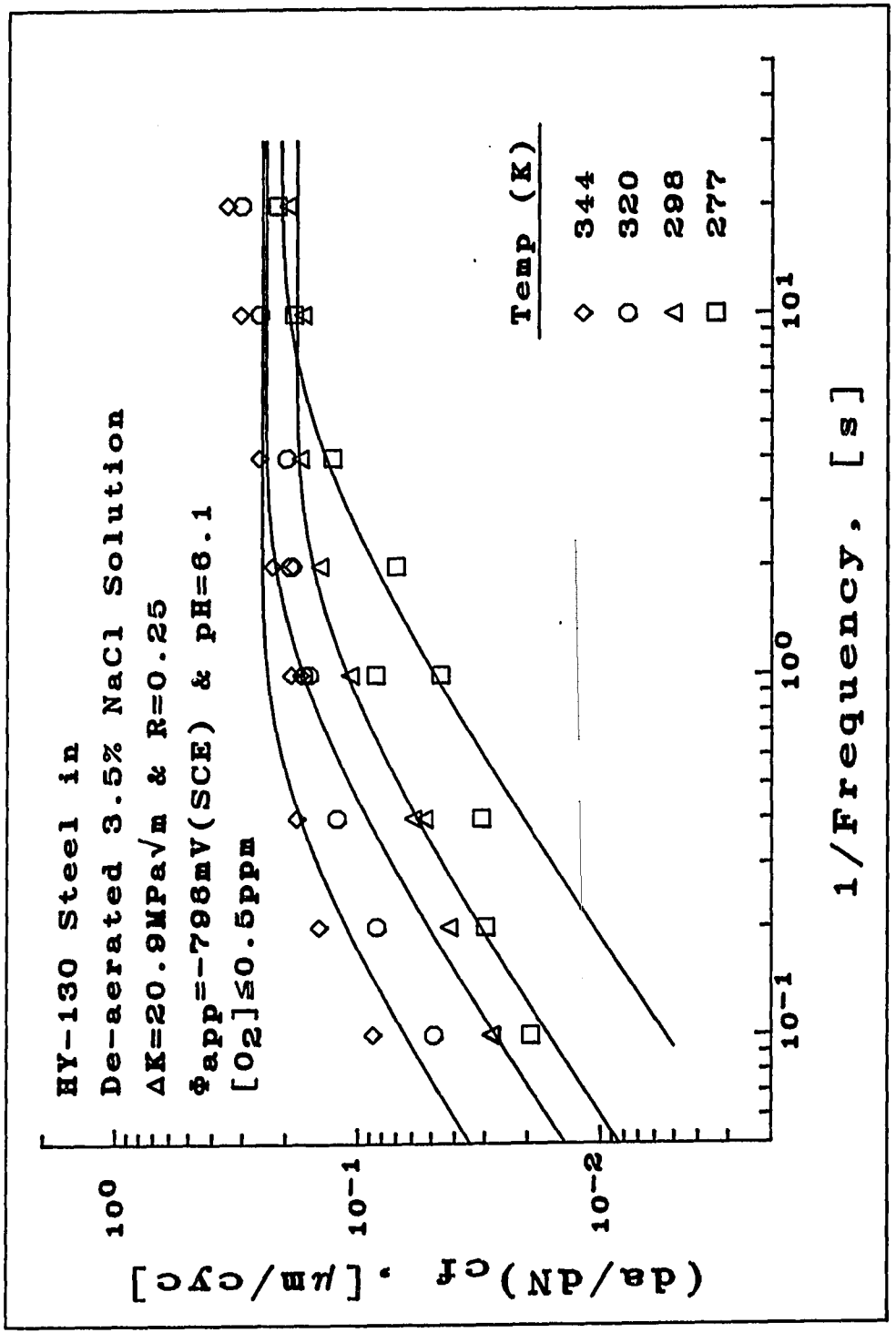

FIGURE 8.2: Comparison of the semi-empirical exponential model for $\phi(\kappa t)$ with the CG response data at $\Delta K=20.9$ MPa$\sqrt{m}$.

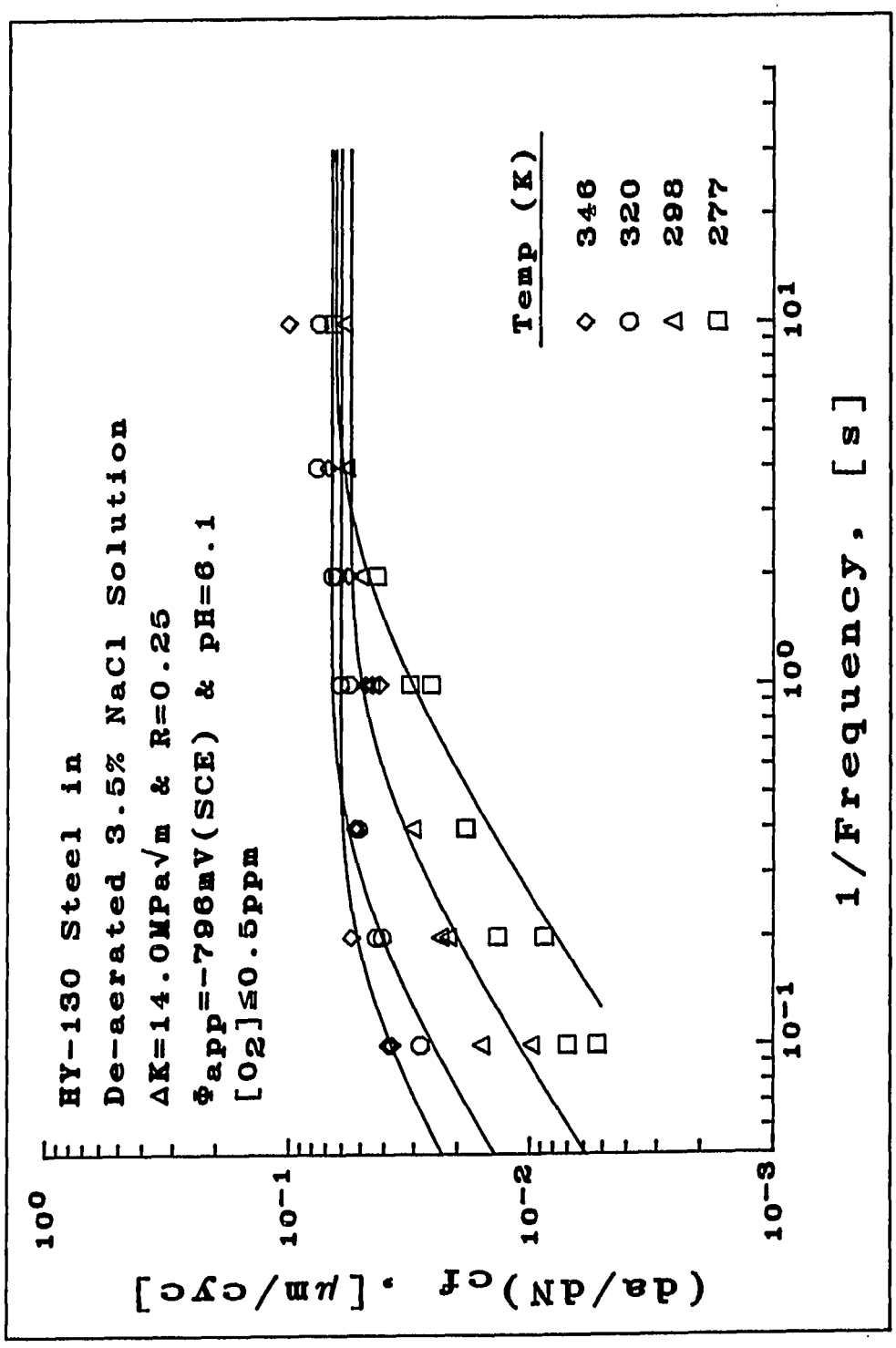

FIGURE 8.3: Comparison of the semi-empirical exponential model for $\phi(\kappa t)$ with the CG response data at ΔK=14.0 MPa$\sqrt{m}$.

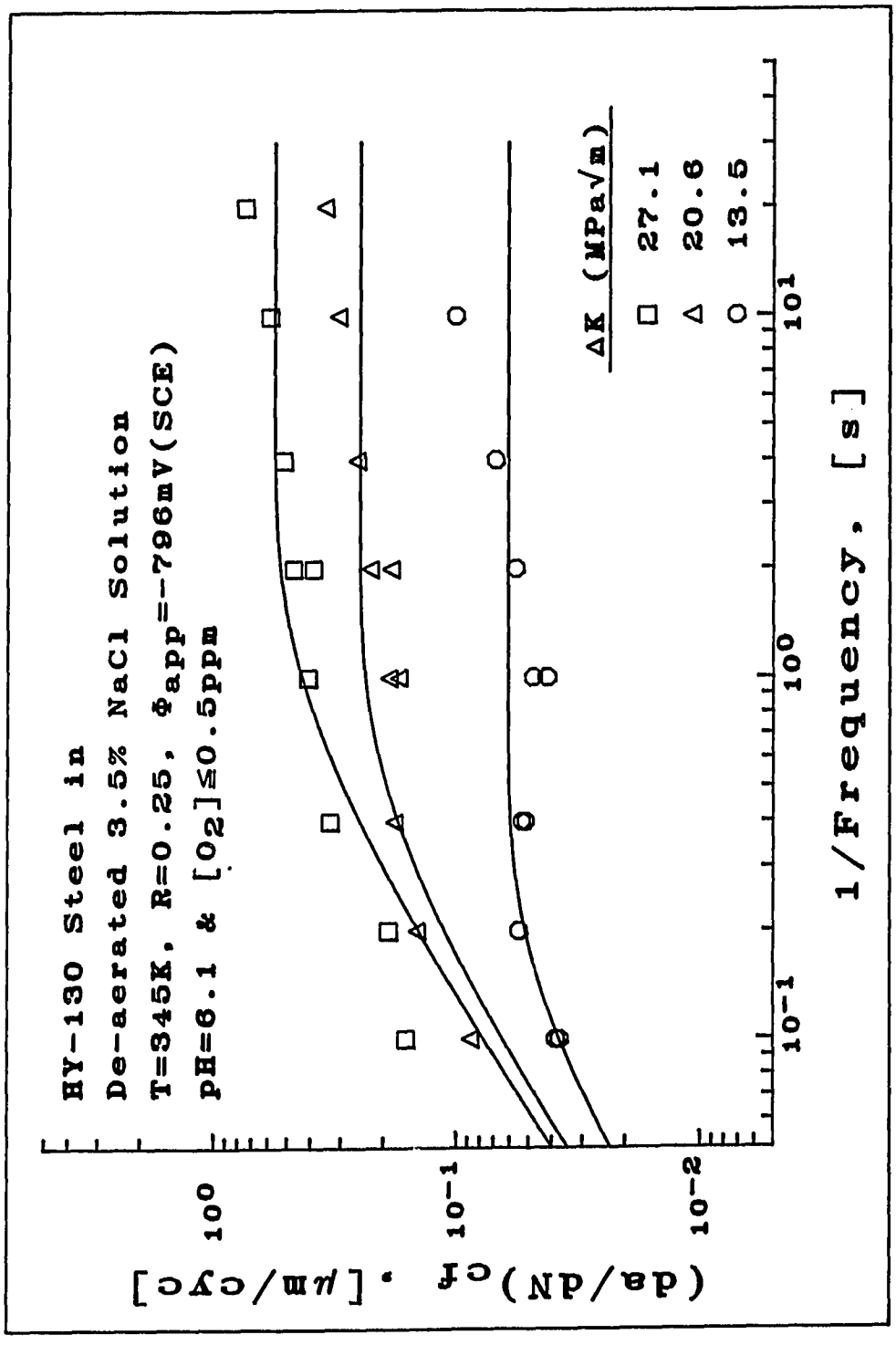

FIGURE 8.4: Comparison of the semi-empirical exponential model for $\phi(\kappa t)$ with the CG response data at T=345K.

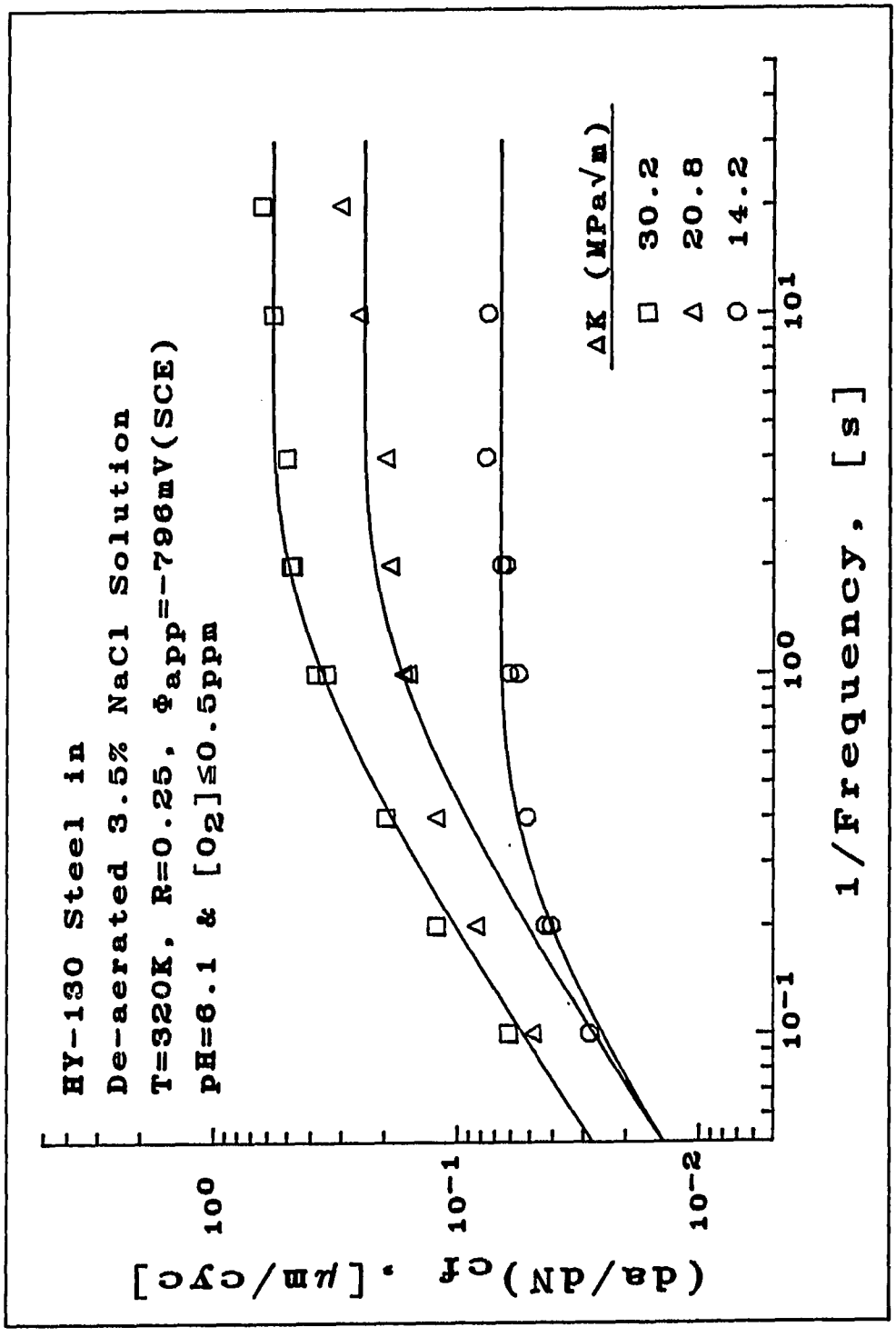

FIGURE 8.5: Comparison of the semi-empirical exponential model for $\phi(\kappa t)$ with the CG response data at T=320K.

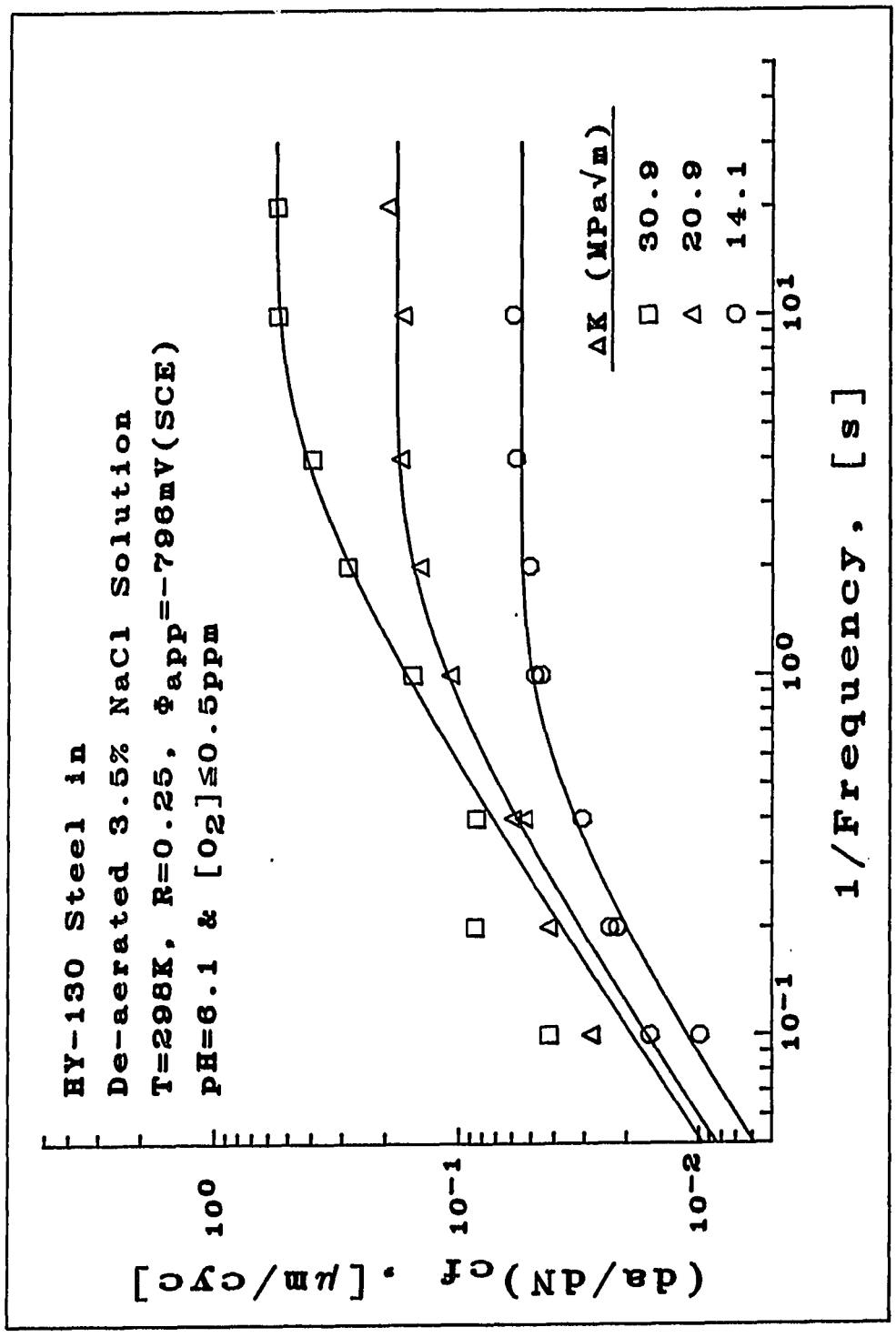

FIGURE 8.6: Comparison of the semi-empirical exponential model for $\phi(\kappa t)$ with the CG response data at T=298K.

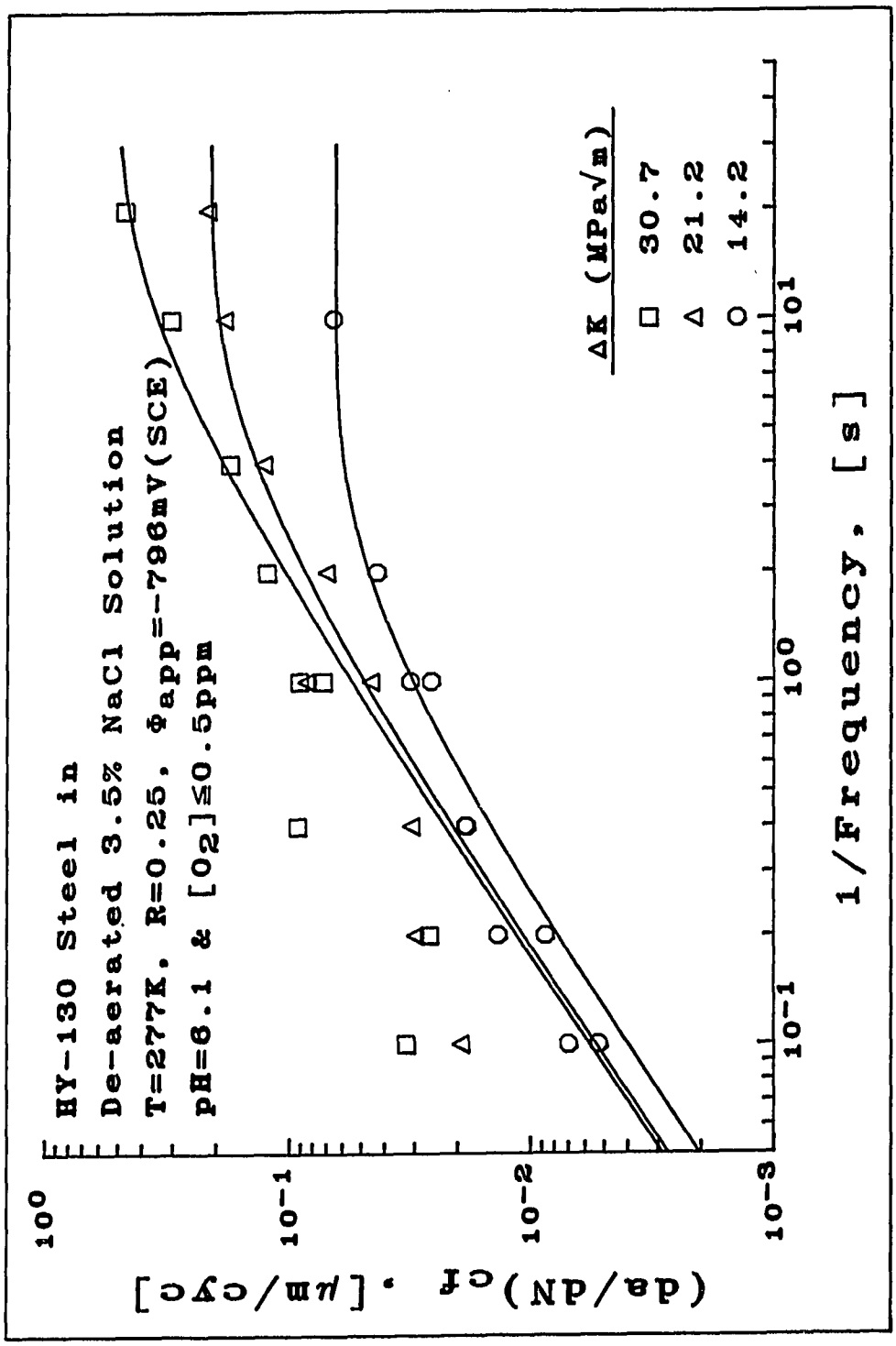

FIGURE 8.7: Comparison of the semi-empirical exponential model for $\phi(\kappa t)$ with the CG response data at T=277K.

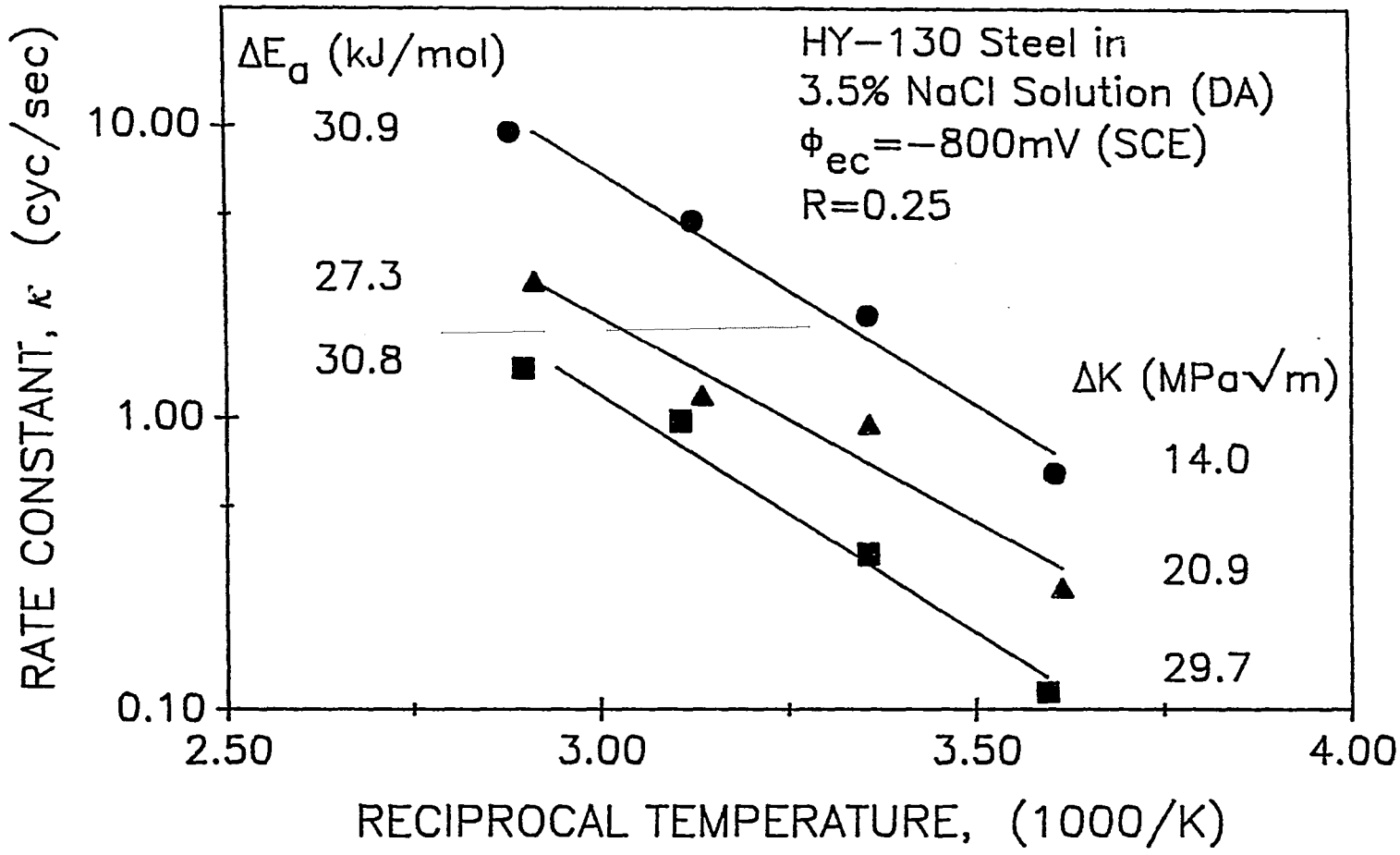

FIGURE 8.8: An Arrhenius plot for the reaction rate constant (κ).

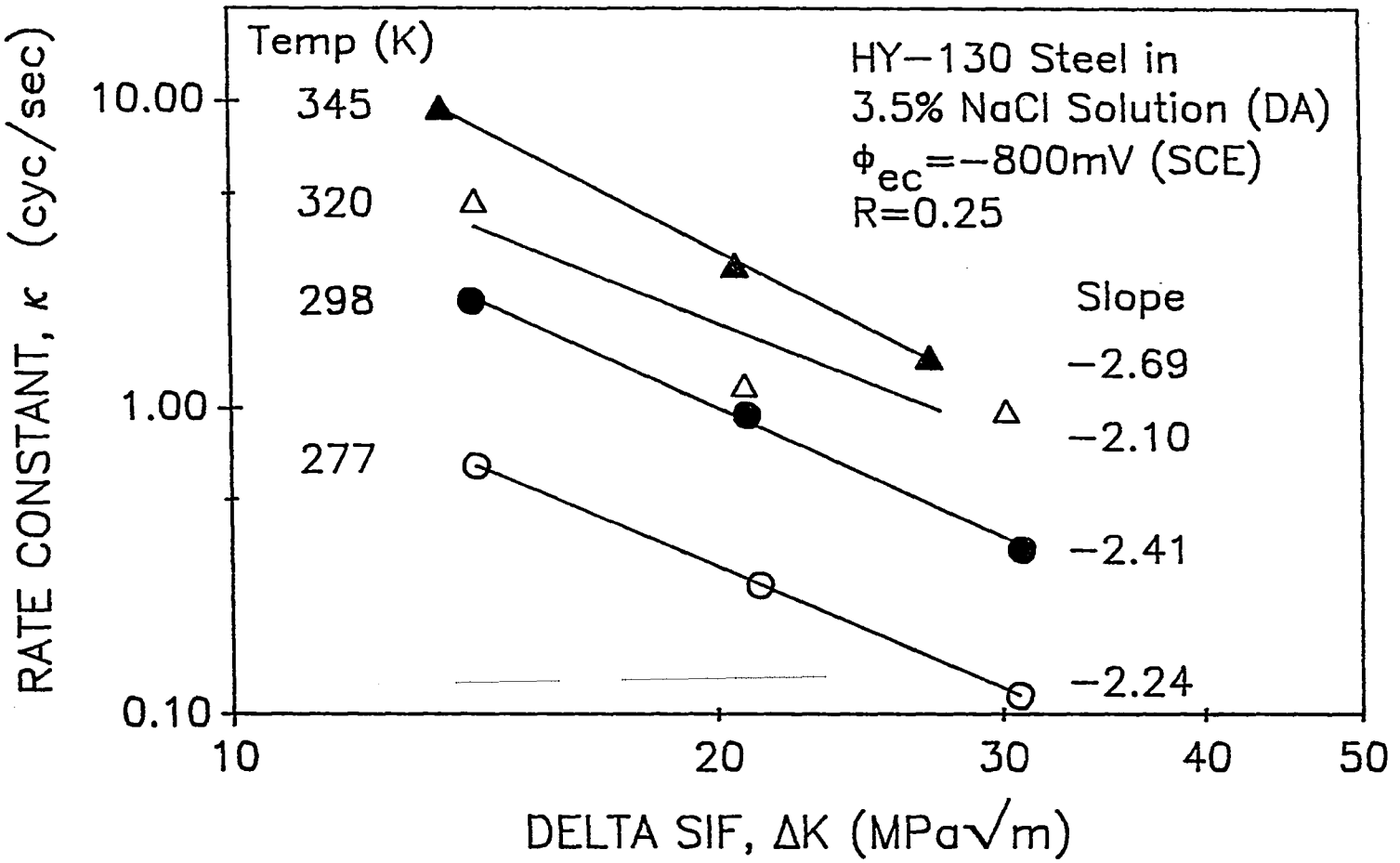

FIGURE 8.9: A plot of the reaction rate constant (κ) versus ΔK in logarithmic coordinates illustrating the power law dependence.

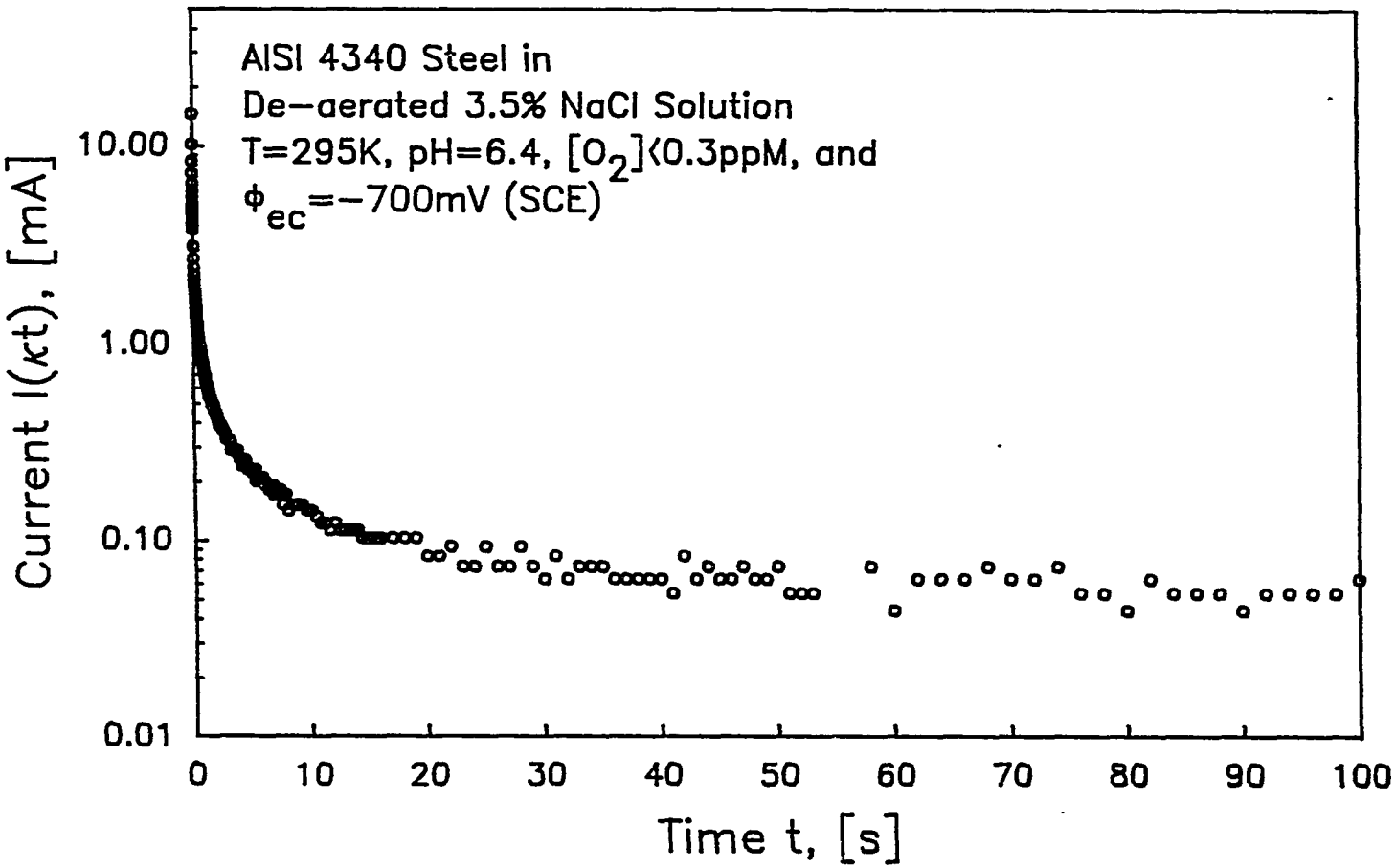

FIGURE 8.10: The experimental bare surface current transient data generated using the in-situ fracture technique. The projected area of the bare surface (A_{bs}) is 0.4 cm^2(Wei & Xu, 1989).

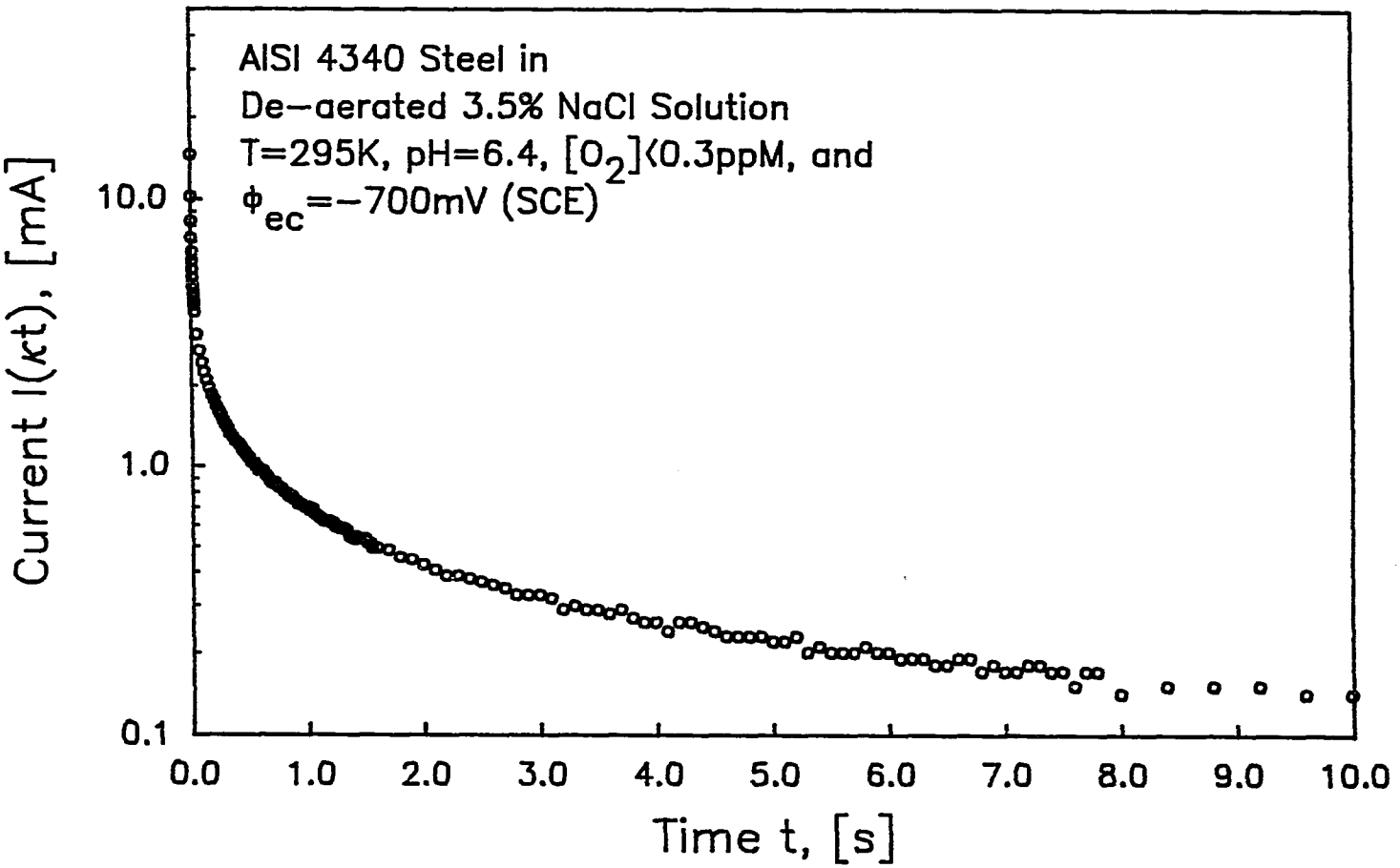

FIGURE 8.11: The experimental bare surface current transient data generated using the in-situ fracture technique, for shorter times. The projected area of the bare surface (A_{bs}) is 0.4 cm^2 (Wei & Xu, 1989).

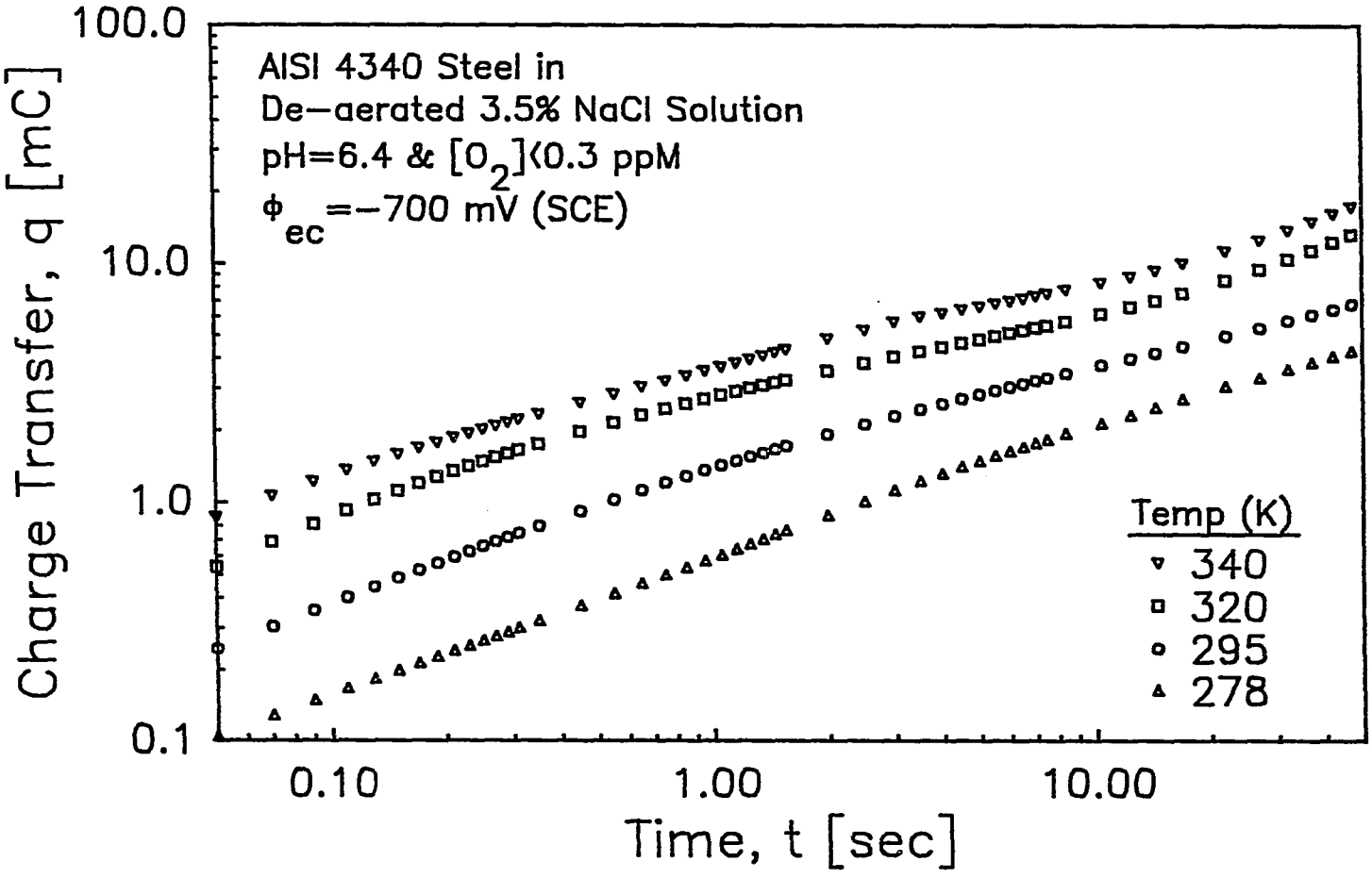

FIGURE 8.12: The charge transfer as a function of time, for different temperatures. The charge transfer is determined by numerical integration of $I(\kappa t)$ without subtracting off the baseline current level (Wei & Xu, 1989).

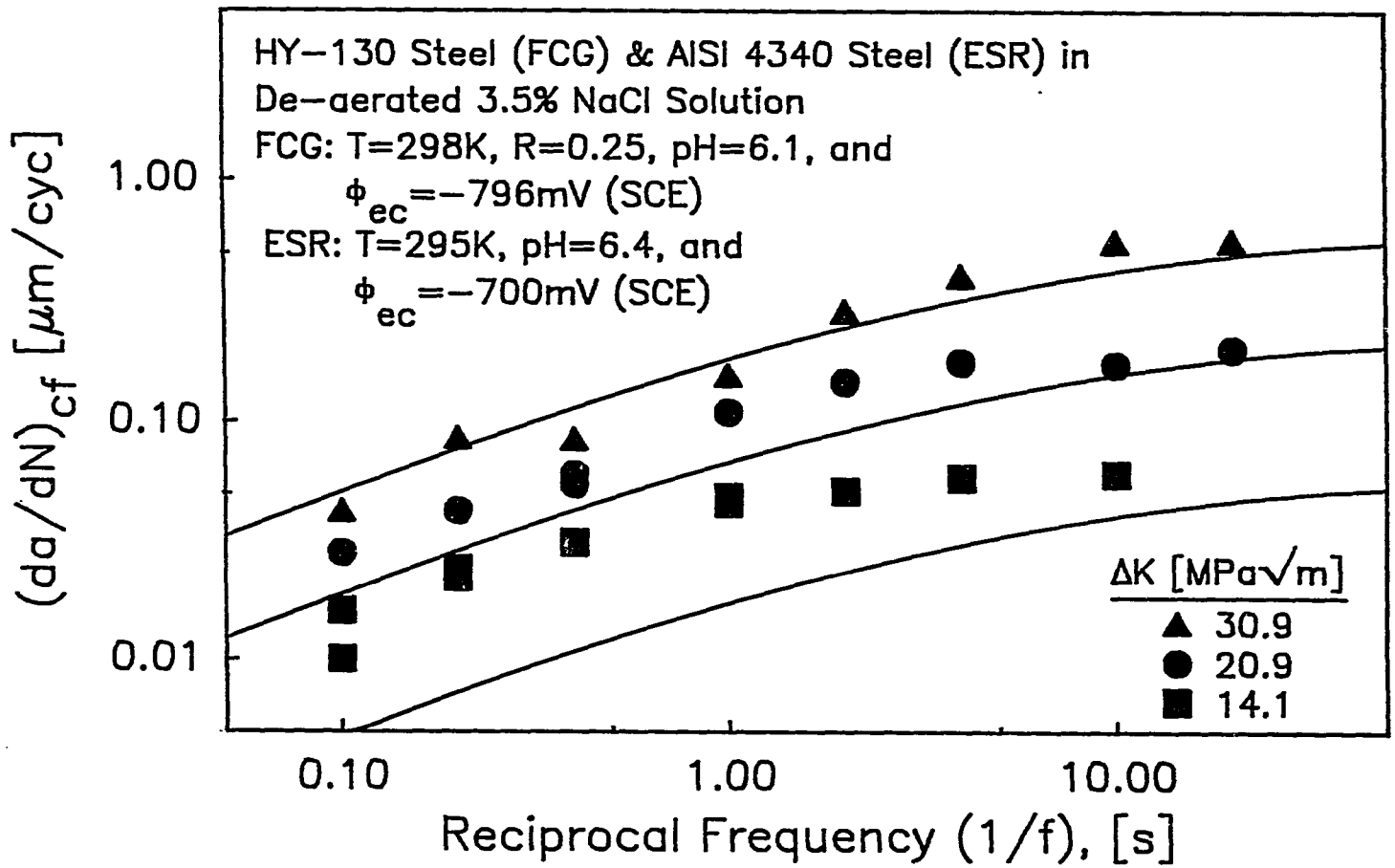

FIGURE 8.13: A direct comparison of the room temperature charge transfer data with the room temperature CG response, for three different ΔK levels. The comparison is made by vertically matching q_{sat} with $(da/dN)_{sat}$, at each ΔK level.

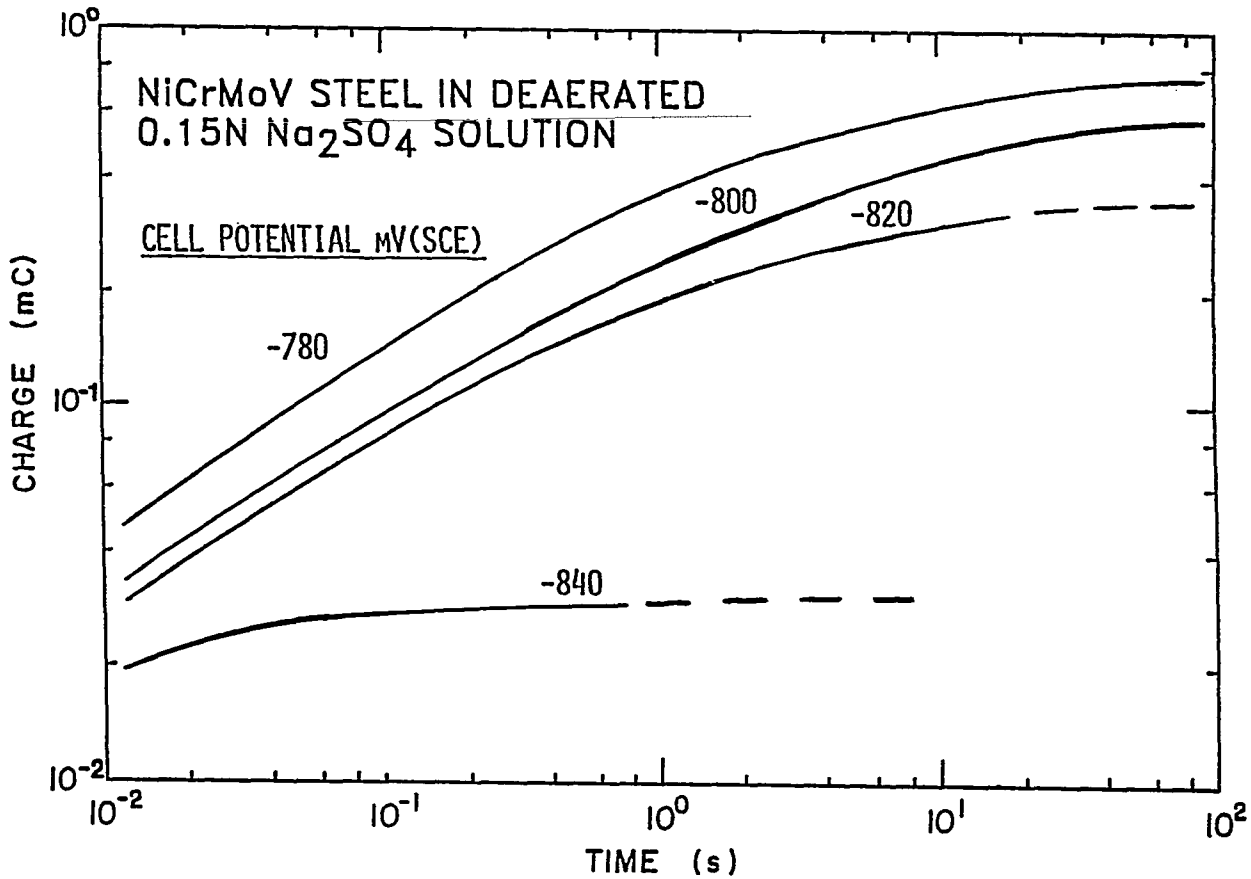

FIGURE 8.14: The effect of applied potential (Φ_{ec}) on the kinetics and magnitude of charge transfer, for a NiCrMoV steel in de-aerated Na_2SO_4 solution. Note that the more positive (anodic) Φ_{ec} curves exhibit a horizontal shift to longer times (smaller κ values) and a vertical shift to larger magnitudes (higher q_{sat} values) (Wei & Alavi, 1988).

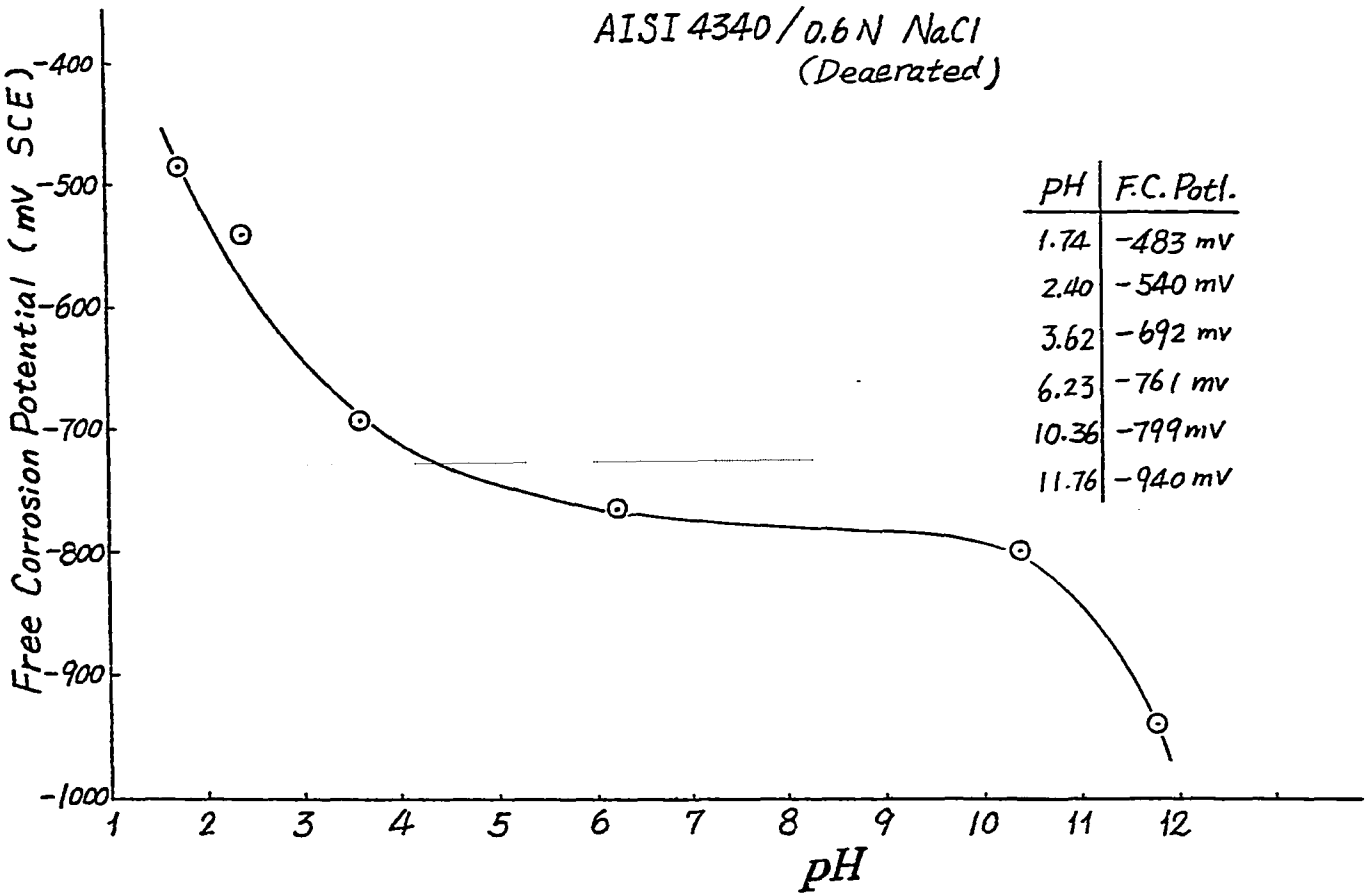

FIGURE 8.15: The influence of pH on the free corrosion potential (Φ_{fc}) of an AISI 4340 steel in de-aerated 0.6N NaCl solution at room temperature (Xu & Wei, 1988).

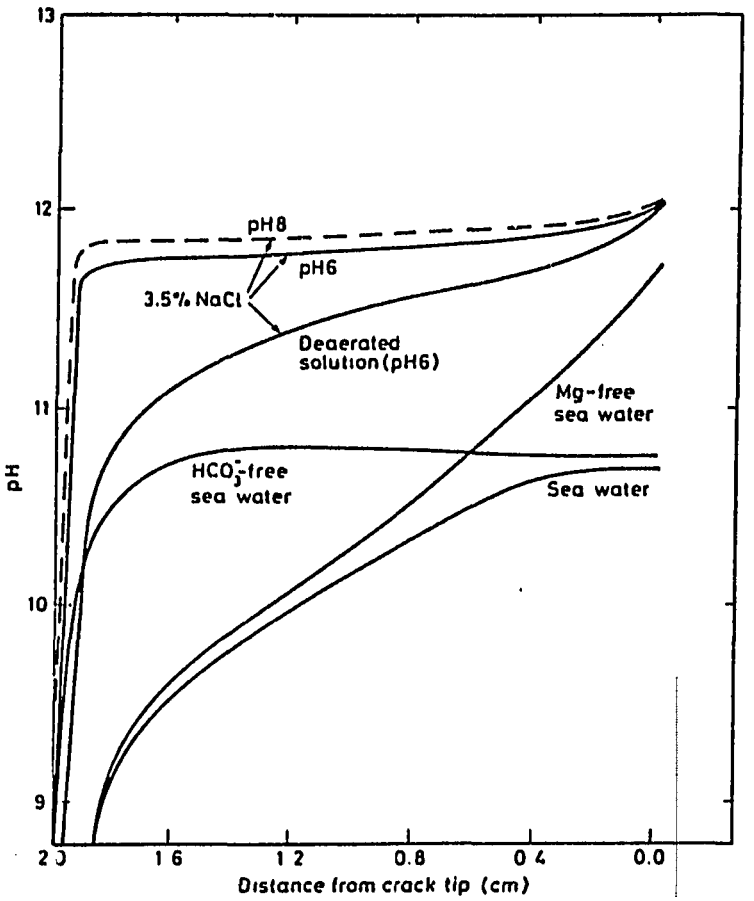

FIGURE 8.16: The variation of pH with distance from the crack-tip ("steady" periodic value at $2\pi ft = 2n\pi$) for different bulk solution chemistries. $E^{ext} = -1.0V$ (SCE); R=0.5; $\Delta K = 20$ MPa$\sqrt{m}$; f=0.1 Hz; T=5°C; and l=2.0 cm (Turnbull & Ferriss, 1986).

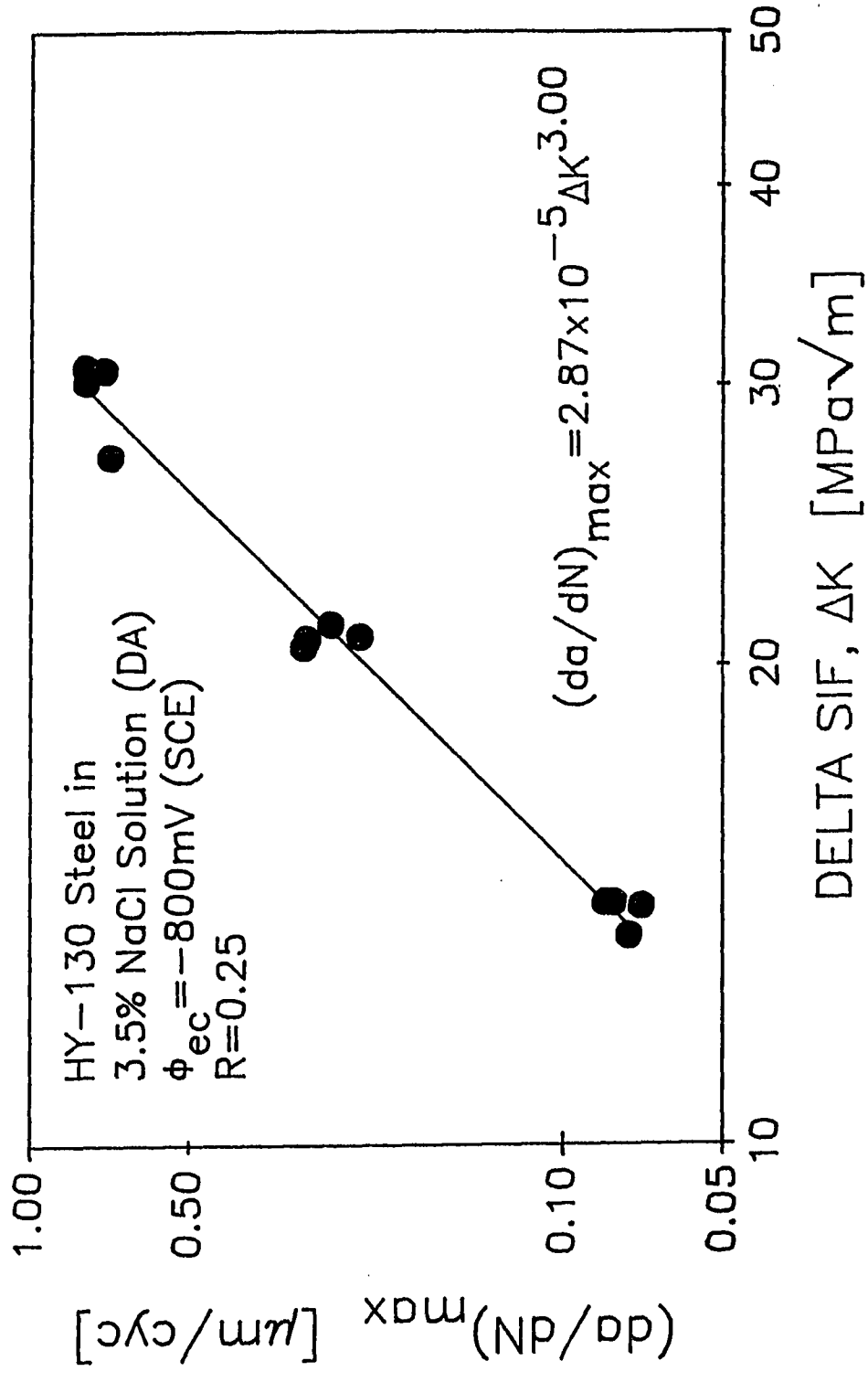

FIGURE 8.17: The influence of ΔK on $(da/dN)_{max}$.

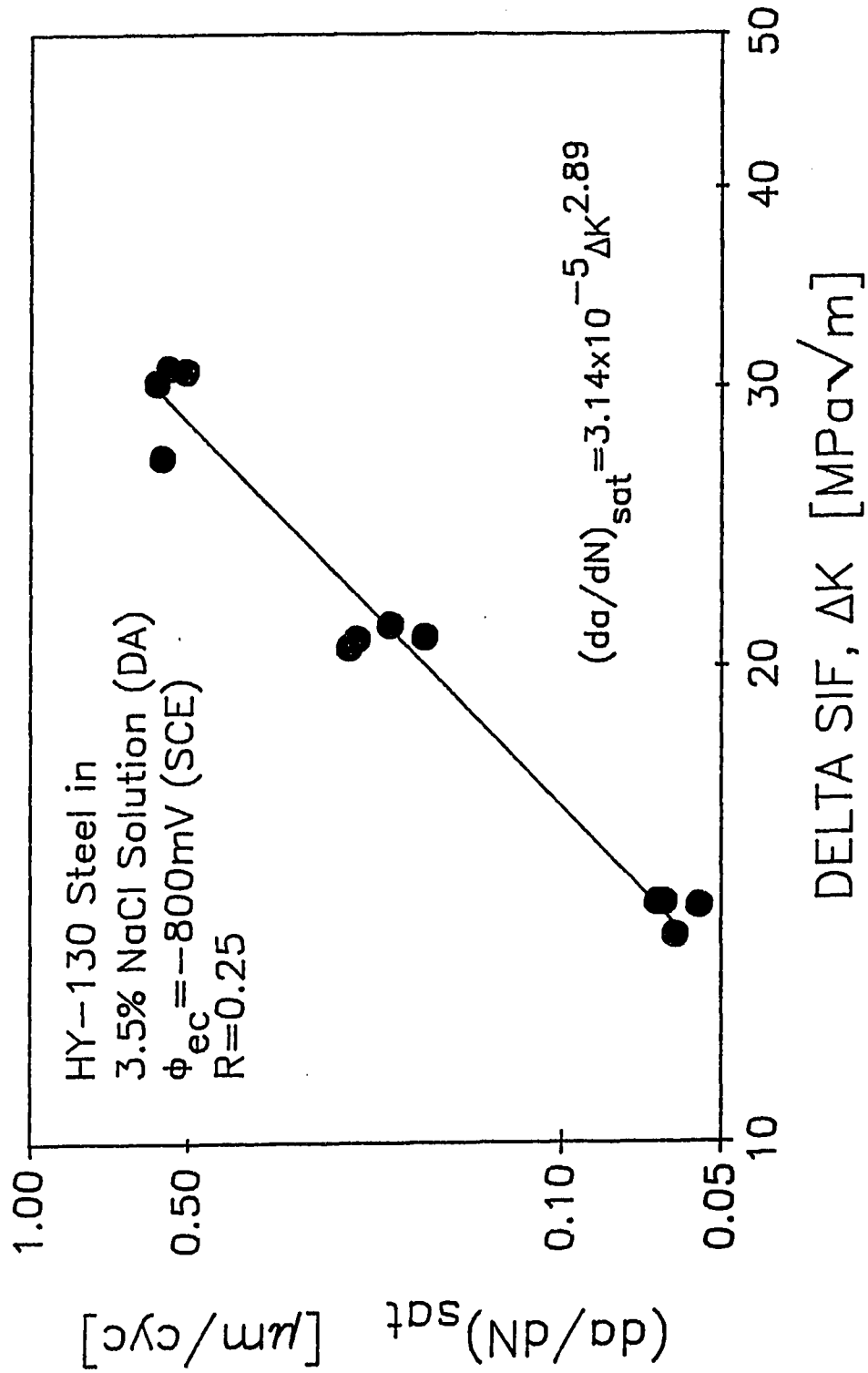

FIGURE 8.18: The influence of ΔK on $(da/dN)_{sat}$.

REFERENCES

Aifantis, E. C., (1980), "On the Problems of Diffusion in Solids", Acta Mechanica, Vol. 37, pp. 265-296.

Aifantis, E. C., (1976), "Diffusion of a Perfect Fluid in a Linear Elastic Stress Field", Mech. Res. Comm., Vol. 3, pp. 245-250.

Aifantis, E. C., and W. W. Gerberich, (1978), "Diffusion of a Gas in a Linear Elastic Solid", Acta Mechanica, Vol. 29, pp. 169-184.

Aifantis, E. C., and W. W. Gerberich, (1977a), "Gaseous Diffusion in a Stressed Thermoelastic Solid - I: The Thermomechanical Formulation", Acta Mechanica, Vol. 28, pp. 1-24.

Aifantis, E. C., and W. W. Gerberich, (1977b), "Gaseous Diffusion in a Stressed Thermoelastic Solid - I: Thermodynamic Structure and Transport Theory", Acta Mechanica, Vol. 28, pp. 25-47.

Ahlberg, J. H., Nilson, E. N., and J. L. Walsh, (1967), The Theory of Splines and Their Applications, Academic Press, New York.

Alavi, A., C. D. Miller, and R. P. Wei, (1987), "A Technique for Measuring the Kinetics of Electrochemical Reactions With Bare Metal Surfaces", Corrosion, Vol. 43, No. 4, pp. 204-207.

Allison, D. E., (1988), "Interaction of Crack Geometry and Electrochemical Processes in Corrosion Fatigue of AISI 304 Stainless Steel", Ph. D. Dissertation, Department of Mechanical Engineering and Mechanics, Lehigh University, Bethlehem, PA.

Anderson, T. N., J. L. Anderson, and H. Erying, (1969), "The Nature of Fresh Metal Surfaces in Aqueous Solutions", J. Phys. Chem., Vol. 73, No. 11, Nov., pp. 3562-3570.

ASM, (1978), Fatigue and Microstructure, 1978 ASM Materials Science Seminar, American Society of Metals, Metals Park, OH.

ASTM, (1989), "Standard Test Method for Constant-Load-Amplitude Fatigue Crack Growth Rates Above 10^{-8}m/cycle; E647-88a", ASTM Book of Standards, Vol. 03.01, American Society for Testing and Materials, Philadelphia, PA, pp. 646-666.

Atkin, R. J., and R. C. Craine, (1976a), "Continuum Theories of Mixtures: Basic Theory and Historical Development", Q. J. Mech. Appld. Math., Vol. XXIX, Pt. 2, pp. 209-244.

Atkin, R. J., and R. C. Craine, (1976b), "Continuum Theories of Mixtures and Applications", J. Inst. Math. Applic., Vol. 17, pp. 153-207.

Badaliance, R., (1978), "A Fatigue Crack Growth Theory Based on Strain Energy Density Factor", in Proc. 15^{th} Ann. Meet. of Soc. Engnrg. Sci., University of Florida.

Badaliance, R., (1980), "Application of Strain Energy Density Factor to Fatigue Crack Growth Analysis", Eng. Frac. Mech., Vol. 13, pp. 657-666.

Barsom, J. M., (1971), "Corrosion-Fatigue Crack Propagation Below $K_{I_{SCC}}$", Eng. Frac. Mech., Vol. 3, pp. 15-25.

Bataille, J., and J. Kestin, (1977), "Thermodynamics of Mixtures", J. Non-Equil. Therm., Vol. 2, pp. 49-65.

Beachem, C. D., (1972), "A New Model for Hydrogen-Assisted Cracking", Met. Trans. A, Vol. 3A, pp. 437-451.

Beck, J. V., (1974), "Parameter Estimation with Cumulative Errors", TECHNOMETRICS, Vol. 16, No. 1, pp. 85-92.

Beck, W., J. O' M. Bockris, J. McBreen, and L. Nanis, (1965), "Hydrogen Permeation in Metals as a Function of Stress, Temperature, and Dissolved Hydrogen Concentration", Proc. Royal Soc., London, Series A, Vol. 290, pp. 220-236.

Beevers, C. J., ed. (1980), The Measurement of Crack Length and Shape During Fracture and Fatigue, EMAS, United Kingdom.

Beevers, C. J., ed., (1978), Advances in Crack Length Measurement, EMAS, United Kingdom.

Bell, J. F., (1973), "The Experimental Foundations of Solid Mechanics", in Handbuch der Physik, Vol. VIa/1, Springer Verlag, New York.

Bell, J. F., (1968), "The Physics of Large Deformation of Crystalline Solids", in Springer Tracts in Natural Philosophy, Vol. 14, Springer Verlag, New York.

Bernstein, I. M., and A. W. Thompson, eds., (1981), Hydrogen Effects in Metals, Met. Soc. of the AIME, Warrendale, PA.

Bernstein, I. M., and A. W. Thompson, eds., (1974), Hydrogen in Metals, ASM, American Society for Metals, Metals Park, OH.

Birnbaum, G., and G. Free, eds., (1981), Eddy Current Characterization of Materials and Structures, ASTM STP 722, American Society for Testing and Materials, Philadelphia, PA.

BMDP, (1985), Statistical Software Manual, University of California Press, Berkeley.

Boblenz, T. L., Fisher, J. M., and S. T. Rolfe, (1966), "Secant and Tangent Moduli Values for 5Ni-Cr-Mo-V Steel", U. S. Steel Applied Research Laboratory Report No. 39.018-001, (54), Pittsburgh, PA.

Bockris, J. O' M., (1977), in Stress Corrosion Cracking and Hydrogen Embrittlement of Iron Based Alloys, NACE-5, National Association of Corrosion Engineers, Houston, TX, pp. 286-305.

Bockris, J. O' M., (1971), "Overpotential", J. Chem. Educ., Vol. 48, No. 6, June, pp. 352-358.

Bockris, J. O' M., and K. N. Reddy, (1977a), Modern Electrochemistry, Vol. 1, Plenum Press, New York.

Bockris, J. O' M., and K. N. Reddy, (1977b), Modern Electrochemistry, Vol. 2, Plenum Press, New York.

Bockris, J. O'M., and P. K. Subramanyan, (1972), "Reply to Comments on 'A Thermodynamic ... Stress Field'", Scripta Met., Vol. 6, pp. 947-954.

Bockris, J. O'M., and P. K. Subramanyan, (1971a), "A Thermodynamic Analysis of Hydrogen in Metals in the Presence of an Applied Stress Field", Acta Met., Vol. 19, Nov., pp. 1205-1208.

Bockris, J. O' M., J. McBreen, and L. Nanis, (1965), "The Hydrogen Evolution Kinetics and Hydrogen Entry into α-Iron", J. Electrochem. Soc., Vol. 112, No. 10, pp. 1025-1031.

Bockris, J. O'M., W. Beck, M. A. Genshaw, P. K. Subramanyan, and F. S. Williams, (1971b), "The Effect of Stress on the Chemical Potential of Hydrogen in Iron and Steel", Acta Met., Vol. 19, pp. 1209-1218.

Bowen, R. M., (1976), in Continuum Physics, Vol. III, A. C. Eringen, ed., Academic Press, NY, pp. 1-127.

Box, G. E. P., Hunter, W. G., and J. S. Hunter, (1978), Statistics for Experimenters, John Wiley and Sons, Inc., New York.

Box, G. E. P., and G. M. Jenkins, (1970), Time Series Analysis: Forecasting and Control, Holden Day, Inc., New York.

Brown Jr., W. F., and J. E. Srawley, (1966), Plane Strain Fracture Toughness Testing of High Strength Metallic Materials, ASTM STP 410, American Society for Testing and Materials, Philadelphia, PA, pp. 53-56.

Conway, B. E., (1965), Theory and Principles of Electrode Processes, The Ronald Press Co., New York.

Cook, R. D., and S. Weisberg, (1982), Residuals and Influence in Regression, Chapman and Hall Publishers, Inc., New York.

Crank, J., (1970), The Mathematics of Diffusion, Oxford University Press, London, UK.

CRC, (1976), "Temperature Correction for Volumetric Solutions", in Handbook of Chemistry and Physics, 57^{th} edition, CRC Press, Cleveland, pg. F-2.

Crooker, T. W., and B. N. Leis, eds., (1983), Corrosion Fatigue, ASTM STP 801, American Society for Testing and Materials, Philadelphia, PA.

de Boor, C., (1987), A Practical Guide to Splines, Applied Mathematical Sciences Vol. 27, Fourth Printing, Springer Verlag, New York.

Devereux, O. F., A. J. McEvily, and R. W. Staehle, eds., (1972), Corrosion Fatigue: Chemistry, Mechanics, and Microstructure, NACE-2, National Association of Corrosion Engineers, Houston, TX.

de Groot, S. R., and P. Mazur, (1984), Non-Equilibrium Thermodynamics, Dover Publications, Inc., NY.

Donald, K. J., (1988), in Mechanics of Fatigue Crack Closure, ASTM STP 982, J. C. Newman Jr. and W. Elber, eds., American Society for Testing and Materials, Philadelphia, PA, pp. 222-229.

Draper, N. R., and H. Smith, (1981), Applied Regression Analysis, John Wiley and Sons, Inc., New York.

Edelen, D. G. B., (1975), in Advances in Chemical Physics, Vol. XXXIII, I. Prigogine and S. A. Rice, eds., John Wiley & Sons, NY, pp. 399-442.

Erdogan, F., (1968), "Crack Propagation Theories", in Fracture, Vol. 2, H. Liebowitz, ed., Academic Press, New York.

Erdogan, F., (1983), "Stress Intensity Factors", Trans. ASME, J. Appl. Mech., Vol. 50, Dec., pp. 992-1002.

Eyring, H., S. Glasstone, and K. J. Laidler, (1939), "Application of the Theory of Absolute Reaction Rates to Overvoltage", J. Chem. Phys., Vol. 7, Nov., pp. 1053-1065.

Flora, M., (1985), "Basic Concepts of Thermistors for Thermometry", Yellow Springs Instrument Company, Inc., Industrial Division, Training Department, pp. 1-20.

Fong, J., ed., (1979), Fatigue Mechanisms, ASTM STP 675, American Society for Testing and Materials, Philadelphia.

Ford, F. P., (1984), in Embrittlement by the Localized Crack Environment, R. P. Gangloff, ed., Met. Soc. of the AIME, Warrendale, PA, pp. 117-142.

Ford, F. P., (1983), in Fatigue: Environment and Temperature Effects, J. J. Burke and V. Weiss, eds., Sagamore Army Materials Research Conf. Proc., 27, pp. 41-57.

Fujii, C. T., (1984), in Environment-Sensitive Fracture: Evaluation and Comparison of Test Methods, ASTM STP 821, S. W. Dean and G. M. Ugiansky, eds., American Society for Testing and Materials, Philadelphia, PA., pp. 383-398.

Funk, A. G., J. C. Giddings, C. J. Christensen, and H. Eyring, (1957a), "Strain Electrometry and Corrosion I: Genreal Considerations on Interfacial Electrical Transients", Proc. N. A. S., Vol. 43, pp. 421-429.

Funk, A. G., J. C. Giddings, C. J. Christensen, and H. Eyring, (1957b), "Strain Electrometry and Corrosion II: Chemical Effects with Copper Electrodes", J. Phys. Chem., Vol. 61, Sept., pp. 1179-1183.

Funk, A. G., D. N. Chakravarty, H. Eyring, and C. J. Christensen, (1958), "Strain Electrometry, Corrosion, and Catalysis III: The Iron Electrode", Z. Physik Chem., Vol. 15, pp. 64-74.

Gallagher, J. P., (1971), "Corrosion Fatigue Crack Growth Rate Behavior Above and Below $K_{I_{scc}}$ in Steels", J. of Materials, JMLSA, Vol. 6, No. 4, Dec., pp. 941-964.

Gangloff, R. P., (1985), "Crack Size Effects on the Driving Force for Aqueous Corrosion Fatigue", Met. Trans. A, Vol. 16A, May, pp. 953-969.

Gangloff, R. P., ed., (1984), Embrittlement by the Localized Crack Environment, Met. Soc. of the AIME, Warrendale, PA.

Gangloff, R. P., (1982), in Advances in Crack Length Measurement, C. J. Beevers, ed., EMAS, United Kingdom, pp. 175-229.

Gangloff, R. P., (1981), "The Criticality of Crack Size in Aqueous Corrosion Fatigue", Res Mechanica Letters, Vol. 1, pp. 299-306.

Gangloff, R. P., and R. O. Ritchie, (1985), in Fundamentals of Deformation and Fracture, B. A. Bilby, K. J. Miller, and J. P. Willis, eds., Cambridge University Press, Cambridge, UK, pp. 529-558.

Gangloff, R. P., and R. P. Wei, (1986), in Small Fatigue Cracks, R. O. Ritchie, and J. Lankford, eds., Met. Soc. of the AIME, Warrendale, PA, pp. 239-264.

Gao, M., and R. P. Wei, (1985), "A 'Hydrogen Partitioning' Model for Hydrogen Assisted Crack Growth", Met. Trans. A, Vol. 16A, Nov., pp. 2039-2050.

Gao, M., P. Pao, and R. P. Wei, (1988), "Chemical and Metallurgical Aspects of Environmentally Assisted Fatigue Crack Growth in 7075-T651 Aluminum Alloy", Met. Trans. A, Vol. 19A, Jul., pp. 1739-1750.

Giddings, J. C., A. G. Funk, C. J. Christensen, and H. Eyring, (1959), "Strain Electrometry and Corrosion IV: Film Properties and Strain Potential", J. Electrochem. Soc., Vol. 106, No. 2, pp. 91-95.

Gill, S. J., Htun, K. M., Jolles, I. M., and T. W. Crooker, (1984), in Embrittlement by the Localized Crack Environment, R. P. Gangloff, ed., Met. Soc. of the AIME, Warrendale, PA, pp. 471-483.

Girifalco, L. A., and D. O. Welsh, (1967), Point Defects and Diffusion in Strained Metals, Gordon and Breach, NY.

Gnedenko, B. V., and A. Ya. Khinchin, (1962), An Elementary Introduction to the Theory of Probability, Dover Publications, Inc., NY.

Greville, T. N. E., ed., (1969), Theory and Applications of Spline Functions, Academic Press, New York.

Gyarmarti, I., (1970), Non-Equilibrium Thermodynamics, Springer-Verlag, Berlin.

Haigh, B. P., (1917), "Experiments on the Fatigue of Brasses", J. Inst. Metals, Vol. 18, pp. 55-86.

Hamburg, E. G., (1971), "Physical Properties of Ultrastrength Steels", U. S. Steel Applied Research Laboratory Report No. 39.018-007, (44), Pittsburgh, PA.

Hayes, J. G., ed., (1970), Numerical Approximation to Functions and Data, The Institute of Mathematics and its Applications, The Athlone Press, London.

Hirth, J. P., (1980), "Effects of Hydrogen on the Properties of Iron and Steel", Met. Trans. A, Vol. 11A, pp. 861-890.

Hoeppner, D. W., and W. E. Krupp, (1974), "Prediction of Component Life by Application of Fatigue Crack Growth Knowledge", Eng. Frac. Mech., Vol. 6, pp. 47-70.

Hudak Jr., S. J., (1988), "Corrosion Fatigue Crack Growth: The Role of Crack-Tip Deformation and Film Formation Kinetics", Ph. D. Dissertation, Lehigh University, Dept. of Materials Science and Engineering, Bethlehem, PA.

Hudak Jr., S. J., and R. J. Bucci, eds., (1981), Fatigue Crack Growth Measurement and Data Analysis, ASTM STP 738, American Society for Testing and Materials, Philadelphia.

Hutchinson, J. W., (1968), "Singular Behavior at the End of a Tensile Crack in a Hardening Material", J. Mech. Phys. Solids, Vol. 16, pp. 13-31.

Hutter, K., and A. A. F. Van de Ven, (1979), Field Matter Interactions in Thermoelastic Solids, Springer Lecture Notes in Physics No. 88, Springer-Verlag, NY.

IMSL, (1987), User's Manual Version 10.0, Mathematical Software, Chapter 3: Interpolation and Approximation, IMSL Corporation, Houston, TX.

Johnson, H. H., (1988), "Hydrogen in Iron", Met. Trans. A, Vol. 19A, Oct., pp. 2371-2387.

Johnson, H. H., and P. C. Paris, (1968), "Sub-Critical Flaw Growth", Eng. Frac. Mech., Vol. 1, pp. 3-45.

Jordan, N. F., and A. C. Eringen, (1964a), "On the Static Nonlinear Theory of Electromagnetic Thermoelastic Solids - I", Int. J. Engnr. Sci., Vol. 2, pp. 59-95.

Jordan, N. F., and A. C. Eringen, (1964b), "On the Static Nonlinear Theory of Electromagnetic Thermoelastic Solids - II", Int. J. Engnr. Sci., Vol. 2, pp. 97-114.

Joseph, P. J., (1986), Private Communication.

Joseph, P. J., and F. Erdogan, (1987), "Surface Crack Problems in Plates", Lehigh University, Department of Mechanical Engineering and Mechanics Report, NASA Grant NAG-1-713, Bethlehem, PA.

Kikukawa, M., Jono, M., and K. Tanaka, (1976), "Fatigue Crack Closure Behavior at Low Stress Intensity Level", in Proc. of 2nd Int. Conf. on Mech. Behvr. of Mat'l., (Special Edition), American Society of Metals, Metals Park, OH., pp. 254-277.

Kaya, A. C., and F. Erdogan, (1980), "Stress Intensity Factors and COD in an Orthotropic Strip", Int. J. of Frac., Vol. 16, No. 2, pp. 171-190.

Kim, C. D., and B. E. Wilde, (1971), "The Kinetics of Hydrogen Absorption into Iron During Cathodic Hydrogen Evolution", J. Electrochem. Soc., Vol. 118, No. 2, pp. 202-206.

Laidler, K. J., (1970), "The Kinetics of Electrode Processes", J. Chem. Educ., Vol. 47, No. 9, Sept., pp. 600-607.

Letzer, S., and N. Webster, (1970), "Noise in Amplifiers", IEEE Spectrum, Aug., pp. 67-75.

Li, J. C. M., R. A. Oriani, and L. S. Darken, (1966), "The Thermodynamics of Stressed Solids", Z. Physik. Chem., Vol. 49, pp. 271-290.

Liaw, P. K., S. J. Hudak Jr., and J. K. Donald, (1982), "Influence of Gaseous Environments on the Rates of Near-Threshold Fatigue Crack Propagation in NiCrMoV Steel", Met. Trans. A, Vol. 13A, Sep., pp. 1633-1645.

Louthan Jr., M. R., and R. P. McNitt, (1976), in Effect of Hydrogen on the Behavior of Materials, A. W Thompson and I. M. Bernstein, eds., Met. Soc. of the AIME, Warrendale, PA, pp. 496-506.

Lui, H. W., (1970), "Stress Corrosion Cracking and the Interaction Between Crack-Tip Stress Fields and Solute Atoms", Trans. ASME- J. Basic Eng., Vol. 92, No. 3, pp. 633-638.

Macha, D. E., Corbly, D. M., and J. W. Jones, (1979), "On the Variation of Fatigue Crack Opening Load With Measurement Location", Experimental Mechanics, June, pp. 207-213.

Mandel, J., (1984), The Statistical Analysis of Experimental Data, Dover Publications, Inc., New York.

Mandel, J., (1964), "Answer to a Query on Regression Analysis of Cumulative Data", TECHNOMETRICS, Vol. 6, No. 2, pp. 225-227.

Mandel, J., (1957), "Fitting a Straight Line to Certain Types of Cumulative Data", Amer. Stat. Assoc. J., Dec., pp.552-566.

McAfee Jr., K. B., (1958a), "Stress-Enhanced Diffusion in Glass - I: Glass Under Tension and Compression", J. Chem. Physics, Vol. 28, No. 2, pp. 218-226.

McAfee Jr., K. B., (1958b), "Stress-Enhanced Diffusion in Glass - II: Glass Under Shear", J. Chem. Physics, Vol. 28, No. 2, pp. 226-229.

McBreen, J. and M. A. Genshaw, (1969), in Fundamental Aspects of Stress Corrosion Cracking, NACE-1, National Association of Corrosion Engineers, Houston TX, pp. 51-63.

McBreen, J., L. Nanis, and W. Beck, (1966), "A Method for the Determination of the Permeation Rate of Hydrogen Through Metal Membranes", J. Electrochem. Soc., Vol. 113, No. 11, pp. 1218-1222.

McCright, R. D., (1977), in Stress Corrosion Cracking and Hydrogen Embrittlement of Iron Based Alloys, NACE-5, National Association of Corrosion Engineers, Houston TX, pp. 306-325.

McEvily, A. J., and R. P. Wei, (1972), in Corrosion Fatigue: Chemistry, Mechanics, and Microstructure, NACE-2, National Association of Corrosion Engineers, Houston, TX, pp. 381-395.

McLachlan, N. W., (1955), Bessel Functions for Engineers, 2nd Edition, Clarendon Press, Oxford, UK.

Measurements Group, (1986), Strain Gage Technology: Product and Technical Reference Binder, Measurements Group, Inc., Raleigh, SC.

Misawa, T., N. Ringshall, and J. F. Knott, (1976), "Fatigue Crack Propagation in a Low Alloy Steel in a De-aerated Distilled Water Environment", Corrosion Science, Vol. 16, pp. 805-818.

Moon, F. C., (1984), Magneto-Solid Mechanics, John Wiley and Sons, Inc., New York.

Moon, P., and D. E. Spencer, (1961), Field Theory for Engineers, D. Van Nostrand Company, Inc., Princeton, NJ.

Moon, P., and D. E. Spencer, (1960), Foundations of Electrodynamics, D. Van Nostrand Company, Inc., Princeton, NJ.

Moon, P., and D. E. Spencer, (1953), "The Meaning of the Vector Laplacian", J. of Franklin Inst., pp. 551-558.

Moyer Jr., E. T., and G. C. Sih, (1984), "Fatigue Analysis of an Edge Crack Specimen: Hysteresis Strain Energy Density", Engr. Frac. Mech., Vol. 19, No. 4, pp. 643-652.

Nakai, Y., K. Tanaka, and R. P. Wei, (1986), "Short-Crack Growth in Corrosion Fatigue for a High Strength Steel", Eng. Frac. Mech., Vol. 24, No. 3., pp. 433-444.

Natrella, M. G., (1966), Experimental Statistics, NBS Handbook 91, National Bureau of Standards, Washington, DC.

Newman, J., (1973), Electrochemical Systems, Prentice-Hall, Inc., Englewood Cliffs, NJ.

Newman, R. C., (1984a), in Corrosion Chemistry Within Pits, Crevices, and Cracks, A. Turnbull, ed., Her Majesty's Stationery Office, London, UK, pp. 317-356.

Newman, R. C., (1984b), in Embrittlement by the Localized Crack Environment, R. P. Gangloff, ed., Met. Soc. of the AIME, Warrendale, PA, pp. 291-304.

Newman Jr., J. C., and W. Elber, eds., (1988), Mechanics of Crack Closure, ASTM STP 982, American Society for Testing and Materials, Philadelphia, PA.

Oriani, R. A., (1969), in Fundamental Aspects of Stress Corrosion Cracking, NACE-1, National Association of Corrosion Engineers, Houston, TX, pp. 32-50.

Oriani, R. A., (1972), "A Mechanistic Theory of Hydrogen Embrittlement of Steels", Berichte der Bunsen-Gesellschaft, Vol. 76, No. 8, pp. 848-857.

Oriani, R. A., and P. H. Josephic, (1974), "Equilibrium Aspects of Hydrogen Induced Cracking of Steels", Acta Met., Vol. 22, Sept., pp. 1065-1074.

Oriani, R. A., (1977), in Stress Corrosion Cracking and Hydrogen Embrittlement of Iron Based Alloys, NACE-5, National Association of Corrosion Engineers, Houston, TX, pp. 351-358.

Oriani, R. A., (1978), "Hydrogen Embrittlement of Steels", Ann. Rev. Mater. Sci., Vol. 8, pp. 327-357.

Oriani, R. A., J. P. Hirth, and M. Smialowski, eds., (1985), Hydrogen Degradation of Ferrous Alloys, Noyes Publications, Park Ridge, NJ.

Pao, P. S., W. Wei, and R. P. Wei, (1977), in Environment-Sensitive Fracture of Engineering Materials, Z. A. Foroulis, ed., Met. Soc. of the AIME, Warrendale, PA, pp. 565-580.

PAR, (1983), "Operating and Service Manual", Models 1900, 1901, &1902 Low Noise Transformers, M1900/1/2:2/83-350-RAU, Princeton Applied Research Corp., Princeton, NJ.

PAR, (1976), "Operating and Service Manual", Model 126 Lock-in Amplifier, M126-10M-12/76, Princeton Applied Research Corp., Princeton, NJ.

PAR, (1976), "Explore the Lock-in Amplifier", Technical Note 115, TN115-10M-12/76, Princeton Applied Research Corp., Princeton, NJ.

PAR, (1976), "Specifying Lock-in Amplifiers", Technical Note 116, TN116-10M-12/76, Princeton Applied Research Corp., Princeton, NJ.

PAR, (1974), "How to Measure Noise That is Quieter Than Your Preamplifyer", Technical Note 127, TN127A-5M-10/74-MG, Princeton Applied Research Corp., Princeton, NJ.

PAR, (1969), "How to Use Noise Figure Contours", Note 226, T226-20M-11/69-MB, Princeton Applied Research Corp., Princeton, NJ.

Paris, P. C., (1964), in Fatigue- An Interdisciplinary Approach, Syracuse Univ. Press, pp. 107-132.

Paris, P. C., and F. Erdogan, (1963), "A Critical Analysis of Crack Propagation Laws", J. Basic Eng.- Trans. ASME, Vol. 88, Dec., pp. 528-534.

Paris, P. C., M. P. Gomez, and W. E. Anderson, (1961), "A Rational Analytical Theory of Fatigue", The Trend in Engineering, Univ. of Wash., Vol. 13, pp. 9-14.

Petch, N. J., (1956), "The Lowering of Fracture-Stress Due to Surface Adsorption", The Phil. Mag., Series 8, Vol. 1, No. 4, Apr., pp. 331-337.

Petch, N. J., and P. Stables, (1952), "Delayed Fracture of Metals Under Static Load", Nature, Vol. 169, No. 4307, May, pp. 842-843.

Petrocelli, J. V., (1951), "The Kinetics of Oxidation-Reduction Electrode Reactions", J. Electrochem. Soc., Vol. 98, No. 5, pp. 187-192.

Prigogine, I., (1967), Thermodynamics of Irreversible Processes, Third Edition, Interscience Publishers, NY.

Powell, M. J. D., (1969), "The Local Dependence of Least Squares Cubic Splines", SIAM J. Numer. Anal., Vol. 6, No. 3, pp. 398-413.

Rice, J. R., (1967), in Symposium on Fatigue Crack Growth, ASTM STP 415, American Society for Testing and MAterials, Philadelphia, PA, pp. 247-311.

Rice, J. R., and G. F. Rosengren, (1968), "Plane Strain Deformation Near a Crack Tip in a Power-Law Hardening Material", J. Mech. Phys. Solids, Vol. 16, pp. 1-16.

Ritchie, R. O., and J. Lankford, eds., (1986), Small Fatigue Cracks, Met. Soc. of the AIME, Warrendale, PA.

Ross, S., (1984), A First Course in Probability, MacMillan Publishing Corporation, New York.

Ryder, J. T., and J. P. Gallagher, (1974), "Temperature Influence on Corrosion Fatigue Behavior of 5Ni-Cr-Mo-V Steel", J. of Test. and Eval., JTEVA, Vol. 2, No. 3, pp. 180-189.

Schoenberg, I. J., (1964), "Spline Functions and the Problem of Graduation", Proc. of the N. A. S., Vol. 54, pp. 947-950.

Scully, J. R., and P. J. Moran, (1988a), "The Influence of Strain on Hydrogen Entry and Transport in a High Strength Steel in Sodium Chloride Solution", J. Electrochem. Soc., Vol. 135, No. 6, Jun., pp. 1337-1348.

Scully, J. R., and P. J. Moran, (1988b), "Influence of Strain on the Environmental Hydrogen-Assisted Cracking of a High-Strength Steel in Sodium Chloride Solutions", Corrosion, NACE, Vol. 44, No. 3, Mar., pp. 176-185.

Shewmon, P. G., (1963), Diffusion in Solids, J. Williams Book Co., Jenks, OK.

Shih, T. T., and R. P. Wei, (1973), "A Study of Crack Closure in Fatigue", NASA Report CR-2319, National Aeronautics and Space Administration, Washington, DC.

Shim, G., Y. Nakai, and R. P. Wei, (1988), in Basic Questions in Fatigue, Vol. 2, ASTM STP 924, R. P. Wei and R. P. Gangloff, eds., American Society for Testing and Materials, Philadelphia, PA, pp. 211-229.

Shim, G., and R. P. Wei, (1987), "Corrosion Fatigue and Electrochemical Reactions in Modified HY-130 Steel", Mater. Sci. Eng., Vol. 86, pp. 121-135.

Sih, G. C., and E. T. Moyer Jr., (1983), "Path Dependent Nature of Fatigue Crack Growth", Engnr. Frac. Mech., Vol. 17, No. 3, pp. 269-280.

Sih, G. C., and B. M. Barthelemy, (1980), "Mixed Mode Fatigue Crack Growth Predictions", Engnr. Frac. Mech., Vol. 13, pp. 439-451.

Simmons, G. W., P. S. Pao, and R. P. Wei, (1978), "Fracture Mechanics and Surface Chemistry Studies of Subcritical Crack Growth in AISI 4340 Steel", Met. Trans. A, Vol. 9A, Aug., pp. 1147-1158.

Staehle, R. W., B. F. Brown, J. Kruger, and A. Agrawal, eds., (1974), Localized Corrosion, NACE-3, National Association of Corrosion Engineers, Houston, TX.

Staehle, R. W., A. J. Forty, and D. van Rooyen, eds., (1969), Fundamental Aspects of Stress Corrosion Cracking, NACE-1, National Association of Corrosion Enginners, Houston, TX.

Staehle, R. W., J. Hochmann, R. D. McCright, and J. E. Slater, eds., (1977), Stress Corrosion Cracking and Hydrogen Embrittlement of Iron Based Alloys, NACE-5, National Association of Corrosion Engineers, Houston TX.

Stuart, A., and J. K. Ord, (1987), Kendall's Advanced Theory of Statistics, Vols. I, II, and III, Oxford University Press, New York.

Tanaka, K., and R. P. Wei, (1985), "Growth of Short Fatigue Cracks in HY-130 Steel in 3.5% NaCl Solutions", Eng. Frac. Mech., Vol. 21, No. 2, pp. 293-305.

Telseren, A., and M. Doruk, (1974), "Temperature Dependence of Water Inhanced Fatigue Crack Growth in Mild Steels", Eng. Frac. Mech., Vol. 6, pp. 283-286.

Tetelman, A. S., (1969), in Fundamental Aspects of Stress Corrosion Cracking, NACE-1, National Association of Corrosion Engineers, Houston TX, pp. 446-464.

Thomas, J. P., A. Alavi, and R. P. Wei, (1986), "Correlation Between Electrochemcial Reactions With Bare Surfaces and Corrosion Fatigue Crack Growth in Steels", Scripta Met., Vol. 20, pp. 1015-1018.

Treitley, H. L., (1985a), "All About Thermistors: Part I", Radio-Electronics, Jan., pp. 47-50, and 68-70.

Treitley, H. L., (1985b), "All About Thermistors: Part II", Radio-Electronics, Feb., pp. 73-76.

Truesdell, C. A., (1984), Rational Thermodynamics, Springer-Verlag, NY.

Truesdell, C. A. , (1965), in The Rational Mechanics of Materials, Vol . 2, Part 8, C. Truesdell, ed., Gordon and Breach, NY, pp. 292-305.

Turnbull, A., (1984a), in Embrittlement by the Localized Crack Environment, R. P. Gangloff, ed., Met. Soc. of the AIME, Warrendale, PA., pp. 3-31.

Turnbull, A., ed., (1984b), Corrosion Chemistry Within Pits, Crevices, and Cracks, Her Majesty's Stationery Office, London, UK.

Turnbull, A., (1983), "The Solution Composition And Electrode Potential in Pits, Crevices and Cracks", Corrosion Science, Vol. 23, No. 8, pp. 833-870.

Turnbull, A., (1982), "Review of the Electrochemcial Conditions in Cracks with Particular Reference to Corrosion Fatigue of Structural Steels in Sea Water", Reviews in Coatings and Corrosion, Vol. 5, No. 1-4, pp. 43-170.

Turnbull, F., and D. H. Ferriss, (1986), "Mathematically Modeling of the Electrochemistry in Corrosion Fatigue Cracks in Structural Steel Cathodically Protected in Sea Water", Corrosion Science, Vol. 26, No. 8, pp. 601-628.

Turnbull, A., and M. Saenz de Santa Maria, (1989), "Discussion on 'The Influence of Strain ... Sodium Chloride Solutions' by J. R. Scully and P. J. Moran", Corrosion-NACE, Vol. 45, No. 4, Apr., pp. 316-319.

Unangst, K. D., Shih, T. T., and R. P. Wei, (1977), "Crack Closure in 2219-T851 Aluminum Alloy", Engnr. Frac. Mech., Vol. 9, pp. 725-734.

Unger, D. J., and E. C. Aifantis, (1983), "On the Theory of Stress-Assisted Diffusion, II", Acta Mechanica, Vol. 47, pp. 117-151.

Van Leeuwen, H. P., (1974), "The Kinetics of Hydrogen Embrittlement: A Quantitative Diffusion Model", Eng. Frac. Mech., Vol. 6, pp. 141-161.

Van Kampen, N. G., (1984), Stochastic Processes in Physics and Chemistry, Elsevier Science Publishing Co., Inc., NY.

Varotsos, P., and E. C. Aifantis, (1980), "Comments on 'The Diffusion of a Gas in a Linear Elastic Solid'", Acta Mechanica, Vol. 36, pp. 129-133.

Vetter, K. J., (1967), Electrochemical Kinetics, Academic Press, NY.

Vosikovsky, O., (1978), "Frequency, Stress Ratio, and Potential Effects on Fatigue Crack Growth of HY-130 Steel in Salt Water", J. of Test. and Eval., JTEVA, Vol. 6, No. 3, pp. 175-182.

Wei, R. P., (1989), in Advances in Fracture Research, Proc. of IFC7, Pergammon Press, NY, pp. 1525-1544.

Wei, R. P., (1985), "Corrosion Fatigue Crack Growth", in Proc. of Int. Symp. on Microstructure and Mechanical Behavior of Materials, Xi'an, People's Republic of China, EMAS, Warley, UK, (In press).

Wei, R. P., (1979), in Fatigue Mechanisms, ASTM STP 675, J. T. Fong, ed., American Society for Testing and Materials, Philadelphia, PA, pp. 816-840.

Wei, R. P., (1978), "Fracture Mechanics Approach to Fatigue Analysis in Design", Trans ASME - J. Eng. Mater. Tech., Vol. 100, pp. 113-120.

Wei, R. P., (1976), in Linear Fracture Mechanics, Envo Publishing Co., PA, pp. 287-302.

Wei, R. P., (1968), "Fatigue-Crack Propagation in a High Strength Aluminum Alloy", Int. J. Frac., Vol. 4, No. 2, Jun., pp. 159-170.

Wei, R. P., and A. Alavi, (1988), "A 4-Electrode Analogue for Estimating Electrochemical Reactions with Bare Metal Surfaces at the Crack Tip", Scripta Met., Vol. 22, pp. 969-974.

Wei, R. P., and R. L. Brazill, (1978), in Fatigue Crack Growth Measurement and Data Analysis, ASTM STP 738, S. J. Hudak Jr. and R. J. Bucci, eds., American Society for Testing and Materials, Philadelphia, pp. 171-193.

Wei, R. P., and M. Gao, (1983), "Reconsideration of the Superposition Model for Environmentally Assisted Fatigue Crack Growth", Scritpa Met., Vol. 17, pp. 959-962.

Wei, R. P., and J. D. Landes, (1969), "Correlation Between Sustained-Load and Fatigue Crack Growth in High Strength Steels", Mater. Res. Stand., Vol. 9, No. 7, pp. 25-28.

Wei, R. P., and G. Shim, (1984), in Corrosion Fatigue: Mechanics, Metallurgy, Electrochemistry, and Engineering, ASTM STP 801, T. W. Crooker and B. N. Leis, eds., American Society for Testing and Materials, Philadelphia, PA, pp. 5-25.

Wei, R. P., and G. W. Simmons, (1981), "Recent Progress in Understanding Environmentally Assisted Fatigue Crack Growth", Int. J. Frac., Vol. 17, pp. 235-247.

Wei, R. P., and M. O. Speidel, (1971), in Corrosion Fatigue: Chemistry, Mechanics, and Microstructure, NACE-2, National Association of Corrosion Engineers, Houston, TX, pp. 379-380.

Wei, R. P., and P. Y. Xu, (1989), "Unpublished Results", Lehigh University, Bethlehem, PA.

Wei, R. P., M. Gao, and P. Y. Xu, (1989), "Peak Bare-Surface Current Densities Overestimated in Straining and Scratching Electrode Experiments", J. Electrochem. Soc., Vol. 136, No. 6, Jun., pp. 1835-1836.

Wei, R. P., G. Shim, and K. Tanaka, (1984), in Embrittlement by the Localized Crack Environment, R. P. Gangloff, ed., Met. Soc. of the AIME, Warrendale, PA, pp. 243-263.

Whittaker, E. T., (1923), "On a New Method of Graduation", Edinburgh Math. Soc., Vol. 41, pp. 63-75.

Wilde, B. E., and C. D. Kim, (1981), "The Kinetics of Hydrogen Absorption and Evolution on a Carbon-Manganese Steel Exposed to Acidified Solutions of Sodium Chloride", Corrosion, NACE, Vol. 37, No. 8, Aug., pp. 449-455.

Williams, S. R., (1931), Magnetic Phenomena, McGraw-Hill Book Company, Inc., New York.

Wilson, R. K., and E. C. Aifantis, (1982), "On the Theory of Stress-Assisted Diffusion, I", Vol. 45, pp. 273-296.

Wold, S., (1974), "Spline Functions in Data Analysis", TECHNOMETRICS, Vol. 16, No. 1, pp. 1-11.

Wold, S., (1971), "Analysis of Kinetic Data by Means of Spline Functions", Chemica Scripta, (Sweden), Vol. 1, No. 3, pp. 97-102.

Xu, P. Y., and R. P. Wei, (1988), "Unpublished Results", Lehigh University, Bethlehem, PA.

APPENDIX A - DETAILED TEST RESULTS

SECTION A.1 - INTRODUCTION

This appendix contains the detailed test results for all of the fatigue crack growth experiments. This includes: (1) a description of calibration experiments 1-12, and some accompanying plots, (2) plots of the crack growth rate (CGR) versus crack length for the short crack growth tests 13-20, (3) tabulated results from tests 21-35, along with plots of the CGR versus crack length for the short crack growth regime of these tests, and (4) plots of the total measured CGR versus reciprocal loading frequency.

SECTION A.2 - THE CALIBRATION TEST RESULTS

A.2.1 Background and Introduction

A total of twelve specimens were involved in the calibration phase of testing. The first ten specimens (tests 1-10) were used in preliminary tests to determine the proper equipment settings and procedures, and the last two specimens (tests 11 & 12) for generating crack length (a) and potential drop (PD) data used for the calculation of the calibration relationship.

Potential drop readings were taken both before and after the crack front marking procedure, and each recorded PD value was based on an average of ten (tests 1-4) or twenty-five (tests 5-12) successive, maximum voltage readings, over one loading cycle. Two procedures were used for marking the crack front. Tests 1-4 used three overload cycles (at 15 to 50% overload) every 0.64 mm, but did this not mark the crack front. Tests 5-12 used alternating blocks of constant stress intensity factor, ΔK, over 0.75 mm intervals of crack growth. The second procedure worked well when the normalized change in ΔK level[1] was above 35%.

The results are listed by test and specimen serial number, and unless otherwise noted, the test objective is to obtain data for the calibration relationship.

A.2.2 - The Result of Tests 1 Through 12

Test Numbers 1 (S16A-58) & 2 (S16A-61): These are room temperature, laboratory air (RTLA) tests conducted with a constant alternating load, ΔP, a load ratio, R, equal to 0.1, and a loading frequency, f, equal to 5 Hz. Test 1 used three, 15% overload cycles and tests 2-4 used three, 50% overload cycles to mark the crack front.

[1] The normalized change in ΔK is defined as $\frac{\Delta K_{high} - \Delta K_{low}}{\Delta K_{ave}}$.

Lines scribed across the crack path, every 0.64 mm, were used to help indicate at which point each overload cycle should be initiated. The results showed the PD ranging from 4 to 80 μV for crack lengths, a, of 0.1 to 15.6 mm; a problem arose with uneven crack initiation in the thickness direction.

Test Number 3 (S16A-53): This was a RTLA test run under constant ΔK control with R=0.1 and f=5 Hz. Crack initiation problems forced a premature end to the test. Reasons for the uneven initiation include: the effects of the large gradient in ΔK with respect to a, for a<0.25 mm, which leads to a large variation in the stress conditions at the tip of an uneven notch whose length varies in the thickness direction, and loading misalignment problems. The remaining specimens had their notch lengths increased, from 0.10 mm to 0.25 mm, via electrical discharge machining, EDM.

Test Number 4 (S16A-30): This was a RTLA test with $\Delta K=16.5$ MPa$\sqrt{m}$, R=0.1, f=5 Hz. The results showed an improvement in the initiation problem, with the increased starter notch length, but that further improvement of the load alignment procedure was still needed. The overload procedure for marking the crack front did not work, and supply current flucuations of up to $\pm$15mA were observed, limiting the usefullness of the a-PD data. Nevertheless, a least squares fit, 4^{th} degree polynomial relating normalized crack length, $a-a_0$, to a normalized potential drop, $(V-V_0)/V_0$, was obtained, where a_0 and V_0 were the initial notch length and PD, respectively.

Test Number 5 (S16A-36): This was a RTLA test with $\Delta K=19.25$ & 13.75 MPa$\sqrt{m}$, R=0.1, and f=5 Hz. This was the first test to use blocks of constant, alternating ΔK to mark the crack front. Large changes in PD were observed when the ΔK level was changed in the crack front marking procedure (see Figure A.1). Also, uneven crack initiation remained a problem but a new load alignment procedure has been developed to insure a proper specimen to load fixture alignment for future tests.

Test Number 6A (S16A-34): This test measured PD as a function of load, P, and supply current, i_{sup}, for a notched specimen. It was a RTLA test with the notch potential initially stabilized by 150 load cycles at "ΔK"=19.25 MPa$\sqrt{m}$, R=0.1, and f=5 Hz. The results showed a linear decrease in PD with increasing P, (slope=-2.25 nV/kN), and a linear increase with increasing i_{sup} (slope=3.4 nV/mA) (see Figures A.2

& A.3). The supply current was discovered to be distorted at currents greater than 965mA, and so i_{sup} was decreased from 1000mA to 950mA, for all future tests.

Test Number 6 (S16A-34): RTLA test with ΔK=19.25 & 13.75 MPa$\sqrt{m}$, R=0.1, and f=5 Hz. This was the first test to run without any problems, resulting in useable a-PD data, from which an a-PD relationship was obtained. Because of the large changes in PD with changes in ΔK, the average of the two PD values (i.e. - the PD at each ΔK level) was used in calculating the a-PD relationship.

Test Number 6B (16A-34): This test was a repeat of test 6A, but with a crack length of 18.4 mm. The results showed a crack length influence on the effects of P and i_{sup} on PD. The magnitude of the P effect was -135 nV/kN for $0 \leq P < 2.67$ kN and -404 nV/kN for $2.67 \leq P < 4.4$ kN (see Figure A.4), and 92 nV/mA for the i_{sup} effect (see Figure A.5).

Test Numbers 7A & 7B (S16A-47): Test 7A was used to determine the effect of P and specimen temperature, T, on the notch PD while 7B measured the effect of f on the notch PD. They were both RTLA tests with the notch PD stabilized by 500 load cycles at "ΔK"=19.25 MPa$\sqrt{m}$, R=0.1, f=5 Hz, at the start of the test. The results of showed that the effect of T was independent of the applied load, with an average effect of 3.3 nV/K, while the effect of P, at different T values, was -1.94 nV/kN (see Figures A.6 & A.7). The results of 7B showed significant increases in the PD, for increasing f, with a logarithmic dependence on f. The effect was measured at 100.5 nV/decade (see Figures A.8 & A.9).

Test Number 7 (S16A-47): This was a RTLA test with ΔK=19.25 & 13.75 MPa$\sqrt{m}$, R=0.1, f=5 Hz. Large errors in crack length prediction occurred at the start of the test, and were attributed to V_0, which is very sensitive to the notch geometry. This led to large uncertainties in the value of $(PD-V_0)/V_0$ when the PD was close to V_0. Because of this, the normalized potential cannot be used in the calkibration relationship. Temperature and current effects will be compensated by multiplicative correction factors (see Chapter 5). An AC ammeter, with 0-10V analog output, has been incorporated in the AC potential system to provide information for the current correction factor.

Test Number 8A (S16A-60): Most of the remaining calibration tests have been performed in de-aerated 3.5% NaCl solution, at room temperature (DSSRT).

The purpose of this test was to determine the effect of f on the notch PD, in a DSSRT environment, with ΔP=900 kN and R=0.1. The results showed two distinct regions of behavior of magnitude 26.3 nV/decade for $0 \leq f < 0.6$ Hz and 98.5 nV/decade for $0.6 \leq f \leq 10$ Hz (see Figure A.10).

Test Number 8 (S16A-60): A number of new experimental methods and hardware were field tested for the first time including: full implementation of the DSS plumbing, a constant delta strain energy density factor (ΔS) computer control program, and implementation of the crack closure measurement system. Unfortunately, errors in the control program caused premature specimen fracture, ruining the a-PD data.

Test Number 9A (S16A-43): The purpose of this test was to determine the effect of f on the notch PD, for different values of ΔP. It was a DSSRT test with ΔP values of 26.7, 17.8, and 4.4 kN, R=0.1, and $0.1 \leq f \leq 10$ Hz. The results showed that the effect of f decreases with decreasing ΔP levels (see Figure A.11).

Test Number 9 (S16A-43): Problems with the computer control program and the electrochemical potential control resulted in faulty a-PD data. Fortunately, the crack closure system was able to prove itself by generating closure data over the range of crack growth. Closure were present during the test, providing important data for comparison with later tests (see Chapter 5). The addition of a peristaltic pump resulted in better regulation of DSS flow rate.

Test Number 9B (S16A-43): The purpose of this test was to determine the effect of f on the PD. It was a DSSRT test with ΔP=2.2 kN, R=0.1, a=19.1 mm, ΔK=28.6 MPa$\sqrt{m}$, and $0.1 \leq f \leq 10$ Hz. The results showed large changes in PD with f, 1500 nV/decade (see Figure A.12). The effect was not linear and might be due to crack growth occurring during the test.

Test Number 10 (S16A-51): This was a DSSRT test with ΔK=33.0 & 27.5 MPa$\sqrt{m}$, R=0.1, f=5 Hz. High ΔK levels were chosen to determine the effect of ΔK on the a-PD relationship. Unfortunately, the crack front was not visibly marked.

Test Number 11A (S16A-50): Changes in load ratio, from 0.1 to 0.25, and Lock-in-Amplifier settings, (reference frequency: from 93 to 377Hz, and low-pass filter: from 30 to 300Hz), were made at this point.

This was a two part test to determine the effects of f and P on the notch PD. It was a RTLA test with $\Delta P=17.8$ kN, $R=0.25$, and $0.1\leq f\leq 10$ Hz for the first part, and $0.0\leq P\leq 35.6$ kN for the second. The results of the first part, though non-linear in nature, resulted in an estimated effect of 114 nV/decade (see Figure A.13); the second test's effect was 15.8 nV/kN (see Figure A.14).

Test Number 11 (S16A-50): This was a DSSRT test with $\Delta K=27.5$ & 22.0 MPa$\sqrt{m}$, $R=0.25$, and $f=5$ Hz. As a result of the changes made in the LIA settings, the PD values increased from their previous values. This was probably due to the decrease in skin depth and increase in induced voltage. The test ran smoothly giving valid a-PD data for use in the a-PD relationship.

Test Number 11B (S16A-50): The purpose of this test was to determine the effect of f on the PD. It was a DSSRT test with $\Delta P=2.0$ kN, $R=0.25$, $a=15.0$ mm, $\Delta K=12.4$ MPa$\sqrt{m}$, and $0.1\leq f\leq 4$ Hz. The results show a large change in PD with f, -2.0 μV/decade (see Figure A.15). This was probably due to large crack face contact, which could be expected because of the decrease in ΔK level, compared with test 11. A recording of the PD and P signal waveforms was obtained for $f=0.1$ Hz, and is shown in Figure A.16. Note the symettric, though non-sinusoidal, PD waveform and its position relative to the P waveform. A similiar recording for test 12B was obtained which provides an interesting contrast (see below).

Test Number 12 (S16A-66): This was a DSSRT test with $\Delta K=13.2$ & 7.7 MPa$\sqrt{m}$, $R=0.25$, and $f=5$ Hz. A most significant change in LIA setting was affected when the DC output filter was changed from a single to a double filter (i.e.-from 6.0 to 12.0 dB/octave). All of the changes in PD, with changes in the loading parameters, were greatly diminished, as shown in test 12B. The calibration data obtained from this test and test 11 (corrected for the change in DC output filter setting) were used to obtain the a-PD relationship.

Test Number 12B (S16A-66): The purpose of this test was to determine the effect of f on the PD. It was a DSSRT test with $\Delta P=1.6$ kN, $R=0.25$, $a=16.2$ mm, $\Delta K=10.6$ MPa$\sqrt{m}$, and $0.1 \leq f \leq 10$ Hz. The effect of f was greatly diminished, as shown in Figure A.17, and equal to ∓ 285 nV/decade, on each side of 1.4 Hz. A recording of P and PD for f=0.1 Hz was obtained, for the two different DC filter settings, showing the dramatic effect of the DC output filter setting (see Figures A.18 and A.19). Note the unusual PD waveform and the relation of P to PD. This is probably due to crack face contact with changing P level.

Test 12B marks the end of the calibration testing phase of the experimental program and the start of the "short" crack growth rate testing phase (tests 13-20).

APPENDIX A - TABLES AND FIGURES

TABLE A-1: TEST NUMBER 21

Specimen Serial Number : S16A-62
Solution Environment: De-aerated 3.5 % NaCl Solution

f (Hz) = 1.0
T (K) = 277.4
ΔK (MPa$\sqrt{m}$) = 30.33
R = 0.250
Φ_{ec} (mV SCE) = -797.2
VAR(da/dN) x 10^6 (μm/cyc)^2 = 1.6339
a @ $(da/dN)_{max}$ (mm) = 6.40
$(da/dN)_{max}$ (μm/cyc) = 0.3107
$(da/dN)_{max}/(da/dN)_{LC}$ = 1.091

Short Crack Data: {0.72≦ a ≦10.12} (mm)

	Spline Coefficients and Breakpoints					
	N_s (kcyc)	α_0	$\alpha_1 x 10^1$	$\alpha_2 x 10^3$	$\alpha_3 x 10^4$	N_f (kcyc)
1.	15.156	10.318	9.3632	80.894	-82.654	22.546
2.	22.546	18.891	13.084	19.814	44.955	28.623
3.	28.623	27.376	15.119	47.133	-38.069	48.405

Long Crack Data: {9.18≦ a ≦18.16} (mm)

Test Order	f (Hz)	$(da/dN)_e$ (μm/cyc)	VAR x 10^6 (μm/cyc)^2	$(da/dN)_{cf}$ (μm/cyc)	VAR x 10^6 (μm/cyc)^2	ΔK (MPa$\sqrt{m}$)	R	T (K)	Φ_{ec} (mV)	No. Obs.
1.	1.0	0.2848	1.7192	0.07191	3.7198	30.35	0.250	277.2	-796.6	33
2.	5.0	0.2403	1.2650	0.02601	3.2656	30.41	0.250	277.2	-796.6	26
3.	10.0	0.2465	1.3673	0.03244	3.3679	30.40	0.251	277.2	-796.6	17
4.	2.5	0.3081	2.1599	0.09216	4.1605	30.48	0.250	277.2	-796.6	25
5.	0.5	0.3411	2.5527	0.1235	4.5533	30.55	0.251	277.2	-796.6	22
6.	0.1	0.5346	6.3153	0.3054	8.3159	31.03	0.248	277.7	-796.6	20
7.	0.05	0.7183	11.306	0.4719	13.307	31.71	0.244	277.6	-796.6	17
8.	0.25	0.3985	2.9793	0.1752	4.9799	30.79	0.251	277.5	-796.6	28
9.	1.0	0.3178	2.8543	0.09081	4.8549	30.94	0.251	277.4	-796.6	35
AVERAGE VALUES:			2.8094			30.72	0.250	277.4	-796.6	190

TABLE A-2: TEST NUMBER 22

Specimen Serial Number : S16A-41
Solution Environment: De-aerated 3.5 % NaCl Solution

f (Hz) = 1.0
T (K) = 277.6
ΔK (MPa$\sqrt{m}$) = 21.08
R = 0.250
Φ_{ec} (mV SCE) = -796.9
VAR(da/dN) x 10^6 (μm/cyc)^2 = 0.56224
a @ $(da/dN)_{max}$ (mm) = 4.48
$(da/dN)_{max}$ (μm/cyc) = 0.1105
$(da/dN)_{max}/(da/dN)_{LC}$ = 1.007

Short Crack Data: {0.29≦ a ≦10.08} (mm)

		Spline Coefficients and Breakpoints				
	N_s (kcyc)	α_0	$\alpha_1 x 10^2$	$\alpha_2 x 10^4$	$\alpha_3 x 10^6$	N_f (kcyc)
1.	19.801	9.9430	47.164	38.331	-42.318	67.745
2.	67.745	36.183	60.678	18.042	43.708	106.483

Long Crack Data: {9.08≦ a ≦17.12} (mm)

Test Order	f (Hz)	$(da/dN)_e$ (μm/cyc)	VAR x 10^6 (μm/cyc)^2	$(da/dN)_{cf}$ (μm/cyc)	VAR x 10^6 (μm/cyc)^2	ΔK (MPa$\sqrt{m}$)	R	T (K)	Φ_{ec} (mV)	No. Obs.
1.	1.0	0.1097	4.1217	0.04576	93.982	21.15	0.250	277.5	-796.3	75
2.	5.0	0.09397	6.3047	0.02983	96.165	21.17	0.250	277.4	-796.3	36
3.	10.0	0.08383	12.423	0.01939	102.28	21.20	0.250	277.3	-796.3	40
4.	2.5	0.09581	34.058	0.03106	123.92	21.23	0.250	277.3	-796.3	43
5.	0.5	0.1352	89.420	0.07015	179.28	21.26	0.250	277.2	-796.3	44
6.	0.1	0.2512	392.23	0.1857	482.09	21.30	0.250	277.7	-796.3	27
7.	0.05	0.2649	486.14	0.2183	576.00	19.23	0.271	277.6	-796.3	12
8.	0.25	0.1947	298.28	0.1282	388.14	21.40	0.250	277.4	-796.3	51
9.	1.0	0.1526	270.91	0.08507	360.77	21.50	0.251	277.5	-796.3	4
AVERAGE VALUES:			85.534			21.24	0.250	277.4	-796.3	257

TABLE A-3: TEST NUMBER 23

Specimen Serial Number : S16A-40
Solution Environment: De-aerated 3.5 % NaCl Solution

f (Hz) = 1.0
T (K) = 277.8
ΔK (MPa$\sqrt{m}$) = 14.33
R = 0.250
Φ_{ec} (mV SCE) = -796.6
VAR(da/dN) x 10^6 (μm/cyc)^2 = 14.294
a @ $(da/dN)_{max}$ (mm) = 5.78
$(da/dN)_{max}$ (μm/cyc) = 0.05307
$(da/dN)_{max}/(da/dN)_{LC}$ = 1.231

Short Crack Data: {0.26≤ a ≤9.90} (mm)

Spline Coefficients and Breakpoints

	N_s (kcyc)	α_0	$\alpha_1 x 10^2$	$\alpha_2 x 10^4$	$\alpha_3 x 10^5$	N_f (kcyc)
1.	23.934	8.5814	14.745	99.758	-70.707	38.000
2	38.000	11.314	21.782	0.30309	3.2313	76.189
3.	76.189	19.995	24.254	12.643	-13.855	218.084

Long Crack Data: {8.91≤ a ≤17.75} (mm)

Test Order	f (Hz)	$(da/dN)_e$ (μm/cyc)	VAR x 10^6 (μm/cyc)^2	$(da/dN)_{cf}$ (μm/cyc)	VAR x 10^6 (μm/cyc)^2	ΔK (MPa$\sqrt{m}$)	R	T (K)	Φ_{ec} (mV)	No. Obs.
1.	1.0	0.04310	47.264	0.02565	55.394	14.32	0.251	278.6	-796.3	66
2.	5.0	0.02609	19.802	0.008685	27.932	14.31	0.250	278.0	-796.3	44
3.	10.0	0.02431	21.510	0.006986	29.640	14.29	0.250	278.1	-796.3	50
4.	2.5	0.03576	50.844	0.01856	58.974	14.26	0.251	277.6	-796.3	53
5.	0.5	0.06009	147.36	0.04301	155.49	14.23	0.251	277.5	-796.3	68
6.	0.1	0.08257	280.71	0.06561	288.84	14.20	0.251	277.5	-796.3	11
7.	5.0	0.03051	38.925	0.01359	47.055	14.19	0.251	277.4	-796.3	41
8.	10.0	0.02203	20.476	0.005265	28.606	14.15	0.250	277.3	-796.3	60
9.	2.5	0.03487	51.417	0.01834	59.547	14.09	0.250	277.2	-796.3	67
10.	1.0	0.04746	94.865	0.03132	102.99	13.99	0.252	277.1	-796.3	59
AVERAGE VALUES:			50.993			14.20	0.251	277.4	-796.3	453

TABLE A-4: TEST NUMBER 24

Specimen Serial Number : S16A-28
Solution Environment: De-aerated 3.5 % NaCl Solution

f (Hz) = 10.0
T (K) = 297.8
ΔK (MPa$\sqrt{m}$) = 21.04
R = 0.250
Φ_{ec} (mV SCE) = -796.6
VAR(da/dN) x 10^6 (μm/cyc)^2 = 0.21647
a @ $(da/dN)_{max}$ (mm) = 2.55
$(da/dN)_{max}$ (μm/cyc) = 0.1093
$(da/dN)_{max}/(da/dN)_{LC}$ = 1.239

Short Crack Data: {0.72≤ a ≤9.98} (mm)

	Spline Coefficients and Breakpoints					
	N_s (kcyc)	α_0	$\alpha_1 x 10^2$	$\alpha_2 x 10^3$	$\alpha_3 x 10^4$	N_f (kcyc)
1.	16.336	10.294	36.584	23.737	-18.369	27.051
2.	27.051	15.200	51.474	4.0555	-2.7665	56.139
3.	56.139	30.754	51.567	-3.9916	14.226	59.298
4.	59.298	32.371	51.016	0.5030	0.1977	112.746

Long Crack Data: {9.01≤ a ≤17.93} (mm)

Test Order	f (Hz)	$(da/dN)_e$ (μm/cyc)	VAR x 10^6 (μm/cyc)^2	$(da/dN)_{cf}$ (μm/cyc)	VAR x 10^6 (μm/cyc)^2	ΔK (MPa$\sqrt{m}$)	R	T (K)	Φ_{ec} (mV)	No. Obs.
1.	10.0	0.08820	4.3767	0.02804	74.685	20.97	0.250	297.8	-796.0	83
2.	2.5	0.1135	17.563	0.05363	87.871	20.94	0.250	297.7	-796.0	51
3.	0.1	0.2312	102.88	0.1713	173.19	20.94	0.250	297.6	-796.0	34
4.	0.05	0.2579	150.94	0.1976	221.25	20.98	0.249	297.7	-796.0	9
5.	0.25	0.2344	161.28	0.1749	231.59	20.90	0.250	298.0	-796.0	32
6.	0.5	0.2045	159.52	0.1451	229.83	20.89	0.250	297.9	-796.0	38
7.	1.0	0.1676	132.20	0.1086	202.51	20.85	0.250	297.8	-796.0	60
8.	5.0	0.1011	67.633	0.04226	137.94	20.83	0.250	297.7	-796.0	37
9.	10.0	0.08661	66.356	0.02833	136.66	20.77	0.250	297.7	-796.0	48
10.	2.5	0.1177	150.35	0.05970	220.66	20.74	0.250	297.7	-796.0	41
AVERAGE VALUES:			122.70			20.87	0.250	297.7	-796.0	350

TABLE A-5: TEST NUMBER 25

Specimen Serial Number : S16A-44
Solution Environment: De-aerated 3.5 % NaCl Solution

f (Hz) = 10.0
T (K) = 298.1
ΔK (MPa$\sqrt{m}$) = 30.38
R = 0.250
Φ_{ec} (mV SCE) = -796.6
VAR(da/dN) x 10^6 (μm/cyc)^2 = 1.2742
a @ $(da/dN)_{max}$ (mm) = 4.98
$(da/dN)_{max}$ (μm/cyc) = 0.2789
$(da/dN)_{max}/(da/dN)_{LC}$ = 1.121

Short Crack Data: {0.72≤ a ≤10.17} (mm)

Spline Coefficients and Breakpoints

	N_s (kcyc)	α_0	$\alpha_1 x 10^1$	$\alpha_2 x 10^3$	$\alpha_3 x 10^4$	N_f (kcyc)
1.	13.856	10.309	8.0540	61.368	-25.002	30.291
2.	30.291	29.985	14.763	20.276	-51.011	37.585
3.	37.585	40.962	14.885	-16.931	47.848	51.240

Long Crack Data: {8.01≤ a ≤16.77} (mm)

Test Order	f (Hz)	$(da/dN)_e$ (μm/cyc)	VAR x 10^6 (μm/cyc)^2	$(da/dN)_{cf}$ (μm/cyc)	VAR x 10^6 (μm/cyc)^2	ΔK (MPa$\sqrt{m}$)	R	T (K)	Φ_{ec} (mV)	No. Obs.
1.	10.0	0.2489	1.2930	0.04192	1.8407	30.48	0.250	298.0	-796.3	115
2.	0.05	0.7726	13.122	0.5611	13.670	30.68	0.250	298.0	-796.3	13
3.	2.5	0.2944	1.9647	0.08448	2.5124	30.61	0.250	298.0	-796.3	41
4.	0.1	0.7692	14.248	0.5563	14.796	30.74	0.250	298.0	-796.3	29
5.	1.0	0.3697	3.1202	0.1552	3.6679	30.31	0.250	298.0	-796.3	55
6.	0.25	0.6191	8.2581	0.4011	8.8058	30.96	0.250	297.9	-796.3	25
7.	5.0	0.3067	2.0194	0.08547	2.5671	31.10	0.250	297.9	-796.3	41
8.	0.5	0.5143	5.2547	0.2859	5.8024	31.40	0.249	297.9	-796.3	53
AVERAGE VALUES:			3.1285			30.85	0.250	297.9	-796.3	257

TABLE A-6: TEST NUMBER 26

Specimen Serial Number : S16A-31
Solution Environment: De-aerated 3.5 % NaCl Solution

f (Hz) = 10.0
T (K) = 297.9
ΔK (MPa$\sqrt{m}$) = 14.40
R = 0.250
Φ_{ec} (mV SCE) = -796.6
VAR(da/dN) x 10^6 (μm/cyc)^2 = 7.5972
a @ $(da/dN)_{max}$ (mm) = 2.00
$(da/dN)_{max}$ (μm/cyc) = 0.03440
$(da/dN)_{max}/(da/dN)_{LC}$ = 1.282

Short Crack Data: {.42≤ a ≤9.85} (mm)

Spline Coefficients and Breakpoints

	N_s (kcyc)	α_0	$\alpha_1 x 10^2$	$\alpha_2 x 10^4$	$\alpha_3 x 10^6$	N_f (kcyc)
1.	14.198	8.8849	12.021	16.128	-28.156	70.278
2.	70.278	17.335	16.639	0.3387	-0.5759	263.112
3.	263.112	49.362	16.221	-0.7719	9.4699	327.661

Long Crack Data: {8.50≤ a ≤17.72} (mm)

Test Order	f (Hz)	$(da/dN)_e$ (μm/cyc)	VAR x 10^6 (μm/cyc)^2	$(da/dN)_{cf}$ (μm/cyc)	VAR x 10^6 (μm/cyc)^2	ΔK (MPa$\sqrt{m}$)	R	T (K)	Φ_{ec} (mV)	No. Obs.
1.	10.0	0.02684	27.823	0.009861	36.941	14.30	0.250	297.9	-796.0	121
2.	2.5	0.04750	92.897	0.03068	102.02	14.26	0.250	297.9	-796.0	77
3.	0.5	0.06737	189.21	0.05066	198.33	14.23	0.250	298.0	-796.0	57
4.	0.1	0.07616	242.74	0.05953	251.86	14.21	0.250	297.9	-796.0	8
5.	1.0	0.06191	160.91	0.04540	170.03	14.18	0.250	297.9	-796.0	54
6.	5.0	0.03816	61.419	0.02180	70.534	14.14	0.250	297.9	-796.0	75
7.	0.25	0.07410	231.97	0.05793	241.09	14.09	0.250	298.1	-796.0	54
8.	1.0	0.06407	173.50	0.04820	182.62	14.01	0.250	297.9	-796.0	54
9.	5.0	0.03898	64.032	0.02352	73.150	13.90	0.251	298.3	-796.0	56
10.	10.0	0.03109	40.555	0.01592	49.673	13.82	0.250	298.4	-796.0	68
AVERAGE VALUES:			93.171			14.13	0.250	297.9	-796.0	503

TABLE A-7: TEST NUMBER 27

Specimen Serial Number : S16A-54
Solution Environment: De-aerated 3.5 % NaCl Solution

f (Hz) = 1.0
T (K) = 320.4
ΔK (MPa$\sqrt{m}$) = 30.22
R = 0.250
Φ_{ec} (mV SCE) = -796.6
VAR(da/dN) x 10^6 (μm/cyc)^2 = 18.358
a @ $(da/dN)_{max}$ (mm) = 5.45
$(da/dN)_{max}$ (μm/cyc) = 0.5543
$(da/dN)_{max}/(da/dN)_{LC}$ = 0.990

Short Crack Data: {0.70≦ a ≦10.04} (mm)

	Spline Coefficients and Breakpoints					
	N_s (kcyc)	α_0	$\alpha_1 x 10^1$	$\alpha_2 x 10^2$	$\alpha_3 x 10^3$	N_f (kcyc)
1.	10.014	10.223	21.606	9.7424	5.2188	15.278
2.	15.278	23.073	27.457	12.489	-59.389	16.229
3.	16.229	25.731	28.376	68.422	-2.5639	27.436

Long Crack Data: {9.01≦ a ≦18.01} (mm)

Test Order	f (Hz)	$(da/dN)_e$ (μm/cyc)	VAR x 10^6 (μm/cyc)^2	$(da/dN)_{cf}$ (μm/cyc)	VAR x 10^6 (μm/cyc)^2	ΔK (MPa$\sqrt{m}$)	R	T (K)	Φ_{ec} (mV)	No. Obs.
1.	1.0	0.5600	9.2600	0.3468	17.980	30.17	0.250	320.3	-796.3	40
2.	0.25	0.7182	9.5172	0.5052	18.237	30.16	0.250	321.5	-796.3	25
3.	0.05	0.8563	23.256	0.6393	31.976	30.33	0.249	321.0	-796.3	12
4.	0.5	0.6993	6.1535	0.4858	14.873	30.18	0.250	320.5	-796.3	17
5.	0.1	0.7888	17.946	0.5753	26.666	30.18	0.250	320.6	-796.3	31
6.	2.5	0.4100	3.4582	0.1968	12.178	30.17	0.250	320.5	-796.3	37
7.	10.0	0.2746	0.79479	0.06139	9.5147	30.17	0.251	320.7	-796.3	29
8.	5.0	0.3369	1.9705	0.1220	10.690	30.24	0.250	321.2	-796.3	35
9.	1.0	0.5993	8.2204	0.3837	16.940	30.27	0.250	320.0	-796.3	20
10.	0.5	0.7023	44.597	0.4770	53.317	30.67	0.247	321.1	-796.3	6
AVERAGE VALUES:			6.0983			30.20	0.250	320.7	-796.3	212

TABLE A-8: TEST NUMBER 28

Specimen Serial Number : S16A-63
Solution Environment: De-aerated 3.5 % NaCl Solution

f (Hz) = 1.0
T (K) = 319.2
ΔK (MPa$\sqrt{m}$) = 21.03
R = 0.250
Φ_{ec} (mV SCE) = -796.6
VAR(da/dN) x 10^6 (μm/cyc)^2 = 1.1155
a @ $(da/dN)_{max}$ (mm) = 3.89
$(da/dN)_{max}$ (μm/cyc) = 0.2277
$(da/dN)_{max}/(da/dN)_{LC}$ = 1.023

Short Crack Data: {0.71≦ a ≦9.97} (mm)

	Spline Coefficients and Breakpoints					
	N_s (kcyc)	α_0	$\alpha_1 x 10^1$	$\alpha_2 x 10^3$	$\alpha_3 x 10^4$	N_f (kcyc)
1.	12.134	10.277	10.593	-10.303	41.565	18.230
2.	18.230	16.700	10.738	15.037	-6.7951	28.329
3.	28.329	28.194	11.910	8.1752	1.1464	53.287

Long Crack Data: {9.00≦ a ≦17.86} (mm)

Test Order	f (Hz)	$(da/dN)_e$ (μm/cyc)	VAR x 10^6 (μm/cyc)^2	$(da/dN)_{cf}$ (μm/cyc)	VAR x 10^6 (μm/cyc)^2	ΔK (MPa$\sqrt{m}$)	R	T (K)	Φ_{ec} (mV)	No. Obs.
1.	1.0	0.2227	1.2715	0.1602	85.752	20.95	0.250	319.3	-796.3	58
2.	0.25	0.2609	1.5908	0.1988	86.071	20.91	0.250	318.9	-796.3	49
3.	0.05	0.3694	4.4459	0.3065	88.926	20.99	0.249	319.4	-796.3	21
4.	0.5	0.2532	1.5063	0.1916	85.986	20.86	0.250	319.8	-796.3	47
5.	0.1	0.3185	2.3757	0.2572	86.856	20.83	0.250	320.2	-796.3	30
6.	2.5	0.1837	0.60034	0.1227	85.080	20.80	0.250	319.7	-796.3	56
7.	10.0	0.1089	0.19457	0.04867	84.675	20.72	0.250	320.1	-796.3	39
8.	5.0	0.1438	0.70080	0.08405	85.181	20.67	0.250	320.5	-796.3	37
9.	1.0	0.2274	4.7437	0.1685	89.224	20.58	0.250	319.8	-796.3	35
10.	0.5	0.2484	7.6721	0.1900	92.152	20.53	0.250	319.8	-796.3	21
AVERAGE VALUES:			1.5209			20.81	0.250	319.8	-796.3	335

TABLE A-9: TEST NUMBER 29

Specimen Serial Number : S16A-65
Solution Environment: De-aerated 3.5 % NaCl Solution

f (Hz) = 1.0
T (K) = 320.3
ΔK (MPa$\sqrt{m}$) = 14.38
R = 0.250
Φ_{ec} (mV SCE) = -796.9
VAR(da/dN) x 10^6 (μm/cyc)^2 = 0.26158
a @ $(da/dN)_{max}$ (mm) = 4.98
$(da/dN)_{max}$ (μm/cyc) = 0.07502
$(da/dN)_{max}/(da/dN)_{LC}$ = 1.020

Short Crack Data: {0.37≤ a ≤9.89} (mm)

Spline Coefficients and Breakpoints

	N_s (kcyc)	α_0	$\alpha_1 x 10^2$	$\alpha_2 x 10^3$	$\alpha_3 x 10^5$	N_f (kcyc)
1.	9.997	8.7162	21.672	24.963	-416.82	15.247
2.	15.247	10.098	29.034	3.0783	-4.3124	59.891
3.	59.891	25.487	38.479	1.1531	-0.3641	132.323
4.	132.323	56.153	45.876	0.8894	46.027	141.085

Long Crack Data: {9.01≤ a ≤17.80} (mm)

Test Order	f (Hz)	$(da/dN)_e$ (μm/cyc)	VAR x 10^6 (μm/cyc)^2	$(da/dN)_{cf}$ (μm/cyc)	VAR x 10^6 (μm/cyc)^2	ΔK (MPa$\sqrt{m}$)	R	T (K)	Φ_{ec} (mV)	No. Obs.
1.	1.0	0.07352	17.653	0.05610	24.897	14.33	0.250	320.3	-796.0	65
2.	0.1	0.09249	43.056	0.07511	50.300	14.32	0.250	320.3	-796.0	27
3.	0.5	0.08327	51.289	0.06597	58.533	14.30	0.250	320.0	-796.0	45
4.	2.5	0.06876	46.974	0.05154	54.218	14.28	0.250	319.8	-796.0	40
5.	10.0	0.04526	31.159	0.02824	38.403	14.23	0.251	319.8	-796.0	53
6.	5.0	0.06007	77.632	0.04309	84.876	14.22	0.250	319.9	-796.0	43
7.	0.25	0.09316	219.04	0.07642	226.28	14.16	0.250	321.0	-796.0	54
8.	1.0	0.07787	168.64	0.06137	175.88	14.10	0.250	320.8	-796.0	64
9.	0.5	0.07946	193.29	0.06323	200.53	14.03	0.251	320.0	-796.0	55
10.	5.0	0.05702	105.71	0.04076	112.95	14.04	0.253	319.8	-796.0	26
AVERAGE VALUES:			82.115			14.20	0.251	320.0	-796.0	407

TABLE A-10: TEST NUMBER 30

Specimen Serial Number : S16A-48 _____ _____
Solution Environment: De-aerated 3.5 % NaCl Solution

f (Hz) = 10.0
T (K) = 344.8
ΔK (MPa$\sqrt{m}$) = 20.95
R = 0.250
Φ_{ec} (mV SCE) = -796.9
VAR(da/dN) x 10^6 $(\mu m/cyc)^2$ = 3.3752
a @ $(da/dN)_{max}$ (mm) = 2.73
$(da/dN)_{max}$ (μm/cyc) = 0.1574
$(da/dN)_{max}/(da/dN)_{LC}$ = 1.092

Short Crack Data: {0.77≦ a ≦9.91} (mm)

	Spline Coefficients and Breakpoints					
	N_s (kcyc)	α_0	$\alpha_1 x 10^2$	$\alpha_2 x 10^4$	$\alpha_3 x 10^5$	N_f (kcyc)
1.	9.468	10.540	71.456	57.508	-11.396	52.271
2.	52.271	44.904	85.632	8.7274	24.567	69.961

Long Crack Data: {9.11≦ a ≦17.73} (mm)

Test Order	f (Hz)	$(da/dN)_e$ (μm/cyc)	VAR x 10^6 $(\mu m/cyc)^2$	$(da/dN)_{cf}$ (μm/cyc)	VAR x 10^6 $(\mu m/cyc)^2$	ΔK (MPa$\sqrt{m}$)	R	T (K)	Φ_{ec} (mV)	No. Obs.
1.	10.0	0.1441	3.3244	0.08696	69.086	20.81	0.250	344.1	-796.3	51
2.	1.0	0.2301	1.2913	0.1732	67.053	20.79	0.250	344.8	-796.3	29
3.	0.05	0.4082	17.392	0.3510	83.154	20.82	0.249	343.8	-796.3	11
4.	0.25	0.3141	1.9742	0.2578	67.736	20.72	0.250	344.3	-796.3	29
5.	0.1	0.3638	13.168	0.3081	78.930	20.66	0.250	344.1	-796.3	39
6.	0.5	0.2820	11.235	0.2269	76.997	20.59	0.250	344.3	-796.3	31
7.	5.0	0.1993	3.6618	0.1452	69.424	20.49	0.251	344.4	-796.3	37
8.	2.5	0.2333	7.7344	0.1804	73.496	20.36	0.251	344.4	-796.3	37
9.	1.0	0.2424	13.762	0.1902	79.524	20.28	0.250	344.5	-796.3	39
10.	0.5	0.2381	17.790	0.1867	83.552	20.19	0.250	343.9	-796.3	17
AVERAGE VALUES:			10.907			20.56	0.250	344.3	-796.3	269

TABLE A-11: TEST NUMBER 31

Specimen Serial Number : S16A-38
Solution Environment: De-aerated 3.5 % NaCl Solution

f (Hz) = 10.0
T (K) = 345.1
ΔK (MPa$\sqrt{m}$) = 28.32
R = 0.250
Φ_{ec} (mV SCE) = -796.6
VAR(da/dN) x 10^6 $(\mu m/cyc)^2$ = 11.939
a @ $(da/dN)_{max}$ (mm) = 3.97
$(da/dN)_{max}$ (μm/cyc) = 0.3344
$(da/dN)_{max}/(da/dN)_{LC}$ = 1.047

Short Crack Data: {0.80≦ a ≦9.67} (mm)

	Spline Coefficients and Breakpoints					
	N_s (kcyc)	α_0	$\alpha_1 x 10^1$	$\alpha_2 x 10^1$	$\alpha_3 x 10^2$	N_f (kcyc)
1.	8.273	10.670	3.8634	33.681	-621.45	8.804
2.	8.804	11.195	12.987	0.6795	-0.4884	19.573
3.	19.573	28.104	17.472	0.1535	0.0072	36.006

Long Crack Data: {9.00≦ a ≦17.37} (mm)

Test Order	f (Hz)	$(da/dN)_e$ (μm/cyc)	VAR x 10^6 $(\mu m/cyc)^2$	$(da/dN)_{cf}$ (μm/cyc)	VAR x 10^6 $(\mu m/cyc)^2$	ΔK (MPa$\sqrt{m}$)	R	T (K)	Φ_{ec} (mV)	No. Obs.
1.	10.0	0.3192	9.6784	0.1606	28.031	27.85	0.251	345.5	-796.0	34
2.	1.0	0.5675	11.132	0.4102	29.485	27.78	0.250	345.2	-796.0	26
3.	0.05	0.8533	36.673	0.7451	55.026	24.97	0.270	344.7	-796.0	8
4.	0.25	0.6702	7.6980	0.5180	26.051	27.52	0.250	344.9	-796.0	21
5.	0.1	0.7382	23.206	0.5887	41.559	27.38	0.250	344.3	-796.0	25
6.	0.5	0.6154	9.2979	0.4699	27.651	27.17	0.250	344.9	-796.0	27
7.	5.0	0.3291	11.887	0.1903	30.240	26.81	0.250	345.0	-796.0	21
8.	2.5	0.4639	5.0093	0.3317	23.362	26.44	0.250	344.9	-796.0	28
9.	1.0	0.5354	37.739	0.4094	56.092	26.08	0.250	344.8	-796.0	18
10.	0.5	0.5108	119.16	0.3896	137.51	25.79	0.250	345.1	-796.0	11
AVERAGE VALUES:			11.179			27.10	0.250	344.9	-796.0	185

TABLE A-12: TEST NUMBER 32

Specimen Serial Number : S16A-49
Solution Environment: De-aerated 3.5 % NaCl Solution

f (Hz) = 10.0
T (K) = 345.0
ΔK (MPa$\sqrt{m}$) = 14.06
R = 0.250
Φ_{ec} (mV SCE) = -796.9
VAR(da/dN) x 10^6 (μm/cyc)^2 = 0.19344
a @ $(da/dN)_{max}$ (mm) = 3.40
$(da/dN)_{max}$ (μm/cyc) = 0.05551
$(da/dN)_{max}/(da/dN)_{LC}$ = 1.057

Short Crack Data: {1.33≤ a ≤9.55} (mm)

Spline Coefficients and Breakpoints

	N_s (kcyc)	α_0	$\alpha_1 x 10^2$	$\alpha_2 x 10^4$	$\alpha_3 x 10^6$	N_f (kcyc)
1.	9.875	13.181	19.350	37.652	-79.446	56.930
2.	56.930	25.075	28.272	0.2687	35.845	101.872
3.	101.872	38.350	32.013	16.378	-86.104	162.875

Long Crack Data: {7.00≤ a ≤17.29} (mm)

Test Order	f (Hz)	$(da/dN)_e$ (μm/cyc)	VAR x 10^6 (μm/cyc)^2	$(da/dN)_{cf}$ (μm/cyc)	VAR x 10^6 (μm/cyc)^2	ΔK (MPa$\sqrt{m}$)	R	T (K)	Φ_{ec} (mV)	No. Obs.
1.	10.0	0.05252	11.159	0.03838	14.665	13.97	0.250	345.3	-796.3	115
2.	1.0	0.06141	44.394	0.04780	47.900	13.82	0.251	346.6	-796.3	28
3.	0.1	0.1139	189.44	0.1004	192.95	13.78	0.250	345.3	-796.3	18
4.	2.5	0.06643	78.374	0.05323	81.880	13.70	0.250	346.1	-796.3	56
5.	0.25	0.08137	141.45	0.06850	144.96	13.60	0.250	345.8	-796.3	34
6.	5.0	0.06722	113.40	0.05478	116.91	13.47	0.251	345.4	-796.3	31
7.	0.5	0.06851	132.63	0.05655	136.14	13.32	0.251	345.9	-796.3	34
8.	2.5	0.06269	123.04	0.05128	126.55	13.14	0.251	345.8	-796.3	41
9.	10.0	0.04758	78.853	0.03712	82.359	12.82	0.252	345.8	-796.3	13
10.	1.0	0.05197	98.734	0.04179	102.24	12.72	0.250	345.8	-796.3	22
AVERAGE VALUES:			114.59			13.54	0.251	345.8	-796.3	277

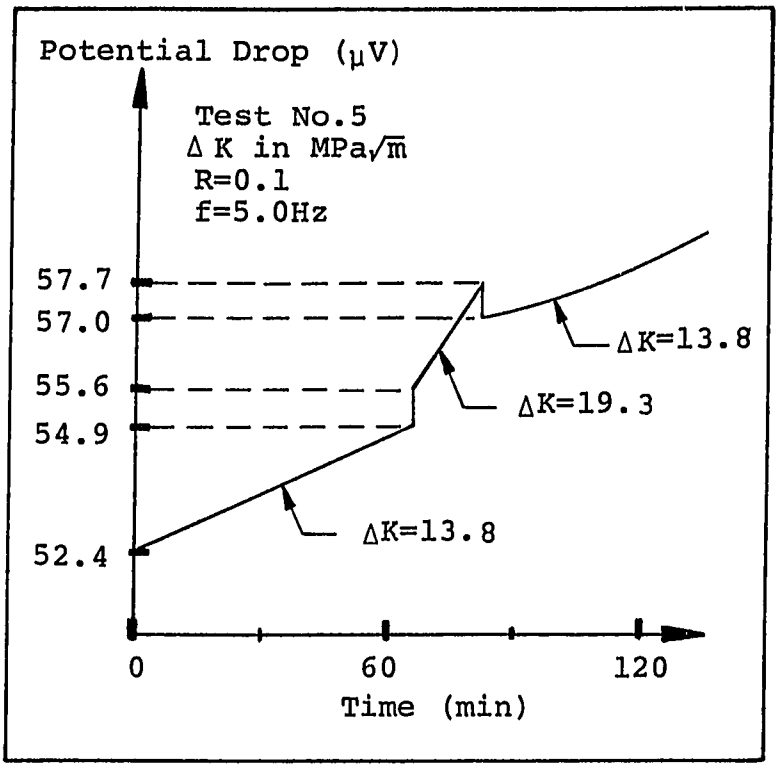

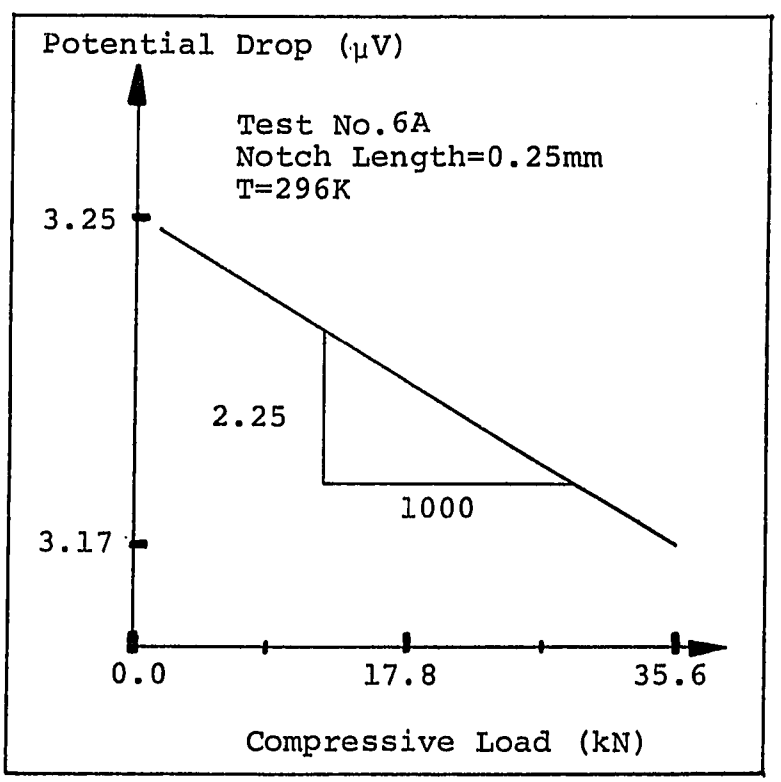

FIGURE A.1 (TOP) & FIGURE A.2 (BOTTOM)

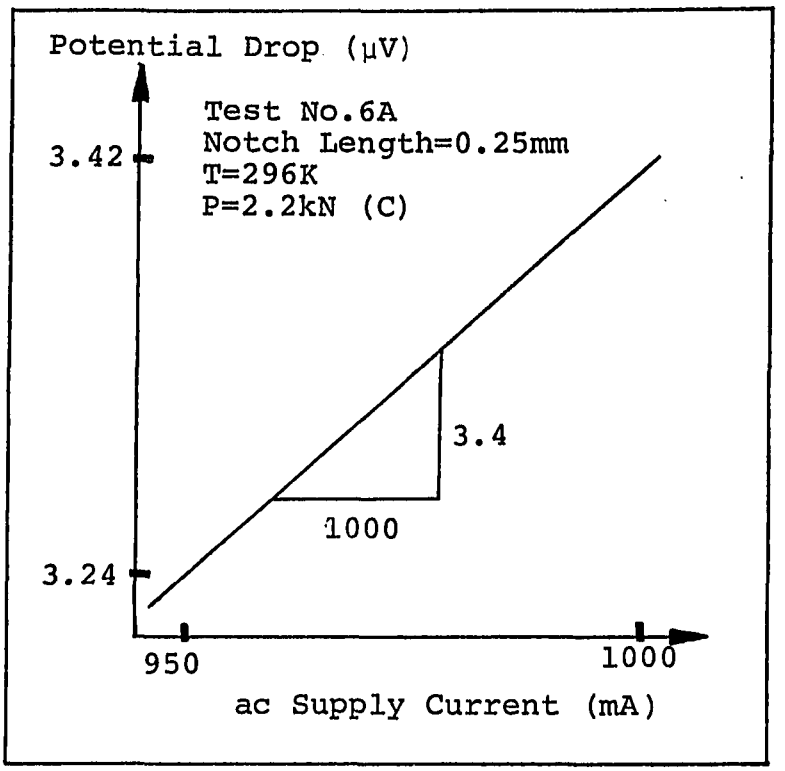

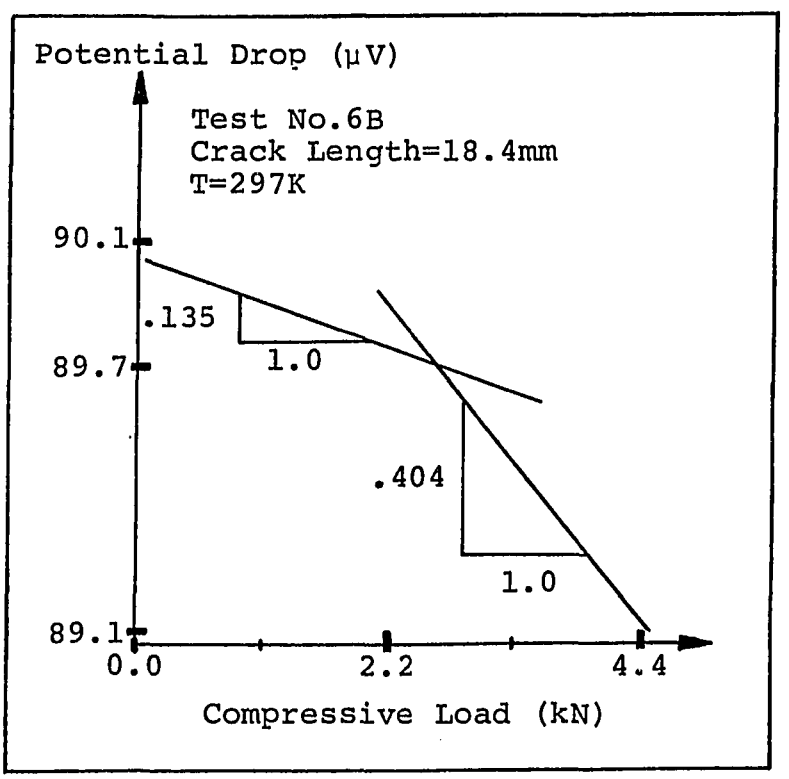

FIGURE A.3 (TOP) & FIGURE A.4 (BOTTOM)

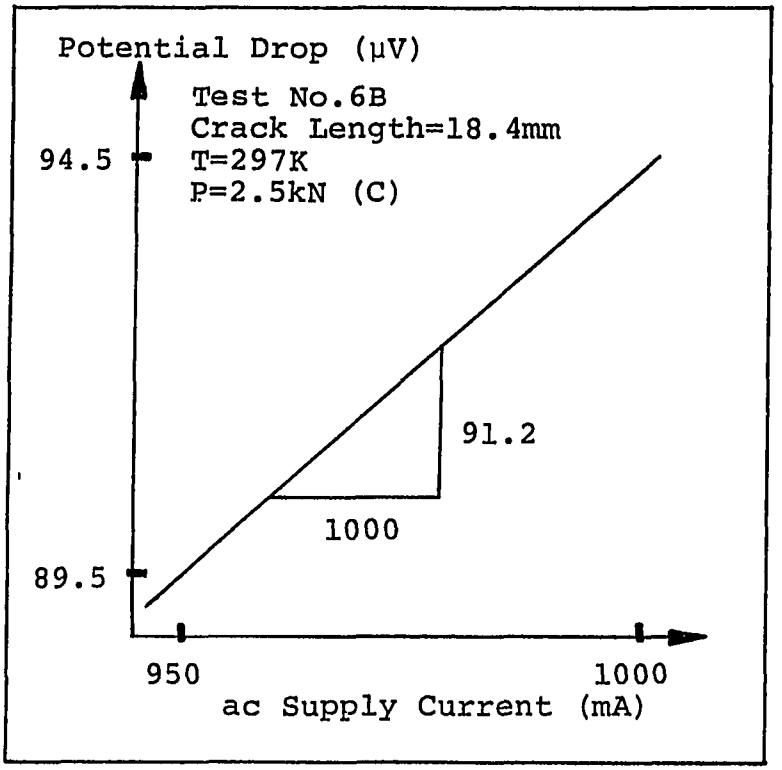

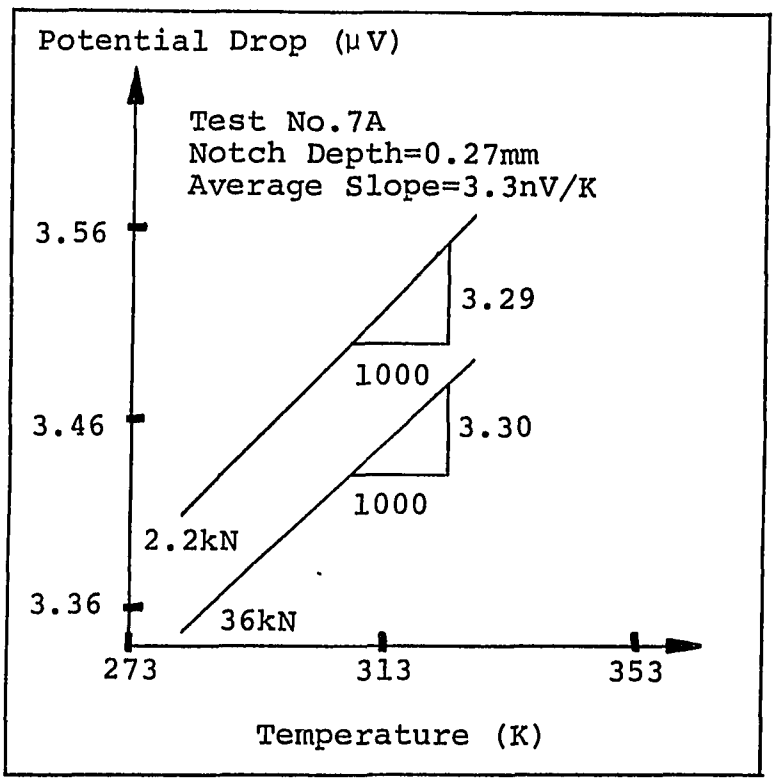

FIGURE A.5 (TOP) & FIGURE A.6 (BOTTOM)

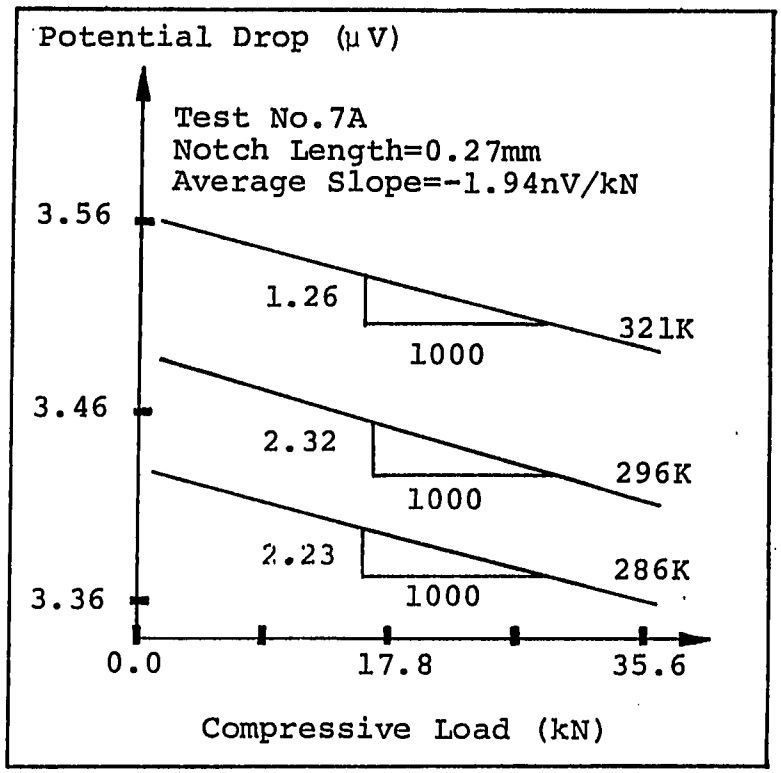

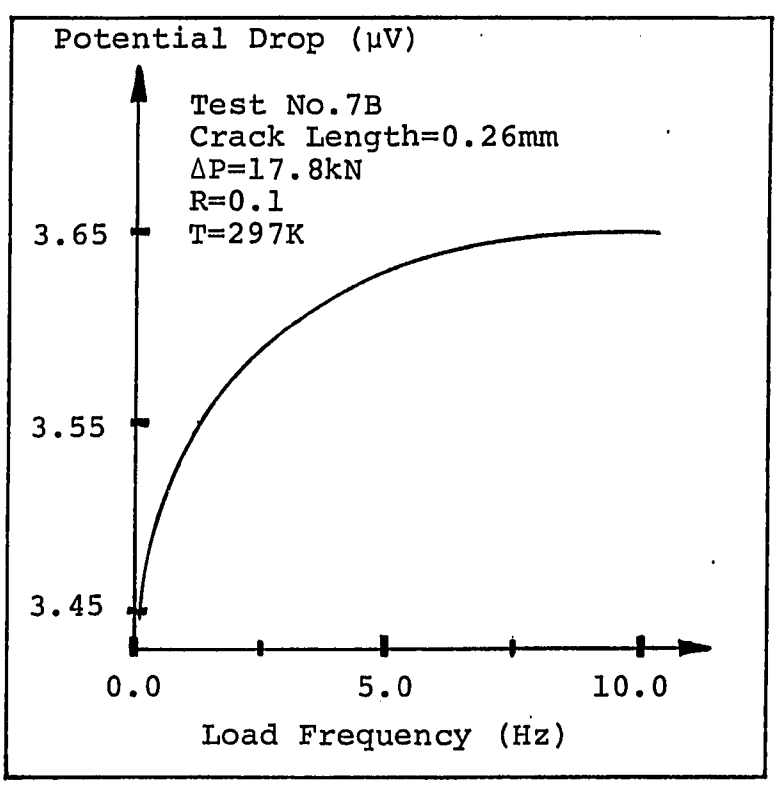

FIGURE A.7 (TOP) & FIGURE A.8 (BOTTOM)

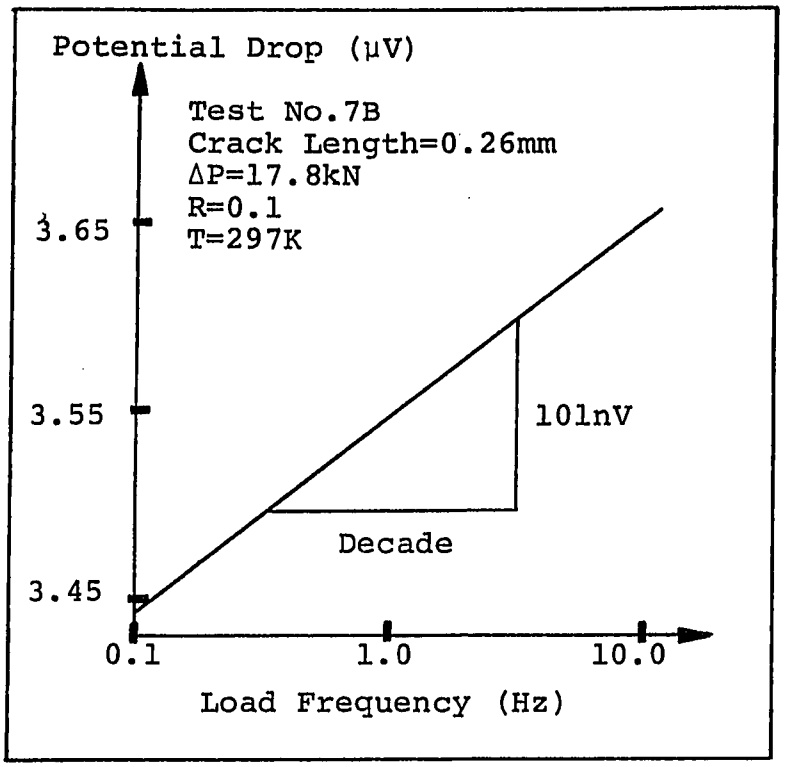

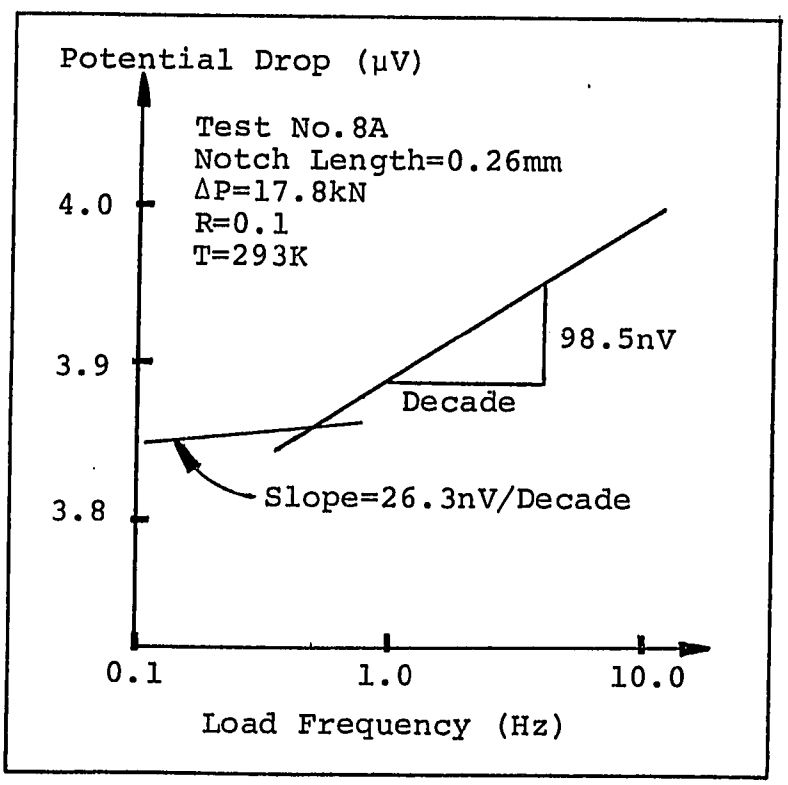

FIGURE A.9 (TOP) & FIGURE A.10 (BOTTOM)

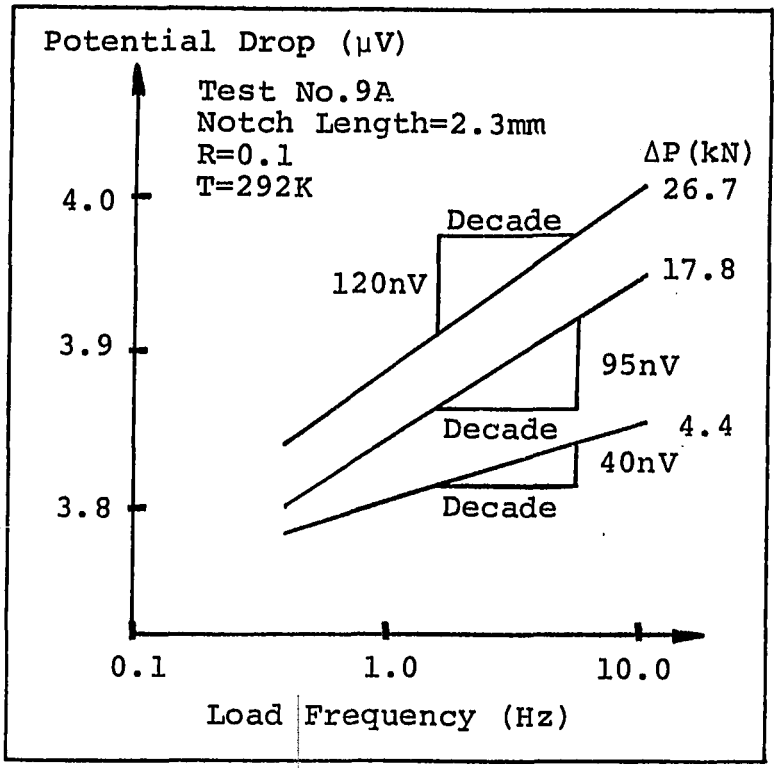

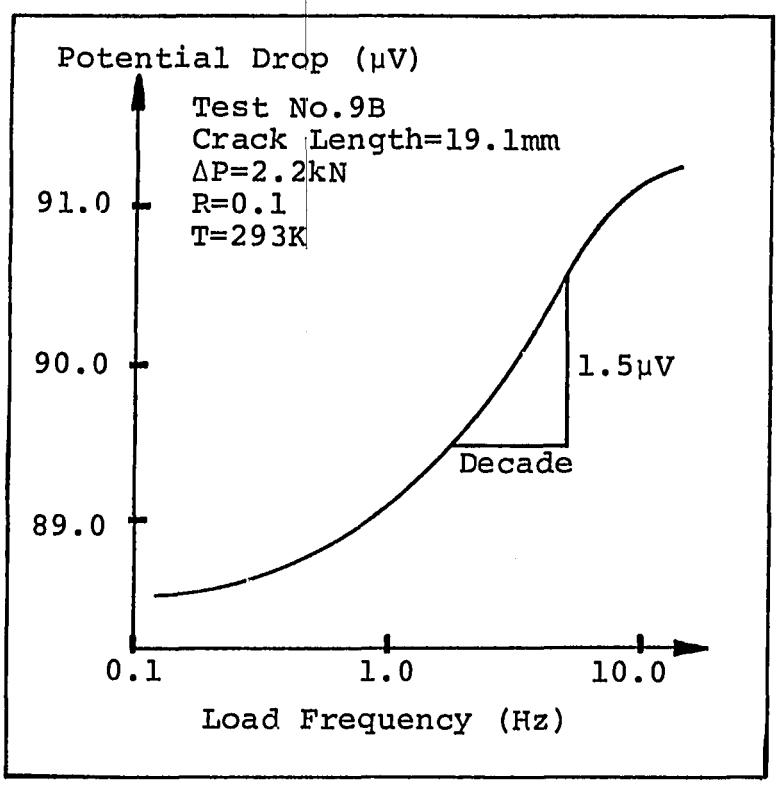

FIGURE A.11 (TOP) & FIGURE A.12 (BOTTOM)

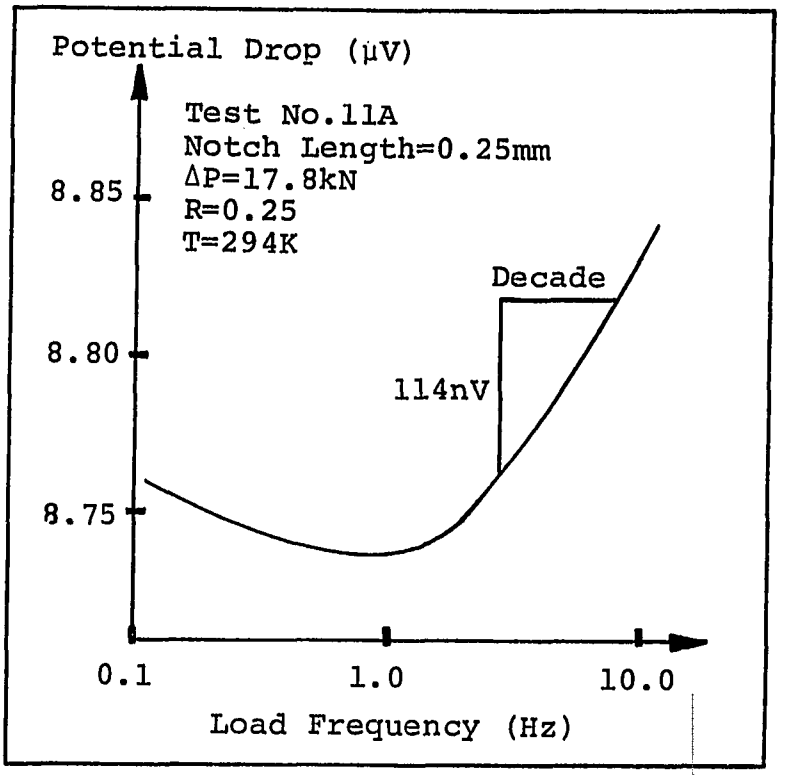

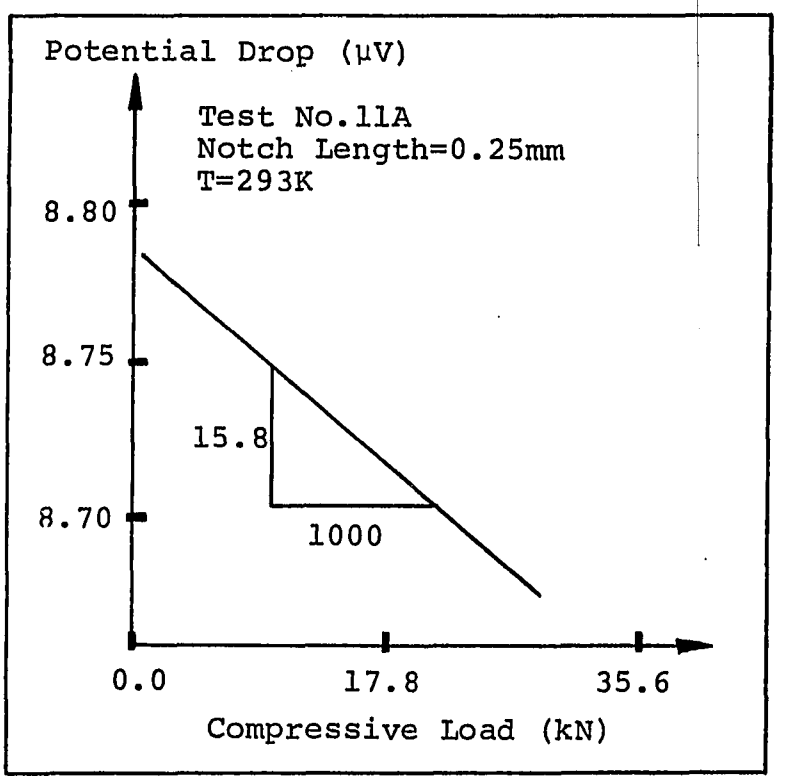

FIGURE A.13 (TOP) & FIGURE A.14 (BOTTOM)

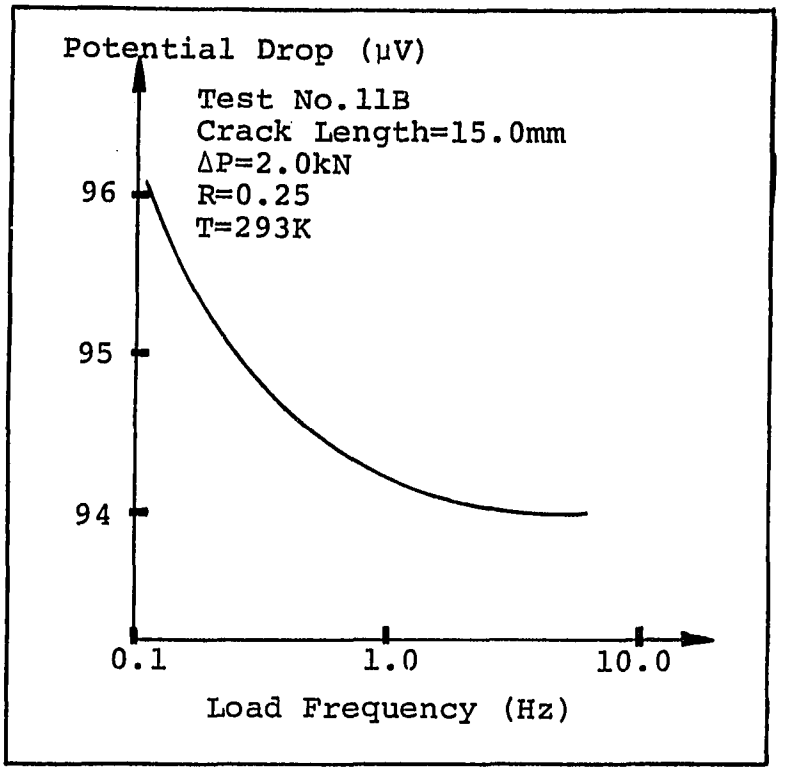

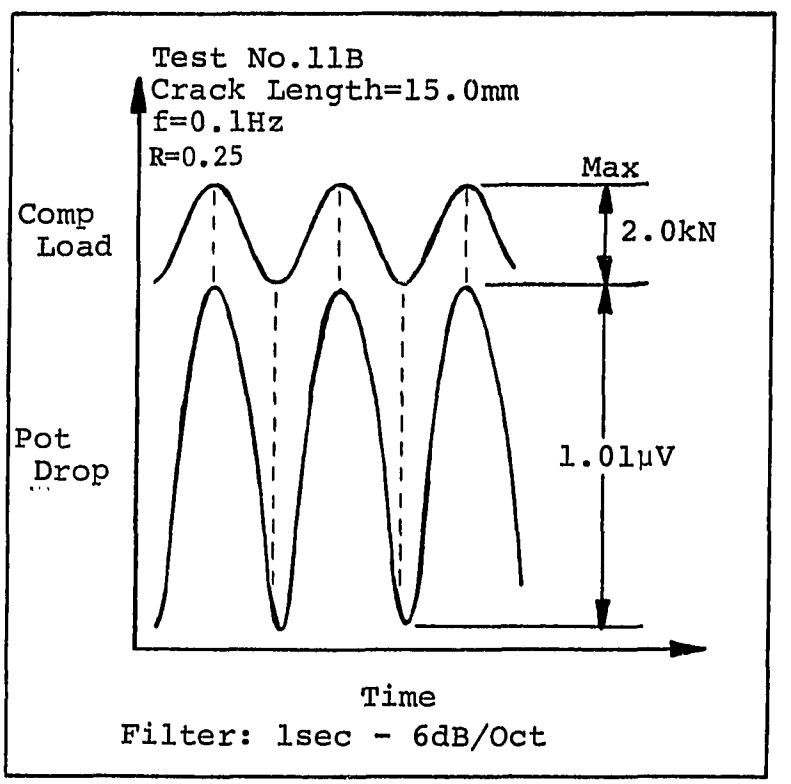

FIGURE A.15 (TOP) & FIGURE A.16 (BOTTOM)

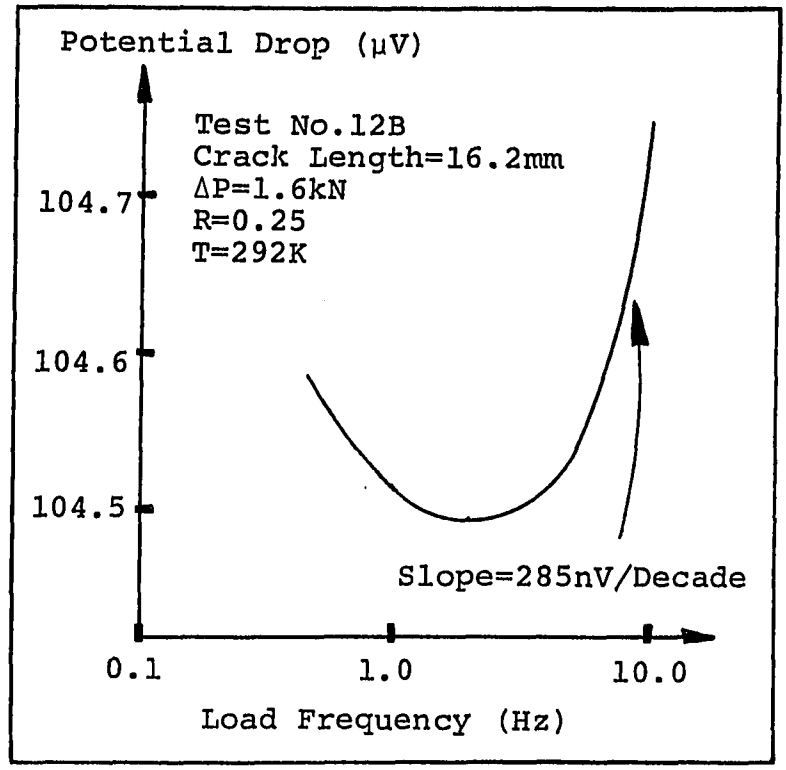

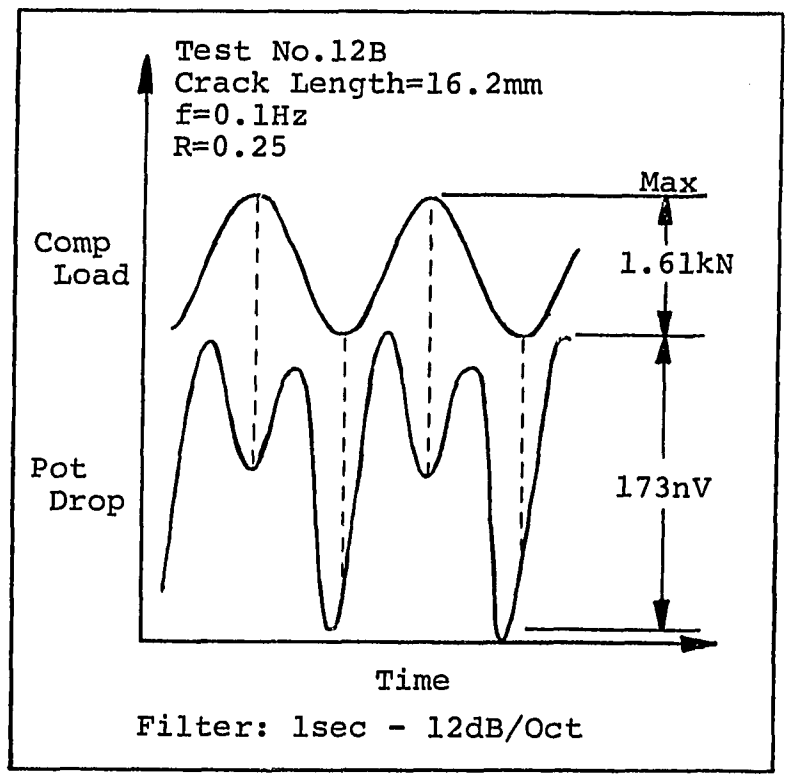

FIGURE A.17 (TOP) & FIGURE A.18 (BOTTOM)

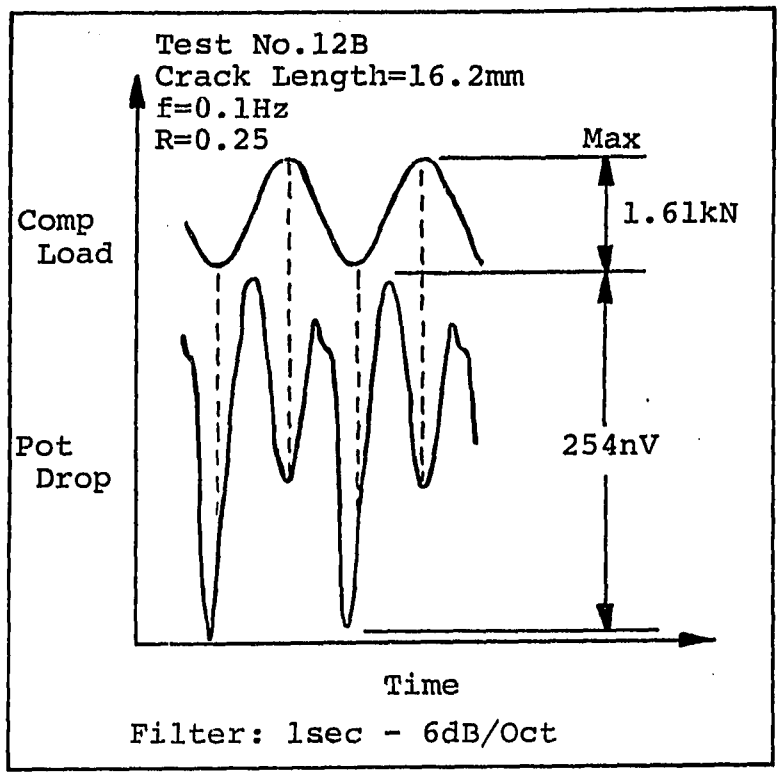

FIGURE A.19

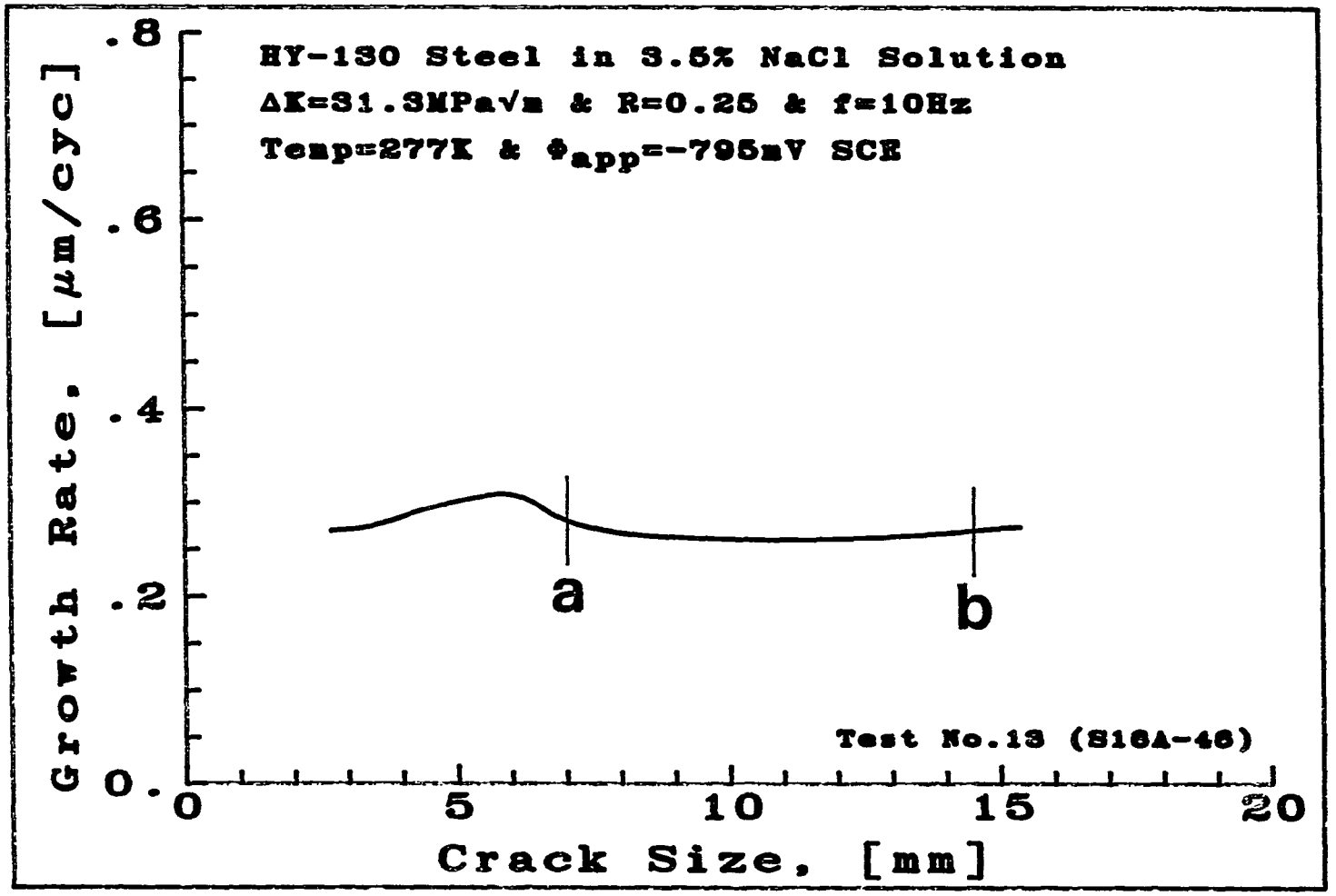

FIGURE A.20: A preliminary short CGR test result showing the influence of crack length on the CGR. The give values for the test variables are only valid between a and b.

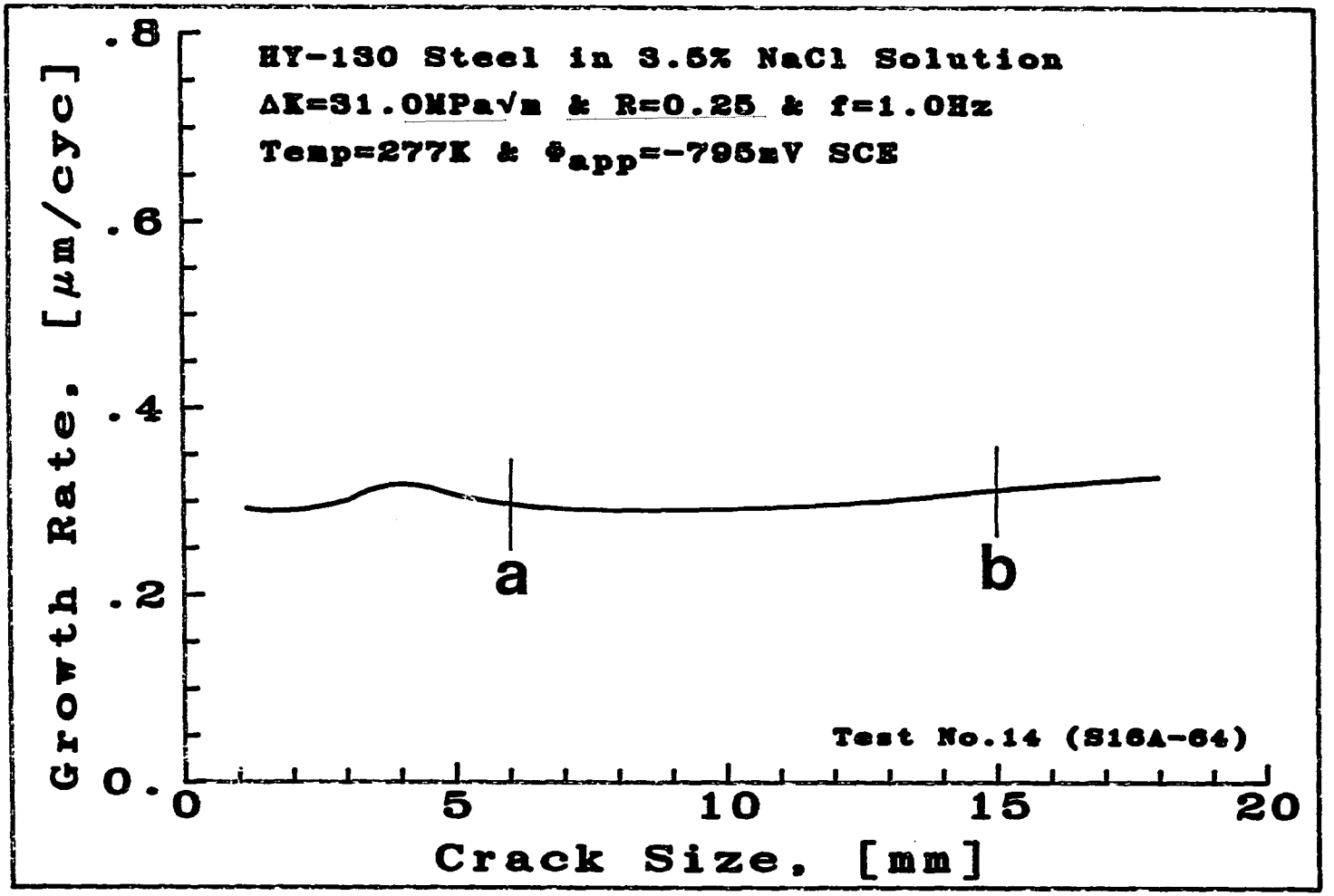

FIGURE A.21: A preliminary short CGR test result showing the influence of crack length on the CGR. The give values for the test variables are only valid between a and b.

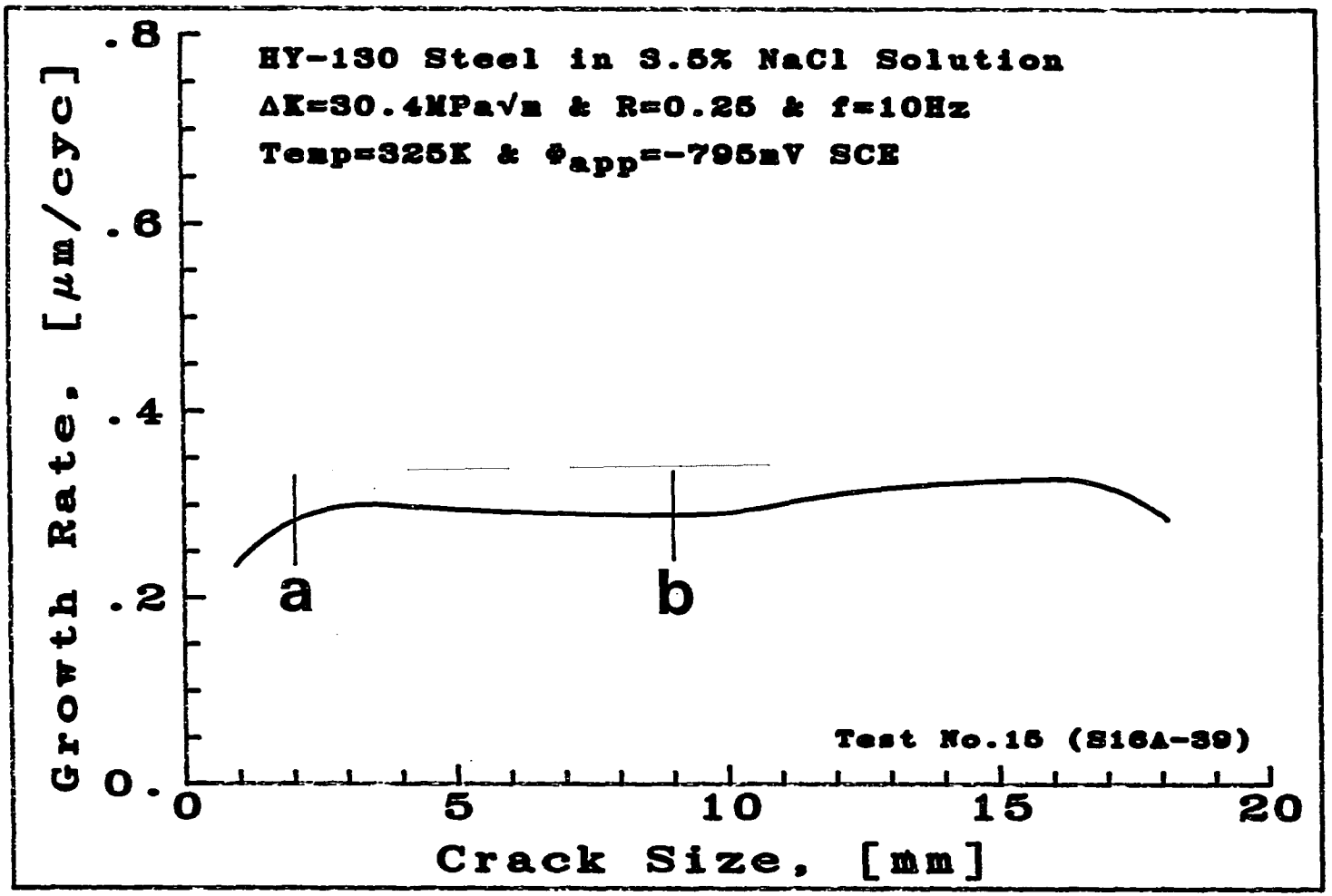

FIGURE A.22: A preliminary short CGR test result showing the influence of crack length on the CGR. The give values for the test variables are only valid between a and b.

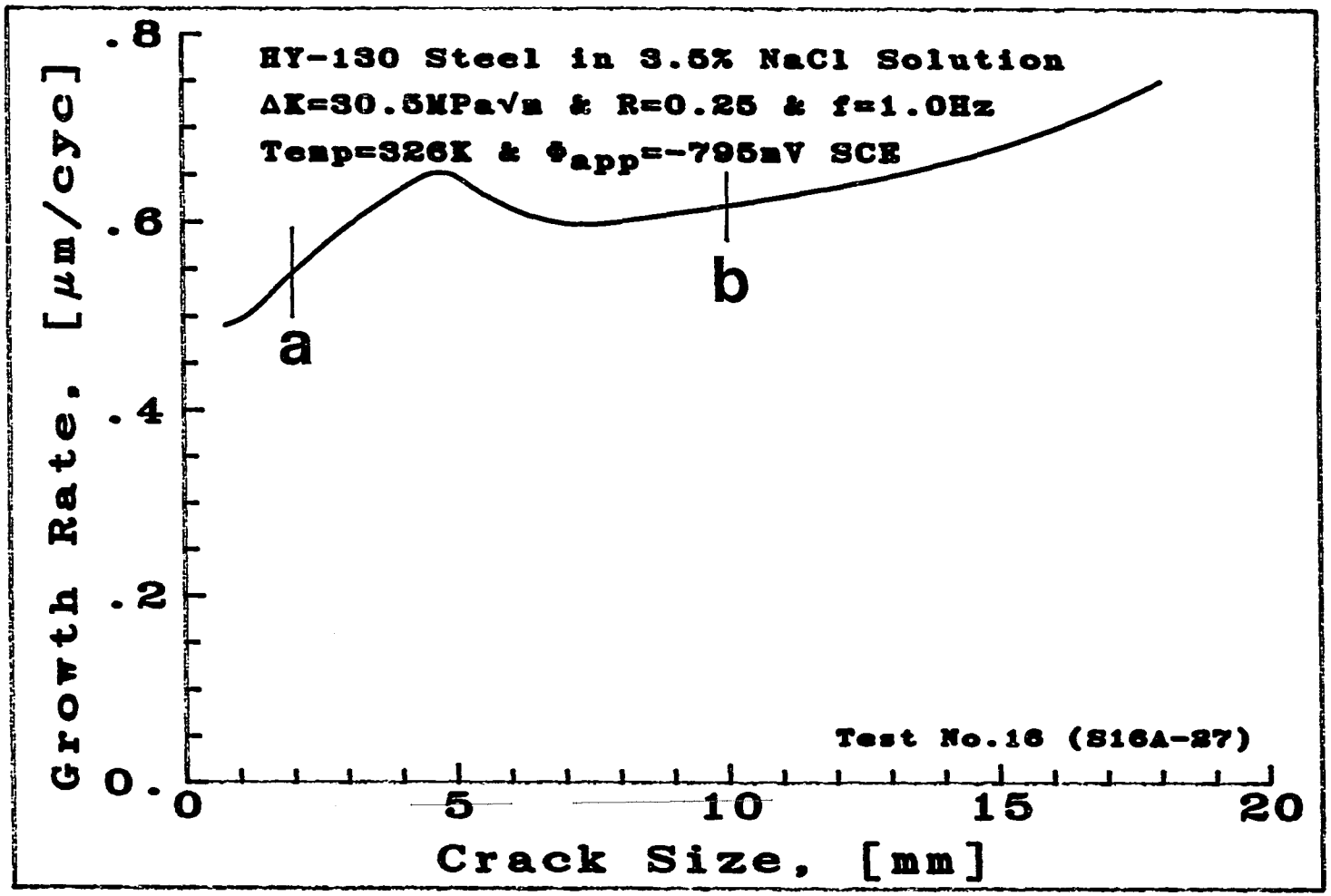

FIGURE A.23: A preliminary short CGR test result showing the influence of crack length on the CGR. The give values for the test variables are only valid between a and b.

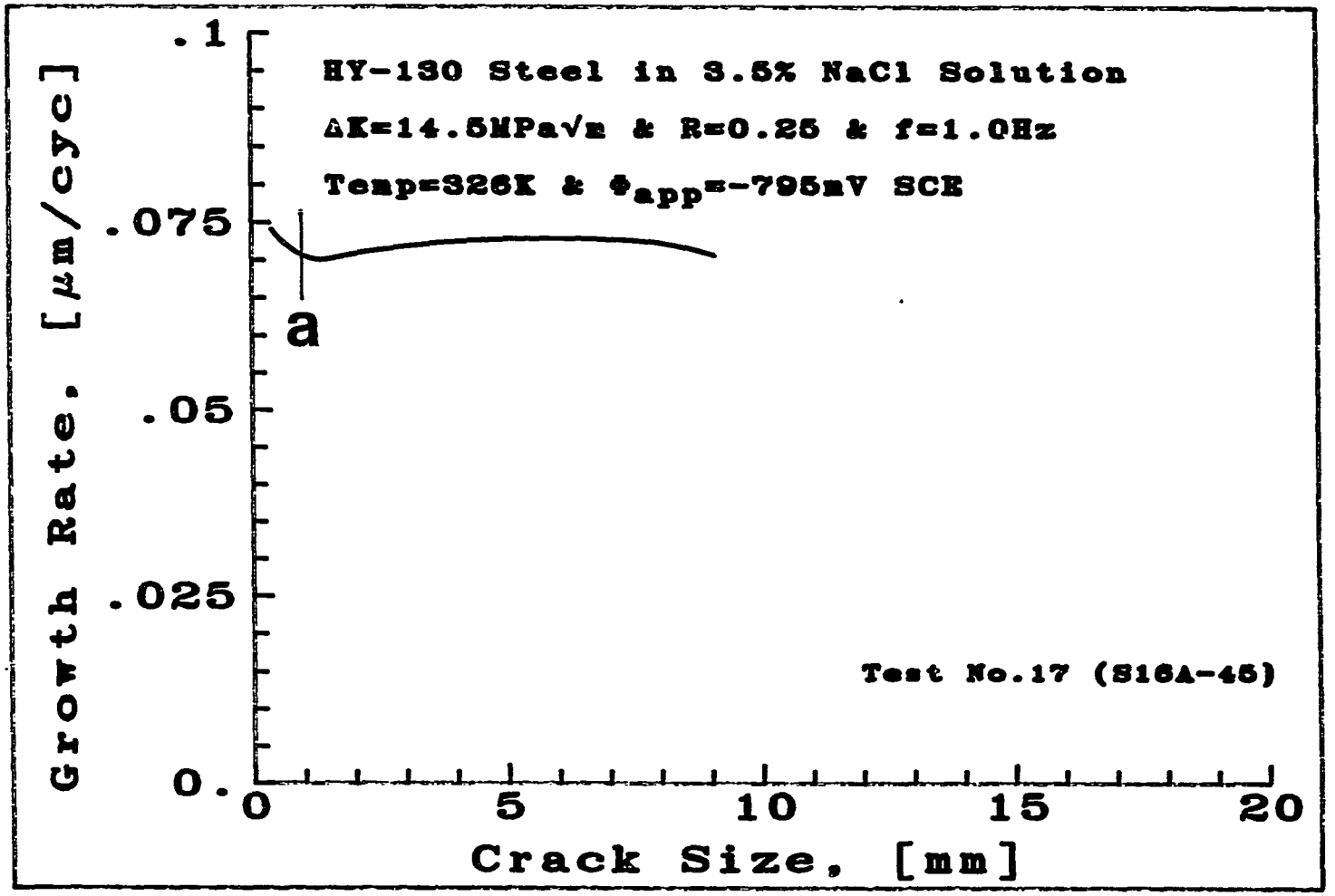

FIGURE A.24: A preliminary short CGR test result showing the influence of crack length on the CGR. The give values for the test variables are only valid between a and b.

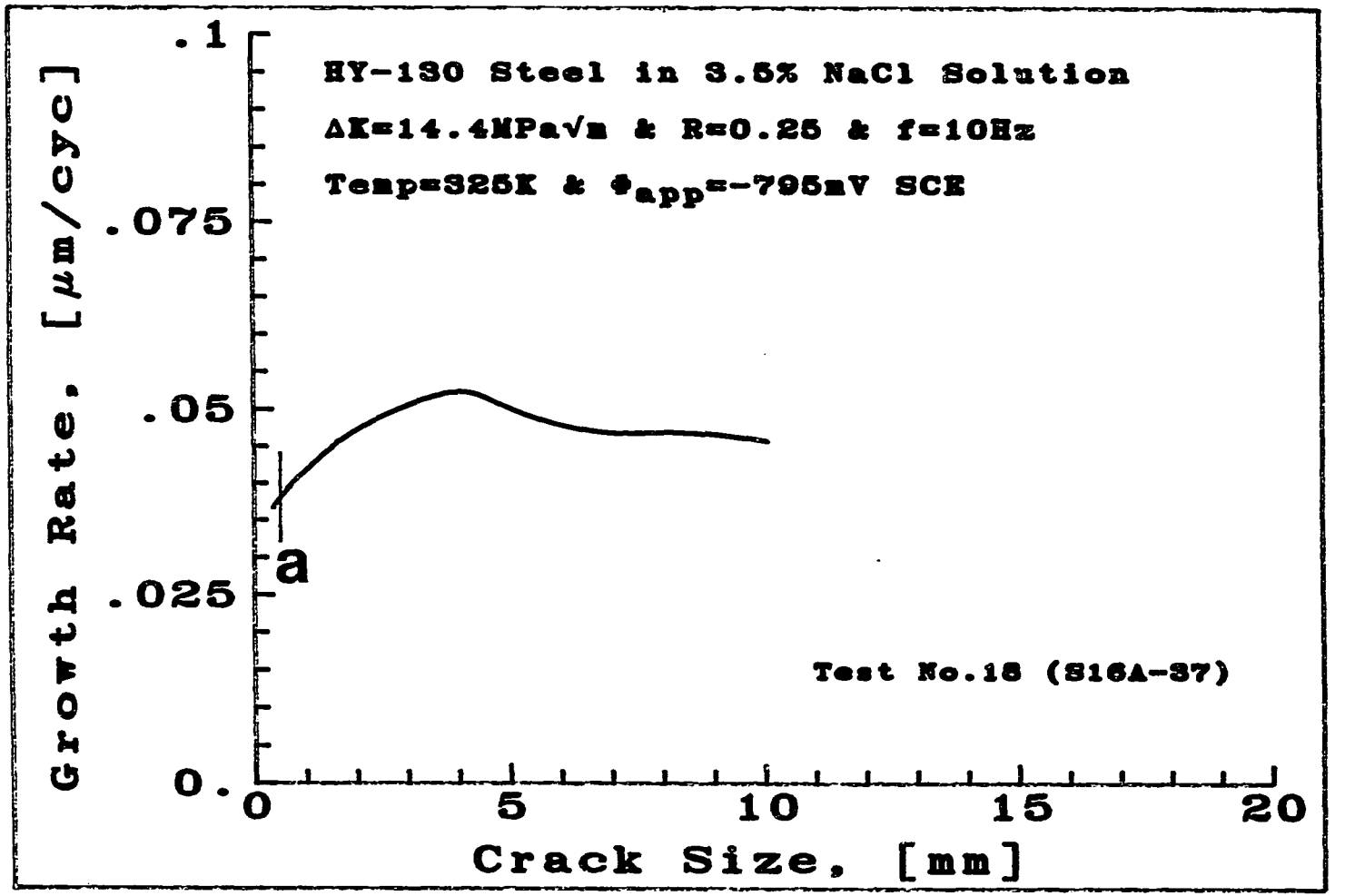

FIGURE A.25: A preliminary short CGR test result showing the influence of crack length on the CGR. The give values for the test variables are only valid between a and b.

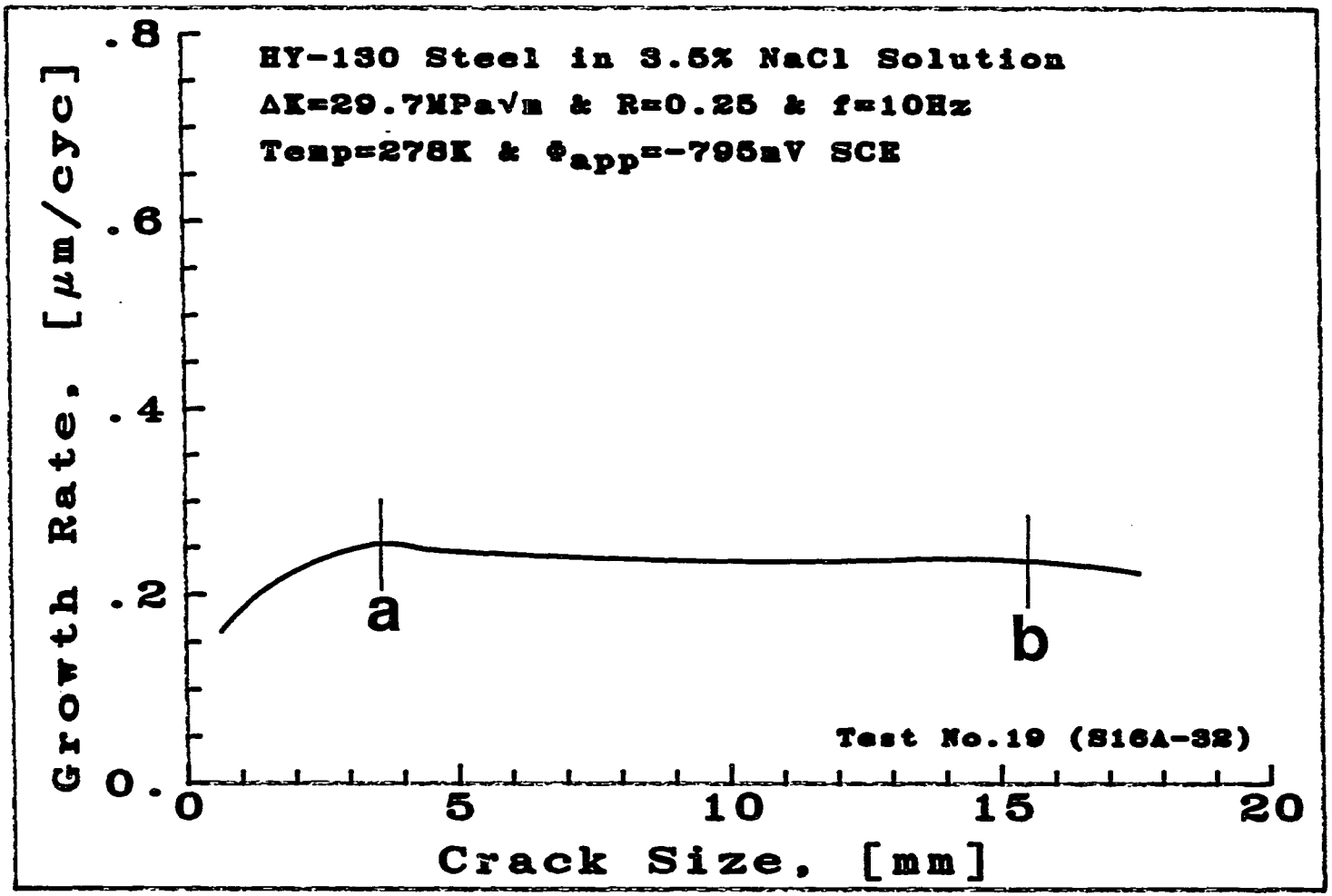

FIGURE A.26: A preliminary short CGR test result showing the influence of crack length on the CGR. The give values for the test variables are only valid between a and b.

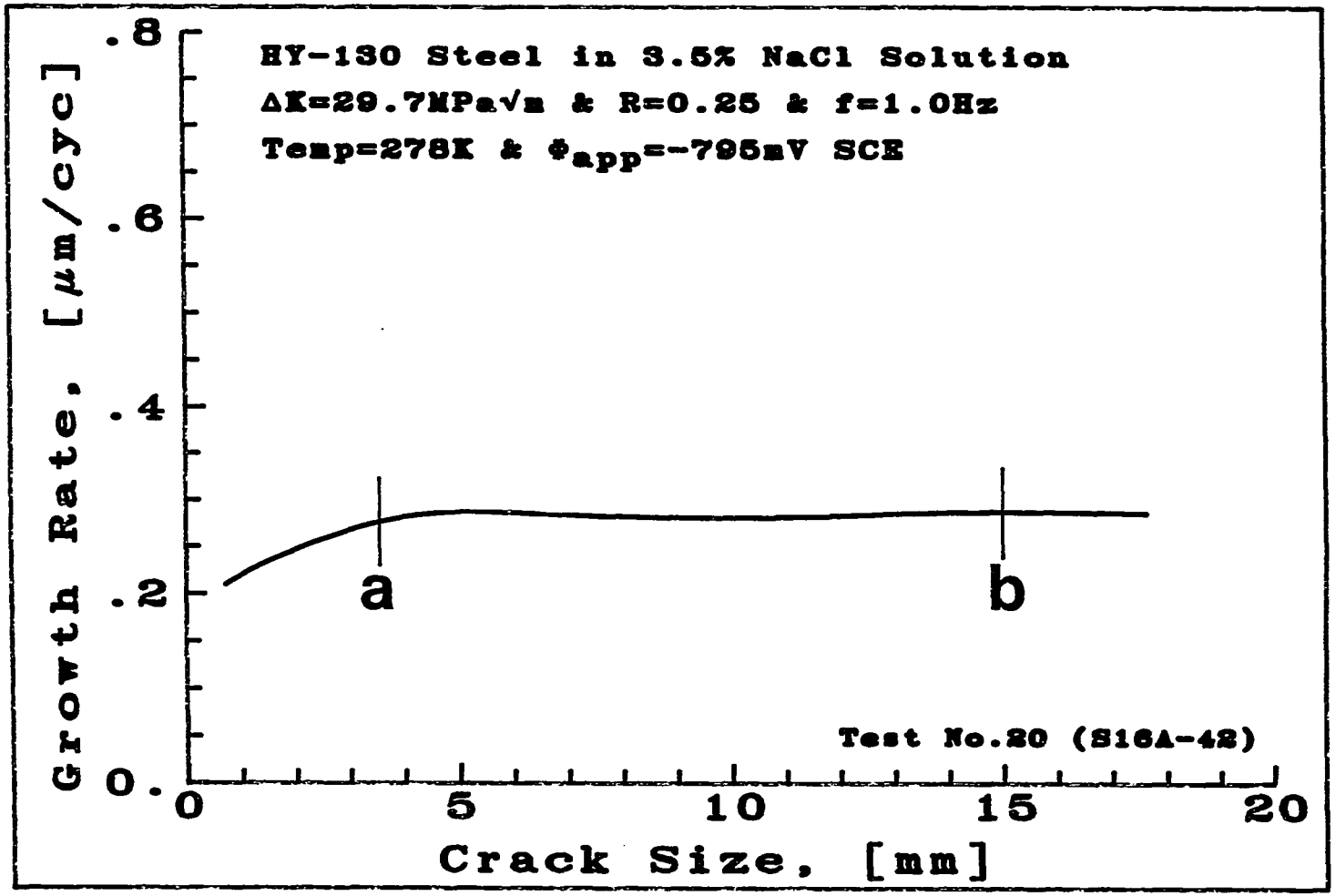

FIGURE A.27: A preliminary short CGR test result showing the influence of crack length on the CGR. The give values for the test variables are only valid between a and b.

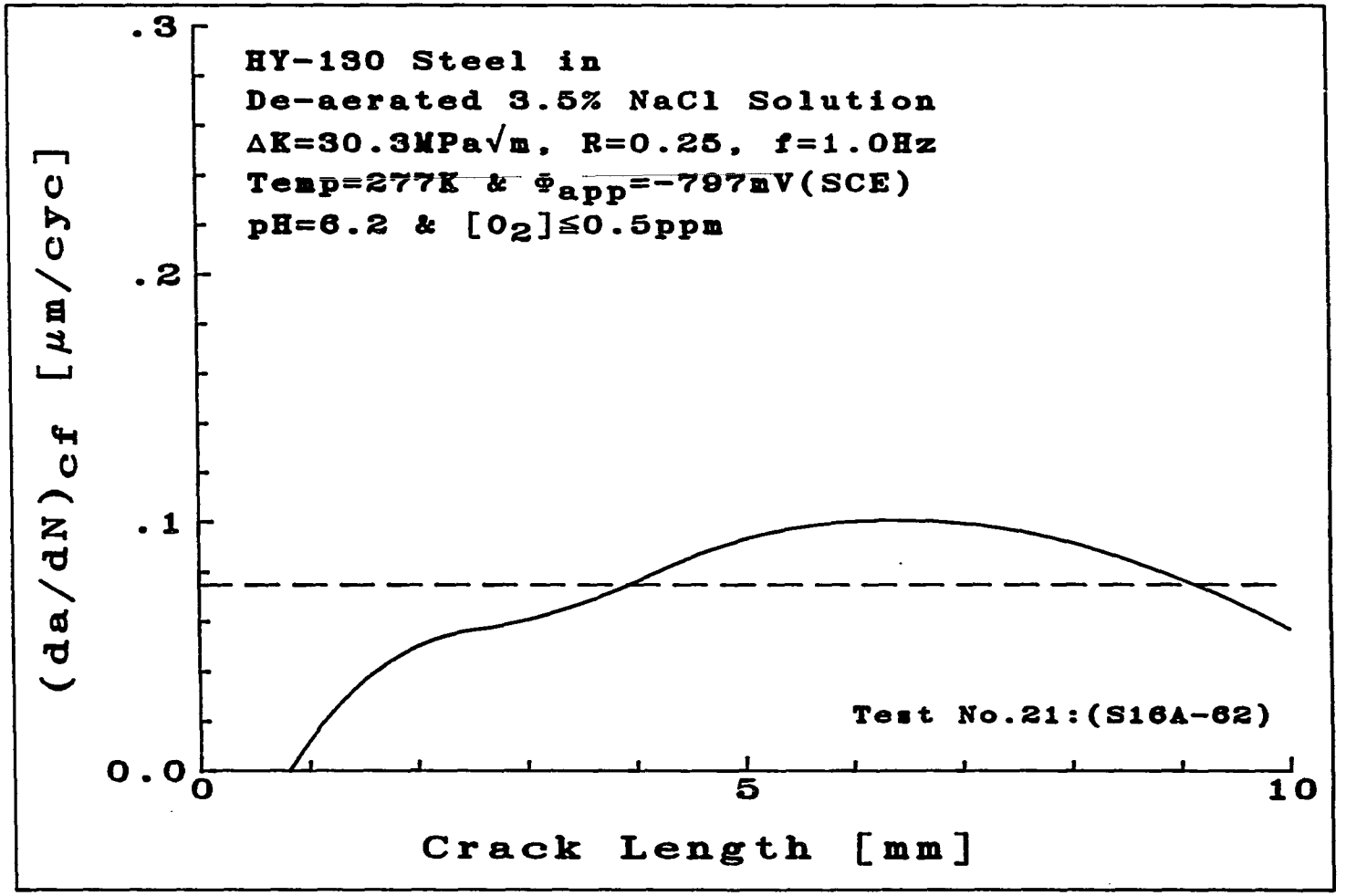

FIGURE A.28: A short CGR test reult showing the influence of crack length on the CGR. The dashed line in the figure corresponds with the long CGR for these test conditions.

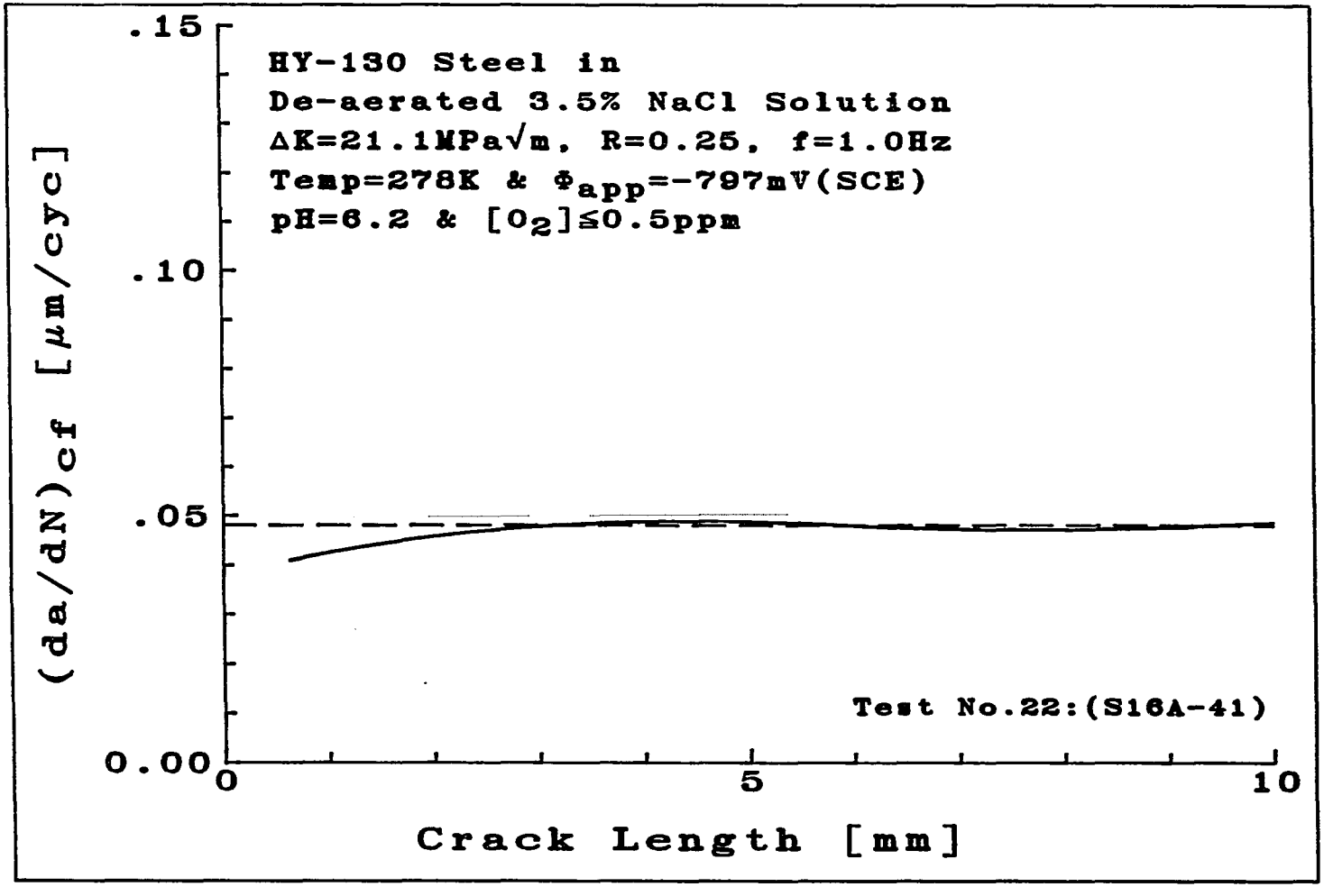

FIGURE A.29: A short CGR test reult showing the influence of crack length on the CGR. The dashed line in the figure corresponds with the long CGR for these test conditions.

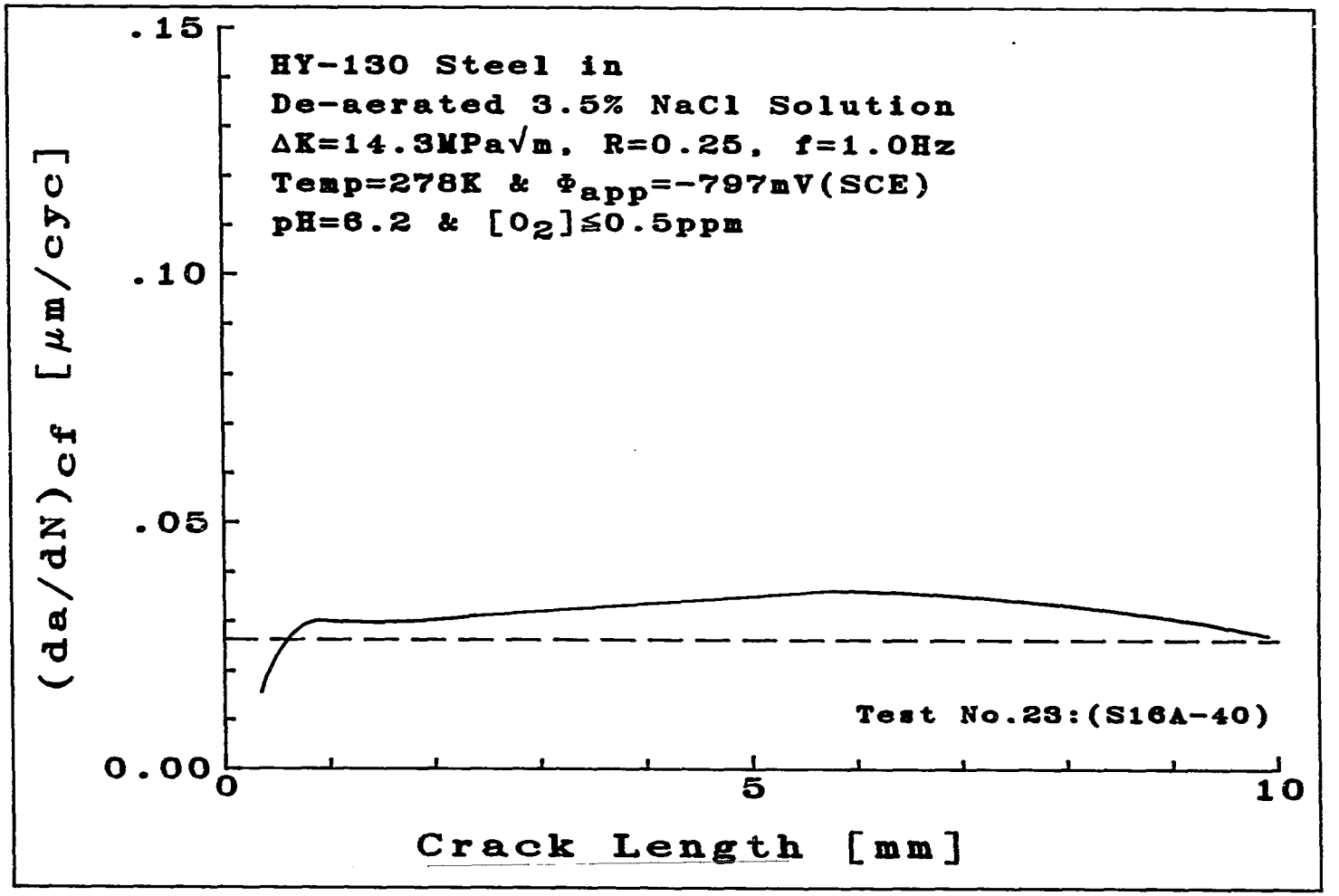

FIGURE A.30: A short CGR test reult showing the influence of crack length on the CGR. The dashed line in the figure corresponds with the long CGR for these test conditions.

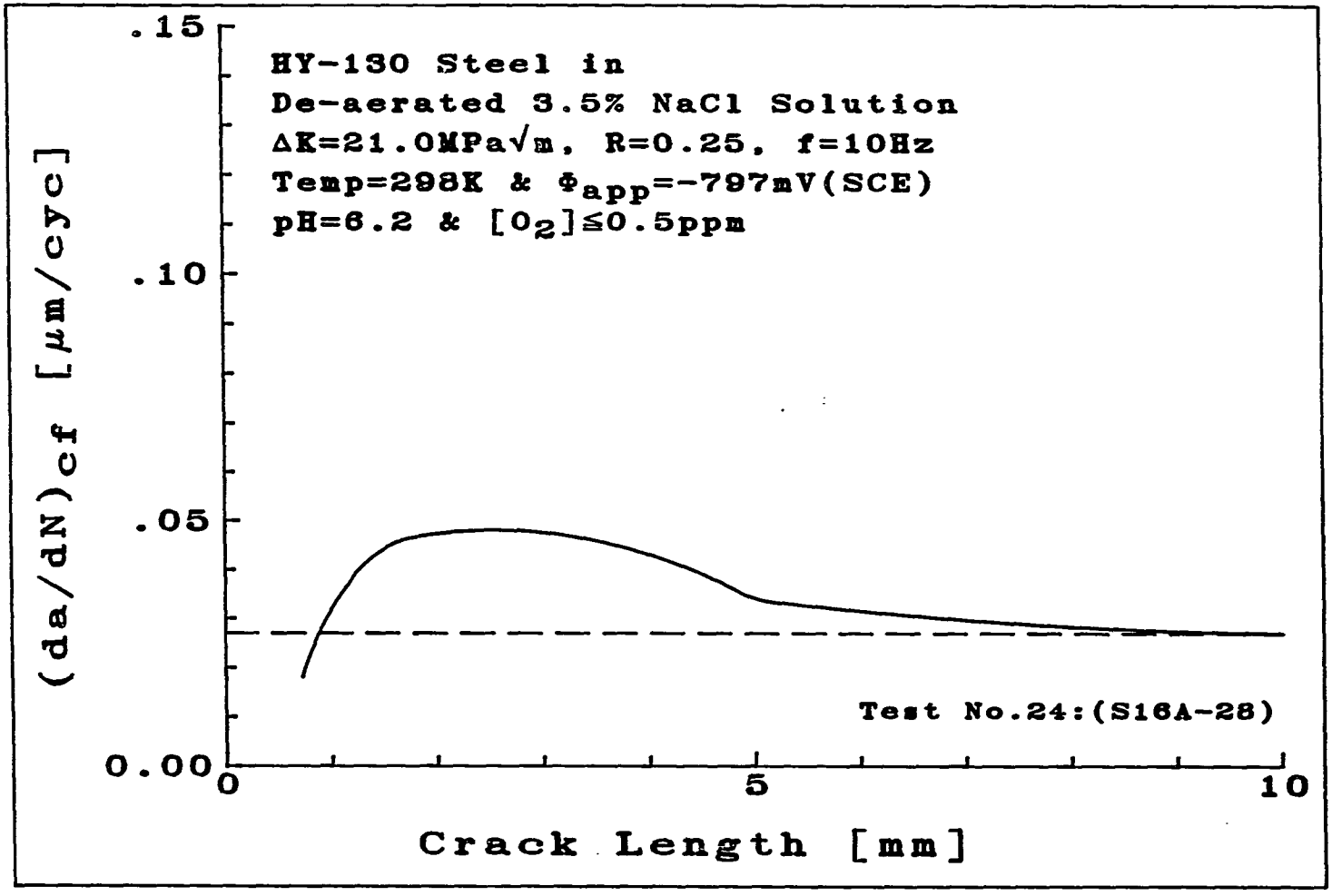

FIGURE A.31: A short CGR test reult showing the influence of crack length on the CGR. The dashed line in the figure corresponds with the long CGR for these test conditions.

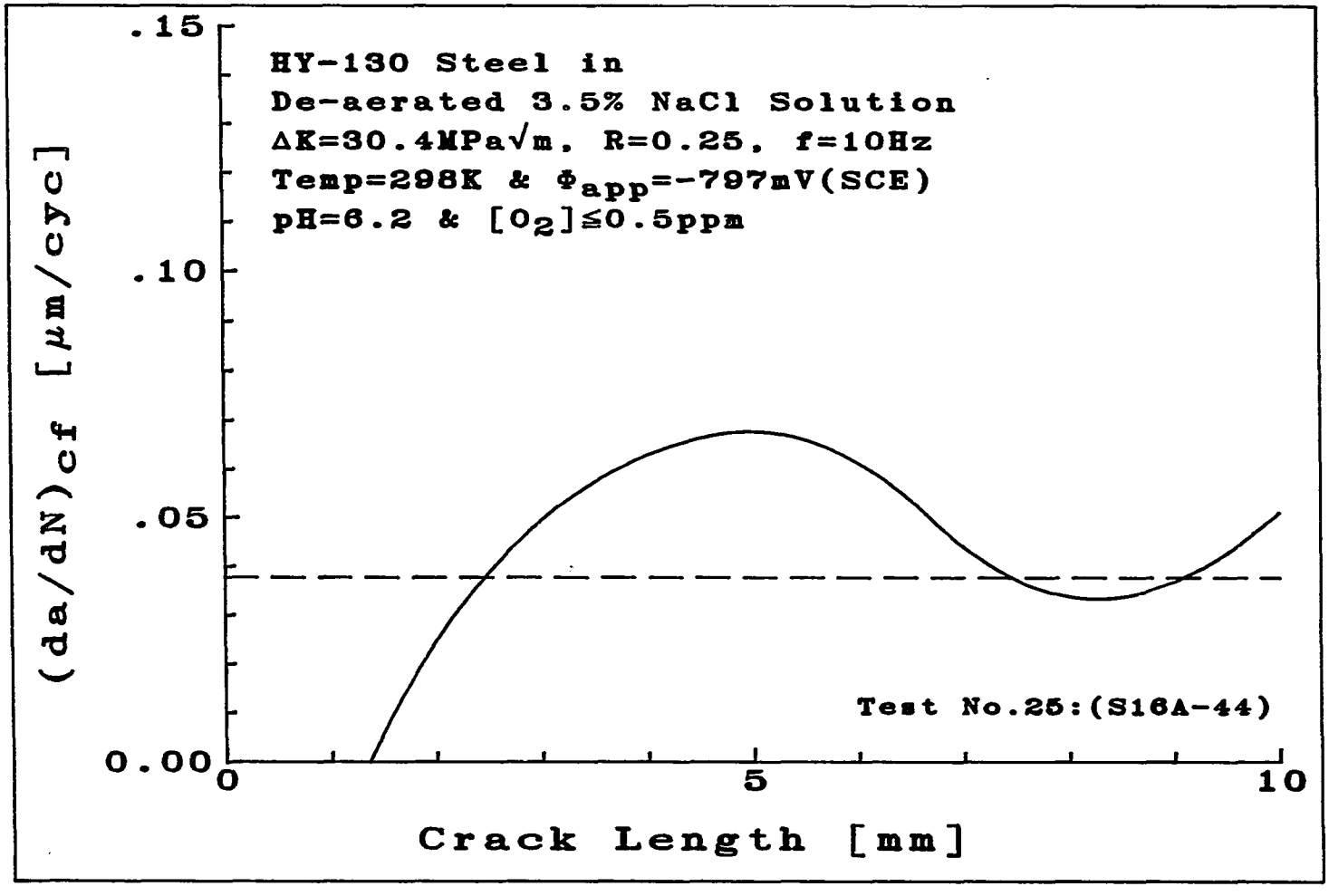

FIGURE A.32: A short CGR test reult showing the influence of crack length on the CGR. The dashed line in the figure corresponds with the long CGR for these test conditions.

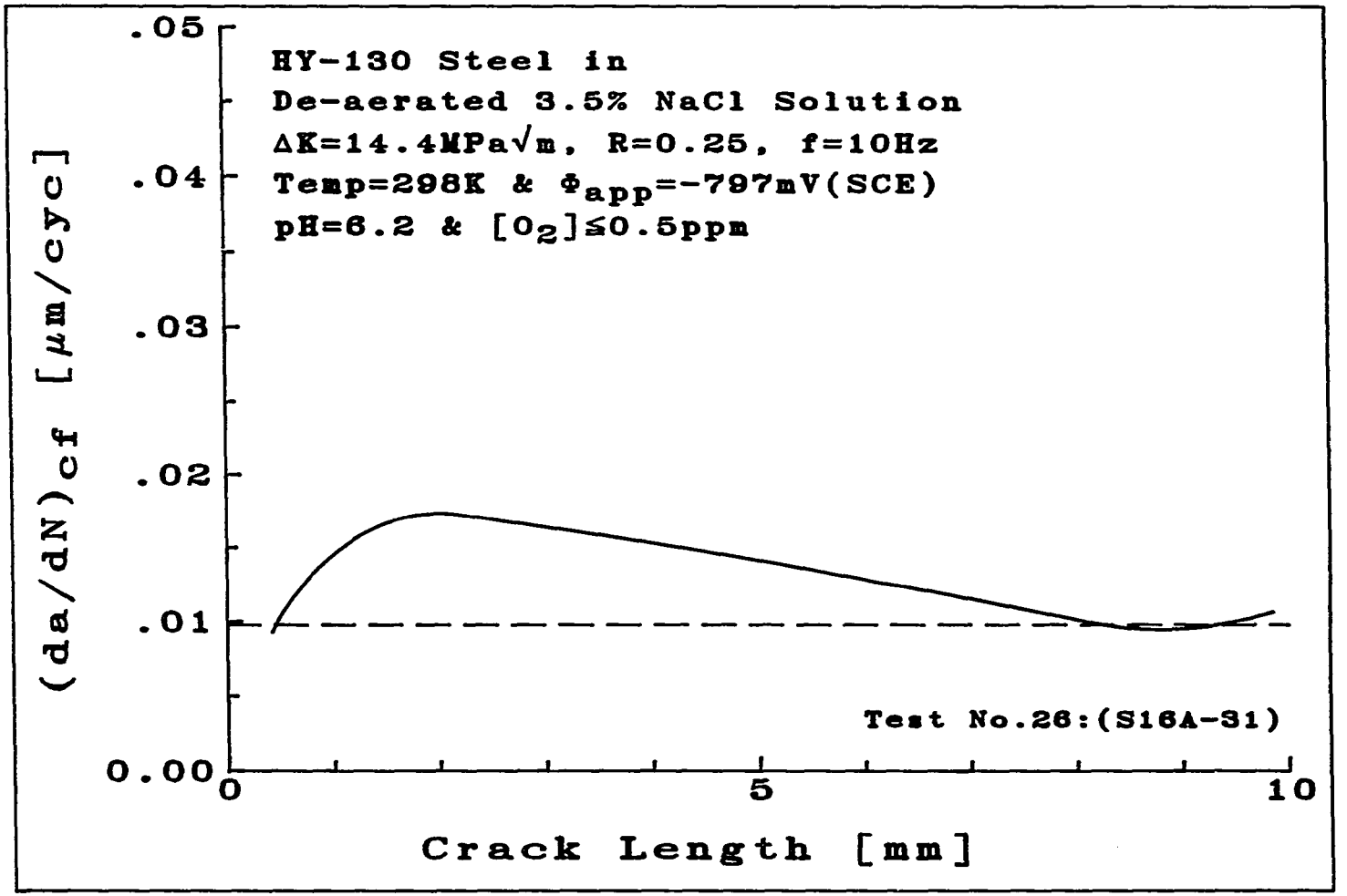

FIGURE A.33: A short CGR test reult showing the influence of crack length on the CGR. The dashed line in the figure corresponds with the long CGR for these test conditions.

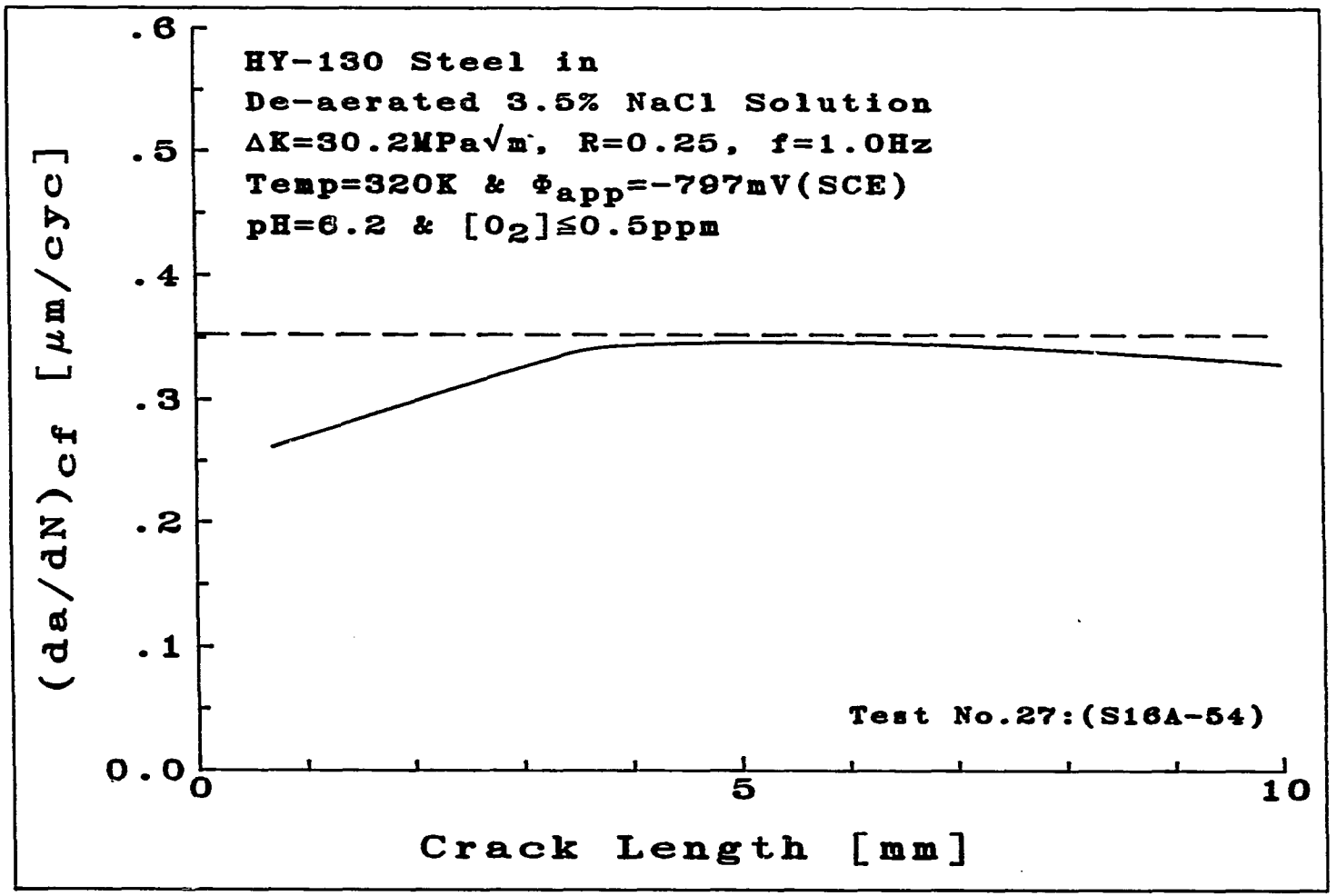

FIGURE A.34: A short CGR test reult showing the influence of crack length on the CGR. The dashed line in the figure corresponds with the long CGR for these test conditions.

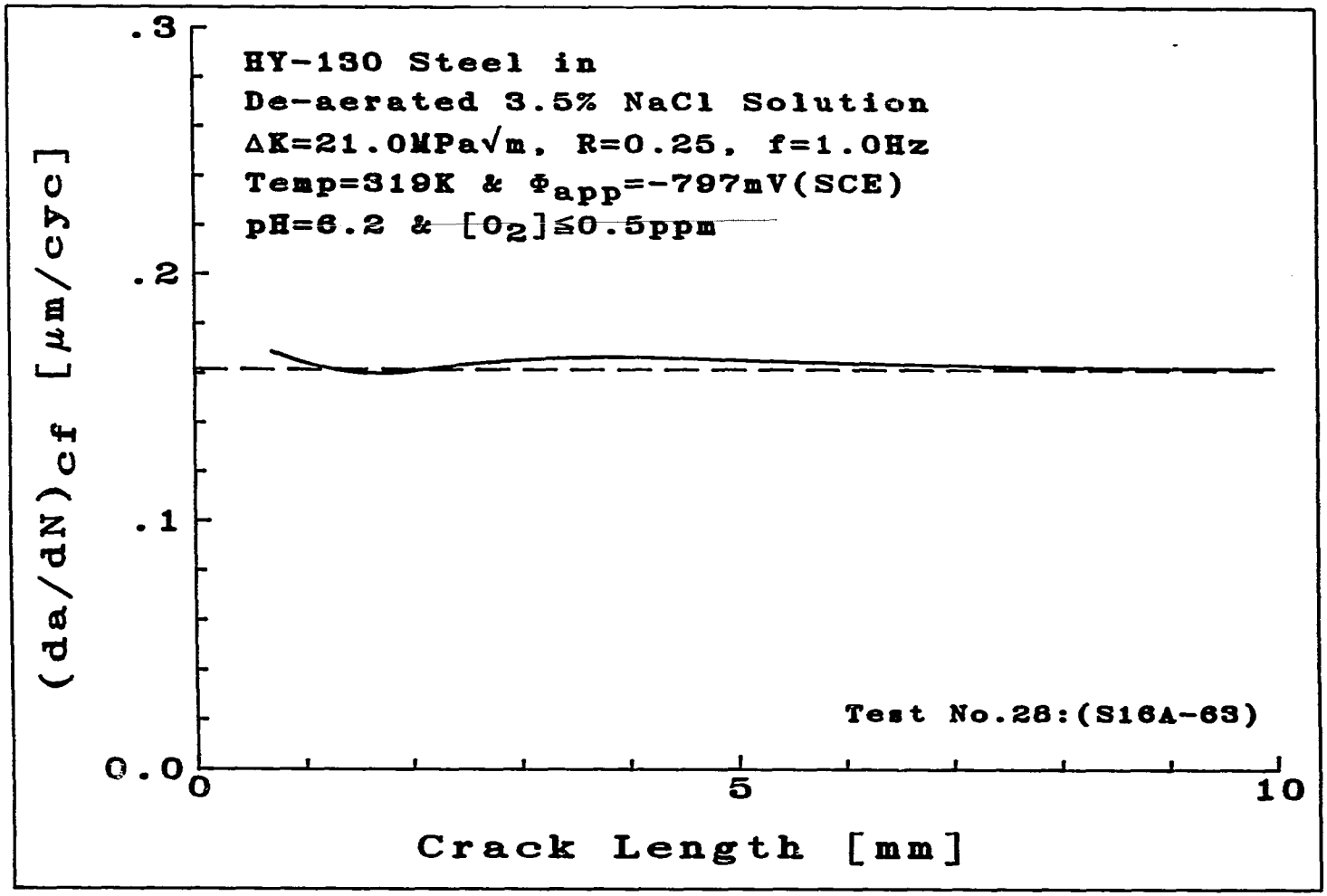

FIGURE A.35: A short CGR test reult showing the influence of crack length on the CGR. The dashed line in the figure corresponds with the long CGR for these test conditions.

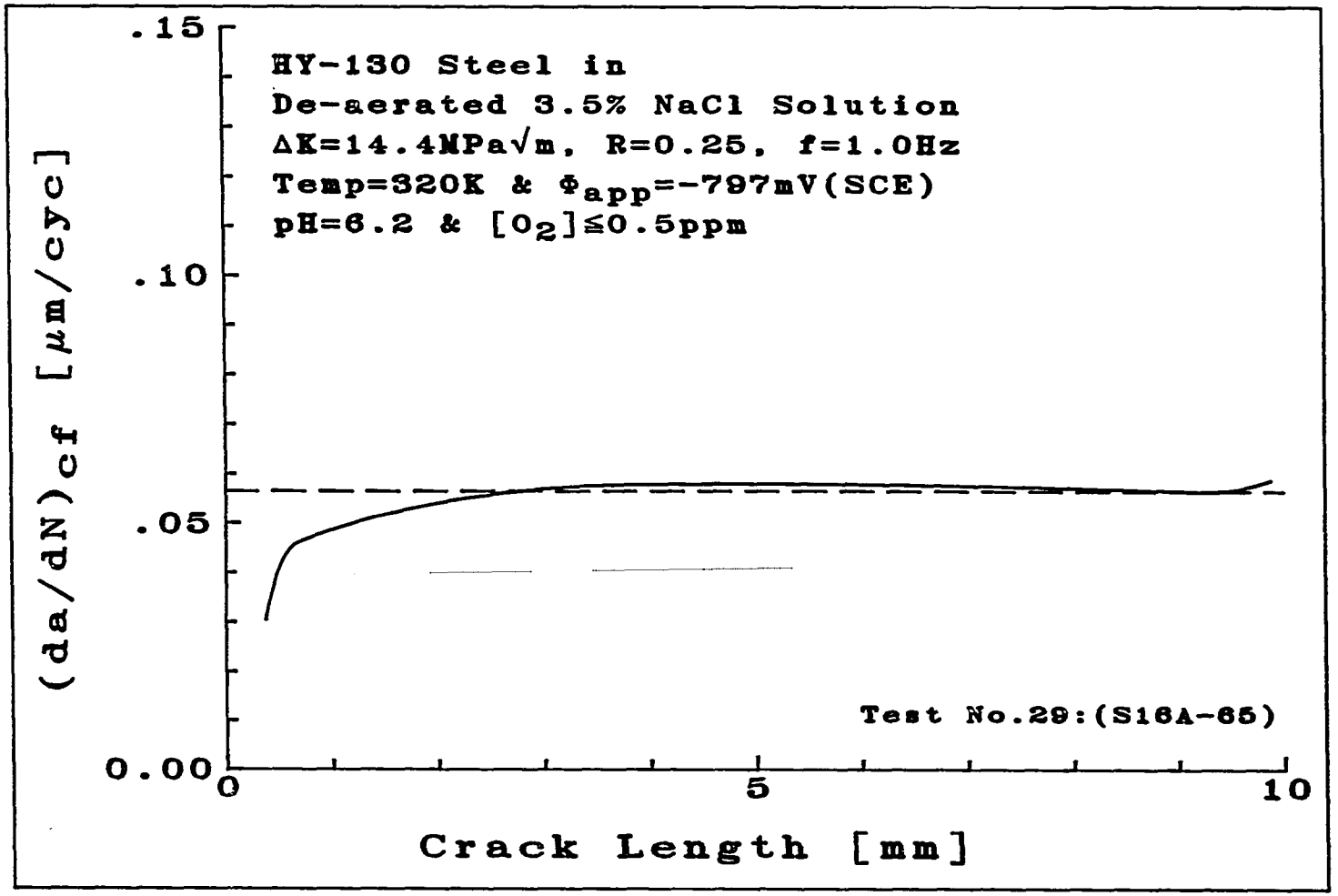

FIGURE A.36: A short CGR test reult showing the influence of crack length on the CGR. The dashed line in the figure corresponds with the long CGR for these test conditions.

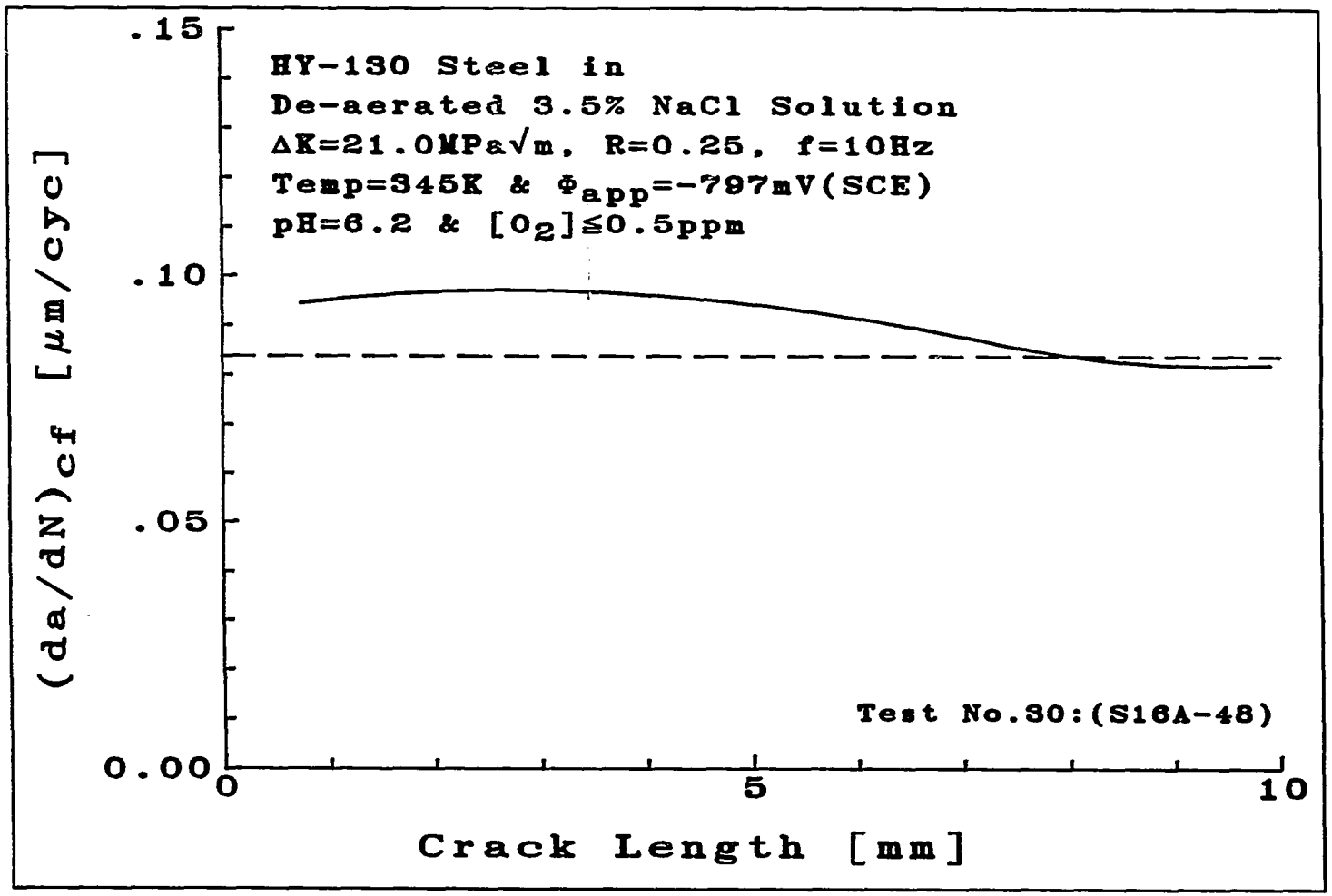

FIGURE A.37: A short CGR test reult showing the influence of crack length on the CGR. The dashed line in the figure corresponds with the long CGR for these test conditions.

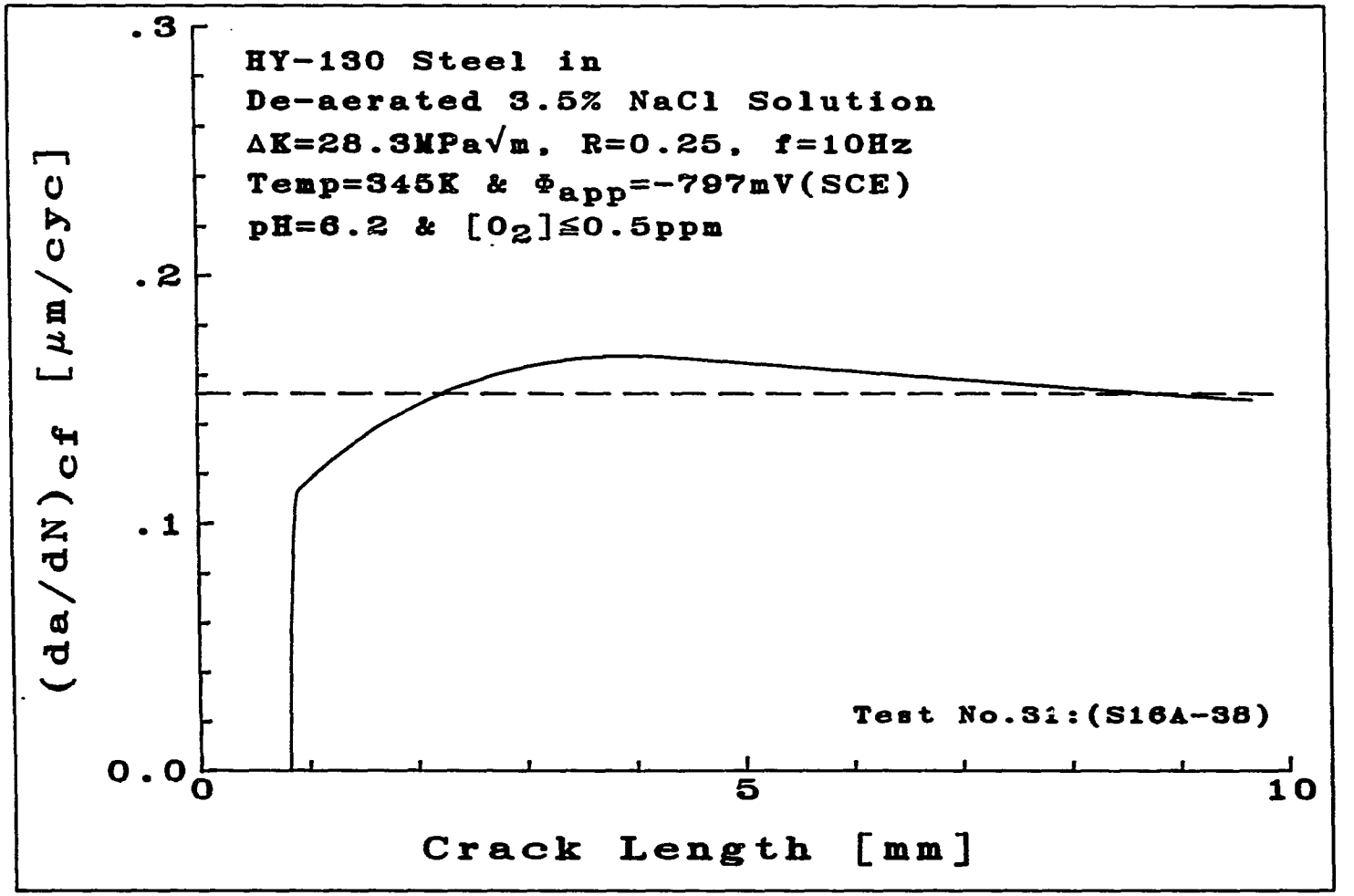

FIGURE A.38: A short CGR test reult showing the influence of crack length on the CGR. The dashed line in the figure corresponds with the long CGR for these test conditions.

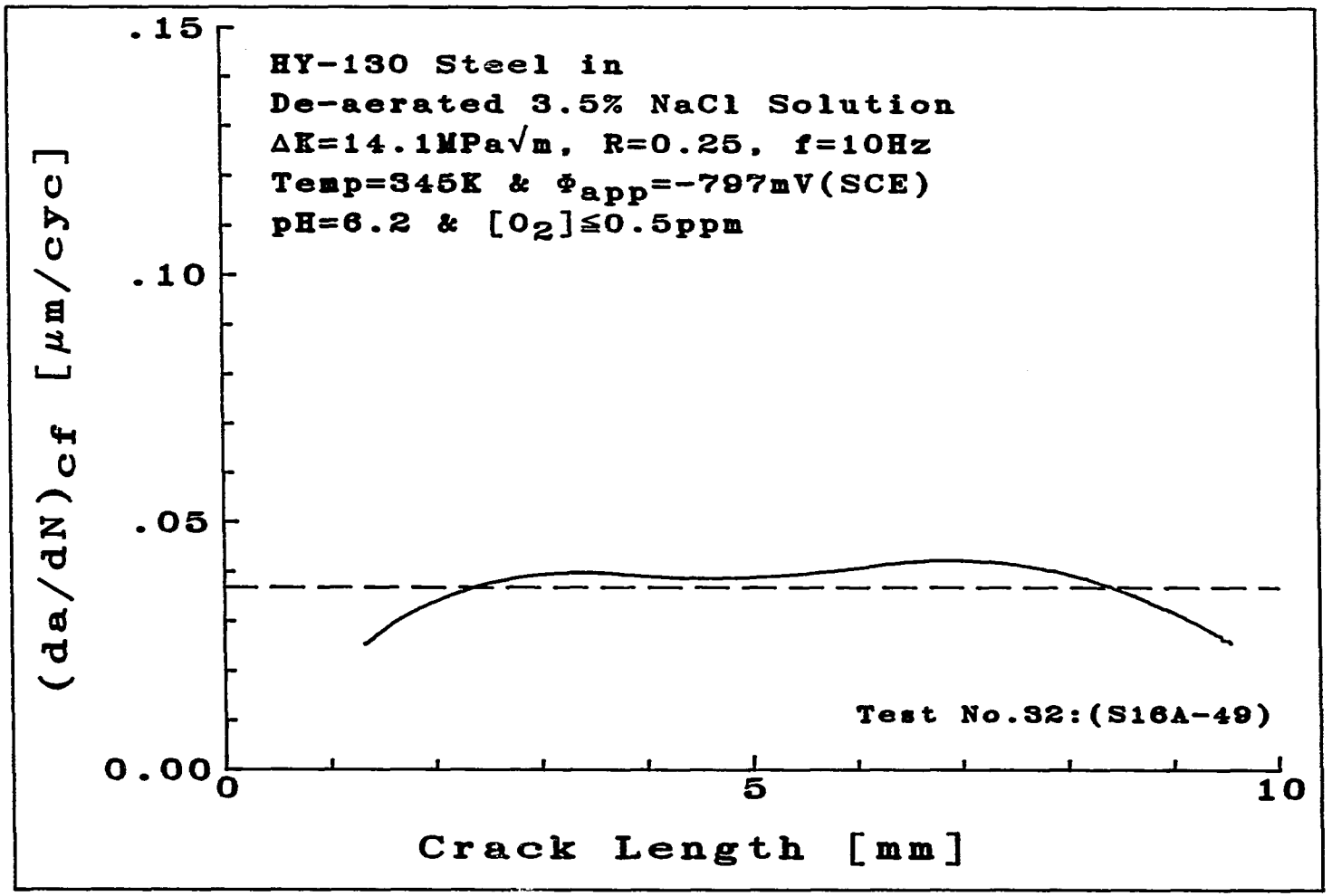

FIGURE A.39: A short CGR test reult showing the influence of crack length on the CGR. The dashed line in the figure corresponds with the long CGR for these test conditions.

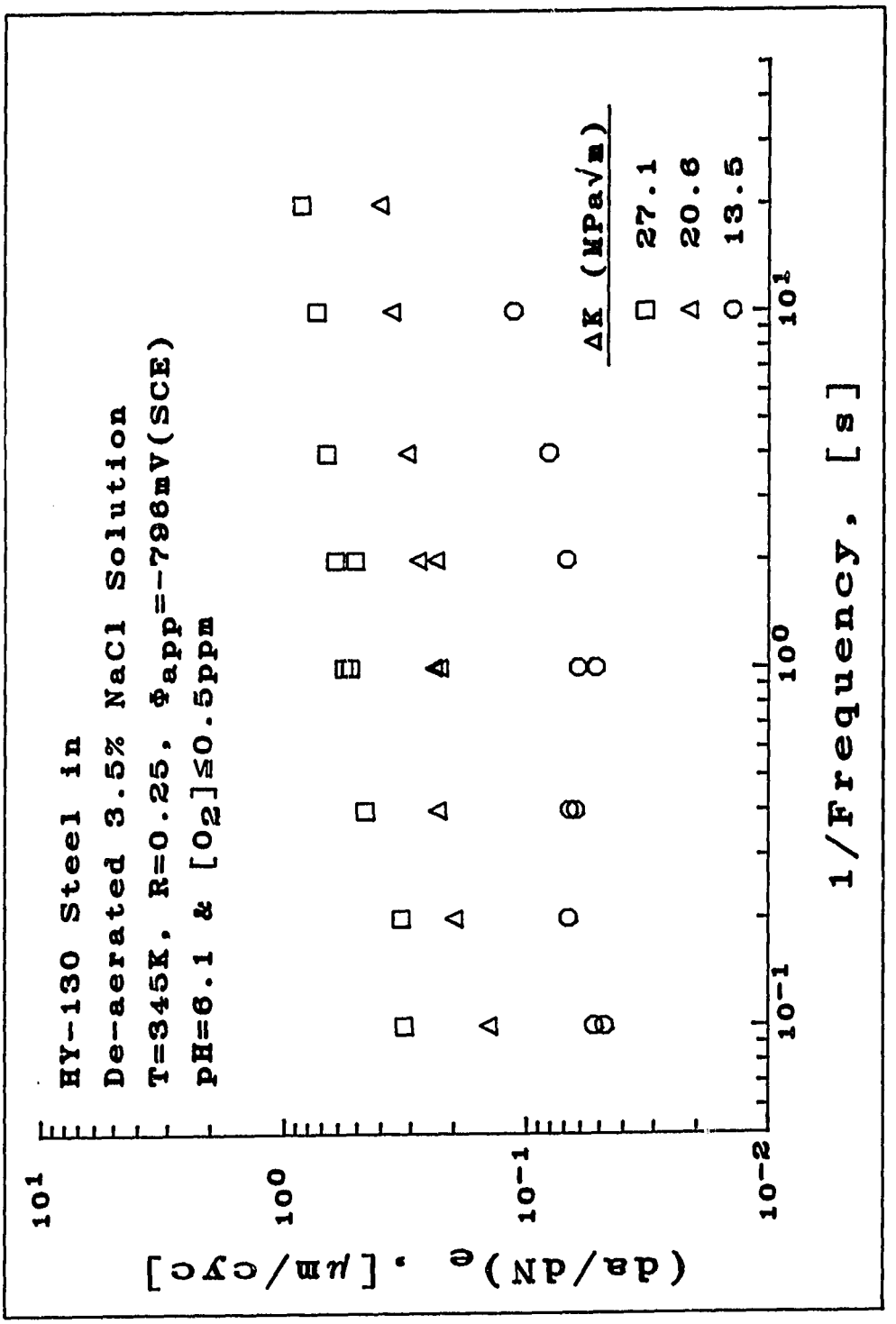

FIGURE A.40: The influence of frequency and ΔK level on the total CGR at T=345 K.

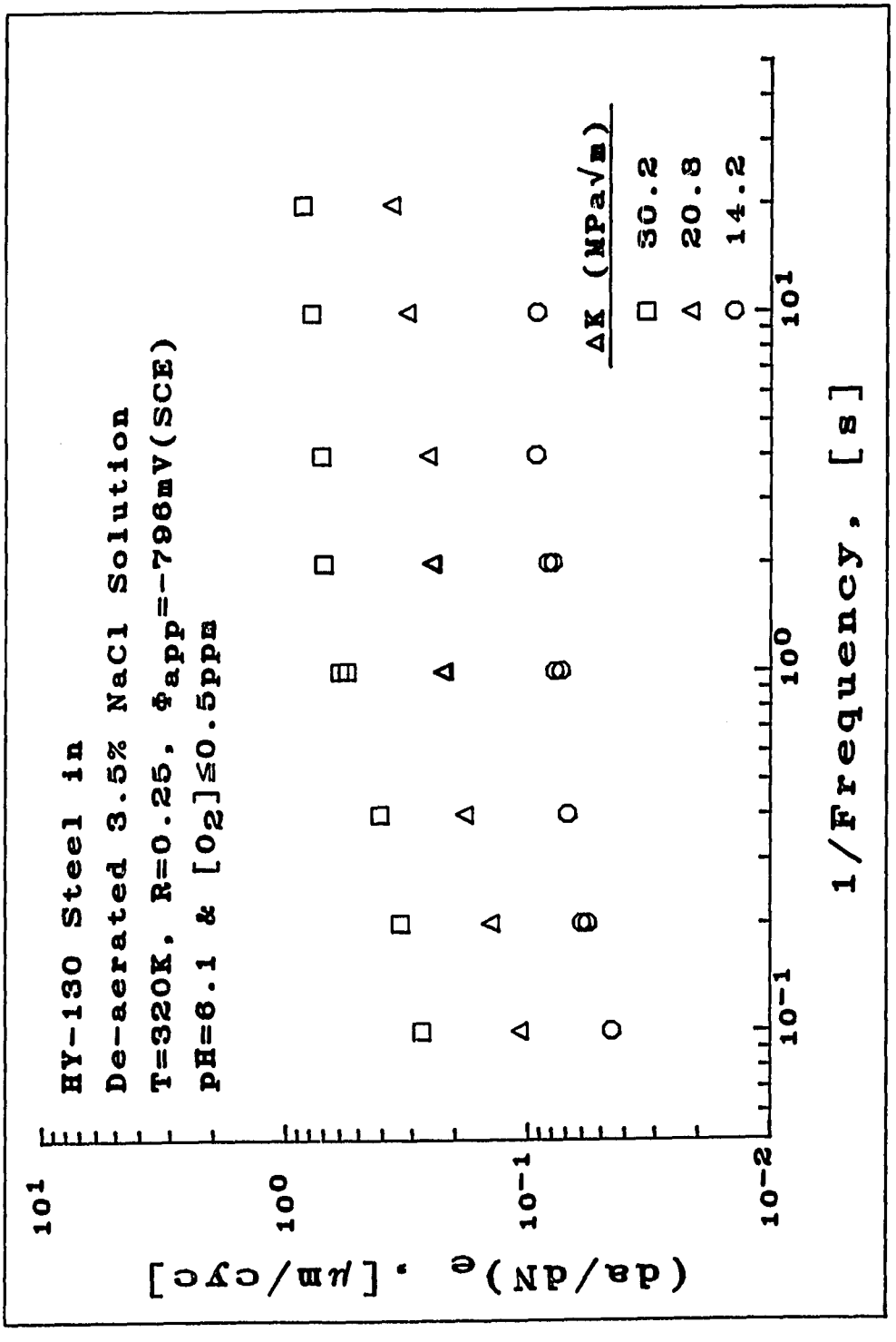

FIGURE A.41: The influence of frequency and ΔK level on the total CGR at T=320 K.

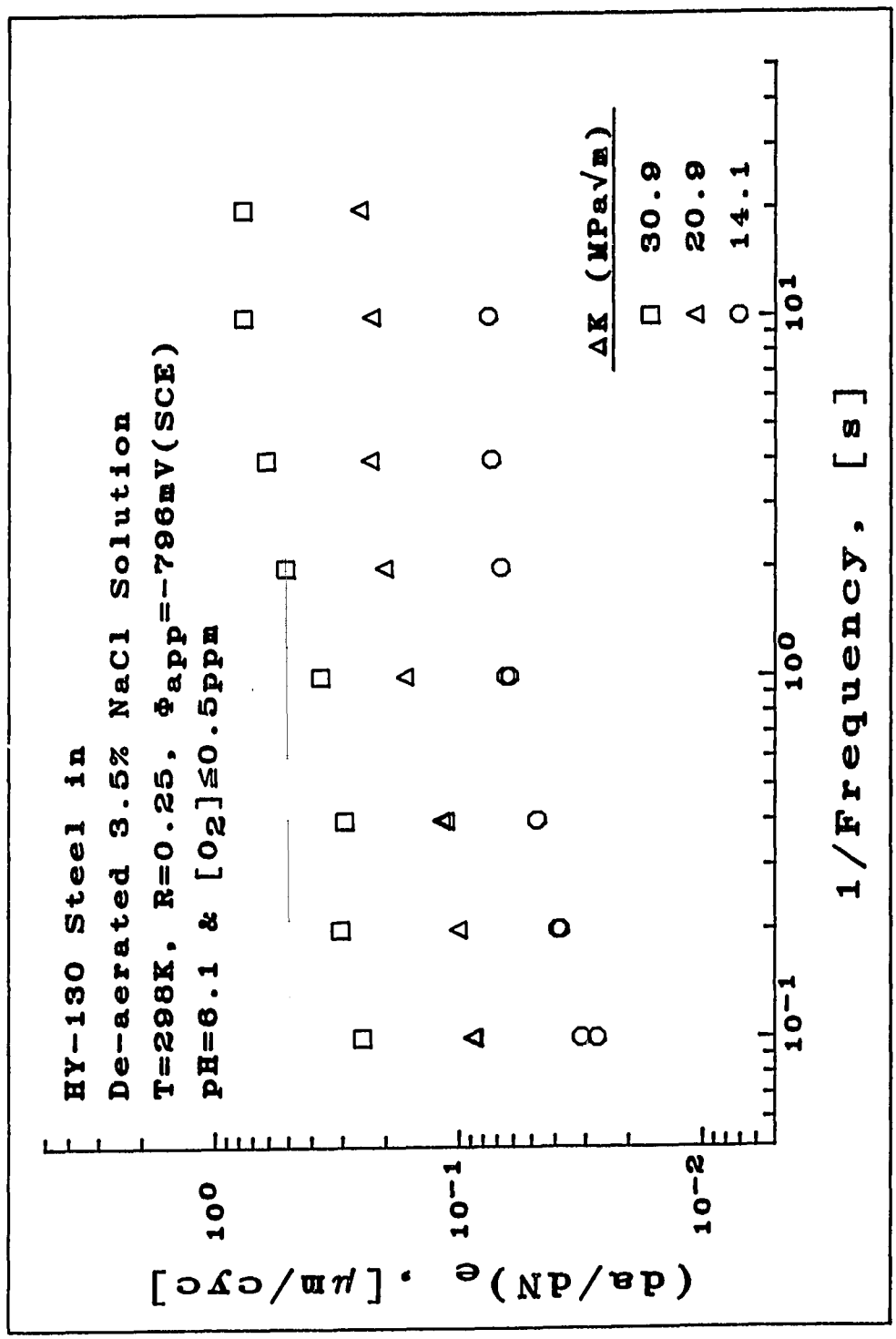

FIGURE A.42: The influence of frequency and ΔK level on the total CGR at T=298 K.

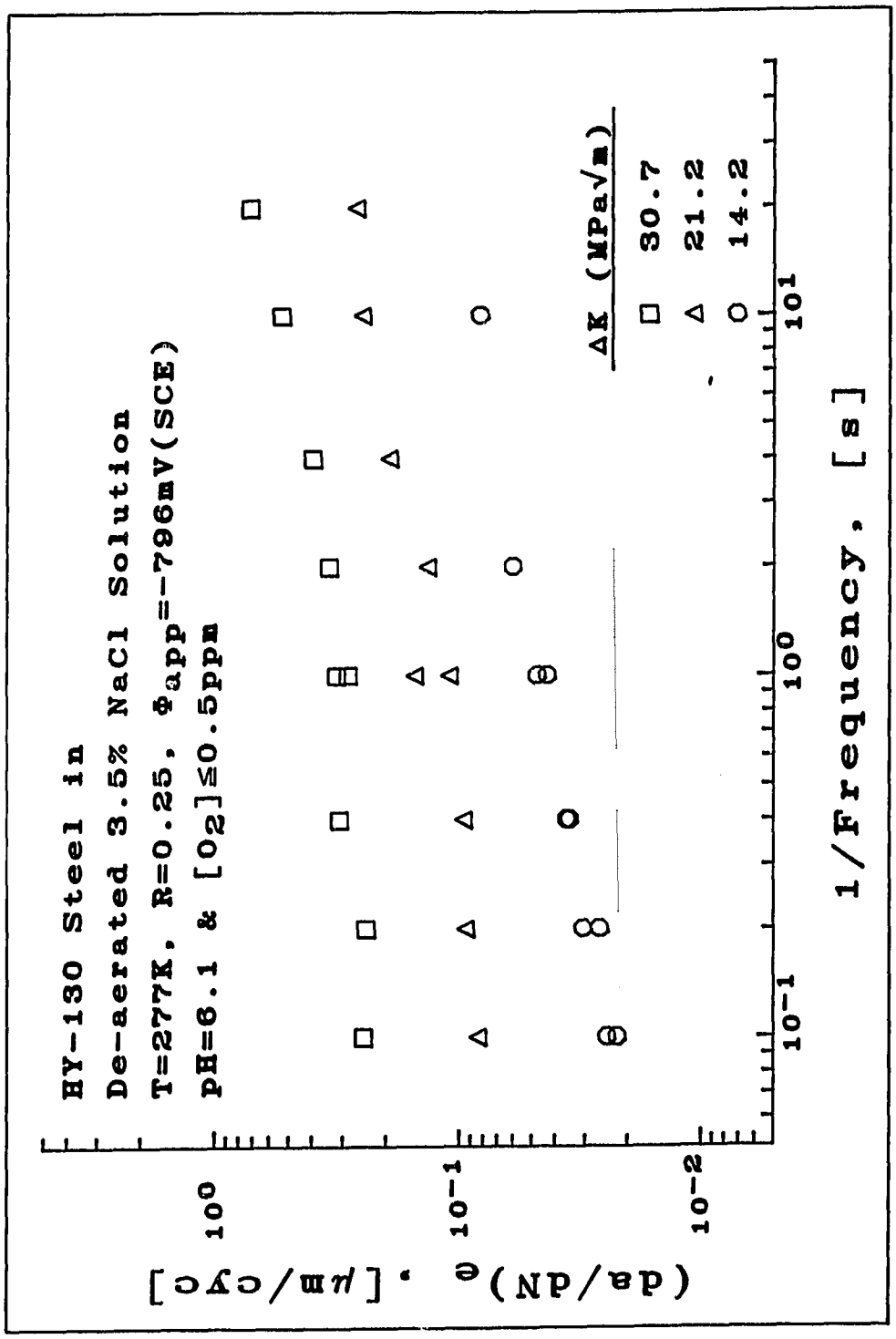

FIGURE A.43: The influence of frequency and ΔK level on the total CGR at T=277 K.

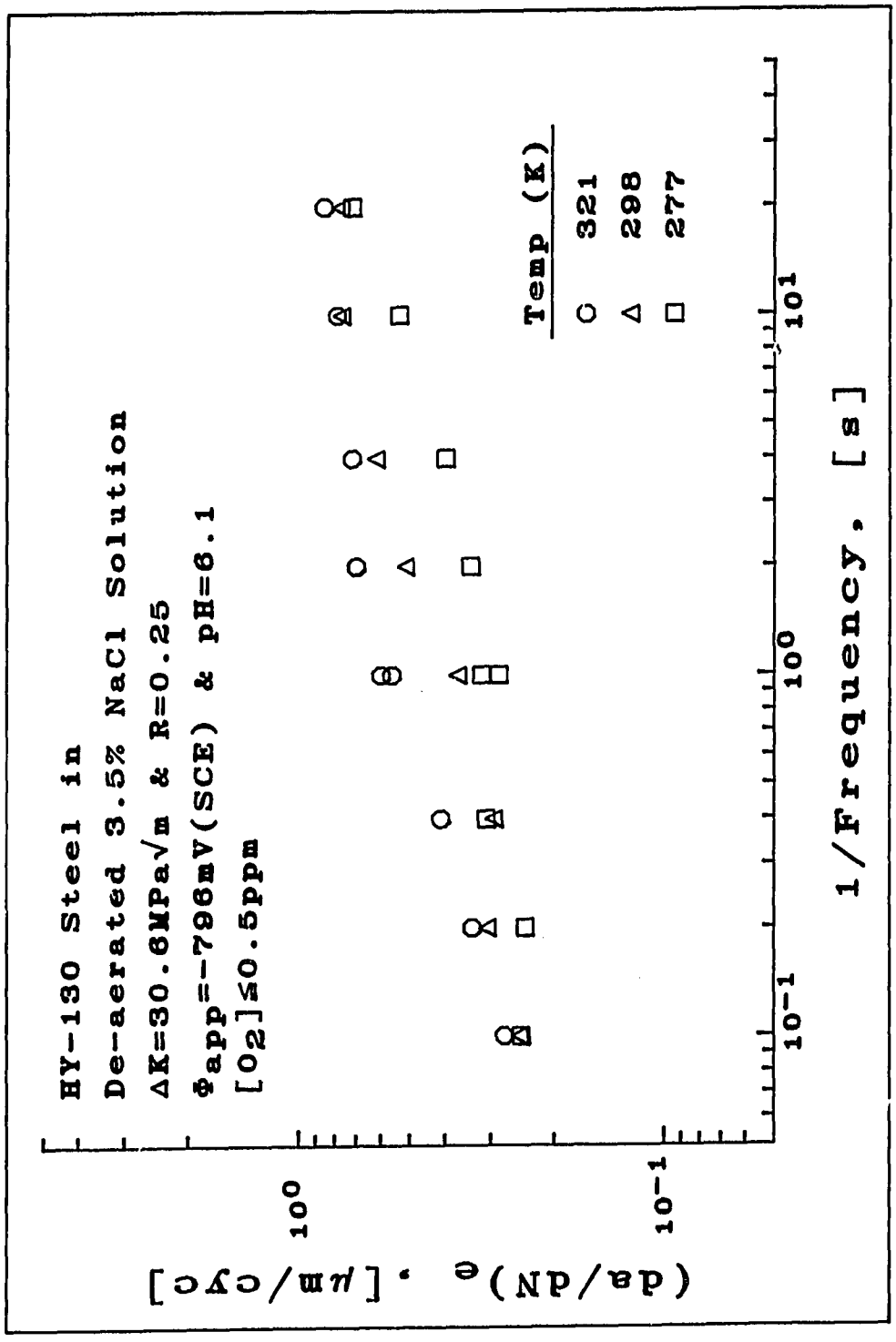

FIGURE A.44: The influence of frequency and T level on the total CGR at ΔK=30.6 MPa$\sqrt{m}$.

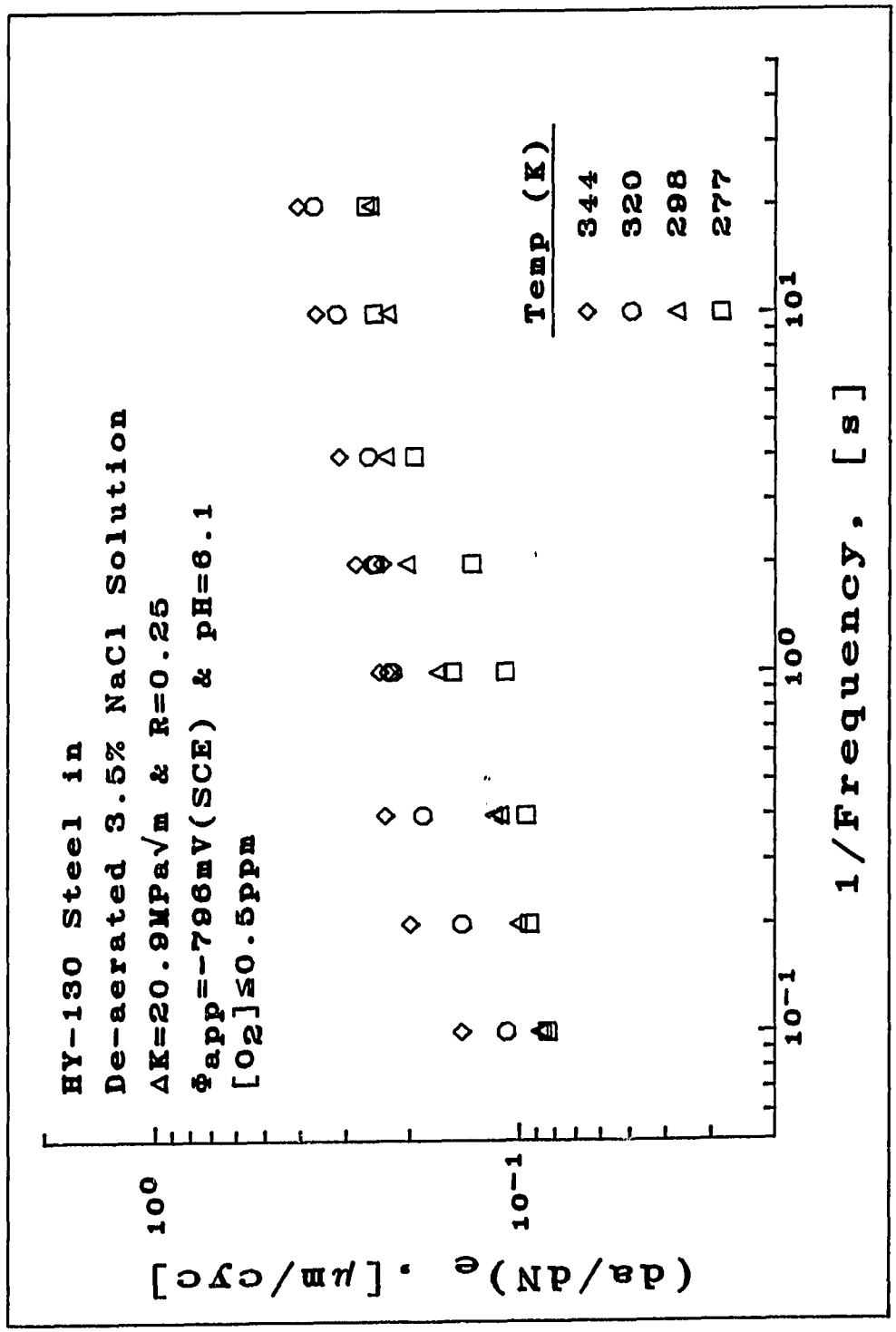

FIGURE A.45: The influence of frequency and T level on the total CGR at ΔK=20.9 MPa$\sqrt{m}$.

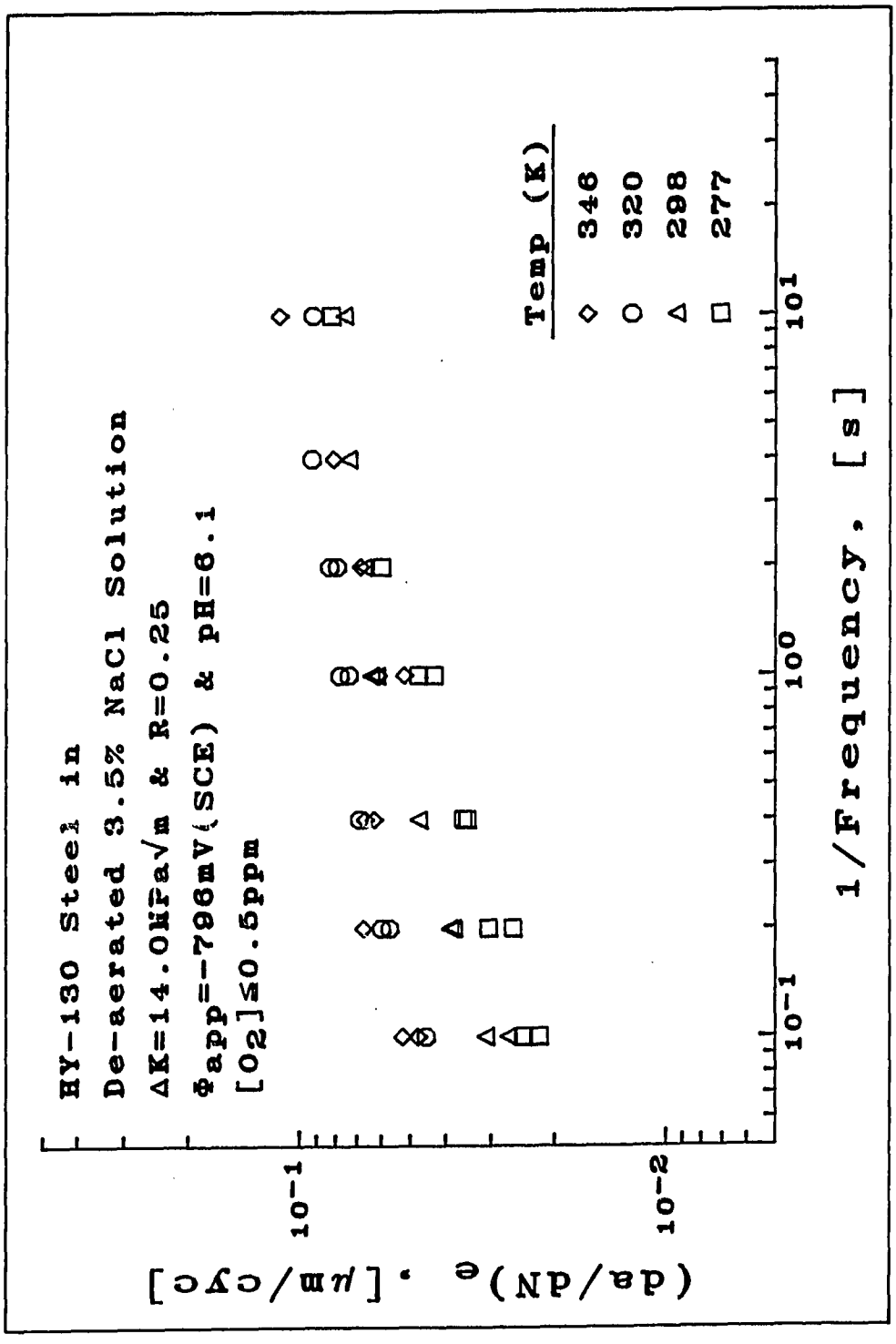

FIGURE A.44: The influence of frequency and T level on the total CGR at ΔK=14.0 MPa$\sqrt{m}$.

VITA

James P. Thomas was born on June 23, 1958 to Clifford and Margaret Thomas in Detroit Michigan. He received his BSE in Mechanical Engineering in 1983 from the University of Michigan-Dearborn, and his MSE in Mechanical Engineering in 1984 from the University of Michigan-Ann Arbor.

During his undergraduate studies, Mr. Thomas worked as an engineering co-op student at the Cadillac Gage Company, Controls Division, in Warren Michigan. The job consisted of assisting mechanical design and test engineers in their duties and lasted four semesters from 1980 to 1982. The association with Cadillac Gage Company continued after Mr. Thomas received his BSE degree where he worked as a Design Engineer for the time period between the finish of the BSE degree and the start of the MSE degree.

Mr. Thomas came to Lehigh University in August of 1984 to begin work on his Ph.D. in Applied Mechanics. His Ph.D. adviser was Professor R. P. Wei, and his research topic was in the field of fatigue and fracture. He was a General Motors Teaching Fellow for four years of his Ph.D. study, and he taught classes during the last year of his studies. He will receive his Ph.D. in 1989 and his dissertation will be titled: "Mechanistic Modeling of Corrosion Fatigue Crack Growth of Steels in Aqueous Solutions."

He is a member of Tau Beta Pi Engineering Honor Society, and a professional member of the American Society for Testing and Materials (E-09 and E-24) and the Society for Experimental Mechanics.

He is unmarried at present, and hopes to teach and do research as a university faculty member in the future.